A Fixed-Target Programme at the LHC:
Physics Case and Projected Performances for Heavy-Ion, Hadron, Spin and Astroparticle Studies

C. Hadjidakis[a,1], D. Kikoła[b,1], J.P. Lansberg[a,1,*], L. Massacrier[a,1], M.G. Echevarria[c,2], A. Kusina[d,2],
I. Schienbein[e,2], J. Seixas[f,g,2], H.S. Shao[h,2], A. Signori[i,2], B. Trzeciak[j,2], S.J. Brodsky[k], G. Cavoto[l],
C. Da Silva[m], F. Donato[n], E.G. Ferreiro[o,p], I. Hřivnáčová[a], A. Klein[m], A. Kurepin[q], C. Lorcé[r], F. Lyonnet[s],
Y. Makdisi[t], S. Porteboeuf[u], C. Quintans[g], A. Rakotozafindrabe[v], P. Robbe[w], W. Scandale[x],
N. Topilskaya[q], A. Uras[y], J. Wagner[z], N. Yamanaka[a], Z. Yang[aa], A. Zelenski[t]

[a]IPNO, CNRS-IN2P3, Univ. Paris-Sud, Université Paris-Saclay, 91406 Orsay Cedex, France
[b]Faculty of Physics, Warsaw University of Technology, ul. Koszykowa 75, 00-662 Warsaw, Poland
[c]Istituto Nazionale di Fisica Nucleare, Sezione di Pavia, via Bassi 6, 27100 Pavia, Italy
[d]Institute of Nuclear Physics Polish Academy of Sciences, PL-31342 Krakow, Poland
[e]Laboratoire de Physique Subatomique et de Cosmologie, Université Grenoble Alpes, CNRS/IN2P3, 53 Avenue des Martyrs,
F-38026 Grenoble, France
[f]Dep. Fisica, Instituto Superior Tecnico, Av. Rovisco Pais 1, 1049-001 Lisboa, Portugal
[g]LIP, Av. Prof. Gama Pinto, 2, 1649-003 Lisboa,Portugal
[h]LPTHE, UMR 7589, Sorbonne Universityé et CNRS, 4 place Jussieu, 75252 Paris Cedex 05, France
[i]Theory Center, Thomas Jefferson National Accelerator Facility, 12000 Jefferson Avenue, Newport News, VA 23606, USA
[j]Institute for Subatomic Physics, Utrecht University, Utrecht, The Netherlands
[k]SLAC National Accelerator Laboratory, Stanford University, Menlo Park, CA 94025, USA
[l]"Sapienza" Università di Roma, Dipartimento di Fisica & INFN, Sez. di Roma, P.le A. Moro 2, 00185 Roma, Italy
[m]P-25, Los Alamos National Laboratory, Los Alamos, NM 87545, USA
[n]Turin University, Department of Physics, and INFN, Sezione of Turin, Turin, Italy
[o]Dept. de Física de Partículas & IGFAE, Universidade de Santiago de Compostela, 15782 Santiago de Compostela, Spain
[p]Laboratoire Leprince-Ringuet, Ecole polytechnique, CNRS/IN2P3, Université Paris-Saclay, Palaiseau, France
[q]Institute for Nuclear Research, Moscow, Russia
[r]CPHT, École Polytechnique, CNRS, 91128 Palaiseau, France
[s]Southern Methodist University, Dallas, TX 75275, USA
[t]Brookhaven National Laboratory, Collider Accelerator Department
[u]Université Clermont Auvergne, CNRS/IN2P3, LPC, F-63000 Clermont-Ferrand, France.
[v]IRFU/DPhN, CEA Saclay, 91191 Gif-sur-Yvette Cedex, France
[w]LAL, Université Paris-Sud, CNRS/IN2P3, Orsay, France
[x]CERN, European Organization for Nuclear Research, 1211 Geneva 23, Switzerland
[y]IPNL, Université Claude Bernard Lyon-I and CNRS-IN2P3, Villeurbanne, France
[z]National Centre for Nuclear Research (NCBJ), Hoża 69, 00-681, Warsaw, Poland
[aa]Center for High Energy Physics, Department of Engineering Physics, Tsinghua University, Beijing, China

Abstract

We review the context, the motivations and the expected performances of a comprehensive and ambitious fixed-target program using the multi-TeV proton and ion LHC beams. We also provide a detailed account of the different possible technical implementations ranging from an internal wire target to a full dedicated beam line extracted with a bent crystal. The possibilities offered by the use of the ALICE and LHCb detectors in the fixed-target mode are also reviewed.

*Corresponding author
[1]Editor
[2]Section editor

arXiv:1807.00603v1 [hep-ex] 2 Jul 2018

Contents

1. Introduction

The objective of this review is to highlight the physics opportunities of using the most energetic proton and ion beams ever in the fixed-target mode and to review the feasibility of an outstanding physics program for heavy-ion, hadron, spin and astroparticle physics with existing (LHCb or ALICE) or new set-ups while complying with constraints of a parasitic running along with the LHC collider program.

Let us first recall that the fixed-target mode offers several unique assets [1] compared to the collider mode which are particularly relevant with the LHC beams in the context of high-energy physics :

- An outstanding luminosity thanks to the high density of the target at no cost for the LHC collider-mode experiments. Both an internal gas target or a bent-crystal-extracted beam from the beam halo allow for yearly luminosities well above those of similar machines, in particular RHIC, in the ballpark of the LHC and Tevatron collider luminosities;

- The accessibility with standard detectors, thanks to the boost between the colliding-nucleon centre-of-mass system (c.m.s.) and the laboratory system, to the far backward c.m.s. region which remains completely uncharted with hard reactions until now. An acceptance of $1 \leq \eta_{(lab)} \leq 5$, combined with high luminosities, essentially allows one to measure any probe down to the very end of the backward phase space;

- An extended number of species for the target, including deuteron and ^{3}He allowing for unique neutron studies with the possibility to change them in a reduced amount of time for short runs;

- The c.m.s. energy per nucleon-nucleon collision ($\sqrt{s_{NN}}$) is identical for all 7 TeV proton and 2.76 TeV lead induced collisions, namely 115 GeV for pp, pd, pA systems and 72 GeV for Pbp, Pbd, PbA systems[3]. This allows for nuclear-modification-factor measurements with drastically reduced systematic uncertainties in an energy domain between the SPS and RHIC experiments in an unexplored rapidity domain;

- The target polarisation –whereas the LHC beams are unpolarised. This offers uncountable opportunities for single spin asymmetry (SSA) measurements –at large momentum fractions– which have been the object of a growing attention in the recent years at RHIC, at CERN and at Fermilab.

Owing to these advantages, we have identified three main topics for a strong physics case motivating a complete fixed-target program at the LHC (referred to AFTER@LHC in what follows) with one or more detectors. These covers studies of

- the high momentum fraction (x) frontiers in nucleons and nuclei with a specific emphasis on the gluon and heavy-quarks and the implication for astroparticle physics;

- the spin content of the nucleons with a focus on single transverse-spin asymmetries (STSAs) and azimuthal asymmetries generated by the spin of the partons;

- the hot medium created in ultra-relativistic heavy-ion collisions with novel quarkonium and heavy-quark observables in a new energy domain and with identified light hadrons down to the target rapidity.

---

[3] $\sqrt{s_{NN}}$ for lighter beams remains on the order of 70 GeV.

The structure of this review is as follows. In the section 2, we quickly review the context in which such a AFTER@LHC program would take place and highlight the motivations for the 3 main aforementioned research axes. In the section 3, we provide a state-of-the-art overview of the different available technologies to initiate collisions of the LHC beams with fixed targets. In the section 4, we elaborate on the detector aspects both for an ideal detector and for existing detectors, *i.e.* those of the LHCb and ALICE collaborations[4]. In the section 5, we extensively review the projected performances for flagship studies and the studies proposed within the community for each of the 3 main topics. The section 6 gathers our conclusions.

2. Motivations

2.1. The high-x frontier

Whereas the need for precise measurements of the partonic structure of nucleons and nuclei at small momentum fractions x is usually highlighted as a strong motivation for new large-scale experimental facilities, such as the Electron-Ion Collider (EIC) or Large Hadron electron Collider (LHeC) projects, the structure of nucleon and nuclei at *high x* is probably as poorly known. Let us mention the long-standing puzzles such as the origin of the nuclear EMC[5] effect in nuclei or a possible non-perturbative source of charm or beauty quarks in the proton which would carry a relevant fraction of its momentum. With an extensive coverage of the backward region corresponding to high x in the target, AFTER@LHC is probably the best program for such physics with hadron beams.
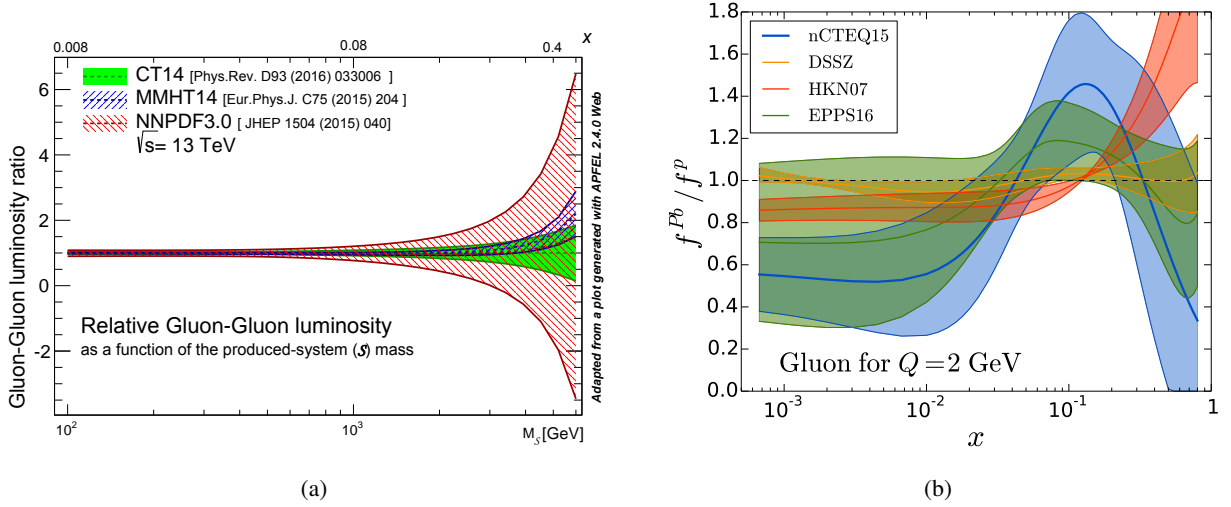
Figure 1: (a) Gluon-Gluon-luminosity uncertainty computed for 3 sets of proton PDFs as a function of the invariant mass (M_S) of a to-be produced system at $\sqrt{s}$ = 13 TeV. For $y \sim 0$, $x \simeq M_S/\sqrt{s}$ at the LHC (indicated on the upper x axis), whereas the kinematics of the AFTER@LHC program is mainly that of high x where the uncertainties blow up. Plot done thanks to the APFEL program [3]. (b) Compilation of the gluon nuclear PDF uncertainties [4, 5, 6, 7] in a lead nucleus at a factorisation scale (here denoted Q) of 2 GeV.

Studying the so-called high-x physics also provides us with novel decisive means to advance our experimental knowledge of the still poorly understood confinement properties of the strong interaction, which

---

[4]In what follows, AFTER@LHC will refer to a generic experimental fixed-target set-up using the LHC beams, AFTER@LHCb, AFTER@ALICE, AFTER@ALICE$_\mu$ and AFTER@ALICE$_{CB}$ to specific implementations using the LHCb or ALICE detectors.

[5]Named after its observation in 1983 by the European Muon Collaboration [2].

is one of the last open questions about the Standard Model. Indeed, studying high-x fluctuations of a nucleon, where a single gluon carries the majority of the confined-system momentum, certainly tests QCD in a new limit never explored before. On the quark side, an improved experimental determination of the d/u PDF ratio for $x \rightarrow 1$ is also crucial to tell which picture is valid between an SU(6) symmetric one where $d/u \rightarrow 1/2$, the dominance of a quark-scalar diquark where $d/u \rightarrow 0$, quark-hadron duality where $d/u \rightarrow 0.42$ or a simple perturbative QCD one where $d/u \rightarrow 1/5$. Beside such fundamental issues touching upon our understanding of confinement, chartering the high-x structure of nucleons and nuclei has very practical implications for instance to improve our knowledge of parton luminosities at existing and future hadron colliders (LHC, RHIC, Tevatron, FCC, ...) (see Fig. 1(a)) but also of ultra high energy cosmic rays (UHECR) in particular the neutrino in the PeV range.

Beyond unbound nucleons, our understanding of the gluon and quark content of the nuclei is also very limited at high x. Since the first observation via DIS measurements of a nuclear suppression of the quark momentum distribution –the aforementioned EMC effect–, DIS data got more precise and confirmed the suppression. Yet, we still do not understand its physical origin. Recently, it was argued that the $x > 1$ scaling plateaux of some nucleus structure functions, attributed to short-range nucleon-nucleon correlations related to high local densities in nuclei, could be related to the EMC effect [8]. In this context, the complete lack of data constraining the gluon density in this region (see Fig. 1(b)) is probably highly detrimental. Only indirect constraints from the scaling violation of the quark distribution exist, which obviously do not give additional experimental information. We are also lacking precise nuclear Drell-Yan (DY) data which provide a unique window on the sea quarks. A precise measurement of the *gluon* EMC and of its nuclear number (A) dependence, combined with precise DY data at high x, would provide decisive insights into the origin of the EMC effects which goes along with understanding how quark and gluons behave in the nuclear medium.
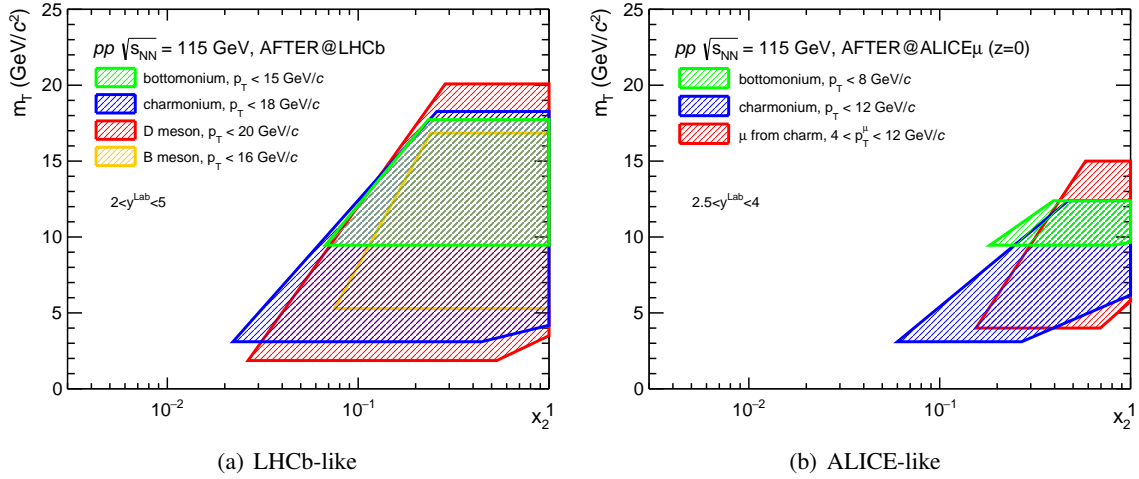
Figure 2: Typical kinematical reach in x_2 and the scale (chosen to be m_T) of the fixed-target mode with a detector acceptance like (a) LHCb and (b) ALICE.

At the interface between the proton and nuclear cases, the deuteron and ^{3}He have a particular place. On the one hand, they can provide us with quasi-free neutron targets allowing us to test assumptions such as $u^p = d^n$, $\bar{u}^p = \bar{d}^n$ based on the isospin symmetry or whether gluons behave differently in protons than in neutrons. On the other hand, it is an appealing playground to test our understanding of the dynamics of simple nucleon-bound system and hidden colour configurations of six quarks (see *e.g.* [9]).

For all these reasons, the unique opportunities offered by AFTER@LHC to probe with unprecedented precision and with reliable as well as novel perturbative probes the high x domain are priceless. Fig. 2 schematically illustrates, with a small set of selected (gluon-sensitive) probes, how the fixed-target mode with multi TeV beams allows one to methodically probe the high x region in the target, namely high x_2. This obviously applies equally for quark, heavy-quark, gluon and antiquark sensitive probes in protons, deuterons and light or heavy nuclei. The case of the lead is even richer, when used as beam particle, which allows one to probe it down to values as small as 0.005. The possibility to study the large-x-charm content in the (nucleon and nucleus) target will also allow one to severely reduce the uncertainty of the prompt neutrino fluxes.

Finally, let us highlight the opportunities connected to antiproton ($\bar{p}$) measurements in new kinematical ranges and for new systems in order to further constrain the modelling of the conventional $\bar{p}$ astrophysical sources. One of the possible very original measurements is that of $\bar{p}$ nearly at rest from fixed He, C, N or O targets bearing on the PID capabilities of the ALICE central barrel. This would constrain highly energetic $\bar{p}$ from (He,C,N,O)+$p \to \bar{p} + X$.

2.2. *Unraveling the nucleon spin*

Despite decades of efforts, the internal structure of the nucleons and, in particular their constituent distribution and dynamics, is still largely unknown. One of the most significant issues is our limited understanding of the spin structure of the nucleon, specifically how its elementary constituents (quarks and gluons) bind into a spin-$\frac{1}{2}$ object. Essentially, there are two types of contributions to the nucleon spin from quarks and gluons: their spin and their Orbital Angular Momentum (OAM). For a longitudinally polarised nucleon, *i.e.* with helicity $+\frac{1}{2}$, one has

$$\frac{1}{2} = \frac{1}{2}\Delta\Sigma + \Delta G + \mathcal{L}_g + \mathcal{L}_q \,, \tag{1}$$

where $\frac{1}{2}\Delta\Sigma$ denotes the combined spin contribution of quarks and antiquarks, ΔG the gluon spin, and $\mathcal{L}_{q,g}$ the quark and gluon OAM contributions (see *e.g.* [10, 11, 12]). Eq. (1) is valid at any energy scale at which the nucleon is probed and this calls for the study of the scale evolution of the individual contributions at different scales. These questions naturally generalise to any spin-J hadron.

We have come a long way since the so-called *spin crisis* (Fig. 3(a)), faced in the eighties when the measurements performed by the European Muon Collaboration (EMC) revealed that only a small fraction of the nucleon spin was generated by the spin of quarks [14]. The crisis has evolved into a puzzle, which consists now in determining how large the different quark and gluon contributions to the nucleon spin are, in disentangling them and in explaining them from first principles in QCD.

Recent experimental data have shown that quarks and antiquarks account for only about 25% of proton total longitudinal spin [15] and the gluon contribution could be as large as 40% [6]. It is thus expected that a significant part of the proton spin arises from the transverse dynamics of quarks and gluons (*i.e.* via $\mathcal{L}_q$ and $\mathcal{L}_g$), which has however not yet been measured. This emphasises how crucial our understanding of the transverse motion of quarks and gluons inside the proton is, in order to validate our current picture of the nucleon structure.

In order to measure the parton OAM, one should in principle access observables which are sensitive to the parton position and momentum. This is the realm of the Generalised Parton Distributions (GPDs) relevant for exclusive processes. Yet, one can also indirectly access information on the orbital motion of the

---

[6]The latter has been tested in the region $x > 0.05$ [16, 17]. Additional studies in other kinematic regions are required.

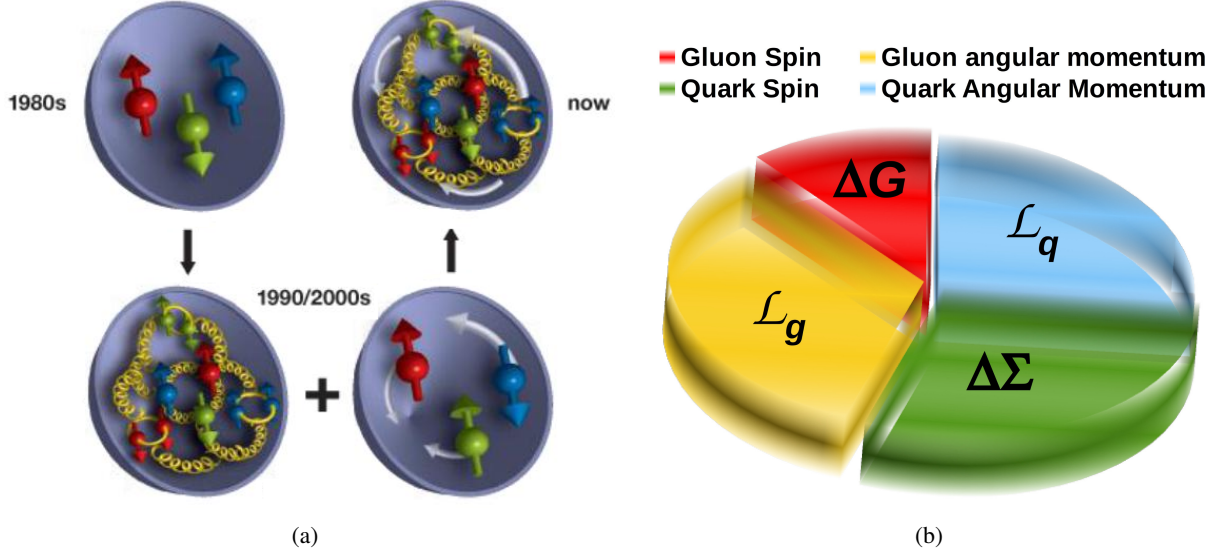(a)   (b)

Figure 3: (a) Evolution of our understanding of the spin content of the nucleon [adapted from [13]]. (b) Decomposition of the nucleon spin relevant for high-energy processes.

partons bound inside hadrons via Single Spin Asymmetries (SSAs) in different hard-scattering processes, in particular with a transversely polarised hadron (see [18, 19] for recent reviews). In these single transverse-spin asymmetries (STSAs), one can access left-right asymmetries in the parton distributions with respect to the plane formed by the proton momentum and spin directions. These asymmetries are naturally connected to the transverse motion of the partons inside the polarised nucleons.

Historically large STSAs (also denoted A_N) have been observed in single forward π [20, 21, 22] and K production [21] in high-energy $p^\uparrow p$ collisions at Fermilab and Brookhaven National Laboratory, towards the valence region. They have also been observed in semi-inclusive DIS (SIDIS) by HERMES [23] and COMPASS [24] collaborations. Studies to look for STSAs in J/ψ production in $p^\uparrow p$ collisions at RHIC [25] have also been carried out. Intense theoretical works have resulted in a widely accepted picture according to which these (large) asymmetries, which were expected to vanish at high energies, are due to re-scatterings of the quarks and gluons with the remnants of the hadron undergoing the interaction [26, 27, 28]. It is also accepted that they vanish for partons which do not carry any transverse momentum.

As for now, these STSAs can be treated via two dual approaches [29]. The first is an extension of the collinear parton model of Feynman and Bjorken with the introduction of three-parton (Efremov-Teryaev-Qiu-Sterman) correlations [30, 31, 32], namely the Collinear Twist-3 (CT3) formalism [7]. The second, called the Transverse-Momentum Dependent (TMD) factorisation [35, 36, 37, 38, 39, 40, 41, 42, 43], relies on a complete three-dimensional mapping of the parton momentum and encodes all the possible spin-spin and spin-orbit correlations between the hadron and its constituents. In particular, the effect of the aforementioned re-scatterings, responsible of the STSAs, is encoded into the gauge links in the definition of the TMD PDFs. A particular case is the so-called Sivers function [44, 45]. Within CT3 formalism, the rescattering effect is explicitly considered in the hard-scattering coefficients.

Both formalisms have their preferred range of applicability. The CT3 approach is better suited to describe A_N for inclusive hadron production [46] but can also be applied to DY pair [47, 48, 49] or isolated

---

[7]Recently it has been found that STSA for pion production in proton-proton collisions seems to be dominantly driven by three-parton fragmentation functions [33, 34]

photon [50] production. With regards to the AFTER@LHC physics case, this mainly concerns heavy-flavour and quarkonium production, whose SSAs are extremely poorly known, if not unknown at all. TMD factorisation is usually used for processes where the transverse momentum of the initial partons is accessible owing to the absence of hard final-state radiations. In the case of AFTER@LHC, this includes pseudo-scalar quarkonium, quarkonium-pair and other associated production of colourless particles, and of course the DY process. With its high luminosity, a highly polarised target and an access towards the large momentum fraction $x^\uparrow$ in the target, AFTER@LHC is probably the best set-up to carry out an inclusive set of A_N measurements both to improve existing analyses and to perform studies which would simply be impossible without. Let us recall that nearly nothing is known from the experimental side about the gluon Sivers function (see e.g. the review [51] and recent measurements [25, 52, 53, 54]). The polarisation of not only hydrogen but also deuterium and helium targets allows for an even more ambitious spin program bearing on the neutron and spin 1 bound states (see e.g. [39, 41] and references therein).

As explained, the TMD approach allows us to investigate the structure of hadrons in a three-dimensional momentum space (see [42] and references therein) in rigorous and systematic way. It is important to note that it is not restricted to the study of A_N. It can help us probe in a direct manner the transverse dynamics of the partons as well as their own polarisation in *unpolarised* nucleons. The latter in particular generates observable azimuthal asymmetries in the final state. These are related to another TMD PDF of great interest, the Boer-Mulders function [55]: it describes the correlation between the quark transverse spin and its transverse momentum in an unpolarised hadron, and it explains the well-known violation of the Lam-Tung relation [56] in unpolarised DY reaction. Its counterpart for the gluon content is the distribution of linearly polarised gluons in unpolarised protons which affects for instance the H^0 kinematical distribution at the LHC. At AFTER@LHC, such a distribution can be probed and extracted, for instance, via pseudo-scalar quarkonium production [57, 58] and associated quarkonium production [59, 60], whereas the quark Boer-Mulders functions can be accessed in DY pair production.

It is important to note that all these measurements (A_N, azimuthal asymmetries or transverse-momentum spectra) have to be measured in *pp* collisions as mandatory complementary pieces of information to similar studies in lepton-induced reactions. Indeed, contrary to usual PDFs, the partonic quantities discussed above are not universal. For instance, some, as the quark Sivers function, are predicted to change sign when generating the STSA in SIDIS and in DY reactions. In other words, the time-reversal odd TMD distributions are process-dependent, but the process dependence is calculable (from the symmetry properties of the theory). This feature, sometimes referred to as *generalised universality*, is driven by the nature of the rescatterings generating the SSA; they can be from the initial or final states. More technically, they are connected to the gauge link in the definition of the TMD PDFs [61, 62, 63]. This "sign change" represents one of the most important predictions of the TMD factorisation and dedicated experiments have been proposed to check it [64, 65, 66, 67]. Such a process dependence is also explicit in the CT3 formalism. Recently the first measurement in DY was performed by the COMPASS collaboration [68], hinting at the sign change. With AFTER@LHC, one could go further than the current proposals and perform quantitative tests of this generalised universality, deeply connected to the symmetries of QCD. AFTER@LHC will be a unique place to probe such aspects of the parton transverse dynamics in the gluon sector, which requires even more experimental inputs both from lepton- and hadron-induced reactions. AFTER@LHC will also provide a unique playground to explore in details the connection between the TMD and CT3 approaches [69, 70, 71, 72, 29]), in particular in the gluon sector. This will open the way for a full three-dimensional mapping of the parton momentum and, in turn, for more insights on the orbital angular momentum of the quarks and gluons.

2.3. The nuclear matter in new rapidity and energy domains

One of the prime objectives of Heavy-ion (HI) physics at high-energy facilities is the search and characterisation of a novel state of matter where the quark and the gluons are deconfined. In this state, which should be the prevailing one of the Universe a few microseconds after the Big Bang, quarks and gluons roam nearly freely over distances of a few femtometers, *i.e.* distances much larger than the hadron sizes in which they are normally confined.

The existence of such a state is a natural consequence of the asymptotic freedom property of QCD whereby the strong interaction becomes weak at small distances and high momentum transfers. It is expected to be reached when the surrounding hadronic matter is extremely compressed or heated – resulting in high momentum transfers in the system. These conditions can be achieved in ultra-relativistic collisions of nuclei and the resulting new phase can be observed using specific probes. Such probes are essentially of three kinds, namely radiated particles from the plasma itself (*i.e.* photons), the destruction of heavy-quark bound states and the momentum-spectrum modification of particles.

(a)   (b)
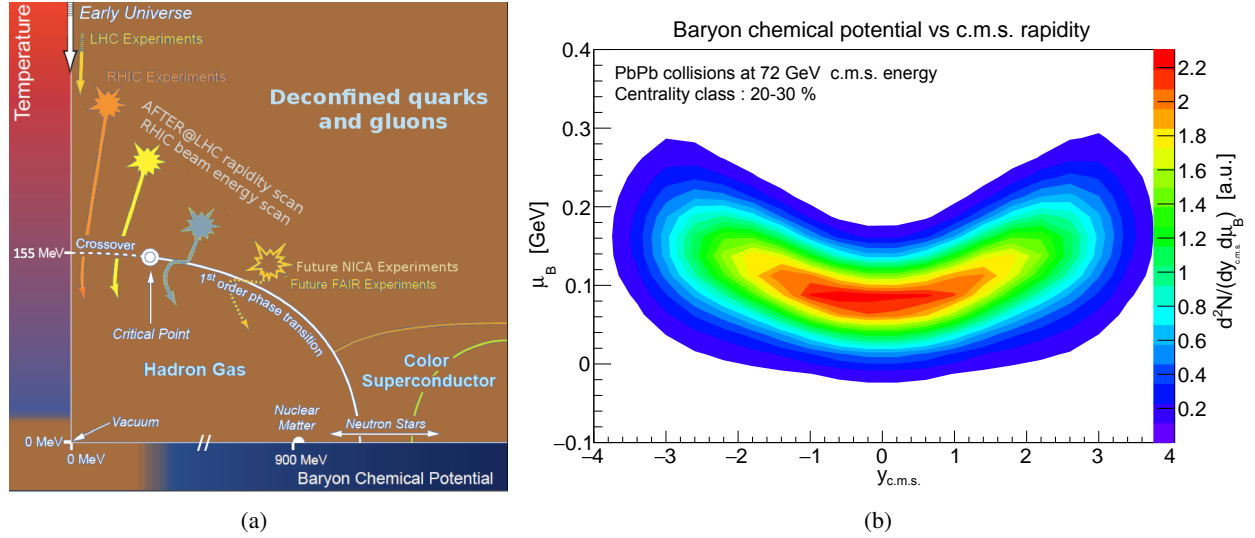
Figure 4:   (a) Phase diagram of the strongly interacting matter and the reach of AFTER@LHC HI program. (b) The baryonic chemical potential μ_B as a function of the rapidity $y_{\text{c.m.s.}}$ in mid-central PbPb $\sqrt{s_{NN}}$ = 72 GeV collisions predicted by the viscous hydro+cascade model vHLLE+UrQMD [Adapted from [73]]. The colour represents the differential density of produced particles as a function of $y_{\text{c.m.s.}}$ and μ_B.

Fig. 4(a) shows the most up-to-date phase diagram of the strongly interaction matter, gathering all our knowledge progressively acquired since the very first relativistic heavy-ion collisions – nearly thirty years ago. With the LHC multi-TeV heavy-ion beams (for now, lead ions with an energy per nucleon of 2.76 TeV), AFTER@LHC with a c.m.s. energy of 72 GeV provides a complementary coverage to the RHIC- and SPS-based experiments in the region of high temperatures and low baryon-chemical potentials where a Quark-Gluon Plasma (QGP) is expected to be produced. Moreover, model calculations indicate that the baryonic chemical potential μ_B and the temperature T depend on the rapidity [74, 75, 73]. Figure 4(b) shows an example of such a μ_B vs. $y_{\text{c.m.s.}}$ relation for mid-central PbPb $\sqrt{s_{NN}}$ = 72 GeV collisions by the vHLLE+UrQMD model [73]. Measurements conducted as a function of $y_{\text{c.m.s.}}$ will give access to different μ_B and T values. As such, the AFTER@LHC HI program can bear on a "rapidity scan" to study both the deconfined regime and the expected phase transition to the hadronic gas. It would be a new approach to investigate the QCD phase diagram, complementary to the RHIC Beam Energy Scan (BES) program.

Let us also recall here a key advantage of the fixed-target mode, namely the possibility to study different colliding systems with short transition periods and while keeping high collected luminosities.[8] Another key advantage is the obvious capacity to instrument the nucleus-target region, namely y_{Lab} or η_{Lab} close to 0, which would be the reach of most of the collider detectors used in the fixed-target mode. Based on these assets, the physics case for HI physics with AFTER@LHC can be outlined as follows.

Given the c.m.s.-energy range, HI measurements at AFTER@LHC have the potential to provide us with crucial information about the QGP properties and the nature of the phase transition to the hadronic gas regime. To do so, three experimental degrees of freedom are at our disposal: (i) scanning the longitudinal extension of this hot medium, (ii) colliding systems of different sizes and (iii) analysing the centrality dependence of these collisions. To our knowledge, no other experimental program could fully rely on these three variables. Together, they should give us a unique lever arm to probe the hot medium at different enough temperatures and energy densities. They will allow one, for instance, to probe the temperature dependence of the shear viscosity to entropy densitiy ratio (η/s) of the created matter by measuring the rapidity dependence of the anisotropic flow as it was shown recently in [76] and presented in Fig. 5.
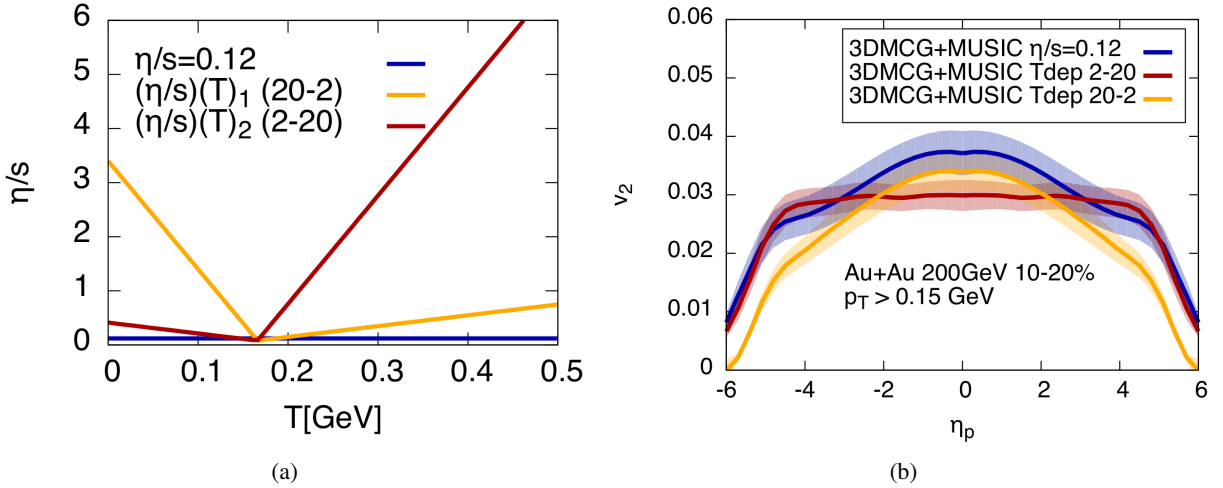

(a)   (b)

Figure 5:   (a) Different scenarios of the temparature dependence of the medium shear viscosity to entropy density ratio (η/s) at μ_B=0 (b) sensibility of the second Fourier coefficient (v_2) of the azimuthal asymmetry measured as a function of rapidity with (η/s) and temperature according to 3D+1 viscous hydrodynamic calculations. [Adapted from [77]].

More generally, one can perform a tri-dimensional tomography of the hot medium produced in ultra-relativistic HI collisions at $\sqrt{s_{NN}} = 72$ GeV. Such a tomography will rely on a set of precise measurements in a kinematical region ($y_{\text{c.m.s.}}$ and $\sqrt{s_{NN}}$) which could so far only be studied with low accuracy and with an extremely limited set of probes [78, 79]. We believe that they will give us drastically new information on the QGP properties in the longitudinal dimension and help us settle long-standing debates about probes such as heavy-quark(onium) production in the range from SPS to RHIC energies [80, 81, 82]. These issues admittedly hinder their potential as golden probes of the QGP [83].

---

[8]At the collider LHC, only 4 colliding systems have been studied so far: *pp*, *p*Pb, XeXe and PbPb. Even though the RHIC complex is more flexible in this regards, only *pp*, *d*Au, CuCu and AuAu collisions could be studied in the first 10 years of running with enough statistics to study heavy-flavour production. Upgrades were for instance needed to look at CuAu, UU, *p*Al, *p*Au or ^{3}HeAu collisions. In comparison, the LHCb SMOG system (see section 3.3.1) which could only so far take data in small periods already collected data for 5 systems (*p*He, *p*Ar, *p*Ne, PbAr and PbNe).

Measurements at $y_{c.m.s.} \simeq 0$ are also at reach with detector coverages about $\eta_{Lab} \simeq 4.0$. Studying an extensive set of hard probes in this region, where the yields are the highest, is meant to provide us with a very reliable calibration of the properties of the system (temperature, viscosity) in order to initiate the scan in the longitudinal direction via the rapidity dependence.

3. How to make fixed-target collisions at the LHC?

3.1. Overview

Several technological options are currently under investigation to perform dedicated fixed-target experiments at the LHC. One can indeed initiate collisions of the LHC beam particles with nucleons or nuclei at rest :

- by letting the full LHC beam go through a gas target in the LHC beam pipe,

- by extracting halo particles by means of a bent-crystal deflector onto a target positioned outside the beam pipe with a dedicated beam line or inside the beam pipe,

- or by placing a wire target intercepting the faint beam halo in the beam pipe.

The aim of this section is to summarise the advantages, the performances as well as the challenges of each solution. We first discuss them and then compare their performances and limitations.

The LHCb collaboration with its SMOG [84] and VELO [85] systems has demonstrated [86] that gas injection within a certain range is tolerable and does not lead to vacuum instabilities thus paving the way toward a genuine gas target with the polarisation of light nuclei with higher densities, as well as for heavy noble gases. It allows one to use an existing LHC detector, resulting in limited costs and a relatively short time-scale installation. As we will discuss in the following sections, the acceptances of the ALICE and LHCb detectors are, in general, well suited for data taking in the fixed-target mode.

A long narrow tube –commonly referred to as a storage cell [87]– placed on-axis of the LHC beam and fed by a polarised or unpolarised gas clearly presents an interesting opportunity to reach high luminosities for the gas-target option (see section 3.3.3). Such a configuration allows for different beam-target combinations including highly polarised ones – pending the cell-coating compatibility with the LHC vacuum constraints. The possibility for a density calibration of the storage-cell targets has still to be studied. If successful this would, together with the known LHC beam current, allow one to measure absolute luminosities and cross sections. For a given (areal) target density, the storage cell requires the lowest – but still sizeable – gas flow into the LHC vacuum system.

Alternatively, higher gas fluxes can directly be injected orthogonally to the beam (see section 3.3.2). This is how the RHIC H-jet polarimeter [88], with (highly) polarised injected hydrogen, operates. In general, this leads to lower luminosities than the storage-cell option. However, if used in conjunction with the ALICE detectors, the luminosities obtainable with a gas-jet system would already be reaching the limit of the detector data-taking capabilities. In the case of polarised ^{3}He and other unpolarised gases, more intense sources can in principle be used to compensate for the smaller target-areal density. The advantage of this option is the very high reachable polarisation of the target and the limited need of R&D for an installation in the LHC complex.

On the other hand, bent crystals are being developed as part of the collimators protecting the machine [89]. They may also be placed near the beam in order to deflect halo particles and guide them onto an external target (see section 3.5.1). Beside thick unpolarised targets, cryogenic polarised targets could be employed. This approach involves a considerable amount of civil engineering, including a new cavern and a

new detector. Another possibility based on such a bent crystal is to directly use the deviated particles of the halo on a semi-internal target system, inside the beam pipe of an existing LHC experiment. The feasibility of such a solution is currently explored by the UA9 collaboration at CERN. Open problems in this case are how to dump the deflected beam, and how to get a suitable polarised target.

Finally, a wire or foil target may be placed in the halo of the LHC beam [90] in order to provide collisions at a near-axis position (see section 3.4). This method has been employed at HERA-B [91] and STAR [92] and is particularly useful for heavy-nucleus targets. However, it may affect the main LHC beam and this solution will require dedicated simulations. In addition, it is probably not compatible with light-nucleus targets –certainly not hydrogen ones– and basically prevents one to perform any direct luminosity measurement.

In the next sections, the aforementioned options are detailed. In section 3.6, the Figure-of-Merit (FOM) for collisions with unpolarised and polarised target is defined and numerical values are given, allowing for a comparison of performances. A qualitative summary table of the performances of the various technological solutions to initiate fixed-target collisions at LHC is also discussed. Finally, expected integrated luminosities for each solutions are compared.

3.2. Relevant LHC parameters and definitions

Let us first recall (in Table 1) some nominal LHC parameters [93, 94] as well as other generic quantities which have been used in the comparison of the various technological solutions.

	proton beam	lead beam	upgraded lead beam
Number of bunches in the LHC	2808	592	1232
Number of particles per bunch	1.15×10^{11}	7×10^7	1.8×10^8
LHC Revolution frequency [Hz]		11245	
Particle flux in the LHC [s^{-1}]	3.63×10^{18}	4.66×10^{14}	2.49×10^{15}
LHC yearly running time [s]	10^7	10^6	10^6
Nominal energy of the beam [TeV]	7	2.76	2.76
Fill duration considered [h]	10	5	5
Usable particle flux in the halo (when relevant) [s^{-1}]	5×10^8	10^5	5×10^5

Table 1: LHC-related quantities used in the calculations in the following sections along the expected parameters for an upgraded Pb beam mode. The usable particle flux in the halo is assumed to be half of the estimated beam losses in the proton and lead beams.

Beside these nominal running conditions, the possibility of p runs at the Pb energy for reference measurements is also possible as already done during the Run 1 & 2. These runs typically last one week, *i.e.* $O(10^5)$ seconds. When relevant, these run durations will be specified. We also note that other beam species (Kr, Ca, O) can be considered for an injection in the LHC (in particular those used in the SPS, *i.e.* Xe and Ar), as it was the case with the short XeXe run which took place by the end of 2017. The injection of other species, like He, would require another ion source than the current one. In most cases, the instantaneous luminosities should be equal or larger than those for Pb beams (see later).

Let us now recall useful quantities to compare the various technological implementations. First, we define the instantaneous luminosity, $\mathcal{L}$, in terms of the particle flux, $\phi_{\text{projectile}}$, impinging the target of areal density θ_{target}:

$$\mathcal{L} = \phi_{\text{projectile}} \times \theta_{\text{target}}. \tag{2}$$

13

If θ_{target} is expressed in cm^{-2}, $\mathcal{L}$ is naturally expressed in cm^{-2}s^{-1}. For a gas target, the flux is ϕ_{beam}, the particle flux in the LHC. For a solid wire target or a solid target put into an extracted beam, it is $\phi_{\text{usable halo}}$, the usable particle flux in the halo, which is of the order of the beam losses (or less) to allow for a parasitic working mode.

To compare the performances of the target for spin-related measurements, in particular single-spin asymmetries (SSAs) discussed in section 5.2, we define an effective polarisation, $\mathcal{P}_{\text{eff}}$ such that, its square multiplied by the instantaneous luminosity defined above, yields a quantity, $\mathcal{F}$:

$$\mathcal{F} = \mathcal{P}_{\text{eff}}^2 \times \mathcal{L}. \tag{3}$$

$\mathcal{F}$ is called the spin figure of merit of the target (and beam), which is inversely proportional to the time needed to reach a fixed precision on SSAs. In other words $\mathcal{F}$ is inversely proportional to the variance of the SSAs. According to these definitions, $\mathcal{L}$ contains the information about the rates, whereas $\mathcal{P}_{\text{eff}}$ contains the information about the polarisability of the material. Depending on the target material type, $\mathcal{P}_{\text{eff}}^2$ can be expressed as:

$$\mathcal{P}_{\text{eff}}^2 = P_T^2 \times f^2 \text{ or } \mathcal{P}_{\text{eff}}^2 = P_T^2 \times \alpha^2, \tag{4}$$

where P_T is the polarisation of the nucleons in the target, f a dilution factor (the fraction of polarised nucleons in the molecule) and α a depolarisation factor.

Since different set-up cannot be used during the same amount of time over a LHC year, it also obviously useful to make comparisons at the level of $\int dt\,\mathcal{L}$ and $\int dt\,\mathcal{F}$. The yearly run duration are taken to be 10^7 s for the proton beam and 10^6 s for the lead beam. These are maxima.

3.3. Internal gas target solutions

3.3.1. SMOG: a feasibility demonstrator

The direct injection in the LHC beampipe (*i.e.*in the VELO vessel) of noble gases at a pressure on the order of 10^{-7} mbar is already being used by the LHCb collaboration with the SMOG (System for Measuring the Overlap with Gas) device. Initially developed inside LHCb to allow for a precise determination of the luminosity with an uncertainty below 4%, SMOG is a system whereby a gas can be injected inside the beam vacuum at the interaction point. The luminosity for the collider mode is then determined thanks to a Beam Gas Imaging (BGI) method, which relies on the interaction vertices between the circulating beam and the gas present at the interaction point [84, 95, 96].

beam	gas	pressure [mbar]	gas length ℓ [cm]	θ_{target} [cm^{-2}]	$\mathcal{L}$ [cm^{-2}s^{-1}]	$\sigma_{\text{beam}-\text{target}}^{\text{had}}$ (barn)	beam fraction lost over a fill
p	{He, Ne, Ar, Kr, Xe}	$1.5 \cdot 10^{-7}$	40	$1.6 \cdot 10^{11}$	$5.8 \cdot 10^{29}$	{0.16, 0.6, 1.0, 1.6, 2.2}	$<< \%o$
Pb	{He, Ne, Ar, Kr, Xe}	$1.5 \cdot 10^{-7}$	40	$1.6 \cdot 10^{11}$	$7.4 \cdot 10^{25}$	{4.5, 7.0, 8.4, 10.3, 11.8}	$<< \%o$

Table 2: The areal density can be expressed for perfect gas as $\theta_{\text{target}}(\text{cm}^{-2}) = (1/22697) \times (P \times \ell \times \mathcal{N}_{\mathcal{A}})$ with P the pressure of the gas in bar, ℓ the usable gas length in cm and $\mathcal{N}_{\mathcal{A}}$ the Avogadro number in mol^{-1}. A usable gas zone of $\ell = 40$ cm has been considered. In this calculation, we considered the nominal flux of protons and ions. The energy of the beam is also the nominal one. The obtained areal density and instantaneous luminosities should therefore be considered as maxima. The hadronic cross-sections used in this chapter to compute the beam fraction lost over a fill, have been obtained using EPOS MC generator [97]. The values are compatible with those from Fluka generator [98] within 6%.

The system and its technology have been extensively tested. A pilot run of p beam (Pb beam) on a Neon gas target was successfully performed in 2012 (2013) at a c.m.s energy of $\sqrt{s_{NN}} = 87$ GeV (54 GeV). This first SMOG campaign was followed by several successful data taking periods in 2015-2017, for which the

injection of other gases than Neon was explored. The system is currently limited to noble gases, namely He, Ne, Ar and, possibly, to Kr and Xe which have not yet been tested. Their impact on the machine is currently under discussion with the LHC vacuum experts. The limitation to noble gas is to avoid altering the Non-evaporable-getter (NEG) coating properties of the beam pipe and this is why SMOG is equipped with a NEG cartridge to ensure the purity of injected gas. These noble gases can thus travel from the injection point (IR 8) to the ion pump stations at ±20 m and some can reach the warm-to-cold transitions of the Q1 magnets, where they can accumulate during extended period of injection. The beam-induced effects due to gas cryosorbed on those surfaces is still being investigated along the successive tests. However, in 2015, Ar was injected in LHCb for about one week in a row, during the heavy-ion run which took place before the Year End Technical Stop (YETS). No decrease of the LHC performances was observed. It therefore opens good perspectives for data taking periods of up to a month per year without additional pumping systems. It would preferably take place at the end of the year, while the beam intensity is low, and before the YETS which could permit to get rid of the accumulated gas if needed. With the current SMOG setup, the gas pressure is about 1.5×10^{-7} mbar, *i.e.* two orders of magnitude higher than the LHC vacuum pressure ($\sim 10^{-9}$ mbar). The pressure might be increased up to 10^{-6} mbar without severe hardware changes along with the support of the LHC vacuum experts. An estimate of the instantaneous luminosity obtained with the SMOG device in p-gas and Pb-gas collisions is given in Table 2. The beam fraction consumed over a fill is negligible. There are prospects to replace SMOG with a multigas system allowing to change the type of injected gas without human intervention onsite. As for now, the gas pressure is not well known with a good precision. The installation of a calibrated Vacuum Gauge Ion (VGI) 6 m from the VELO has been performed during the YETS of 2016-2017. The luminosity is estimated by the parameters of the beam (number of bunches and bunch intensity), as well as the gas-target pressure measured by the pressure gauge. The uncertainty is dominated by the measured pressure, which varies as a function of the *z* position along the beam. The luminosity is also determined from the yield of electrons scattering off the target atoms, with a precision of about 6% [99]. In addition to the luminosity determination challenge, it is also worth noting that one has to cope with colliding-bunch events if the detector is also used in the collider mode. Fixed target heavy-flavour analyses are currently limited to the analyses of non-colliding bunch events, with a vertex position limited to -20 and 20 cm, *i.e.* in a region where the detector efficiencies are mostly constant with respect to the *z*-vertex position [100]. Such requirements affect the effective recorded luminosities. One has to keep in mind that besides the limitation of the SMOG system itself in term of delivered gas pressure, the contamination of the collider events by fixed target events has also to be considered as a constraint on the maximum pressure which can be delivered to LHCb. This consideration applies only in parasitic operation mode (during *pp* runs), in order not to affect the current main LHCb B physics programme.

3.3.2. Gas-jet target

Out of all the proposed solutions, the internal gas target cell is a genuine solution to make fixed target at the LHC, at limited cost by re-using an existing LHC experiment, and with a variety of polarised and unpolarised gas target. From the experience gained with SMOG, and further tests of gas injection in LSS4 and near ALICE, ATLAS and CMS, we consider the option of direct-injection of gas in the LHC beampipe as a viable solution to be run parallel to the collider mode. As highlighted above, the SMOG system is however not optimised and faces some limitations: the gas pressure –thus the target density– is limited, only noble gases can be injected, the heavier noble gases may only be used before long YETS and the injection period are currently significantly limited. Last but not least, a SMOG-like system does not allow to inject polarised gases.

Some of these limitations can be lifted by the installation of specific pumping systems, which would

however reduce the portability of the system[9]. In addition, a specific injection system would allow one to inject a jet of polarised gases such as H, D and ^{3}He as well as heavier noble gases. One illustrative example of such an option is the H-jet system [88] used on the BNL-RHIC collider as a proton-beam polarimeter (see Appendix 7.1). In short, it offers much higher target densities than the current SMOG system, opens the possibilities for highly polarised target and can be coupled to a collider.

Let us briefly describe its main characteristics : it consists of a free atomic beam vertically crossing the collider beam at a speed of approximately $1560 \, \text{m} \cdot \text{s}^{-1}$. With the current Atomic Beam Source (ABS) [88], operated at 80K, the polarised H inlet flux was measured to be $(1.26 \pm 0.05) \times 10^{17}$ H$^{\uparrow}$/s. With a redesigned system, it may be doubled. Similar numbers should be reachable for a polarised deuterium. Higher fluxes can easily be obtained with polarised ^{3}He but would require a dedicated system. Using deuterium target would require proper RF cavities which may prevent optimising both hydrogen and deuterium target performances with a single system.

At the interaction point, the H-jet target profile is nearly Gaussian with a full width at half maximum of 5.5 mm. This is a significant advantage compared to a SMOG-like system where the gas diffuses along the beampipe and results in beam-gas collisions over distances of a few meters. A vacuum in the RHIC ring of 2×10^{-8} mbar was achieved with the H-jet system in operation at its nominal 10^{17} atoms/s inlet flux thanks to turbomolecular pumps (TMP) with a 1000 l/s pumping speed. The current H-jet system size is 375 cm high (225 cm for ABS above and 150 cm for Breit-Rabi polarimeter below the beampipe), 110 cm wide and 70 cm long. A redesigned system could be made more compact down to 200 (75) cm high above (below) the beam pipe. The current free ABS corresponds to a target areal density of $(1.2 \pm 0.2) \times 10^{12}$ H$^{\uparrow}$.cm^{-2}.

beam	gas	inlet flux [atoms·s^{-1}]	θ_{target} [atoms/cm^{-2}]	$\mathcal{L}$ [cm^{-2}s^{-1}]	$\sigma^{\text{had}}_{\text{beam−target}}$	beam fraction lost over a fill
p	H$^{\uparrow}$	$1.25 \cdot 10^{17}$	$1.2 \cdot 10^{12}$	$4.3 \cdot 10^{30}$	48 mb	$\ll \permil$
p	D$^{\uparrow}$	$1.25 \cdot 10^{17}$	$1.2 \cdot 10^{12}$	$4.3 \cdot 10^{30}$	90 mb	$\ll \permil$
p	^{3}He$^{\uparrow}$	$1.0 \cdot 10^{19}$	$1.0 \cdot 10^{14}$	$3.6 \cdot 10^{32}$	124 mb	0.5 %
p	H$_2$	$1.1 \cdot 10^{20} - 10^{21}$	$10^{15} - 10^{16}$	$3.6 \cdot 10^{33} - 10^{34}$	48 mb	1.9 - 19 %
Pb	H$^{\uparrow}$	$1.25 \cdot 10^{17}$	$1.2 \cdot 10^{12}$	$5.6 \cdot 10^{26}$	3.0 b	$\sim \permil$

Table 3: Target areal density θ_{target} and luminosity $\mathcal{L} = \phi_{\text{LHC}} \theta_{\text{target}}$ achievable by using the gas-jet target inspired from the RHIC proton-beam polarimeter. The proton and lead beam fluxes in the LHC and the fill durations were taken from Tab. 1. The hadronic cross-section are obtained as described in Tab. 2.

The H-jet system is designed to be moveable. It can be uninstalled and reinstalled in 2-3 days. It is coupled to a Breit-Rabi polarimeter monitor to measure with a high accuracy the atomic hydrogen polarisation which is as high as 0.96. The gas jet is however contaminated by hydrogen atoms bound into unpolarised proton molecules which slightly dilutes the average jet-proton polarisation down to $P^{\text{H−jet}} = 93\%$ [101].

It was recently demonstrated [102] that the molecular hydrogen atomic mass fraction is about 0.4% in the jet center. However since the molecular-hydrogen distribution is a factor 30-40 wider than the jet one, an integral dilution of the jet polarisation may be as large as 0.85. Detecting recoil protons from elastic pp scatterings, it was possible to reconstruct the z-coordinate of the vertex which allowed the *in-situ* normalisation of the molecular-hydrogen contribution and its proper subtraction. For the actually used event-selection cuts, the effective jet-target polarisation was found to be $95 \pm 0.5\%$. To employ this method

---

[9]A SMOG-like system essentially reduces to a gas bottle, some valves and pressure gauges, a NEG filter and a small capillary to the beam pipe.

of the jet-polarisation control, the vertex *z*-coordinate has to be measured with an accuracy of $\sigma_z \lesssim 1$ mm. We further note that the polarisation could reach 96-98% if coupled with a higher holding magnetic field than the present one of 0.14 T. For the H-jet system, the field strength was also chosen to minimise the bending of the scattered recoil protons for the use as a polarimeter.

The gas-jet parameters, the instantaneous luminosities using typical LHC beam currents, and the beam fraction consumed over a fill are shown in Tab. 3, for each type of beam-gas collisions. In particular, an estimation of target areal density is given for polarised ^{3}He target and unpolarised jet targets. In the former case, a higher areal density is achievable since ^{3}He, if cooled down, can be injected with lower velocity than H. For what concerns unpolarised heavier ions, a aeral target density of $1 \div 5 \times 10^{13}$ cm^{-2} can be envisioned.

3.3.3. Storage-cell gas target

Besides a gas jet solution, using an internal gas-target cell is another genuine solution to make fixed-target experiments at the LHC, at a limited cost by re-using existing LHC detectors, and with a variety of polarised and unpolarised gas target.

In such a case, the target [103] consists of a polarised or unpolarised gas source in combination with an open storage cell (see Fig. 6) which increases the target density by more than two orders of magnitude compared to a free atomic beam jet. The storage cell consists of a narrow straight tube with thin walls located in the machine vacuum along the beam axis, into which the gas is injected at the center, in two modes:

- polarised atomic beam (H, D or ^{3}He) into a feed tube of low gas conductance;

- unpolarised gas (e.g. H_2, He, Ne, Ar, Kr, Xe) via a capillary from a gas handling system.

The gas diffuses through the cell openings into the machine vacuum system, which usually requires a powerful differential pumping system. The cell consists of two movable halfs that can be opened in order to provide space for beam injection or manipulation. Polarised gas targets for storage rings are reviewed in [87]. Targets for proton beams at intermediate energies have been applied at the cooler ring COSY (FZ Jülich) [104, 105, 106] as well as at the IUCF Cooler Ring [107]; and for electron beams at HERA (DESY Hamburg) [108].

Such a polarised H or D target (the HERMES target)[108] consists of three main components: the polarised *Atomic Beam Source* (ABS), the *Storage Cell* in a longitudinal or vertical holding field *B* and a *Diagnostic System* for analyzing a small sample of gas from the target cell, consisting of the polarimeter (BRP) measuring the sub-state population of the atoms, and the target gas analyzer (TGA) detecting the molecular fraction and thus the degree of recombination within the cell. From these parameters, the target polarisation *P* as seen by the beam is deduced (typical values $P \approx 0.85$, corrected for magnetic guide field and degree of dissociation). It was however recently noted that the cell coating used then does not comply with the LHC requirements. R&D is thus needed to find a proper coating which would not significantly degrade the polarisation performances.

The ABS injects polarised H into the feed tube (here 100 mm long, 10mm inner diameter) of a storage cell of 1000 mm length with a proposed inner diameter of 14 mm (see Fig. 6). Dimension of 300 mm by 10 mm however seems to be more adapted to match the LHC requirements [109]. The maximum areal density θ_{target} is limited by the flux of the ABS and the geometry of the storage cell which needs to permit the transmission of the LHC beam and the injection of the polarised atomic beam. The target described here is also able to deliver polarised D with similar densities. Injecting optically pumped polarised ^{3}He into the storage cell could be another possibility. In such a case, the holding field must be very homogeneous in order to prevent motional depolarisation.
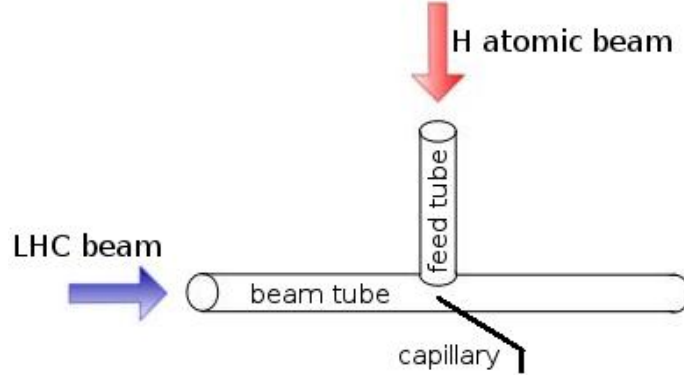
Figure 6: Schematic view of the target cell. Polarised gas can be injected ballistically - unpolarised gas via a capillary - into the cell center.

beam	target gas	inlet flux [s^{-1}]	θ_{target} [cm^{-2}]	$\mathcal{L}$ [cm^{-2}s^{-1}]	$\sigma_{\text{beam}-\text{target}}^{\text{had}}$	beam fraction lost over a fill
p	H$^{\uparrow}$	$6.5 \cdot 10^{16}$	$2.5 \cdot 10^{14}$	$0.92 \cdot 10^{33}$	48 mb	0.4 %
p	D$^{\uparrow}$	$5.2 \cdot 10^{16}$	$2.9 \cdot 10^{14}$	$1.1 \cdot 10^{33}$	90 mb	1.1 %
p	^{3}He$^{\uparrow}$	$1.5 \cdot 10^{17}$	10^{15}	$3.7 \cdot 10^{33}$	124 mb	4.4 %
p	H$_2$	$2.8 \cdot 10^{17}$	$1.6 \cdot 10^{15}$	$5.8 \cdot 10^{33}$	48 mb	3.1 %
p	{Ne, Ar, Kr, Xe}	$1.3 \cdot 10^{15}$	$6.44 \cdot 10^{13}$	$2.34 \cdot 10^{32}$	{0.6,1.0,1.6,2.2} b	{1.6, 2.6, 4.2, 5.7} %
Pb	H$^{\uparrow}$	$6.5 \cdot 10^{16}$	$2.54 \cdot 10^{14}$	$1.18 \cdot 10^{29}$	3.0 b	15.4%
Pb	Xe	$1.3 \cdot 10^{15}$	$6.44 \cdot 10^{13}$	$3 \cdot 10^{28}$	11.8 b	15.4 %

Table 4: Target areal density θ_{target} and luminosity $\mathcal{L}$ achievable by using a storage cell target with a cell temperature of 300K and obtained as described in Tab. 3.

Unpolarised target gas could also be injected into the cell via a capillary for the study of heavy ion collisions. The gas flow from a gas feed system and thus the gas density in a target cell can be very high. Limits are imposed *e.g.* by the maximum gas flow that a possible LHC target station can take, and by the capability of the detector system. Another requirement is that the gas target must not shorten the lifetime of a Pb beam fill by an unrealistically large amount. On top of hadronic interactions, photo-nuclear interactions including Bound-Free Pair Production, in which an e^+e^- pair is created with the electron bound to one of the colliding nuclei, and Electromagnetic Dissociation [110] can affect the Pb beam lifetime. The photo-nuclear interactions are enhanced with the target gas atomic number and can be up to twenty times the hadronic cross section in case of Xe gas with Pb beam [111]. The storage cell parameters, the instantaneous luminosities obtained using typical LHC beam currents, and the beam fraction consumed over a fill, considering hadronic interactions, are shown in Table 4, for each type of beam-gas collisions [103].

3.4. Internal solid target intercepting the beam halo

Another possible internal target solution for the LHC is to use a wire, a ribbon or a foil positionned in the halo of the beam as first proposed in [90]. Such an approach was adopted by the HERA-B [91] experiment with the prerequisite of not affecting the other experiment functionning on the 920 GeV proton HERA Beam. The HERA-B system consisted of 2 stations of 4 wires each, made of Ti and W, positionned in a

square shape around the beam. For C, flat ribbons were used[10]. These could be positionned independently and adjusted with respect to the beam condition in order to scrap the beam halo. Other materials were also considered such as Al, Fe and Cu. One of the main limitations for HERA-B was the widening of the beam due to multiple Coulomb scattering in the target, which is reduced with low Z materials. Multiple Coulomb scattering is not a limitation anymore when the beam halo is used, due to the lower halo intensity. For the LHC, simulations and tests (as done for the bent crystals discussed in the next section) are therefore needed to completely assess the feasibility and then the perfomance of such a system.

In principle, such a target system can be placed in the vicinity (or even inside) ALICE or LHCb at a moderate cost. If the system was found to be incompatible with high intensity runs, it could be used only for heavy-ion runs or during special runs; this would in turn reduce the collected luminosity in pA collisions. Another limiting factor is the impossibility to carry out pp collisions which are extremely important to quantify the nuclear effects. In the absence of such reference, it is mandatory to have at one's disposal measurements made with species with sufficiently different A. However, there are strong constraints from the LHC on the species which can be placed inside the LHC beam pipe. Therefore the mechanics for the positioning of the target should allow one to shift the target during the tuning of the beam. We have considered so far C, Ti, and W as possible species but further studies might be required (also for other species). Finally, let us note that such a system does not allow to use a polarised target.

beam	target	ρ [g cm^{-3}]	M [g mol^{-1}]	ℓ [μm]	θ_{target} [cm^{-2}]	beam flux [s^{-1}]	$\mathcal{L}$ [cm^{-2}s^{-1}]
p	C	2.25	12	500	$5.6 \cdot 10^{21}$	5×10^8	$2.8 \cdot 10^{30}$
p	Ti	4.43	48	500	$2.8 \cdot 10^{21}$	5×10^8	$1.4 \cdot 10^{30}$
p	W	19.25	184	500	$3.1 \cdot 10^{21}$	5×10^8	$1.6 \cdot 10^{30}$
Pb	C	2.25	12	500	$5.6 \cdot 10^{21}$	10^5	$5.6 \cdot 10^{26}$
Pb	Ti	4.43	48	500	$2.8 \cdot 10^{21}$	10^5	$2.8 \cdot 10^{26}$
Pb	W	19.25	184	500	$3.1 \cdot 10^{21}$	10^5	$3.1 \cdot 10^{26}$

Table 5: Selection of instantaneous luminosities for internal wire targets positioned in the halo of the LHC beams. The target areal density θ_{target} is equal to $\mathcal{N}_{\mathcal{A}} \times \ell \times \rho / M$. The instantaneous luminosity is the product of θ_{target} and the usable particle flux in the halo.

3.5. External/internal target solution with a slow beam extraction using a bent crystal

3.5.1. Crystal-assisted extraction of the LHC beams

The idea of a controlled non-resonant slow extraction of the CERN LHC beams –on the order of 10^8 protons per second– to be used for fixed target physics is not new. Already, in the early 90's, the LHB collaboration submitted a letter of intent to the LHCC to get an experiment based on bent-crystal extraction approved. At the time, it was not clear whether such a technique could be used in the LHC conditions.

Since then, significant progresses were achieved with successful tests for protons at the SPS [112], Fermilab [113], Protvino [114] and for Pb ions at the SPS [115]. These were made possible by numerous experimental advances, like the improvement of the crystal quality with a production technique allowing to reach a channeling efficiency close to the theoretical one, or like the development of goniometers matching the critical angle requirements for a 6.5 TeV beam channeling. Thanks to this legacy, the UA9 collaboration proposed this technique as a smart alternative for the upgrade of the LHC collimation system [116, 117] following the concept developed in the frame of the INTAS programme 03-51-6155, see for instance the ref

---

[10]The diameter of the wires was 50 μm whereas the ribbons were 100 μm wide in the direction perpendicular to the beam and 500 μm along the beam (which can thus be considered as the target thickness).

[118] issued in 2002. Tests were recently successfully carried out at the betatron cleaning insertion (IR7) both at injection and top energy (6.5 TeV) in 2015. [89]. Tests have also been performed with lead beam at injection and top energies (2.5 TeV) at the end of 2016. They clearly demonstrated the feasibility of crystal-assisted collimation and, in turn, gave a new momentum in the plans for crystal-assisted extraction. Let us also stress that the crystal degradation due to radiation, once thought to be an issue, is negligible as demonstrated by tests [119] with the HiRadMat facility of the SPS.

The generic requirements for such an extraction system were already outlined in 1990 at the Aachen LHC workshop where it was identified that [120]:

- an extraction outside the ring is preferred to avoid interferences with the main tunnel and the experimental cavern;
- an extraction in the horizontal plane would probably be more favourable since an enhanced deflection[11] could be achieved by an appropriate re-design of the separation recombination dipoles D1 and D2;
- the extraction would be at one of the odd points of the LHC;
- the crystal location would be between the quadrupoles Q3 and Q4 and it would provide a deflection of about 1 mrad;
- a further deflection up to 20mrad could be achieved at 250 m;
- increasing the size of the halo would result in a higher extraction efficiency with more particles crossing the crystal.

To be more quantitative about the required modifications of the beam pipe, since the halo is located at approximately 3 mm from the beam pipe axis, a deflection by an angle of 1 mrad would result in these particles exiting the beam pipe at 30m downstream, considering a LHC beam pipe radius of 3-4 cm in the LHC tunnel. Another proposal was made in 2005 [121] consisting in "replacing" the kicker-modules in LHC section IR6 (the beam dump) by a bent crystal that will provide the particles in the beam halo with a sufficient kick to overcome the septum blade and to be extracted. It is however not clear to which extent the beam-dump area, even with obvious modifications to move the beam-dump facility, can be used for experiments. As for now, beyond the generic requirements above, the possible locations of a possible extraction zone have not been listed. Currently, there is an active project, CRYSBEAM [122], whose objective is to demonstrate the feasibilty of crystal-assisted extraction on the LHC and which should upon its completion give us better insight on the technical realisation of this solution. Operating the crystal in real parasitic mode still requires further studies.

Another possibility, which would avoid further manipulating the beam downstream of the crystal, is to directly use the extracted –and highly collimated– particles of the halo (which we refer to as the split beam) on an (semi) internal target system which would however not interact with the main LHC beam. Such a solution would probably allow one to limit the civil-engineering work to a minimum and also to use an existing experiment. Two caveats have however to be adressed. First, only a fraction of the split beam would interact with the target and the remaining 10^8 protons per second should be absorbed or deviated from the experiment. Second, this would probably induce a non-negligible azimuthal asymmetry in the experimental system. For spin-related analyses, this may be a serious limitation in the cancellation of some systematical uncertainties. A first setup (see Appendix 7.2), compatible with the LHCb detector, has been proposed to measure the electric and magnetic dipole moments of charmed charged baryons at LHC top energies [123, 124, 125]. A first bent crystal, located at 5σ from the center beam line, deflects the halo particles by about 150 μrad at about 100 meter upstream of the LHCb interaction region, in order to separate them

---

[11]beyond the one resulting from the crystal pass.

from the circulating beam. A target, 1cm long and 5mm thick along the beam direction, inserted in the pipe intercepts the halo, producing short-lived baryons. A second crystal[12] channels part of the baryons and deflects them by 7 mrad[13] into the LHCb detector, where the spin orientation is measured. An additional absorber intercepts the halo particles non-interacting with the target, thereby allowing the possibility of fixed-target operation in parasitic mode. An initial test of the beam splitting concept and of the double crystal use in an accelerator was made in the SPS by the UA9 collaboration in 2017 [126]. However, there is still a long way before achieving a fully effective scenario, compatible with the LHC collimation system and with the LHCb detector.

3.5.2. Unpolarised targets

As aforementioned, the LHC beams can be extracted by means of a bent crystal with typical proton fluxes on the order of 5 x 10^8 s^{-1} and 10^5 s^{-1} for the lead beam. We will consider 5mm-thick targets, which are in principle compatible with both the split beam option and a dedicated beam line. Table 6 displays the corresponding instantaneous luminosities with the same species as for the internal wire target as well as for solid hydrogen to illustrate the case of light elements.

beam	target	ρ [g cm^{-3}]	M [g mol^{-1}]	ℓ [mm]	θ_{target} [cm^{-2}]	beam flux [s^{-1}]	$\mathcal{L}$ [cm^{-2}s^{-1}]
p	solid H	0.088	1	5	$2.6 \cdot 10^{22}$	5×10^8	$1.3 \cdot 10^{31}$
p	C	2.25	12	5	$5.6 \cdot 10^{22}$	5×10^8	$2.8 \cdot 10^{31}$
p	Ti	4.43	48	5	$2.8 \cdot 10^{22}$	5×10^8	$1.4 \cdot 10^{31}$
p	W	19.25	184	5	$3.1 \cdot 10^{22}$	5×10^8	$1.6 \cdot 10^{31}$
Pb	solid H	0.088	1	5	$2.6 \cdot 10^{22}$	10^5	$2.6 \cdot 10^{27}$
Pb	C	2.25	12	5	$5.6 \cdot 10^{22}$	10^5	$5.6 \cdot 10^{27}$
Pb	Ti	4.43	48	5	$2.8 \cdot 10^{22}$	10^5	$2.8 \cdot 10^{27}$
Pb	W	19.25	184	5	$3.1 \cdot 10^{22}$	10^5	$3.1 \cdot 10^{27}$

Table 6: Selection of instantaneous luminosities for unpolarised targets and an extracted beam of protons or of lead ions by means of a bent crystal. The target areal density and its thickness, ℓ, are also indicated. With a beam splitting option, there is currently no clear solution to allow for the usage of a light target (solid/liquid H, D).

We stress that for an experiment with a specific target system away from the beampipe, targets as thick as a meter can be used for light species like hydrogen or deuterium. Thicker target can also be used for heavier species provided that the effect of multiple scatterings in the target can be mitigated. In general, the targets being thicker than in the internal-wire-target case (5 mm vs. 0.5mm), instantaneous luminosities are larger.

3.5.3. Polarised targets

One of the main thrusts of the proposed physics with AFTER@LHC will be the measurement of the Sivers asymmetry which will require a transversely polarised target. In the following, we present two possible target systems for AFTER@LHC, one inspired from the E1039 project at Fermilab [64] and the other inspired by the polarised target of COMPASS experiment at CERN [127, 128, 129]. In both cases,

---

[12]Note that this second crystal is needed only in the case of electric or magnetic dipole moment measurements.

[13]Let us remind that the deflection angle is related to the critical radius of the bent crystal, which increases linearly with the energy. At high energy, to reach larger angles, the length of the crystal has to be increased.

the polarization of the target relies on the Dynamic Nuclear Polarization (DNP) method, whose general principle is described in [130]. Both targets could be envisionned in the case of crystal-assisted extraction of the LHC beams into a new cavern, however, if redesigned, the E1039 target might also be usable with the crystal beam splitting solution.

The E1039 target. This target consists of a split coil superconducting magnet, operating at 5T. The coils are arranged such that the B field is either parallel or antiparallel to the vertical direction, resulting in a transverse polarization. Inside the magnet there is a refrigerator, which provides the necessary cooling power to keep the target at 1K. In the center of the whole system resides the target stick, which contains the target cells, the microwave horn and the NMR coils to measure the actual polarization. The target insert has 2 active cells filled with frozen NH_3 beads, one empty and one with a carbon target. The cells have an elliptical cross section, with one half axis being 1.9 cm diameter and the other one 2.1 cm while the length is 8 cm. The target material is positioned in a liquid He bath, cooled to 1K, by lowering the vapor pressure of liquid Helium to .117 Torr. This is achieved with a system of large 8 ROOTS blower pumps which have a capacity of pumping 15,000 m^3/hr He gas. The microwave horn is sitting above the two top cells, which contain NH_3 and ND_3, thus allowing to measure polarised p and n under identical run and target conditions. This greatly reduces the systematic uncertainties by comparing p and n. While both cells see the radiation from the microwave, only the one in the center region of the coils will be polarised. Since the material has to be uniformly cooled, the ammonia is in the form of small frozen beads, which reduces the maximum density by a packing fraction of about 0.6. From the planned beam intensities, we estimate that the material has to be changed every 140 days, due to radiation damage. In Appendix 49 a schematic view of the E1039 target is shown.

The COMPASS target. The target consists of two identical, 55 cm long cylindrical cells with a diameter of 4 cm. Each cell has 5 NMR coils to measure the polarisations [131]. The cells can be polarised in opposite direction and there is a 20 cm long gap between the cells, in order to cleanly separate interactions from the respective target cells. The orientations are reversed by changing microwave frequency at 2.5 T at regular intervals in order to reduce the systematic error. The polarization is obtained by the DNP method with a high cooling power dilution refrigerator with a 13500 m^3/h pumping speed of 8 Root's blowers in series, a 2.5 T solenoid magnet and two microwave systems of about 70 GHz [129]. The spin can be oriented perpendicular to the beam direction by using a 0.6 T dipole magnet. Under this magnetic condition the polarization can not be enhanced by the DNP method, but can be maintained at a lattice temperature below 100 mK. The proton polarization achieved in 2015 with NH_3 was 80 % in 1 day and about 90 % after 2 days. In a beam intensity of 8×10^7 pions/s the beam intensity for each NH_3 bead of 2-3 mm is about 10^6 s^{-1} which will not lead to a significant depolarization in the frozen spin mode. No significant radiation damage could be observed in more than half a year of data taking in 2015 at COMPASS. However, the target material may be considered to be annealed in the case of 5×10^8 p/s beam intensity. A spin relaxation time of about 1000 hours was measured at 0.6 T and 50 mK for the proton in NH_3. In Appendix 50 a schematic view of the COMPASS target is shown.

Comparison. In the Table 7, we present the parameters of the E1039 target and of the COMPASS target, which could be used for AFTER@LHC. The COMPASS target permits to reach higher luminosities than the E1039 target, however the E1039 target offers several advantages. The later is smaller and could therefore be used in beam splitting mode if a significant modification of the beam line and target is performed. It also permits the usage of polarised deuterium target (ND_3), complementary to the hydrogen one (NH_3).

	target species	ρ [g/cm^3]	ℓ [cm]	M [g.mol^{-1}]	θ_{target} [cm^{-2}]	beam flux [s^{-1}]	PF	$\mathcal{L}$ [cm^{-2}s^{-1}]	current size [mm x mm]
E1039	NH$_3^\uparrow$	0.86	8	17	2.4 x 10^{23}	5x10^8	0.6	7.2 x 10^{31}	
target	ND$_3^\uparrow$	1.007	8	20	2.4×10^{23}	5x10^8	0.6	7.2 x 10^{31}	1853 x 975
COMPASS	NH$_3^\uparrow$	0.86	110	17	3.4 x 10^{24}	5x10^8	0.6	1.0 x 10^{33}	
target	butanol$^\uparrow$	0.99	110	74	8.9 x 10^{23}	5x10^8	0.6	2.7 x 10^{32}	3120 x 2820

Table 7: E1039 and COMPASS target parameters. The target areal density is defined as $\theta_{target} = (\mathcal{N}_{\mathcal{A}} \times \ell \times \rho) / M$. To evaluate the perfomances for SSA measurements, a packing factor PF which account for the fact that the target material is filled under a liquid nitrogen bath is additionally considered. The instantaneous luminosity accounting for the PF is labelled $\mathcal{L}$. The rest space factor accounting for the fact that unpolarised He can be present in the target has been neglected. It might further reduce the luminosity by about 10%.

3.6. Comparison of technologies

In this section we will discuss a qualitative comparison of the various technological solutions which have been developed. More quantitative comparisons of the instantaneous luminosities which could be achieved and performances for Single Transverse Spin Asymmetry measurements for the various solutions will also be presented.

3.6.1. Qualitative comparison of the various technological solutions

Table 8 gathers our qualitative judgement of the different solutions with regards to a number of decisional criteria and to the reach in the three physics cases developed in section 5.1, 5.2 and 5.3. In particular, it is assumed here that one uses a detector without specific data-taking-rate limitations, while the physics reach when using the ALICE and LHCb detectors will be discussed in the section 4.

For the internal gas target solutions, the current SMOG system in LHCb has the advantage to be mostly parasitic to other LHC experiments due to its low gas density. Also, various noble gases up to Argon have already been used. However its duration time is limited as well as the possible yearly integrated luminosity and it can not run with polarised gas. Furthermore, the luminosity can barely be directly estimated.

To achieve the physics reach proposed in this report with gas target solution, it is important to increase the gas density with respect to SMOG and opt for a more flexible gas system with polarised gases for spin physics. Also running with the hydrogen gas allows one to obtain a reference measurement with protons as target for high-x and heavy-ion physics. For that purpose, the gas-jet and storage-cell solutions are probably the most promising – with the highest luminosity for the storage cell solution. Note, however, that the cell coating has to be compatible with the LHC vacuum constraints, which seems not to be the as of the original HERMES target. In the target chamber of the gas jet system, one may also inject nuclear target gases, however this was not tested at RHIC and the possible gas density in that case is not known.

The internal solid target solution directly on the beam halo has the advantage to be compatible with various target species. This solution suffers however from a low luminosity and will likely impact the LHC beam stability. The beam splitting solution, by using a slow beam extraction with a bent crystal, will probably have less impact on the LHC beam and will allow one to run for a longer period and with thicker targets. If coupled with a redesigned E1039 target, it would allow for spin physics.

Characteristics	Internal gas target			Internal solid target with beam halo	Beam splitting	Beam extraction
	SMOG	Gas Jet	Storage Cell			
Run duration[14]	★	★★	★★	★	★★	★ ★ ★
Parasiticity[15]	★ ★ ★	★★	★★	★	★★	★ ★ ★
Integrated luminosity[16]	★	★★	★★	★	★★	★ ★ ★
Absolute luminosity determination[17]	★	★★	★★	★	★★	★ ★ ★
Target versality[18]	★★	★★	★ ★ ★	★★	★★	★ ★ ★
Target polarisation[19]	-	★★	★★	-	- / ★[20]	★
Use of existing experiment[21]	★★	★	★	★	★	-
Civil engineering or R&D [22]	★ ★ ★	★★	★★	★★	★★	★
Cost	★ ★ ★	★★	★★	★★	★★	★
Implementation time	★ ★ ★	★★	★★	★★	★★	★
High x[23]	★	★★	★ ★ ★	★	★/ ★ ★	★ ★ ★
Spin Physics[24]	-	★ ★ ★	★ ★ ★	-	- / ★★	★ ★ ★
Heavy-Ion[25]	★	★★	★★	★/ ★ ★	★★	★ ★ ★

Table 8: Qualitative comparison of the various technological solutions.

Finally the beam extraction solution is more suitable for the physics reach. However the necessary civil engineering would largely increase the cost by more than one order of magnitude and the implementation time with respect to the other solutions that are at reach with limited technical developments.

3.6.2. Comparison of the luminosities achieved for AFTER@LHC with the various technological solutions
    Table 9 compares the instantaneous luminosities, the expected running time with the proton or lead beam

---

[14]★ ★ ★: no limitation; ★★: possible limitation;★: data taking for special runs only

[15]★ ★ ★: no impact on the LHC performance that could reduce the luminosity delivered to the other LHC experiments; ★★: small impact; ★: significant impact

[16]Luminosity corresponding to 1 LHC year ★ ★ ★: high luminosity provided in many collision systems; ★★: high luminosity in few collisions systems;★: low luminosity

[17]direct luminosity determination with ★ ★ ★: small uncertainty; ★★: reasonable uncertainty (not clear);★: not precise enough

[18]★ ★ ★: no limitation; ★★: limited number of target types; ★: only few target types possible

[19]Target polarisation value including correction factors ★★: high; ★: low

[20]with a redesigned E1096 target

[21]★★: without any modification of the existing experiment; ★: with slight modification of the experiment and/or beam pipe

[22]★ ★ ★: none; ★★: limited;★: large

[23]based on the possible luminosity and its precise determination and possibility to use hydrogen target ★ ★ ★: very good; ★★: good;★: poor

[24]high spin figure of merit ★ ★ ★: very good; ★★: good;★: poor

[25]nuclear target versatility, high lumi ★ ★ ★: very good; ★★: good;★: poor

Target			Beam					
			p			Pb		
			$\mathcal{L}$ [cm^{-2}s^{-1}]	Δt [s]	$\int\mathcal{L}$ [nb^{-1}]	$\mathcal{L}$ [cm^{-2}s^{-1}]	Δt [s]	$\int\mathcal{L}$ [nb^{-1}]
Internal gas target	SMOG	He, Ne, Ar	5.8×10^{29}	2.5×10^5	145	7.4×10^{25}	10^6	0.074
	Gas-Jet	H$^\uparrow$	4.3×10^{30}	10^7	4.3×10^4	5.6×10^{26}	10^6	0.56
		H$_2$	$3.6 \times (10^{33} - 10^{34})$	10^7	$3.6 \times (10^7 - 10^8)$	$4.66 \times (10^{29} - 10^{30})$	10^6	466–4660
		D$^\uparrow$	4.3×10^{30}	10^7	4.3×10^4	5.6×10^{26}	10^6	0.56
		^{3}He$^\uparrow$	3.6×10^{32}	10^7	3.6×10^6	4.66×10^{28}	10^6	47
	Storage Cell	H$^\uparrow$	0.92×10^{33}	10^7	9.2×10^6	1.18×10^{29}	10^6	118
		H$_2$	5.8×10^{33}	10^7	5.8×10^7	7.5×10^{29}	10^6	750
		D$^\uparrow$	1.1×10^{33}	10^7	1.1×10^7	1.4×10^{29}	10^6	140
		^{3}He$^\uparrow$	3.7×10^{33}	10^7	3.7×10^7	4.7×10^{29}	10^6	474
		Xe	2.34×10^{32}	10^7	2.34×10^6	3.0×10^{28}	10^6	30
Internal solid target with beam halo	Wire Target (0.5 mm)	C	2.8×10^{30}	10^7	2.8×10^4	5.6×10^{26}	10^6	0.56
		Ti	1.4×10^{30}	10^7	1.4×10^4	2.8×10^{26}	10^6	0.28
		W	1.6×10^{30}	10^7	1.6×10^4	3.1×10^{26}	10^6	0.31
	E1039	NH$_3^\uparrow$	7.2×10^{31}	10^7	7.2×10^5	1.4×10^{28}	10^6	14
		ND$_3^\uparrow$	7.2×10^{31}	10^7	7.2×10^5	1.4×10^{28}	10^6	14
Beam splitting	Unpolarised solid target (5 mm)	C	2.8×10^{31}	10^7	2.8×10^5	5.6×10^{27}	10^6	5.6
		Ti	1.4×10^{31}	10^7	1.4×10^5	2.8×10^{27}	10^6	2.8
		W	1.6×10^{31}	10^7	1.6×10^5	3.1×10^{27}	10^6	3.1
Beam extraction	E1039	NH$_3^\uparrow$	7.2×10^{31}	10^7	7.2×10^5	1.4×10^{28}	10^6	14
		ND$_3^\uparrow$	7.2×10^{31}	10^7	7.2×10^5	1.4×10^{28}	10^6	14
	COMPASS	NH$_3^\uparrow$	1.0×10^{33}	10^7	1.0×10^7	2.0×10^{29}	10^6	200
		butanol$^\uparrow$	2.7×10^{32}	10^7	2.7×10^6	5.3×10^{28}	10^6	53

Table 9: Summary table of the achievable integrated luminosities for the various technical solutions described in this section.

and the integrated luminosities achievable in one year of data taking, for the various technical solutions described in this section. These numbers should be interpreted as maxima, and can be decreased according to data taking detector capabilities (see section 4). For the internal solid target with beam halo, beam splitting and beam extraction solutions, the fluxes of proton and lead on target are assumed to be 5×10^8 s^{-1} and 10^5 s^{-1}, respectively. As can be seen from Table 9, the highest luminosity which can be achieved in pH$^{\uparrow}$ collisions is about 10 fb^{-1} with a gas storage cell. Integrated luminosities of about the same order of magnitude could be reached with the E1039 target with a beam splitting or beam extraction option. The Gas-jet solution gives luminosity about two order of magnitude smaller than the storage cell for polarised hydrogen. For unpolarised pH$_2$ collisions, the performances of the storage cell and Gas-jet targets are similar, of the order of 40-50 fb^{-1}. In proton-nucleus collisions for large nuclei, the storage cell also gives the best integrated luminosities ($\sim$ 2.3 fb^{-1}). In order to obtain similar luminosities in pW collisions with an internal solid target would require the width of the target to be of about 50 mm (or the usage of serial targets). In lead-nucleus collisions, the performances of the storage cell are also the best, allowing for the collection of 750 nb^{-1} in PbH$_2$ and 30 nb^{-1} in PbXe collisions.

3.6.3. Comparison of the polarised-target performances for STSA measurements

target	P_{T}	f or α	PF	θ_{target} [cm^{-2}]	$\mathcal{L}$ [cm^{-2}s^{-1}]	$\mathcal{P}^2_{\mathrm{eff}}$	$\mathcal{F}$ [cm^{-2} s^{-1}]	$\int \mathcal{F}$ [cm^{-2}]
NH$_3$ E1039	0.85	0.17	0.6	2.4×10^{23}	7.2×10^{31}	0.0209	1.505×10^{30}	1.505×10^{37}
ND$_3$ E1039	0.32	0.30	0.6	2.4×10^{23}	7.2×10^{31}	0.0092	6.624×10^{29}	6.624×10^{36}
NH$_3$ COMPASS	0.9	0.176	0.6	3.4×10^{24}	1.0×10^{33}	0.0251	2.510×10^{31}	2.510×10^{38}
butanol COMPASS	0.9	0.135	0.6	8.9×10^{23}	2.7×10^{32}	0.0148	3.996×10^{30}	3.996×10^{37}
H HERMES-like storage cell [26]	0.85	0.95	None	2.5×10^{14}	0.92×10^{33}	0.6521	5.999×10^{32}	5.999×10^{39}
^{3}He HERMES-like storage cell[27]	0.70	0.33	None	6.8×10^{13}	0.25×10^{33}	0.0533	1.334×10^{31}	1.334×10^{38}
H RHIC-like gas jet	0.958	0.97	None	1.2×10^{12}	4.3×10^{30}	0.864	3.715×10^{30}	3.715×10^{37}
^{3}He RHIC-like gas jet	0.70	0.33	None	1.0×10^{14}	3.6×10^{32}	0.0533	1.919×10^{31}	1.919×10^{38}

Table 10: Comparison of the target performances for SSA measurements (P_{T} : target polarisation; f : dilution factor; α : depolarisation factor; PF: packing factor.

Table 10 shows the comparison of the figure of merit for Single Transverse Spin Asymmetry measurements, for the various polarised targets described in this section. The nominal LHC proton beam flux is considered for the gaseous targets while the expected proton beam flux extracted by means of a bent crystal is considered for the E1039 and COMPASS targets. While the absolute error on STSA measurement is governed by the precision on the luminosity measurement for the two polarization states, the relative error will mainly come from the knowledge of the polarisation (usually determined with a precision of about 4%).

---

[26]$T = 300K$, $\ell = 100$cm
[27]$T = 300K$, $\ell = 100$cm

The 'HERMES' H gas target has the best figure of merit, of the order of 6×10^{32} cm$^{-2}s^{-1}$. Using a cooled storage cell at $T = 100$ K, the gas density would increase by a factor of $\sqrt{3}$, leading to an increase in the instantaneous luminosity to 1.59×10^{33} cm$^{-2}s^{-1}$, which is about 16% of the pp collider luminosity. The figure of merit $\mathcal{F}$ would increase up to 1.04×10^{33} cm$^{-2}s^{-1}$. The 'RHIC' H-jet gas target figure of merit is smaller by two order of magnitudes with respect to the 'HERMES' H gas target, because of the smaller achievable gas density. Similar performances as the 'RHIC' H-jet gas target can be reached with the solid E1039 and COMPASS targets. Due to the larger length of the COMPASS target, the figure of merit of the COMPASS target is better with respect to the E1039 one, at the cost of less portability and the likely impossibility to couple it to the beam split option.

4. Detector requirements and expected performances

The ambitious physics case outlined in this document imposes significant requirements on the detector needed for such an experiment. The particle production is shifted towards larger angles, and the rapidity shifts are $\Delta y = 4.2$ and 4.8 for a beam energy per nucleon of 2.76 and 7 TeV, respectively. Figure 7 shows the rapidity acceptances of ALICE and LHCb detectors in the collider and fixed-target modes, in comparison with the STAR and PHENIX detectors at RHIC. As outlined by this comparison of LHC detectors used
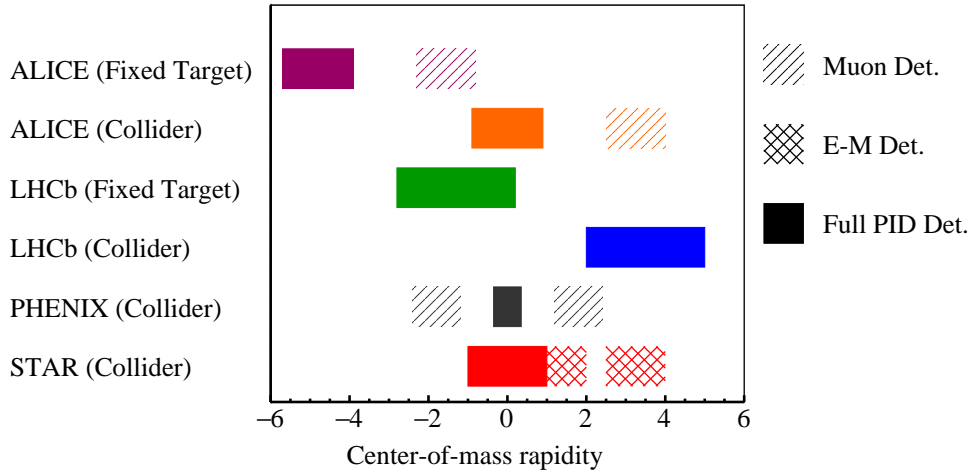
Figure 7: Comparison of the kinematic coverages of the ALICE and LHCb detectors at the LHC and the STAR and PHENIX detectors at RHIC. For ALICE and LHCb, the acceptance is shown in the collider and the fixed-target modes with a target position at the nominal Interaction Point (IP) for a 7 TeV proton beam. The "Full PID Det." label indicates detector with particle identification capabilities, "E-M Det." - an electromagnetic calorimeter, "Muon Det." - a muon detector.

in a fixed-target mode, the major advantage of a fixed-target experiment is that particle production can be easily measured at very large values of negative-$y_{\text{c.m.s.}}$ with standard detector technologies. On the other hand, the full forward hemisphere is compressed into a very small solid angle area. The instantaneous luminosities with a fixed-target experiment by using the LHC beams are expected to be high, as described in the previous section, leading to large inelastic rates and allowing one to probe the full rapidity range with high statistics for many processes. In this section, we will describe the detector requirements in order to achieve the rich physics program proposed for a fixed-target experiment at the LHC, and we will discuss the possible implementations with the existing detectors of the ALICE and LHCb experiments. The two implementations will be compared in terms of rapidity coverage, integrated luminosities and physics reach.

4.1. Detector requirements
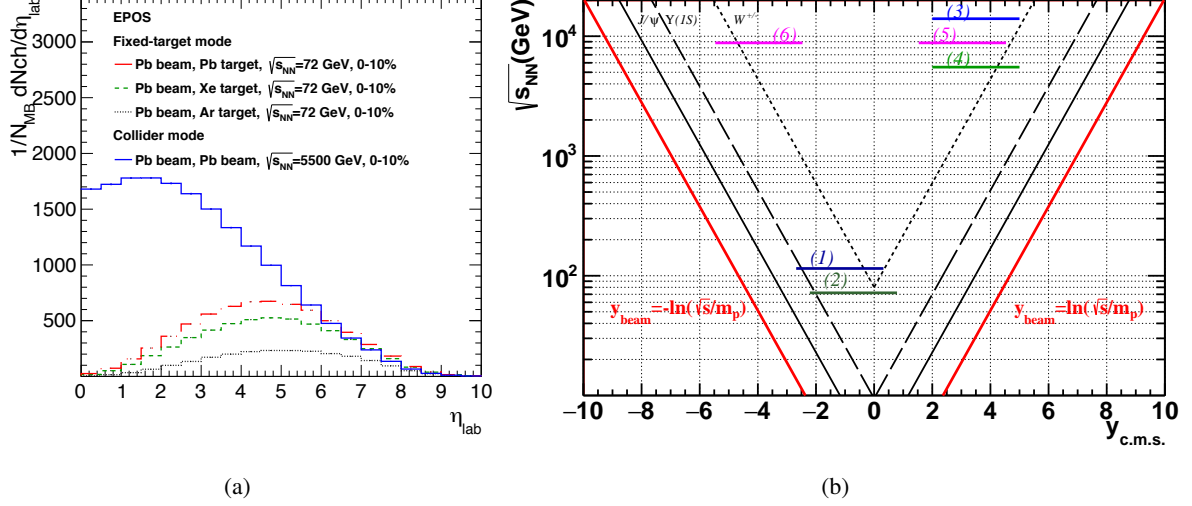
Figure 8: (a) The averaged charged-particle multiplicity as a function of the pseudorapidity in the laboratory frame for various heavy-ion systems. (b) The $y_{\text{c.m.s.}}$ coverage as a function of the colliding energies per nucleon pair ($\sqrt{s_{NN}}$). The red solid lines represent the beam rapidity. The solid, dashed and dotted black lines respectively show the $y_{\text{c.m.s.}}$ coverage for the J/ψ, $\Upsilon(1S)$ and W production. The horizontal lines show the $y_{\text{c.m.s.}}$ acceptance of a detector with a pseudorapidity coverage in the laboratory frame of $2 < \eta < 5$ for different colliding systems and modes using the 7 TeV proton and 2.76 A.TeV Pb LHC beams: (1) pp and pA collisions in the fixed-target mode at $\sqrt{s_{NN}} = 115$ GeV, (2) PbA collisions in the fixed-target mode at $\sqrt{s_{NN}} = 72$ GeV; (3) pp collisions in the collider mode at $\sqrt{s} = 14$ TeV, (4) PbPb collisions in the collider mode at $\sqrt{s_{NN}} = 5.5$ TeV, (5) pPb collisions in the collider mode at $\sqrt{s_{NN}} = 8.8$ TeV, (6) Pbp collisions in the collider mode at $\sqrt{s_{NN}} = 8.8$ TeV.

The rapidity range in the laboratory frame of a fixed-target experiment should be as broad as possible covering the regions of backward and mid-rapidity in the center of mass, i.e. from $y_{\text{lab}} = 0$ to $y_{\text{lab}} = 4.2$ and 4.8 with a beam energy per nucleon of 2.76 and 7 TeV, respectively. A multi-purpose experiment with detectors able to identify particles such as electrons, hadrons, photons as well as muons down to low p_T would fit better the rich physics programme proposed here. A high-resolution vertex detector would allow one to measure precisely the primary and secondary vertices associated to the production of heavy-flavour hadrons. A polarised target requires space, e.g. for pumping system and diagnosis apparatus in the case of a gas target, and it is challenging, but possible, to couple it with a large angle detector.

The physics case comprises lead-nucleus collisions with the instantaneous luminosity up to 3×10^{28} cm^{-2}s^{-1} as well as proton-proton and proton-nucleus collisions with the instantaneous luminosity up to 10^{33} cm^{-2}s^{-1}. The detectors must be able to cope with the occupancies and fluences for both of these configurations. In the case of the heaviest nuclear collisions foreseen, PbXe collisions at $\sqrt{s_{NN}} = 72$ GeV, the average number of charged particles is maximal at $\eta_{\text{lab}} = 4.2$ and amounts to $dN_{ch}/d\eta \sim 600$ for the most 10% central collisions according to EPOS [97, 132]. The charged particles multiplicity is shown on the left panel of Fig. 8 for various heavy-ion system as a function of the pseudorapidity in the laboratory frame and is compared to the one obtained at the LHC in a collider mode. In a fixed-target mode, the multiplicity does not exceed the one obtained in PbPb collisions at $\sqrt{s_{NN}} = 5.5$ TeV in a collider mode. If one considers the instantaneous luminosities quoted above and the inelastic cross-sections from EPOS [28]

---

[28]In order to compute the inelastic rate, we use the inelastic cross sections from EPOS, $\sigma_{inel} = 39$ mb in pp collisions at $\sqrt{s}$

one ends up with inelastic rates corresponding to 36 MHz, 300 MHz and 190 kHz in *pp*, *p*Xe and PbXe collisions, respectively. These numbers are, for the *pp* and *AA* cases, of the same order of magnitude than the maximum rates planned for LHC in a collider mode in Run 3 and 4.

4.2. Possible implementations with existing apparatus

The proposed physics programme is rich and it is clear that building a completely new experiment would allow one to cope with the various requirements briefly detailed above. However one could already use an existing detector at the LHC in order to cover a large part of the physics programme. In this respect, the right panel of Fig. 8 shows the evolution of the rapidity coverage in the center-of-mass frame with $\sqrt{s_{NN}}$. The rapidity phase-space decreases while lowering the energy. While in a collider mode a forward-angle detector with $2 < \eta < 5$ covers approximately a forward-rapidity region of $2 < y_{\text{c.m.s.}} < 5$, in a fixed-target mode the same detector covers the mid-rapidity region as well as half of the backward-rapidity region. In the case of a proton beam of 7 TeV on a fixed target, the rapidity coverage for the mentionned pseudorapidity range is $-2.8 < y_{\text{c.m.s.}} < 0.2$.

In the following sections, we will discuss possible implementations of the fixed-target programme at the LHC with two existing experiments: ALICE and LHCb. The detectors will be briefly presented in both cases as well as their upgrades planned for LHC Run 3 and 4 and we will discuss their ability to cover the physics programme described in this document. In the case of LHCb, a fixed-target programme has recently started with a reduced luminosity and some aspects of the fixed-target mode will be described. For both experiments, the rapidity acceptance, the achievable luminosities as well as the physics reach will be discussed for various fixed-target systems and based on experimental constraints.

4.2.1. ALICE as a fixed-target experiment

The detectors of ALICE [133, 134] are optimised for studying the QCD matter created in high-energy collisions of lead nuclei. They are able to cope with high-multiplicity events and to track charged particles down to $p_T \sim 0.15$ GeV/c at mid-rapidity.

The Central Barrel (CB) detectors are embedded into the L3 solenoid magnet that provides a field of 0.5 T parallel to the beam line. The inner most detector, the Inner Tracking System (ITS), tracks charged particles within $|\eta| < 0.9$ and allows to reconstruct primary and secondary vertices. The two innermost layers of the ITS cover $|\eta| < 2$ and $|\eta| < 1.4$ for the first and second layer, respectively. The resolution on the longitudinal position of the primary vertex ranges from 10 to 150 μm decreasing with the charge multiplicity. The Time Projection Chamber (TPC) provides track reconstruction as well as particle identification (PID) via the measurement of the specific ionisation energy loss dE/dx in the gas volume. The phase space covered by the TPC in pseudorapidity is $|\eta| < 0.9$ with full radial track length. The TPC acceptance can be extended by considering only 1/3 of the full radial track length (also denoted as "TPC reduced track length" in the following) at the cost of worsening the momentum resolution. In that case, the pseudorapidity acceptance is $|\eta| < 1.5$. The Time Of Flight (TOF) detector extends the PID via the measurement of the flight time of the charged particles from the Interaction Point (IP). Its pseudorapidity coverage is $|\eta| < 0.9$. For that purpose the T0 detector located along the beam line measures the event collision time. The CB includes also High Momentum Particles Identification Detector (HMPID), calorimeters (Electromagnetic Calorimeter: EMCal and Photon Spectromete: PHOS) and Transition Radiation Detector (TRD) for particle identification purpose. The transverse momentum relative resolution measured with both ITS and TPC ranges from 0.8 to 2% for $p_T = 1$ to 10 GeV/c.

= 115 GeV, $\sigma_{inel} = 1.3$ b in *p*Xe collisions at $\sqrt{s} = 115$ GeV and $\sigma_{inel} = 6.2$ b in PbXe collisions at $\sqrt{s_{NN}} = 72$ GeV, and the instantaneous luminosities of 10^{33}cm^{-2}s^{-1}, 2.10^{32}cm^{-2}s^{-1} and 3.10^{28}cm^{-2}s^{-1} in *pp*, *p*Xe and PbXe collisions, respectively.

At forward rapidity, the Muon Spectrometer (MS) covers the pseudorapidity range $2.5 < \eta < 4$ in the laboratory frame. It includes a dipole magnet with an integrated field of 3 T·m, five tracking stations and two trigger stations. A system of absorbers located in front of the tracking and trigger stations and around the beam pipe is used for filtering out the hadrons and to protect the chambers from secondary particles produced in interactions of large-η primary particles with the beam pipe. The combined effect of the front absorber and of the iron wall implies the detection of tracks matching the trigger chambers with $p > 4$ GeV/c. The relative muon momentum resolution is $\delta p/p \approx 1\%$.

The ALICE upgrade is scheduled for the second LHC Long Shutdown (LS2) that will take place in 2019 and 2020. In order to allow for a continuous readout at an interaction rate of 50 kHz in PbPb collisions at $\sqrt{s_{NN}}$ = 5.5 TeV, many detectors or their electronics will be upgraded. In pp and pA collisions, the detector upgrade will allow to record data with a rate of 200 kHz. Figure 51 presents a schematic view of the ALICE detectors for Run 3. A new detector, the Muon Forward Tracker (MFT), a Si-tracking detector, is designed to add vertexing capabilities to the MS by measuring charged tracks with a high spatial resolution. It is positionned along the beam axis between the ITS inner barrel and the MS front absorber. The MFT will cover the pseudorapidity acceptance $2.5 < \eta < 3.6$. The MFT capability to identify tracks coming from secondary vertices is measured by experimental resolution on the track offset to the primary vertex, the latter being measured by the ITS. Resolutions below 100 and 1000 μm are found for $p_T > 1$ GeV/c in the transverse and longitudinal direction, respectively. These resolutions decrease with increasing p_T down to 25 and 180 μm at large p_T in the transverse and longitudinal direction, respectively. It is worth noting that the mass resolution will be greatly improved for the low mass dimuon ($M_{\mu\mu} < 1.5$ GeV/c^2) by adding the MFT to the MS. The mass resolution has been evaluated to be lower than 20 MeV/c^2 for η, ϕ and ω mesons.

(a)   (b)
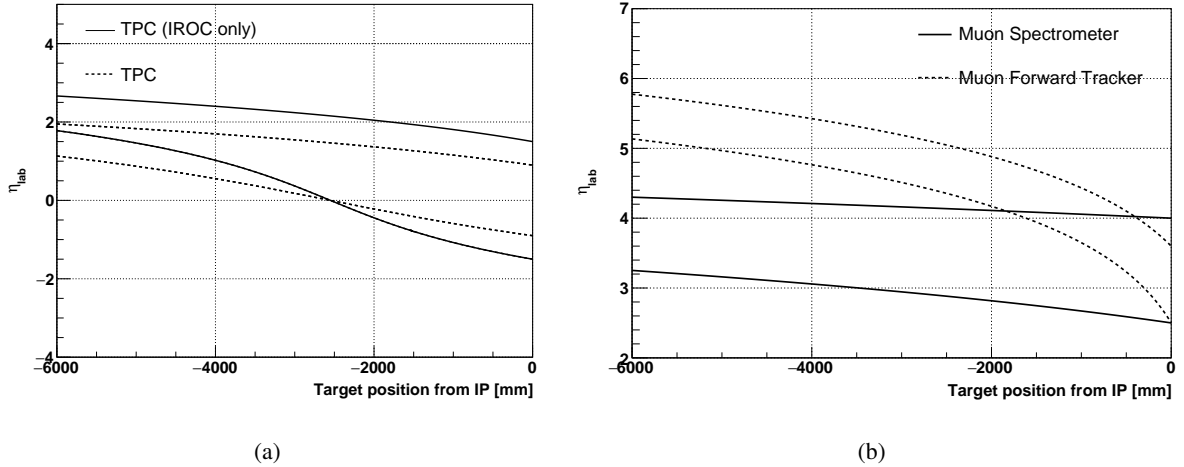
Figure 9: (a) $\eta_{Lab.}$ acceptance of the ALICE TPC as a function of the target position (z_{target}) upstream from the nominal Interaction Point (IP). Full (dashed) lines refer to reduced (full) radial track length in the TPC; (b) $\eta_{Lab.}$ acceptance of the ALICE MS (full line) and MFT (dashed line) as a function of z_{target}.

In a fixed-target mode and with a target positioned at the IP, the acceptance of the MFT and MS allow measurements in the rapidity regions of $-2.3 < y_{c.m.s.} < -1.2$ with a 7 TeV proton beam and of $-1.7 < y_{c.m.s.} < -0.6$ with a 2.76 A.TeV Pb beam. The CB covers the very rear region with a center-of-mass rapidity of $y_{c.m.s.} < -3.9$ and $y_{c.m.s.} < -3.3$ respectively, i.e. it allows one to access the very high-x region. The target can also be displaced upstream of the nominal IP (on the A-side of ALICE, opposite to the MS). Fig. 9 shows the pseudorapidity acceptance of some ALICE detectors as a function of the target position,

where the acceptance is computed considering the geometry of the active detectors. The acceptances are shifted towards the forward region when the target is displaced upstream of the nominal IP, in the opposite direction of the MS. If the vertex is displaced by a large amount and if one wants to measure the primary and secondary vertices precisely, a new vertex detector close to the target is then required. In case of a polarised target, its polarisation may be modified with the magnetic field of the L3 magnet. This brings additional constraints on the target position.

The readout rate of ALICE in Run 3 should allow one to run at 50 kHz inelastic rate in PbXe collisions and some further studies are needed to demonstrate if a higher rate is sustainable. In *pp* and *pA* collisions, the ALICE readout rate is however smaller than the maximal rate foreseen with a proton beam on a fixed target of 40 MHz rate. While the ALICE upgrade is designed to run with a 200 kHz inelastic rate in *pp* and *pA* collisions, it might be possible to run up to 1 MHz in *pp* and *pA* collisions.

The occupancy of the *AA* collision systems is not an issue in ALICE since the detectors were designed to measure PbPb collisions at $\sqrt{s_{NN}}$ = 5.5 TeV and the average charged particle multiplicity in a fixed-target mode does not exceed the one in a collider mode as shown in Fig. 8.

The MS and the MFT will cover the physics programme described above with the detection of single muon from heavy-flavours, muon pairs (such as Drell-Yan) and quarkonia down to low p_T. Further works are needed to estimate the level of background for the critical analyses such as Drell-Yan in *AA* collisions and in case the vertex is displaced upstream from the ALICE IP. The CB can detect and identify neutral and charged particles in the very backward region. Further studies will determine if the achievable luminosities allow one to complete some of the physics cases in this rear region.

There are ongoing feasibilities studies on the installation of an internal solid target in the ALICE experiment. The beam splitting option is currently investigated, where the beam halo is deflected by a crystal placed ~ 70 m upstream from the nominal IP, and the deflected particles hit the target located inside the L3 magnet. The target holder is envisioned as an adjustable device, which facilitates moving the target from the parking position (outside of the beam pipe) to the working point, 13 mm from the beam axis [135]. The mechanical design of the system is currently under study.

4.2.2. LHCb as a fixed-target experiment

The LHCb detector [136, 137] is a single-arm forward spectrometer, designed for studies of hadrons containing *b* and/or *c* quarks. Its pseudorapidity coverage in the laboratory frame is $2 < \eta < 5$. This geometry coverage allows one to use the LHCb detector for fixed-target experiments. The LHCb detector comprises a high precision tracking system, two ring-imaging Cherenkov detectors for the identification of different types of charged hadrons, a calorimeter system for identifying photons, electrons and hadrons, and a muon system for the muon identification. The tracking system includes a silicon-strip vertex locator (VELO) and four stations with a dipole magnet between the first and the other three stations. It can achieve a relative momentum uncertainty of charged particles varying from 0.5% to 0.8% for the momentum between a few GeV/c to 100 GeV/c. The calorimeter system is composed of a scintillating pad, a preshower detector, an electromagnetic calorimeter, and a hadron calorimeter. The muon system consists of five muon stations with alternating layers of iron and multiwire proportional chambers. As described below, some detectors will be upgraded for Run 3 and a schematic view of the upgraded detectors are shown on Fig. 52.

- VELO. The current VELO of LHCb is composed of 84 single-sided silicon strip sensors, operated in a secondary vacuum inside the LHC beam pipe [136]. The VELO length is about 1 m along the beam. The pitch of the *R* sensors varies from 40 to 102 µm, and that of the ϕ sensors varies from 38 to 97 µm. The length of the shortest (longest) strip is 3.8 mm (33.8 mm) for R sensors; The length of the shortest (longest) strip is 5.9 mm (24.9 mm) for ϕ sensors. The resolution of the reconstructed

primary vertex is 13 μm in the $x - y$ plane and 71 μm in the z direction, assuming that the number of tracks of the primary vertex is 25. When the number of tracks reduces, the resolution becomes slightly worse. The resolution of the impact parameter is about $15 - 50$ μm [85, 137]. The excellent vertex reconstruction ability allows one to well separate the primary vertex and the secondary vertex of B or charmed hadron decays. For the LHCb upgrade during the LS2, the current VELO detector will be completely replaced by a new detector based on hybrid silicon pixel sensors [138]. The pixel pitch is 50 μm × 50 μm. It will have the same physics performance and can deliver a readout at 40 MHz. Compared to the current silicon strip VELO, the new VELO can cope with events with much higher track multiplicity.

- Tracking. The first station of the current tracking system is based on silicon micro-strip. The other three station, which are located after the LHCb dipole magnet, are composed of silicon micro-strip inner trackers and straw drift tube outer trackers. The relative momentum resolution is about $0.5 - 1\%$. The mass resolution of K_S^0 mesons is 3.5 (7) MeV/c^2 if they decay inside (outside) the VELO. For the LHCb upgrade, the first station will be replaced by high granularity silicon micro-strip planes, and the other stations will be replaced by scintillating fibre trackers [139]. The momentum resolution will be about $10 - 20\%$ better than the current resolution.

- Calorimeter. The electromagnetic calorimeter is composed of a sampling scintillator-lead structure. The hadron calorimeter is a sampling scintillator-iron structure. The mass resolution of low transverse momentum π^0 mesons, reconstructed with well-separated photons, is 8 MeV/c^2. For π^0 mesons with transverse momentum greater than 2 GeV/c, the mass resolution is around 20 (30) MeV/c for those reconstructed with well separated (merged) photons. If using converted photons, the resolution of the mass difference between $M(\mu^+\mu^-\gamma)$ and $M(\mu^+\mu^-)$ is around 5 MeV/c^2 for χ_c states. LHCb is now discussing an upgrade of the calorimeter in Run-3 [140], replacing the current electromagnetic calorimeter by a silicon-tungsten sampling calorimeter.

- Muon system. The muon system includes five rectangular shaped stations. The first station is made of triple Gas Electron Multiplier detectors, while the other four are composed of multiwire proportional chambers. The dimuon invariant mass resolution is about 14 (43) MeV/c^2 at the J/ψ ($\Upsilon(1S)$) mass. The muon identification efficiency is above 95% for the tracks with transverse momentum above 1.7 GeV/c.

- Readout. The current LHCb detector reduces the event rate from 40 to 1 MHz at the first level hardware trigger. After the LHC LS2, the upgraded hardware trigger will have the ability to read full event information at a rate up to 40 MHz.

- HERSCHEL detector [141]. LHCb installed a HERSCHEL (High Rapidity Shower Counters for LHCb) subdetector for Run 2 of the LHC. It is a system of forward shower counters consisting of five scintillator planes with PMTs. These five stations are installed perpendicular to the beam, their z coordinates are -114 m, -19.7 m, -7.5 m, $+20$ m, and $+114$ m, respectively. The z direction of the coordinate system is from VELO to the muon system along the beam, and the origin is the interaction point inside VELO. Combining with other LHCb subdetectors, HERSCHEL greatly extends sensitivity of detecting charged particles at high pseudorapidity: $-10 < \eta < -5$, $-3.5 < \eta < -1.5$, $2 < \eta < 5$, and $5 < \eta < 10$.

The capability of LHCb to cope with high-multiplicity events and the limit on the event charged track multiplicity will be defined with the ongoing data reconstruction of PbPb collisions at 5 TeV and PbAr

collisions at 69 GeV. The occupancy of the VELO is essential to determine the track reconstruction, since the VELO provides the best position precision among all subdetectors of the tracking system. As shown in Fig. 19 of Ref. [85], the cluster occupancy in the current VELO varies from 0.4% to 0.6% depending on the positions of the silicon strips. This result is obtained with a data sample passing a random trigger on beam crossing, and the average number of visible interactions per beam crossing is $\mu = 1.7$. The occupancy of the upgraded VELO significantly reduced owing to the replacement of silicon strips by hybrid silicon pixels. As shown in Fig. 20 of Ref. [138], the cluster occupancy is 0.08% for the pixels closest to the IP (0.5 mm). It drops rapidly below 0.01% as the radius increases. This result is obtained using simulated minimum-bias events at $\mu = 5.2$. When the difference of the data samples is taken into account, the occupancy of the upgraded VELO is expected to be reduced by a factor of approximately 20.

As discussed in Section 3.3.1, since the pilot runs of pNe and PbNe in 2012 and 2013, the direct injection system SMOG [95] is used in a fixed-target mode by injecting different gases inside the VELO vessel. For the 6.5 TeV proton beams, only special runs, like van der Meer scans or the period corresponding to the ramp up of the beam energy, were used. The time duration of pHe, pNe and pAr collisions was typically 10–20 hours for each year, respectively. For 2.5 TeV proton beams, the proton-gas data were taken in parallel with pp collisions; the time duration of pHe collisions was around 100 hours, and that of pNe was around 200 hours. Only Neon and Argon gases were used with lead beams. During the PbPb LHC run in 2015, PbAr data were taken with a time duration of approximately 50 hours.

Even though the data taking time was limited, SMOG delivered physics results [100, 86]. The LHCb collaboration reported the anti-proton differential cross section in pHe collisions. The pAr run demonstrated the LHCb capabilities for charmed meson and charmonium reconstruction in the fixed-target mode. Both the $J/\psi \to \mu^+\mu^-$ and $D^0 \to K^\mp\pi^\pm$ were measured with a decent mass resolution and an adequate efficiency [100]. Fig. 10 shows the ratio of J/ψ and D^0 yields evaluated in pAr collisions at $\sqrt{s_{NN}} = 110$ GeV.
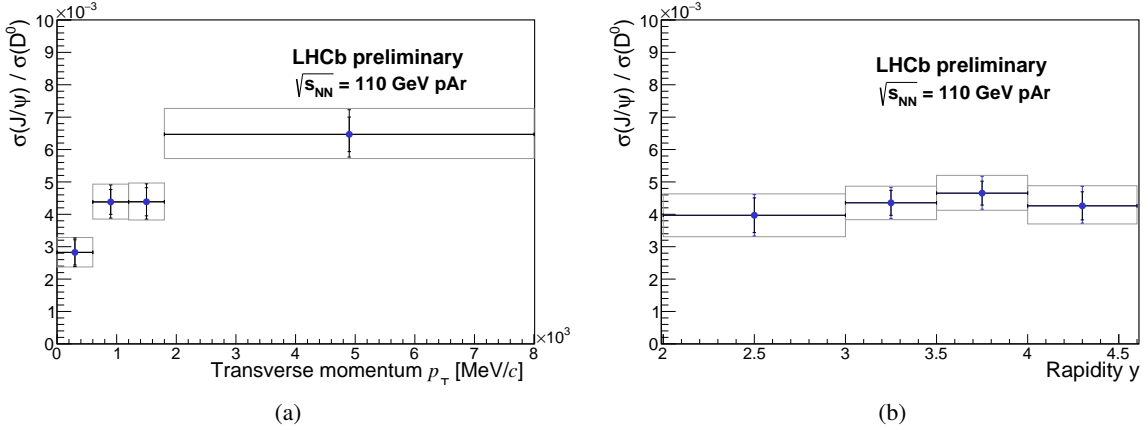
Figure 10: The J/ψ to charmed meson ratio as a function of transverse momentum and rapidity in pAr collisions collected by the LHCb detector in a fixed-target mode. [Taken from [86]].

When the SMOG data were taken in parallel with pp or PbPb collisions, the trigger of the SMOG related events was designed to fully utilize the data acquisition (DAQ) potential. When the DAQ busy time was too large, tighter cuts were used for the SMOG trigger. It was also proposed to inject the gases in a storage cell (as described in Section 3.3.3) attached to the end of the VELO RF shields [142]. This proposal, denoted SMOG2, will significantly increase the luminosity, by up to a factor of 100 [142, 143]. With the

storage cell, a baseline scenario was proposed in [143] for Run 3 with the following integrated luminosities: $\mathcal{L}_{pH}$ = 10 pb^{-1}, $\mathcal{L}_{pD}$ = 10 pb^{-1} and $\mathcal{L}_{pAr}$ = 10 pb^{-1} at $\sqrt{s_{NN}}$ = 115 GeV as well as $\mathcal{L}_{PbAr}$ = 5 nb^{-1} and $\mathcal{L}_{pAr}$ = 1 pb^{-1} at $\sqrt{s_{NN}}$ = 72 GeV. This proposal is very promising and is a first step towards the fixed-target programme described in this paper, for $2 < \eta < 5$.

4.2.3. Comparison of possible implementations

Fig. 11 shows the $y_{\text{c.m.s.}}$ acceptances of the ALICE and LHCb detectors for two fixed-target colliding energies, namely $\sqrt{s}$ = 72 GeV and 115 GeV. The rapidity coverages with a target position at the nominal IP are shown as full lines. This corresponds to the case of LHCb as a fixed-target detector with the SMOG system. In the case of ALICE, the acceptance with two other target positions are also shown. While the ALICE MS and the LHCb detectors cover the central $y_{\text{c.m.s.}}$ region as well as half of the backward rapidity acceptance ($y_{\text{c.m.s.}} < 0$), the ALICE CB has the particularity to probe the target rapidity region and the end of the phase space ($x_F \to -1$). In the ALICE and LHCb cases, the wide $y_{\text{c.m.s.}}$ range makes these detectors suitable to study the rapidity dependence of various probes.
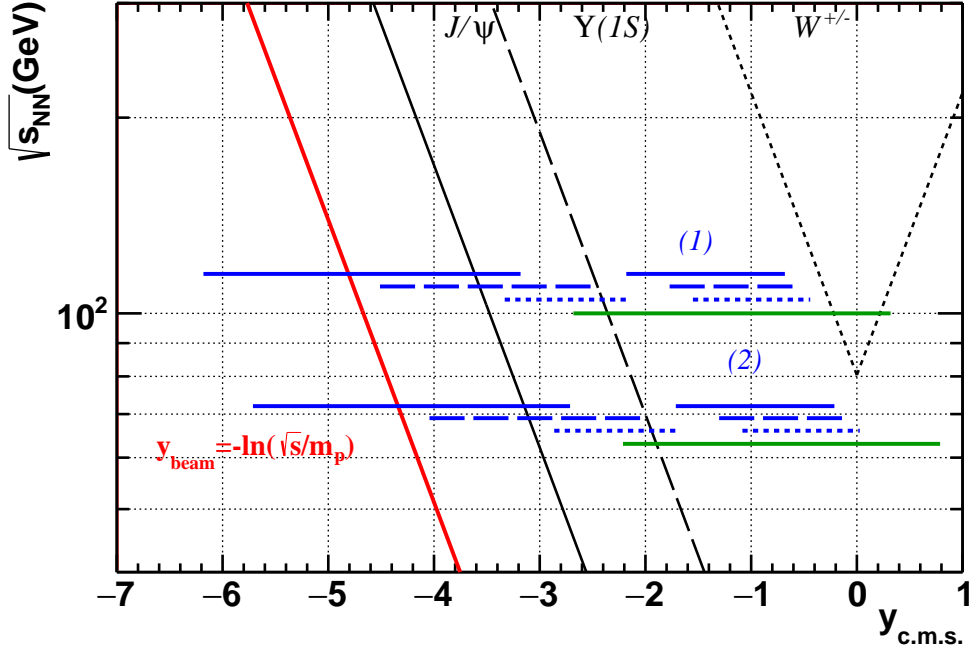
Figure 11: Center-of-mass-rapidity ($y_{\text{c.m.s.}}$) coverage as a function of the colliding energies per nucleon pair ($\sqrt{s_{NN}}$) as in Fig. 8. The blue lines represent the acceptance of the TPC and MS of ALICE. The full, long-dashed and short-dashed lines correspond to targets located at the IP, upstream of the IP by z_{target} = 2.75 and 4.7 m, respectively. The green lines represent the acceptance of the LHCb detector with a target at the IP. The long-dashed and short-dashed blue lines as well as the green lines are shifted in energy for a better visibility.

Tables 11 and 12 show the achievable luminosities using the ALICE and LHCb detectors during one LHC year, if one considers as a limitation the aforementioned experimental data-taking rates and by considering the luminosities of Table 9. We have also assumed that ALICE and LHCb could run in the fixed-target

---

[29] Target length considering the proton beam.
[30] Target length considering the Pb beam.

Target			ALICE proton beam ($\sqrt{s_{NN}}$ = 115 GeV) $\mathcal{L}$ [cm^{-2}s^{-1}]	σ_{inel}	Inel rate kHz	$\int\mathcal{L}$	ALICE Pb beam ($\sqrt{s_{NN}}$ = 72 GeV) $\mathcal{L}$ [cm^{-2}s^{-1}]	σ_{inel}	Inel rate kHz	$\int\mathcal{L}$
Internal gas target	Gas-Jet	H$\uparrow$	4.3 x 10^{30}	39 mb	168	43 pb^{-1}	5.6 x 10^{26}	1.8 b	1	0.56 nb^{-1}
		H$_2$	2.6 x 10^{31}	39 mb	1000	0.26 fb^{-1}	2.8 x 10^{28}	1.8 b	50	28 nb^{-1}
		D$\uparrow$	4.3 x 10^{30}	72 mb	309	43 pb^{-1}	5.6 x 10^{26}	2.2 b	1.2	0.56 nb^{-1}
		^{3}He$\uparrow$	8.5 x 10^{30}	117 mb	1000	85 pb^{-1}	2.0 x 10^{28}	2.5 b	50	20 nb^{-1}
	Storage Cell	H$\uparrow$	2.6 x 10^{31}	39 mb	1000	0.26 fb^{-1}	2.8 x 10^{28}	1.8 b	50	28 nb^{-1}
		H$_2$	2.6 x 10^{31}	39 mb	1000	0.26 fb^{-1}	2.8 x 10^{28}	1.8 b	50	28 nb^{-1}
		D$\uparrow$	1.4 x 10^{31}	72 mb	1000	140 pb^{-1}	2.2 x 10^{28}	2.2 b	50	22 nb^{-1}
		^{3}He$\uparrow$	8.5 x 10^{30}	117 mb	1000	85 pb^{-1}	2.0 x 10^{28}	2.5 b	50	20 nb^{-1}
		Xe	7.8 x 10^{29}	1.3 b	1000	7.8 pb^{-1}	8.1 x 10^{27}	6.2 b	50	8.1 nb^{-1}
Internal solid target with beam halo	Wire Target	C (500 μm)	2.8 x 10^{30}	271 mb	760	28 pb^{-1}	5.6 x 10^{26}	3.3 b	1.8	0.56 nb^{-1}
		Ti (500 μm)	1.4 x 10^{30}	694 mb	971	14 pb^{-1}	2.8 x 10^{26}	4.7 b	1.3	0.28 nb^{-1}
		W (184 μm^{29} / 500 μm^{30})	5.9 x 10^{29}	1.7b	1000	5.9 pb^{-1}	3.1 x 10^{26}	6.9 b	2.1	0.31 nb^{-1}
Beam splitting	E1039	$NH_3^\uparrow$	2.6 x 10^{31}	39 mb	1000	0.26 fb^{-1}	1.4 x 10^{28}	1.8 b	25	14 nb^{-1}
		$ND_3^\uparrow$	1.4 x 10^{31}	72 mb	1000	140 pb^{-1}	1.4 x 10^{28}	2.2 b	30	14 nb^{-1}
	Unpolarised solid target	C (658 μm / 5000 μm)	3.7 x 10^{30}	271 mb	1000	37 pb^{-1}	5.6 x 10^{27}	3.3 b	18	5.6 nb^{-1}
		Ti (515 μm / 5000 μm)	1.4 x 10^{30}	694 mb	1000	14 pb^{-1}	2.8 x 10^{27}	4.7 b	13	2.8 nb^{-1}
		W (184 μm / 5000 μm)	5.9 x 10^{29}	1.7b	1000	5.9 pb^{-1}	3.1 x 10^{27}	6.9 b	21	3.1 nb^{-1}

Table 11: Summary table of the achievable integrated luminosities with the ALICE detector accounting for the data-taking-rate capabilities and by considering the luminosities of Table 9. The inelastic cross sections are taken from EPOS [97, 132].

Target		proton beam ($\sqrt{s_{NN}}$ = 115 GeV)				Pb beam ($\sqrt{s_{NN}}$ = 72 GeV)			
		$\mathcal{L}$ [cm^{-2}s^{-1}]	σ_{inel}	Inel rate kHz	$\int\mathcal{L}$	$\mathcal{L}$ [cm^{-2}s^{-1}]	σ_{inel}	Inel rate kHz	$\int\mathcal{L}$
Gas-Jet	H$^\uparrow$	4.3 x 10^{30}	39 mb	168	43 pb^{-1}	5.6 x 10^{26}	1.8 b	1	0.56 nb^{-1}
	H$_2$	1.0 x 10^{33}	39 mb	40000	10 fb^{-1}	2.8 x 10^{30}	1.8 b	5000	2.8 pb^{-1}
	D$^\uparrow$	4.3 x 10^{30}	72 mb	309	43 pb^{-1}	5.6 x 10^{26}	2.2 b	1.2	0.56 nb^{-1}
	^{3}He$^\uparrow$	3.4 x 10^{32}	117 mb	40000	3.4 fb^{-1}	4.7 x 10^{28}	2.5 b	118	47 nb^{-1}
Internal gas target — Storage Cell	H$^\uparrow$	0.92 x 10^{33}	39 mb	35880	9.2 fb^{-1}	1.2 x 10^{29}	1.8 b	216	120 nb^{-1}
	H$_2$	1.0 x 10^{33}	39 mb	40000	10 fb^{-1}	7.5 x 10^{29}	1.8 b	1400	750 nb^{-1}
	D$^\uparrow$	5.6 x 10^{32}	72 mb	40000	5.6 fb^{-1}	1.4 x 10^{29}	2.2 b	308	140 nb^{-1}
	^{3}He$^\uparrow$	1.3 x 10^{33}	117 mb	40000	13 fb^{-1}	4.7 x 10^{29}	2.5 b	1175	470 nb^{-1}
	Xe	3.1 x 10^{31}	1.3 b	40000	0.31 fb^{-1}	3.0 x 10^{28}	6.2 b	186	30 nb^{-1}
Internal solid target with the beam halo — Wire Target	C (500 μm)	2.8 x 10^{30}	271 mb	760	28 pb^{-1}	5.6 x 10^{26}	3.3 b	1.8	0.56 nb^{-1}
	Ti (500 μm)	1.4 x 10^{30}	694 mb	972	14 pb^{-1}	2.8 x 10^{26}	4.7 b	1.3	0.28 nb^{-1}
	W (500 μm)	1.6 x 10^{30}	1.7 b	2720	16 pb^{-1}	3.1 x 10^{26}	6.9 b	2.1	0.31 nb^{-1}
E1039	NH$_3^\uparrow$	7.2 x 10^{31}	39 mb	2808	0.72 fb^{-1}	1.4 x 10^{28}	1.8 b	25	14 nb^{-1}
	ND$_3^\uparrow$	7.2 x 10^{31}	72 mb	5100	0.72 fb^{-1}	1.4 x 10^{28}	2.2 b	30	14 nb^{-1}
Beam splitting — Unpolarised solid target	C (5000 μm)	2.8 x 10^{31}	271 mb	7600	280 pb^{-1}	5.6 x 10^{27}	3.3 b	18	5.6 nb^{-1}
	Ti (5000 μm)	1.4 x 10^{31}	694 mb	9720	140 pb^{-1}	2.8 x 10^{27}	4.7 b	13	2.8 nb^{-1}
	W (5000 μm)	1.6 x 10^{31}	1.7 b	27200	160 pb^{-1}	3.1 x 10^{27}	6.9 b	21	3.1 nb^{-1}

LHCb

Table 12: Same as Table 11 for the LHCb detector.

mode during the full year with proton (10^7 s) and lead beams (10^6 s) with the corresponding instantaneous

luminosities. In some cases, namely the gas-jet, the storage cell and the solid target coupled to the beam splitting by a crystal, the resulting interaction rates are high and close to the ones expected in the collider mode for the LHC Runs 3 and 4. Additional limitations may then arise from various constraints such as the disk storage, the high-level trigger, the radiation level, the simultaneous running with the collider mode, etc. These constraints are not discussed in this review as they deserve dedicated studies. In the following, we discuss the luminosities obtained with these three technical implementations in both the ALICE and LHCb set-ups and comment on the luminosity needs for some of the physics cases that will be described in sections 5.1, 5.2 and 5.3.

With LHCb, the luminosity reach with a proton beam on an hydrogen target can be very large, up to yearly luminosity on the order of 10 fb^{-1}, if one can run at 40 MHz. As discussed in section 5.1, this will allow one to measure hard probes such as W or associated J/ψ production, to collect very large statistics for Drell-Yan and probe the D meson production at the most backward rapidity range. For example, Drell-Yan measurements is very useful to probe the light quark and anti-quark PDFs at high-x at a low scale, μ_F. By using nuclear solid or gas targets, one can reach luminosities on the order of 100 pb^{-1}, and even more depending on the target option, allowing one to probe the nuclear PDFs with a very high precision by measuring Drell-Yan, open heavy flavour and quarkonium production. With proton and lead beams, the luminosity reach in the case of ALICE is lower than in that of LHCb because of the lower data-taking rates. However, the rapidity coverage is complementary as well as the physics reach. Even though with ALICE the yearly luminosity can be as high as 250 pb^{-1} with a p beam on a H-gas target, a luminosity of about 40 pb^{-1} with the ALICE detectors would allow one to measure low energy $\bar{p}$, thanks to the very backward rapidity coverage, in $p + p \to \bar{p} + X$ in order to improve our knowledge of the cosmic $\bar{p}$ spectrum. The $\bar{p}$ spectrum could be further measured with various target types, such as He or C with the gas or solid target option, respectively.

With a transversally polarised H-gas target, luminosities from about 40 pb^{-1} to 250 pb^{-1} can be expected with ALICE for one LHC year. As discussed in section 5.2, this will allow one to access the spin asymmetry of probes such as Λ in the CB and J/ψ in the MS. With a larger luminosity with LHCb, on the order of 10 fb^{-1}, similar rare probes as those mentioned above for the unpolarised case (W, associated J/ψ, Drell-Yan, ...) will be accessible. These studies will definitely advance our understanding of the internal spin structure of the proton and neutron.

With a Pb beam on a heavy nuclear target, the luminosity is mainly limited by the impact on the beam lifetime for the gas target and by the usable beam flux for the beam splitting case. The luminosities do not differ by more than a factor of four between ALICE ($\mathcal{L} = 8$ nb^{-1}) and LHCb ($\mathcal{L} = 30$ nb^{-1}) for PbXe. In the case of the beam splitting option, large luminosities are also expected ($\mathcal{L} = 3$ nb^{-1}) for PbW. When the nuclear target is lighter, the Pb beam lifetime is less affected and the luminosities are larger for the case of LHCb coupled to a gas target. A full programme of heavy-ion studies can be carried out in the fixed-target mode at the LHC in particular with precise quarkonium measurements, with studies of the heavy-quark energy-loss mechanism and a rapidity scan of the yield and elliptic flow of identified charged particles over a broad rapidity range. These studies can be performed with large statistics in PbA collisions but also in pp and pA collisions (see *e.g.* Table 20 for the Υ case), with the ALICE and LHCb detectors. In the latter case, it is not yet established up to which event centrality the tracks can efficiently be reconstructed, in particular for the heaviest nuclear target such as Xe. As discussed in section 4.2.2, on-going studies will give more information on the event-centrality reach with LHCb for the Run 3.

In sections 5.1, 5.2 and 5.3, the assumptions considered for the generation of pseudo-data for LHCb and ALICE will be given. Figures-of-Merits (FoM) will refer to AFTER@LHCb, AFTER@ALICE$_\mu$ or AFTER@ALICE$_{CB}$ for pseudo-data generated in the acceptance of LHCb, the ALICE MS and the ALICE

CB, respectively.

5. Physics Projections

5.1. High-x frontier for particle and astroparticle physics

The purpose of this section is to address the question whether a modern fixed-target experiment with a record energy and with high luminosities can help answer problems at the frontier of particle and astroparticle physics. We divide this section in three parts for which the physics cases are quite distinct. In the first part, we discuss the impact of such an experiment on our understanding of the high-x structure of nucleons. In the second part, the physics case for the high-x structure of complex nuclei is considered. Finally, the third part is devoted to astroparticle-physics applications.

5.1.1. Nucleon structure

Much progress has been made in the past 30 years in our understanding of the partonic structure of nucleons. The parton distribution functions (PDFs) are determined in global analyses [144, 145, 146, 147, 148, 149] using a wealth of experimental information from fixed target and collider experiments. The analyses are routinely performed at next-to-leading order (NLO) and next-to-next-to-leading order (NNLO) of perturbative QCD and the uncertainties of the PDFs are carefully evaluated. Still, at high momentum fractions x, the PDFs are poorly known, in particular the smaller distributions. For example, the uncertainty of the gluon distribution gets very large at $x \gtrsim 0.4$ and the strange, charm and bottom PDFs are completely unconstrained in this kinematic range. A better understanding of the high-x structure of the nucleon is warranted for several reasons:

- First, while it is well-known that the gluon carries over 40% of the nucleon momentum, most of the gluons carry a small momentum fraction. On the other hand, in a constituent quark picture, it is rather the gluon distribution carrying a high momentum fraction which can be interpreted as binding the constituent quarks together. Furthermore, light cone models predict a relatively sizeable high-x component of the strange, charm and bottom PDFs. This means that the higher the probed x-values will be the better these fundamental aspects of QCD can be studied. Needless to say, that progress on the high-x gluon, strange and charm PDFs will lead to a refined picture for the light quark valence and sea distributions in this kinematic region.

- At the same time, PDFs are a crucial input for making theoretical predictions for observables at the LHC. In many cases, the PDF uncertainty has become the limiting factor in the accuracy of the predictions. This is particularly true for processes involving heavy new states in Beyond the Standard Model (BSM) theories where the high-x PDFs are probed. Clearly, an improved understanding of the high-x PDFs is crucial for BSM searches at the LHC and any future hadron colliders, and AFTER@LHC offers the unique opportunity to study these aspects of high-x hadron structure in detail.

Kinematic coverage of lepton pair production. As is well-known, at leading order (LO) the cross section for Drell-Yan (DY) lepton pair production is given by the following expression:

$$\frac{d^2\sigma}{dx_1 dx_2} = \frac{4\pi\alpha^2}{9sx_1x_2} \sum_i e_i^2 \left[q_i^A(x_1)\bar{q}_i^B(x_2) + \bar{q}_i^A(x_1)q_i^B(x_2) \right] , \tag{5}$$

where e_i is the electric charge of the quark (in units of e) and the sum runs over all active quark flavors. Therefore, it is clear that this process provides information on the (light) quark sea. Existing DY data which

are used in global PDF analyses come from fixed target experiments at Fermilab (E866/NuSea, E605) and the LHC.

Experimentally, the cross section is usually given as a function of the invariant mass of the lepton pair M (at LO $M^2 = x_1 x_2 s$) and Feynman variable $x_F = x_1 - x_2$ from which the momentum fractions $x_{1,2}$ can be recovered using the relation $x_{1,2} = (\sqrt{x_F^2 + 4\tau} \pm x_F)/2$ where $\tau = M^2/s$.

In Fig. 12 the kinematical reach for DY lepton pair production is shown assuming pp collisions at a c.m.s. energy of $\sqrt{s} = 115$ GeV with an integrated luminosity of 10 fb^{-1} and an acceptance of $2 < \eta_\mu^{lab} < 5$ and $p_{T,\mu} > 1.2$ GeV. It should be noted that each cell contains at least 30 events. For comparison, the kinematic coverage of existing DY data (E605, E866/NuSea) used in global proton PDF analyses is depicted.[31] The NuSea data have been obtained in 800 GeV pp and pd collisions ($\sqrt{s} = 38.8$ GeV) covering the di-muon mass ranges from 4.2 to 8.7 GeV and 10.85 to 16.85 GeV and the Feynman-x_F range from -0.05 to 0.8. As can be seen, AFTER@LHC will be able to extend the coverage up to even higher x-values close to one. Furthermore, while the NuSea data are dominated by statistical uncertainties reaching 100% at the kinematic boundaries, AFTER@LHC will considerably improve the precision due to the higher center-of-mass energy and the higher luminosity.
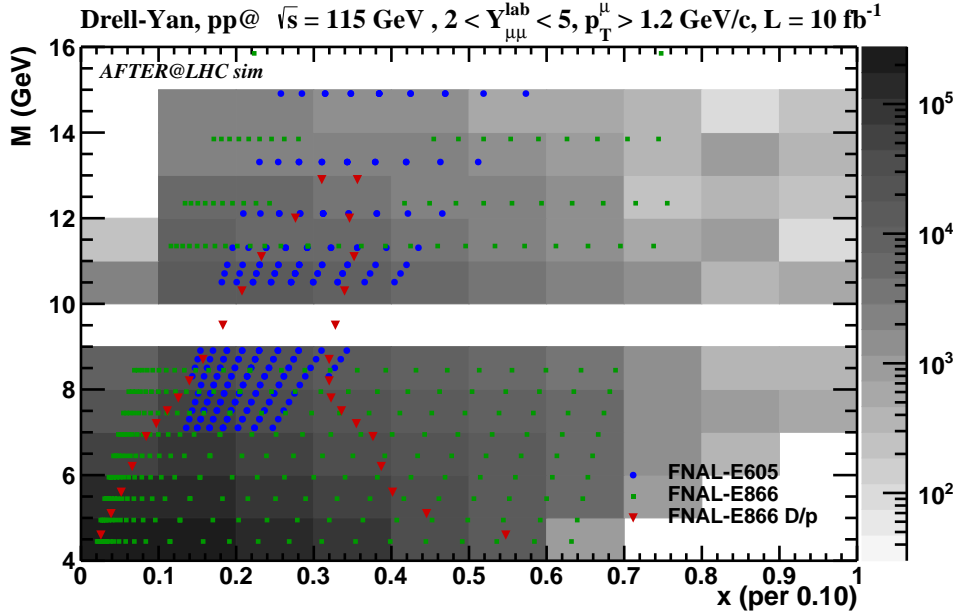
Figure 12: Kinematical reach for DY lepton-pair production with AFTER@LHCb in pp collisions at $\sqrt{s} = 115$ GeV with an acceptance of $2 < \eta_\mu^{lab} < 5$ and $p_{T,\mu} > 1.2$ GeV compared to the existing DY data [150, 151, 152, 153] used in current global PDF fits. (Each coloured cell contain at least 30 events).

The DY measurements at AFTER@LHC provide important tests of nucleon structure. In the limit $x_F \rightarrow -1$ and moderate or small invariant masses M, we have $x_1 \simeq M^2/(s|x_F|)$, $x_2 \gtrsim |x_F|$. For example, for $x_F = -0.8$, $M = 10$ ($M = 15$) GeV we have $x_2 \simeq 0.8$ and $x_1 \simeq 0.01$ ($x_1 \simeq 0.02$). In this kinematic region the ratio of the DY cross section in pn collisions with the one in pp collisions is approximately given by

---

[31]We are grateful to V. Bertone from the NNPDF collaboration for providing us the points.

(LO, $\bar{u}(x_2), \bar{d}(x_2), s(x_2), \bar{s}(x_2) \ll u_v(x_2), d_v(x_2)$, neglecting Z-exchange):

$$R = \frac{\sigma^{\mathrm{DY}}(pn)}{\sigma^{\mathrm{DY}}(pp)} \simeq \frac{4\bar{u}(x_1)d(x_2) + \bar{d}(x_1)u(x_2)}{4\bar{u}(x_1)u(x_2) + \bar{d}(x_1)d(x_2)} \simeq \frac{4d(x_2) + u(x_2)}{4u(x_2) + d(x_2)} = \frac{1 + 4r_v}{4 + r_v} \tag{6}$$

where $\bar{d}(x_1) \simeq \bar{u}(x_1)$ has been used to arrive at the third equality and $r_v = d(x_2)/u(x_2) \simeq d_v(x_2)/u_v(x_2)$. Interestingly, exactly the same LO parton model expression is found for the ratio of structure functions $F_2^n(x, Q^2)/F_2^p(x, Q^2)$ in the limit $x \to 1$ which corresponds to elastic scattering. As a further consequence, the ratio R is bounded, $1/4 \leq R \leq 4$, similarly to the famous bounds for the ratio of deep inelastic structure functions, $1/4 \leq F_2^n/F_2^p \leq 4$, derived by Nachtmann [154]. The PDFs vanish for $x \to 1$ and generally, the high-x behavior of the PDFs at the initial scale Q_0 is parameterized as $xf_i(x, Q_0) \propto (1-x)^{b_i}$ where b_i depends on the parton flavor 'i'. Currently, only b_{u_v} is relatively well constrained with values in the range $2.6 \lesssim b_{u_v} \lesssim 3.6$ which is in agreement with the expectation from counting rules [155] ($b_{u_v} = b_{d_v} = 3$), whereas b_{d_v} is less well known and varies strongly between 1.4 and 4.6 for different sets of PDFs, see Figs. 2 and 5 in [156].[32] Note also that the CJ15 analysis [157] which has a particular focus on the high-x region points to a constant $d(x)/u(x) \sim 0.1$ for $x \to 1$ implying $R \to \sim 0.34$. However, for the time being it is reasonable to allow for the possibilities that r_v can vanish, approach a finite value k, or diverge in the limit $x \to 1$ (see Fig. 8 in [156]). Consequently, we find in the limit $x_2 \to 1$ that a measurement of R could constrain r_v and provide important tests of different models of nucleon structure [158, 159, 160, 161, 162, 163].

Experimentally, it is the ratio of cross sections in pd over pp collisions which is accessible. Neglecting any nuclear effects in deuterium the ratio can be written as

$$R_{d/p}(x_2) = \frac{\sigma^{\mathrm{DY}}(pd)}{\sigma^{\mathrm{DY}}(pp)} = 1 + \frac{\sigma^{\mathrm{DY}}(pn)}{\sigma^{\mathrm{DY}}(pp)} \simeq 5\frac{1 + r_v(x_2)}{4 + r_v(x_2)}. \tag{7}$$

Consequently, we find in the limit $x_2 \to 1$

$$R_{d/p} \to \begin{cases} 2 & ; \quad r_v = 1 \\ 2.5 & ; \quad r_v = 0 \\ 5 & ; \quad r_v \to \infty \end{cases}, \tag{8}$$

and a sufficiently precise measurement of the ratio will allow to determine $r_v(x) = d(x)/u(x)$ at high x. Of course, in practice, a full fledged QCD analysis at NLO or NNLO of the data will be performed.

Drell-Yan lepton pair production and PDFs. In order to estimate the possible impact of the DY lepton pair production in pp collisions at AFTER@LHC on the PDFs we have performed a profiling analysis [164] using the xFitter package [165]. For this purpose we have used pseudo-data constructed out of NLO QCD predictions for the rapidity distributions in the c.m.s. using MCFM program [166] and projected experimental uncertainties adding the statistical uncertainty from the DY yield and the uncertainty from the underlying minimum bias event in quadrature. No additional systematic uncertainty has been taken into account. The pseudo-data have been generated for several bins in the invariant mass of the muon pair ($M_{\mu\mu} \in [4, 5], [5, 6], [6, 7], [7, 8]$ GeV and $M_{\mu\mu} > 10.5$ GeV) and have been constructed such that the central values of the "measurements" and predictions coincide. This is illustrated in Fig. 13 for the invariant mass bin $4 < M_{\mu\mu} < 5$ GeV. In some cases the uncertainties are smaller than the data points and therefore not

---

[32]Needless to say that the exponents for the gluon and the quark sea are very poorly known.

visible.[33] As can be seen, the band showing the uncertainty of the theory prediction due to the NLO CT14 error PDFs is much larger than errors of the simulated data.
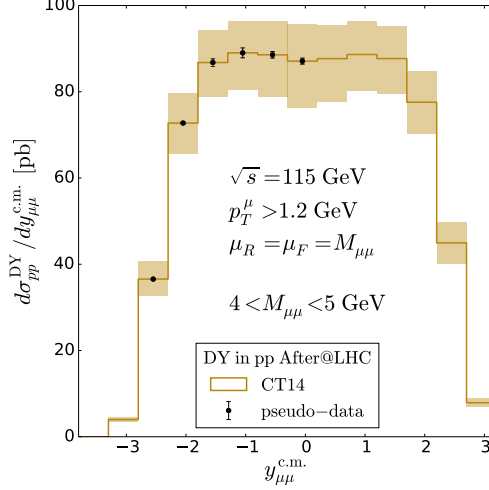
Figure 13: Drell-Yan lepton-pair-production cross-section in pp collisions as a function of the muon-pair c.m.s. rapidity in bins of the invariant mass, $M_{\mu\mu}$, with $p_T^\mu > 1.2$ GeV. The NLO theory predictions obtained using CT14 PDFs are overlaid by pseudo-data.

The effect of the profiling analysis, showing the decrease of the PDF uncertainties after including these data in a PDF global fit, is presented in Figs. 14 (logarithmic in x) and 15 (linear in x) for the light quark ($f = u, d, \bar{u}, \bar{d}$) distributions. To be precise, for each of these PDFs the upper and lower curves delimiting the bands are defined as

$$R_f(x, Q) = 1 \pm \frac{1}{2f_0(x, Q)} \sqrt{\sum_i [f_{i+}(x, Q) - f_{i-}(x, Q)]^2}, \qquad (9)$$

where $f_0(x, Q)$ is the central PDF and $f_{i\pm}(x, Q)$ are the 'i-th' error PDF in the plus or minus direction and a sum over all eigenvector directions is performed. Remarkably, Fig. 14 shows a sizable reduction of the PDF uncertainties not only in the high-x but also in the intermediate and small x region ($x \sim 0.1 \ldots 10^{-4}$). The effect is largest for the u and $\bar{u}$ distributions but it is also substantial for the d and $\bar{d}$ PDFs. The main focus of this section is the high-x region which is highlighted in Fig. 15. Here it can be seen that our knowledge of the valence quark distributions can be considerably improved for $x \gtrsim 0.4$ where the effect is again more pronounced for the up quark. However, even some information on the light quark sea at high x can be obtained.

W boson production close to the threshold. Due to the high center-of-mass energy of 115 GeV it is possible to study the production of W bosons close to the production threshold.[34] Assuming a yearly integrated luminosity of 10 fb^{-1} we expect roughly 250 W^+ and 60 W^- events per year before taking into account the experimental efficiencies.[35] These event numbers are based on NNLO cross sections calculated by integrat-

---

[33]Note that the covered rapidity range in the c.m.s. is from $-2.8 < y < 0.2$ such that there are no generated data at rapidities $y > 0.2$.

[34]Note that the cross section for Z boson production is too low to be accessible at AFTER@LHC.

[35]These numbers are for one leptonic decay channel. In a more realistic estimate it will be necessary to sum up the electron and muon channels taking into account the different efficiencies.
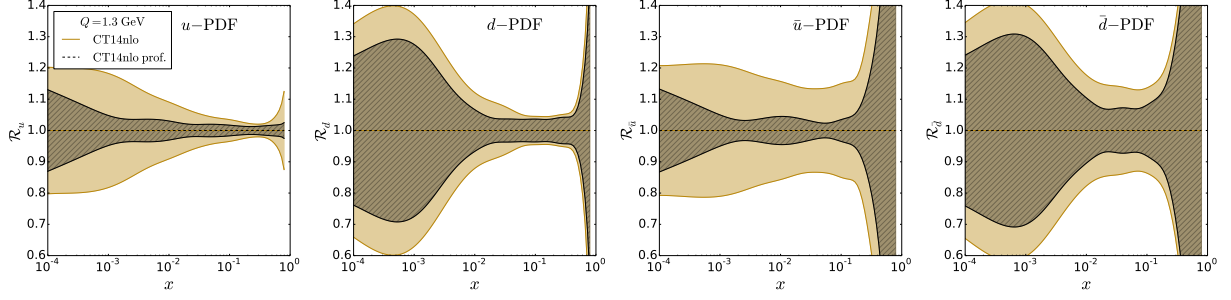
Figure 14: Impact of the Drell-Yan lepton pair production in pp collisions at $\sqrt{s} = 115$ GeV on the PDF uncertainties. The $u, d, \bar{u}$ and $\bar{d}$ PDFs from CT14 [167] are plotted as a function of x at a scale $Q = 1.3$ GeV before and after including AFTER@LHCb pseudo-data in the global analysis using the profiling method [164, 165].
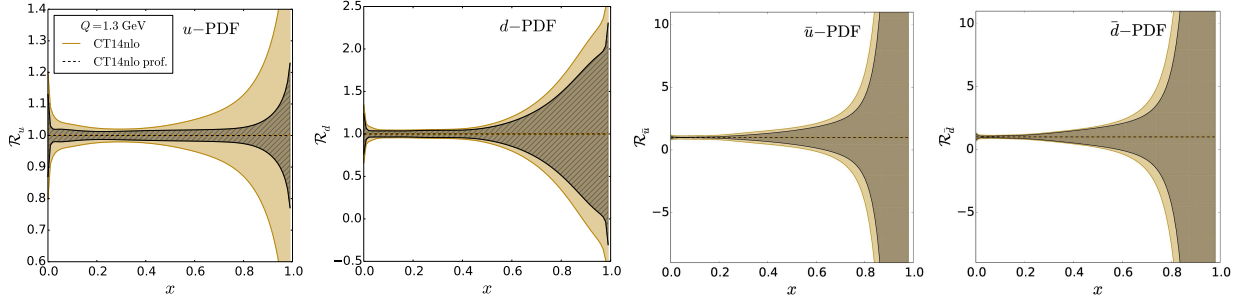
Figure 15: Same as in Fig. 14 on a linear scale highlighting the high-x region.

ing over the rapidity range $2 < \eta_\ell^{\text{lab}} < 5$ and imposing a cut $p_T^\ell > 10$ GeV on the transverse momentum on the W-decay lepton using FEWZ [168] together with NNLO CT14 PDFs [167]. The factorisation and renormalisation scales have been chosen to be $\mu_R = \mu_F = M_W$. For convenience, the cross sections at NLO and NNLO along with the event numbers and the PDF uncertainties are summarised in Tab. 13 for a selection of p_T^ℓ cuts.

In Fig. 16, we show NNLO predictions for the differential cross section for W^+ production in pp collisions at AFTER@LHC as a function of the transverse mass M_T for the case of a cut $p_T^\ell > 10$ GeV (left) and the transverse momentum p_T^ℓ of the produced lepton (right). The yellow band represents the PDF uncertainty and the error bars represent the uncertainty due to renormalization/factorization scale variation by a factor 2 around the central scale choice $\mu_R = \mu_F = M_W$. As can be seen, the PDF uncertainty dominates over the scale uncertainty for $M_T > 20$ GeV. It is also interesting to note that the M_T distributions peaks at $M_T \sim 25$ GeV far below M_W.

In the following, we illustrate that even a rough measurement of the W cross section at AFTER can provide interesting information on the high-x behavior of the light sea quarks. The LO cross section for W boson production reads

$$\frac{d\sigma}{dy} = \frac{2\pi}{3} \frac{G_F}{\sqrt{2}} \sum_{i,j} |V_{ij}|^2 \left[q_i^A(x_1) \bar{q}_j^B(x_2) + \bar{q}_j^A(x_1) q_i^B(x_2) \right], \tag{10}$$

where the momentum fractions $x_{1,2}$ are related to the (c.m.s.) rapidity of the W-boson in the usual way, $x_{1,2} = (M_W/\sqrt{s}) e^{\pm y}$. Assuming a diagonal CKM matrix and neglecting the contribution from the sc-channel

pp	W^+			W^-		
	NLO	NNLO	Counts/year	NLO	NNLO	Counts/year
$p_T^l > 10$ GeV	$22.5^{+4.8}_{-4.3}$	$25.9^{+4.8}_{-5.0}$	259 ± 49	$5.5^{+1.3}_{-1.3}$	$6.2^{+1.1}_{-1.4}$	62 ± 13
$p_T^l > 20$ GeV	$1.9^{+1.2}_{-0.7}$	$2.3^{+1.3}_{-1.1}$	23 ± 12	$0.38^{+0.29}_{-0.20}$	$0.50^{+0.25}_{-0.25}$	5 ± 2.5
$p_T^l > 30$ GeV	$0.28^{+0.91}_{-0.27}$	$0.27^{+0.72}_{-0.24}$	2.7 ± 4.8	$0.035^{+0.091}_{-0.039}$	$0.04^{+0.09}_{-0.04}$	0.4 ± 0.7

Table 13: Cross sections in [fb] at NLO and NNLO integrated over the rapidity range $2 < \eta_\mu^{\text{lab}} < 5$ and imposing a cut $p_T^\mu > 10$ GeV. The results have been obtained for pp collisions at $\sqrt{s} = 115$ GeV with FEWZ [168] using the NLO and NNLO CT14 PDFs [167], respectively. The renormalisation and factorisation scales have been set to $\mu_R = \mu_F = M_W$. The asymmetric uncertainties have been calculated using the error PDFs. The expected number of events has been obtained with a yearly luminosity of 10 fb^{-1}.
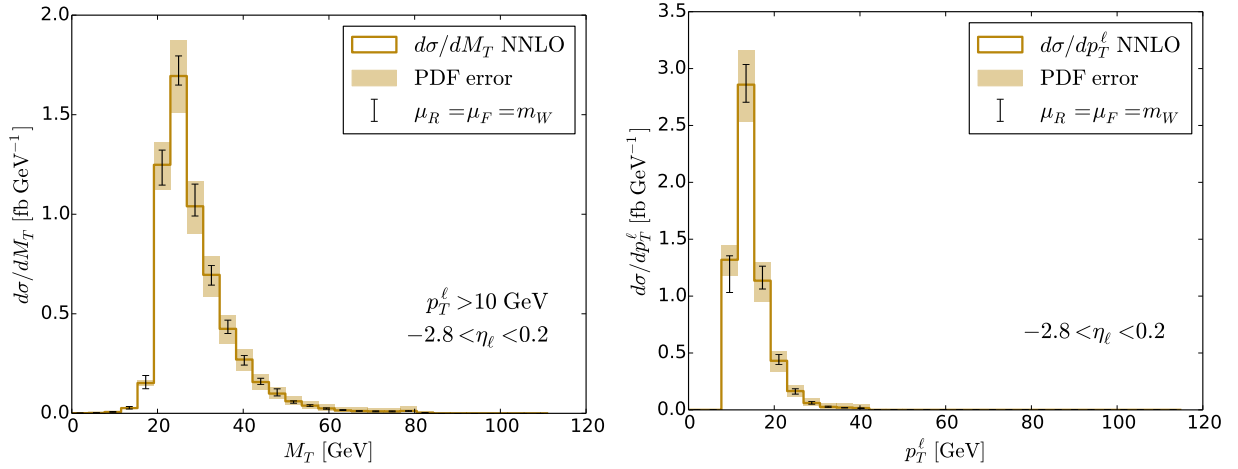
Figure 16: NNLO Cross section in [fb/GeV] for W^+ production in pp collisions at AFTER@LHC as a function of a) the transverse mass M_T and b) the transverse momentum p_T^ℓ of the produced lepton. The cross section has been obtained by integrating over the rapidity range $2 < \eta_\ell < 5$ (in the laboratory frame) using FEWZ [168]. For the M_T-distribution (left) a cut $p_T^\ell > 10$ GeV has been imposed. The yellow bands represents the PDF uncertainty and the error bars represent the uncertainty due to renormalization/factorization scale variation by a factor 2 around the central scale choice $\mu_R = \mu_F = M_W$.

one can easily derive the following ratio of cross sections:

$$R^W = \frac{\frac{d\sigma}{dy}(pn \to W^+ + W^-) - \frac{d\sigma}{dy}(pp \to W^+ + W^-)}{\frac{d\sigma}{dy}(pn \to W^+ + W^-) + \frac{d\sigma}{dy}(pp \to W^+ + W^-)} = 1 - 2\frac{\frac{d\sigma}{dy}(pp \to W^+ + W^-)}{\frac{d\sigma}{dy}(pd \to W^+ + W^-)}$$

$$= \frac{[u(x_1) - d(x_1)][\bar{u}(x_2) - \bar{d}(x_2)] + [\bar{u}(x_1) - \bar{d}(x_1)][u(x_2) - d(x_2)]}{[u(x_1) + d(x_1)][\bar{u}(x_2) + \bar{d}(x_2)] + [\bar{u}(x_1) + \bar{d}(x_1)][u(x_2) + d(x_2)]}. \tag{11}$$

At central rapidity, $x_1 = x_2 = x$, the ratio reduces to the remarkably simple expression[36]

$$R^W(y_{\text{c.m.s.}} = 0) = \frac{(1 - r_v)(1 - r_s)}{(1 + r_v)(1 + r_s)}, \tag{12}$$

---

[36]At central rapidity in the c.m.s., $y = 0$, one has $x_1 = x_2 = M_W/\sqrt{s}$. However, as shown in Fig. 16, most W bosons are produced off-shell. In that case one can effectively replace $x_1 = x_2 \sim M^*/\sqrt{s}$ with $M^* \sim 35$ GeV.

where $r_v(x) = d(x)/u(x)$ and $r_s(x) = \bar{d}(x)/\bar{u}(x)$ at $x \sim 0.3$. Therefore, even a rough measurement of this ratio with about 30% precision could provide valuable information on the barely known ratio $r_s = \bar{d}/\bar{u}$ at high x.

Another interesting aspect is that a measurement of vector boson production close to the threshold could serve as a proxy for searches of new heavy resonances at the LHC. As was highlighted above the W boson production at AFTER@LHC is predominantly off-shell. Therefore, one can expect a similar behaviour for a heavy new resonance with a mass close to the c.m.s. energy. The current mass limits for such heavy resonances are typically on the order of 3 to 4 TeV depending on the model. With increasing statistics even higher resonance masses will be probed, and we are approaching the region of the production threshold where the high x PDFs are probed and the PDF error becomes the dominant theoretical uncertainty in precision calculations [169, 170]. Furthermore, soft gluon resummation effects are expected to become important [169] which could be tested at AFTER@LHC.

The charm quark PDF at high x. The high-x heavy-quark PDFs can be important for BSM physics in which new heavy particles have couplings to the SM fermions which are proportional to the fermion mass or for models which predominantly couple to the second and/or third generation [171]. Most global analyses of PDFs rely on the assumption that the charm and bottom PDFs are generated perturbatively by gluon splitting, $g \to Q\bar{Q}$, and do not involve any non-perturbative degrees of freedom. It is clearly necessary to test this hypothesis with suitable QCD processes. Conversely, a non-perturbative, intrinsic contribution to the heavy quark PDF in the proton comes from QCD diagrams in which the heavy quark pair is attached by two or more gluons to the valence quarks. It thus depends on the nonperturbative intrinsic structure of the proton [172, 173]. For a recent review, see [174].

There are extensive indications for charm production at high x which are, however, not yet fully conclusive and new data from the LHC, a future Electron-Ion collider and a fixed target experiment like AFTER@LHC will be necessary. One example is the EMC measurement of $c(x, Q^2)$ in deep inelastic muon scattering [175]. The rate observed by the EMC was found to be approximately 30 times higher at $x = 0.42$, $Q^2 = 75$ GeV^2 than predicted by gluon splitting [176]. In a more recent analysis, the EMC data have been described in the context of a fitted charm quark distribution which increase the stability of the fit with respect to variations of the charm quark mass [177]. In this study NNPDF collaboration found a fitted high-x component peaking at $x \sim 0.5$ and carrying about 1% of the total proton momentum. At the same time they observe that the EMC data cannot be fitted with a perturbatively generated charm PDF and the additional parameters, effectively parameterizing the high-x intrinsic component, are need to describe these data. Therefore, there is already some evidence for a high-x intrinsic charm (IC) component carrying about 1% of the total momentum of the proton. Intrinsic charm also predicts the observed features of the ISR data for $\frac{d\sigma}{dx_F}(pp \to \Lambda_c X)$ [178] and more recently by SELEX [179]. In this process, the comoving c, u and d coalesce to produce the Λ_c at high x_F where $x_F = x_c + x_u + x_d$. Other observations at high x_F include Λ_b, Λ_c, single and double quarkonium, double-charm baryons ccu, ccd, we refer to [174] for a more complete overview. We also note here recent works [180, 181, 182] providing predictions for doubly heavy baryons, B_c mesons and all-charmed tetra quarks at AFTER@LHC based on the intrinsic heavy quark mechanism, showing that this mechanism should dominate at high-x_F allowing for its observation at AFTER@LHC and potentially confirming the existence of the IC. Ξ_{cc} production at AFTER@LHC was also studied from DGLAP-generated charm in [183]. Besides, the production of the hidden charm pentaquark P_c^+ was found to peak, for the AFTER@LHC kinematics, at about $y_{\text{Lab}} \simeq 1.4$ [184] using the same formalism as that of a previous study for the LHC kinematics [185].

A non-perturbative intrinsic charm component modifies the predictions for a number of processes at the LHC such as inclusive D meson production [186, 187] or the associated production of a heavy quark with

a photon [188] or $Z + c$ production [177]. However, in these examples, one has to go to relatively large transverse momenta or to very forward rapidities to expect a sizeable effect.

Simply owing to the large boost between the laboratory frame and the c.m.s., the fixed-target mode is the ideal set-up to uncover an excess of charm at high-x. To illustrate this statement we show in Fig. 17, the relative yield uncertainty for inclusive D^0 meson production at AFTER for three rapidity bins ($2 < y_{Lab} < 3$, $3 < y_{Lab} < 4$, $4 < y_{Lab} < 5$) as a function of the transverse momentum (p_T) of the D^0 meson. An integrated luminosity of 10 fb^{-1} has been assumed to compute the expected yields –accounting for the expected efficiency and the branching ratio– from the theoretical cross sections which have been obtained using the setup described in [174]. From these yields, we derived the expected uncertainties shown in the figures. The red and green bands correspond to an intrinsic charm with average momentum fraction $\langle x_{c\bar{c}} \rangle = 0.57\%$ and 2%, respectively. As can be seen, even for $p_T \lesssim 15$ GeV the expected precision of the measurement will clearly allow to considerably constrain the intrinsic-charm model, by up to an order magnitude.

(a) $2 < y_{Lab} < 3$ (b) $3 < y_{Lab} < 4$ (c) $4 < y_{Lab} < 5$
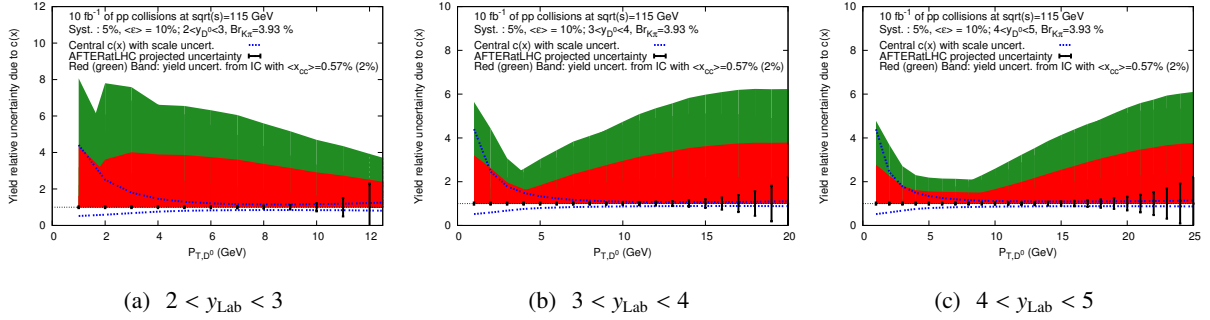
Figure 17: Impact of the uncertainties on the charm content of the proton on the D^0 yield as function of p_T compared to projected uncertainties from the measurement of the D^0 yield in pp collisions at $\sqrt{s} = 115$ GeV in the LHCb acceptance. Systematic uncertainties of 5% are included and the statistical uncertainty for the background subtraction is assumed to be negligible which is reasonable assuming LHCb-like performances, see [100].

The gluon PDF at high x. The available data from deep inelastic scattering (DIS) structure functions and from DY lepton pair production provide only rather weak constraints on the gluon PDF, particularly at high x. Important information on the gluon density can be drawn from inclusive jet data and from top quark pair production data. In the latter case the differential distributions ($y_{t\bar{t}}$, y_t, p_T^t, $m_{t\bar{t}}$) have been shown to considerably reduce the uncertainty of the gluon PDF at high x [189]. Nevertheless, these data provide constraints at quite large factorisation scales $Q \sim 100$ GeV and the knowledge of the gluon PDF at $x \gtrsim 0.5$ remains limited.

In this paragraph we discuss a number of possibilities to obtain information on the gluon PDF within the AFTER@LHC program. As can be seen in Fig. 2, open heavy flavoured mesons and heavy quarkonia will be abundantly produced at AFTER@LHC covering an important region in the (x, m_T) plane. As should be clear from the discussion above on the charm quark PDF, the gluon and the heavy quark distributions are inextricably linked. Therefore, in the context of a global analysis, the heavy quark data have the potential to constrain both the heavy quark and the gluon distribution at high x. It should also be noted that in the case of b quark production the contribution from an intrinsic bottom component is expected to be very small [171]. One should mention that normalized rapidity distributions of D and B mesons from LHCb have been already used with success to study low-x gluon [190, 191].

In addition to the inclusive heavy quark observables, the associated production of a heavy quarkonium with a photon is sensitive to the high x gluon distribution. This is illustrated in Table 14 which shows that this process is largely dominated by the gluon-gluon initiated subprocess probing x_2 values in the range from 0.1 to 0.6.

Isolated $J/\psi + \gamma$	$\langle x_2 \rangle \sim \frac{M_{\psi\gamma}}{\sqrt{s}} e^{-Y_{\psi\gamma}}$	$\sigma_{gg} \times \mathcal{B}_{\mu\mu}$ [fb]	$\sigma_{q\bar{q}} \times \mathcal{B}_{\mu\mu}$ [fb]	counts/year
$\|Y_{\psi\gamma}\| < 0.5$	0.1	$\mathcal{O}(100)$	$\mathcal{O}(0.2)$	$\mathcal{O}(1000)$
$-1.5 < \|Y_{\psi\gamma}\| < -0.5$	0.25	$\mathcal{O}(50)$	$\mathcal{O}(0.2)$	$\mathcal{O}(500)$
$-2.5 < \|Y_{\psi\gamma}\| < -1.5$	0.6	$\mathcal{O}(10)$	$\mathcal{O}(0.04)$	$\mathcal{O}(100)$

Table 14: Isolated $J/\psi + \gamma$ production for three bins in the c.m.s. rapidity of the pair. From left to right: the x_2 ranges, the partial contributions to the cross section from the gg-initiated and $q\bar{q}$-initiated subprocesses (multiplied by the J/ψ branching into di-muons) [60] and the order of magnitude of the expected number of events per year assuming a luminosity of 10 fb^{-1} and a detector efficiency on the order of unity.

Along these lines one can also study double-J/ψ production which is dominated by the gg-channel up to large values of the target x_2 as is shown in Table 15. It is also interesting to notice that AFTER@LHC provides the unique opportunity to study double-parton scatterings and double-parton correlations in the nucleon at energies around 100 GeV via di-J/ψ production [192], where the similar studies already exist at the Tevatron and the LHC [193, 194].

$J/\psi + J/\psi$	$\langle x_2 \rangle \sim \frac{M_{\psi\psi}}{\sqrt{s}} e^{-Y_{\psi\psi}}$	σ_{gg} [pb]	$\sigma_{q\bar{q}}$ [pb]	counts/year
$4.5 < Y_{\psi\psi} < 5.0$	0.13	$\mathcal{O}(1)$	$\mathcal{O}(0.3)$	$\mathcal{O}(50)$
$4.0 < Y_{\psi\psi} < 4.5$	0.29	$\mathcal{O}(10)$	$\mathcal{O}(3)$	$\mathcal{O}(400)$
$3.5 < Y_{\psi\psi} < 4.0$	0.45	$\mathcal{O}(10)$	$\mathcal{O}(3)$	$\mathcal{O}(400)$
$3.0 < Y_{\psi\psi} < 3.5$	0.60	$\mathcal{O}(3)$	$\mathcal{O}(3)$	$\mathcal{O}(200)$
$2.5 < Y_{\psi\psi} < 3.0$	0.77	$\mathcal{O}(1)$	$\mathcal{O}(0.5)$	$\mathcal{O}(50)$

Table 15: $J/\psi + J/\psi$ production for five bins in the laboratory rapidity of the pair. From left to right: the x_2 ranges, the partial contributions to the cross section from the gg-initiated and $q\bar{q}$-initiated subprocesses (without the J/ψ branching into di-muons) and the order of magnitude of the expected number of events per year assuming a luminosity of 10 fb^{-1} and a detector efficiency on the order of unity.

Another interesting observable which probes the gluon distribution directly at LO via the $qg \to \gamma q$ subprocess is inclusive prompt photon production. It was shown that the theoretical pQCD predictions at NLO describe well the collider data for c.m.s. energies ranging from 200 GeV to 7 TeV [195]. However, a series of measurements carried out at c.m.s. energies $\sqrt{s} \sim 20 \ldots 40$ GeV by the fixed target E706 experiment [196, 197, 198] were not well described by NLO pQCD calculations [199, 200, 201]. This discrepancy was only partially cured by the inclusion of resummed soft-gluon contributions in the theoretical predictions [202, 203, 204, 205, 206]. Therefore, a new measurement at a fixed target experiment with c.m.s. energy $\sqrt{s} = 115$ GeV would be interesting in itself to shed additional light on the data-theory discrepancy at fixed-target energies. Furthermore, such a measurement has the potential to improve our knowledge of the gluon distribution at $x > 0.3$ provided isolated photons can be measured with transverse momentum $p_T \gtrsim 10 \ldots 20$ GeV [195].

5.1.2. Nuclear structure

As a fixed-target experiment, AFTER@LHC allows one to study *pA* collisions with different nuclei *A* and some fundamental open questions can be addressed in this case. More than 30 years ago, the EMC collaboration discovered that nuclear structure functions in DIS are suppressed compared to the prediction from the naive combination of free proton and neutron structure functions in the high-*x* region [2]. The physics mechanism behind this EMC effect is still not fully understood and subject of an active experimental program at Jefferson LAB [207, 208]. A modern precision measurement of the DY lepton pair production at AFTER@LHC would allow to study the EMC effect in this process (at high negative x_F and with much higher precision) and to compare it to the DIS case. In addition, as in the nucleon case, nuclear PDFs (nPDFs) are determined in global analyses of DIS and DY data [4, 5, 6, 209, 210, 7] and are a crucial ingredient for predicting hard processes in *pA* and *AA* collisions at the LHC. Compared to the proton PDFs, the nPDF determinations are clearly lagging behind both at the level of sophistication but most importantly due to the much smaller number of experimental constraints. Currently, the analyses are statistically dominated by DIS data with only about 90 data points from the DY process entering the fits. Incorporating data from various processes is essential for flavour separation in PDF analyses. Therefore, access to the DY data with a wide kinematic coverage will provide a unique opportunity not only for more precise PDF determinations but will also allow to test their universality which is a fundamental property of QCD and basis for all high energy hadron scattering computations.

The kinematic reach of AFTER@LHC (Fig. 18) would allow to probe much higher x_2 (target *x*) values than the currently available data (data points in Fig. 18) for a variety of targets. In particular, AFTER@LHC could shed new light on the origin of the EMC effect by verifying its presence/absence in DY lepton pair production. As Fig. 18 shows, a modern precision measurement of DY lepton pair production at AFTER@LHC covering a wide range in invariant masses of the lepton pairs and extending to higher x_F would lead to spectacular improvements over the current state of the art and would be complementary to results from a future Electron-Ion-Collider (EIC). Clearly, it would be invaluable input for nuclear PDF determinations.

As an example we present here a reweighting analysis [213, 214, 215, 216] showing the potential impact of the DY lepton pair production data from AFTER@LHC in *p*Xe and *p*W collisions on the nCTEQ15 nPDFs. In this analysis we use pseudo-data for the nuclear ratios $R_{p\text{W}} = \sigma_{\text{DY}}^{\text{W}}/\sigma_{\text{DY}}^{pp}$ and $R_{p\text{Xe}} = \sigma_{\text{DY}}^{\text{Xe}}/\sigma_{\text{DY}}^{pp}$ to estimate the effect these data can have on the current nPDFs. In Fig. 19 we display the nPDFs before and after the reweighting using the AFTER@LHC $R_{p\text{W}}$ and $R_{p\text{Xe}}$ pseudo-data. We can see a significant decrease of the errors for up and down quark distributions showing the potential of the AFTER@LHC for constraining nPDFs. In practice, due to the limited amount of data, the current nPDF errors are considerably underestimated and the actual importance of these data can not be fully demonstrated in this kind of study. However, just looking at the kinematical coverage of the AFTER@LHC and current DY data in Fig. 18 makes it obvious that the contribution of AFTER@LHC to nPDF determination would be unprecedented.

Similarly to the proton case, the $W^{\pm}$ data could be used for a determination of the high-*x* nPDF in particular the light quark sea distributions.

AFTER@LHC is also able to constrain the high-*x* nuclear gluon distribution, which is the least known nPDF. A prime example we show here is to use heavy flavour production at AFTER@LHC, where the gluon shadowing effect on J/ψ and Υ production in p+Pb collisions in AFTER@LHC energies has been studied in Ref. [217]. We will explore the potential of both open and hidden heavy flavour mesons (D^0, J/ψ, B^+, $\Upsilon(1S)$) production in p+Xe collision at $\sqrt{s_{NN}} = 115$ GeV to pin down the high-*x* gluon density in nPDF by performing a Bayesian-reweighting analysis. A similar study in the LHC energies has been carried out in Ref [218]. We used the data-driven approach proposed in Ref. [219] to fit matrix elements of the heavy flavour hadrons, and then convolved them with proton CT14 PDFs and nCTEQ15 [5] nPDFs to get the
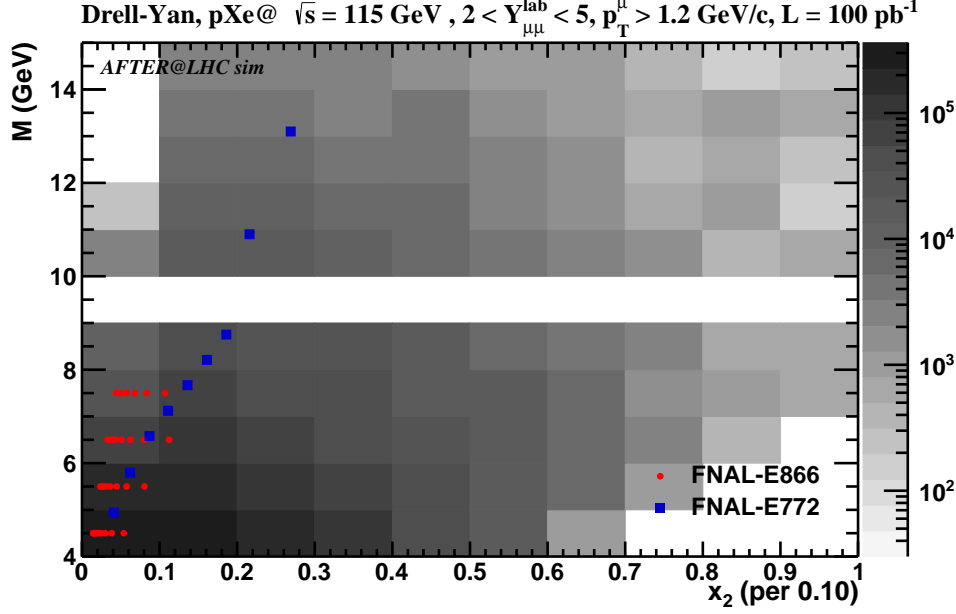
Figure 18: The kinematical reach for DY pair-production at AFTER@LHCb for pXe collisions with an acceptance of $2 < \eta_\mu < 5$ and $p_{T,\mu} > 1.2$ GeV compared to existing DY data [211, 212] used in global PDF fits. (Each coloured cell contains at least 30 events).
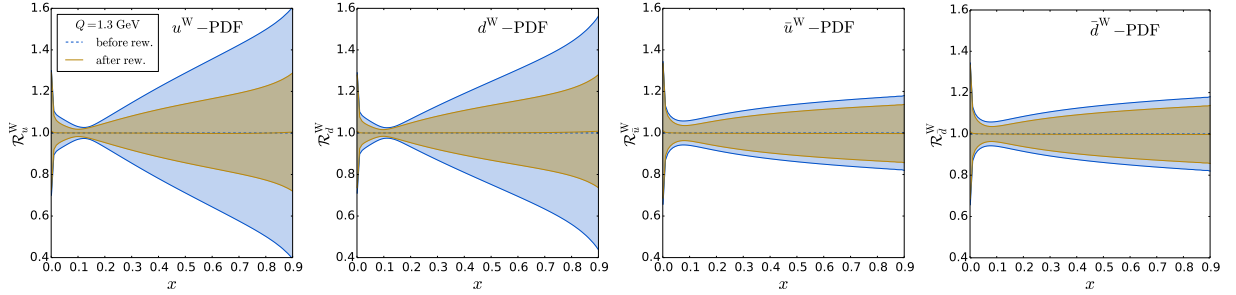
Figure 19:   nCTEQ15 nPDFs before and after the reweighting using R_{pW}^{DY} and R_{pXe}^{DY} AFTER@LHCb pseudo-data in the range indicated on Fig. 18. The plots show ratio of nPDFs for tungsten (W) and the corresponding uncertainties compared to the central value at the scale $Q = 1.3$ GeV.

yields and the nuclear modification factors.[37] The pesudo-data are generated to match the central theoretical predictions. Their projected statistical uncertainties are estimated by assuming the yearly integrated luminosities $\mathcal{L}_{pp} = 10$ fb^{-1}, $\mathcal{L}_{pXe} = 100$ pb^{-1} and the reconstruction efficiency $\varepsilon = 0.1$. The branching ratios of $D^0 \rightarrow K\pi$, $B^+ \rightarrow K(J/\psi \rightarrow \mu^+\mu^-)$, $J/\psi \rightarrow \mu^+\mu^-$ and $\Upsilon(1S) \rightarrow \mu^+\mu^-$ have also been taken into account. For D^0 and B^+, their charge-conjugated particles are also summed up. After considering a 2% systematic error and a 5% global error, the nuclear modification factors R_{pXe} for the four hadron productions are shown in Fig. 20 before (red bands) and after (blue bands) reweighting, together with the variations of factorisation scales. The uncertainty from the factorisation scale can be the dominant theoretical error after nPDF reweighting as already pointed out in Ref. [218]. The impact of these pesudo-data can be transfered

---

[37]The calculations are carried out in the framework of HELAC-Onia [220, 221].

into nPDFs as illustrated in Fig. 21 and 22. We can see that even accounting for the scale uncertainty, a substaintial reduction of nPDF uncertainty at high x values ($x \gtrsim 0.3$) is still achieved. It clearly demonstrates the uniqueness of AFTER@LHC program in exploring gluon density in nuclei especially at high x.
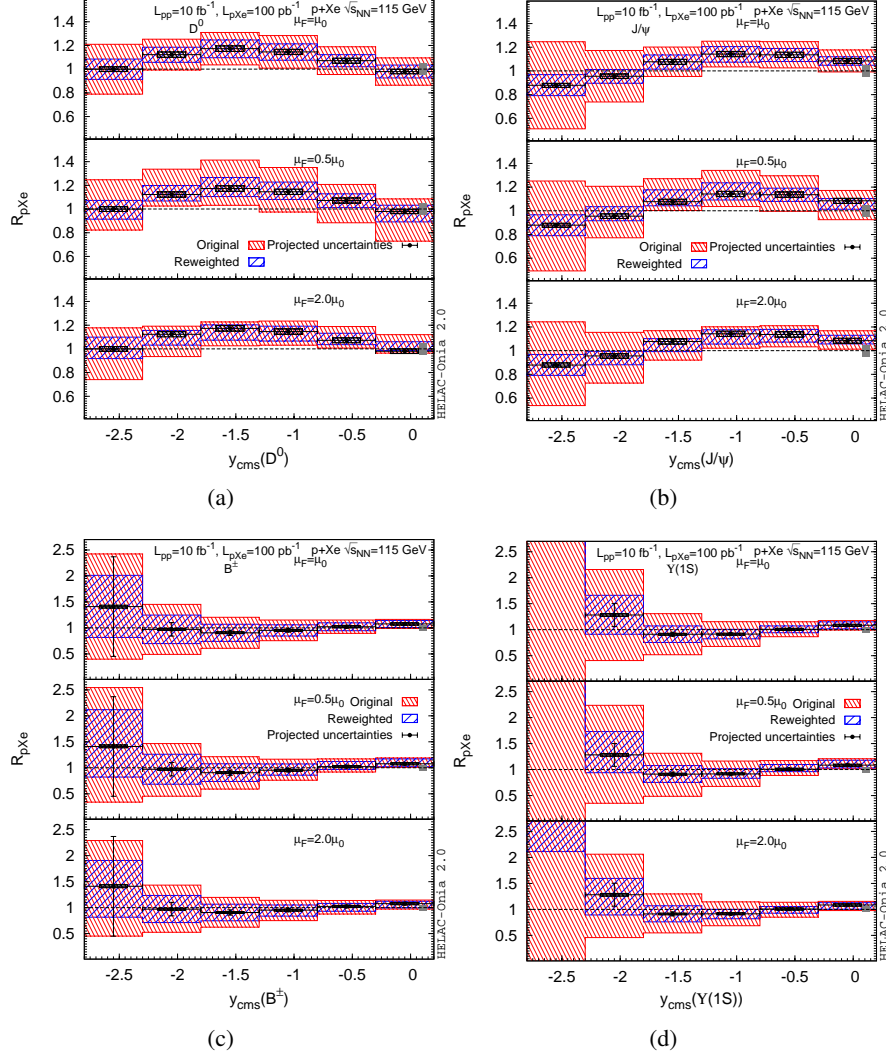
Figure 20: Projection of the statistical uncertainties for (a) D^0, (b) J/ψ, (c) B^+, and (d) $\Upsilon(1S)$ production in pXe collisions compared to the uncertainties encoded in nCTEQ15 nPDFs, which are representative of typical nPDF uncertainties, evaluated at different typical choices of the factorisation scale. A 2% uncorrelated systematic uncertainty and a 5% global uncertainty are also shown. The projected statistical uncertainties are estimated assuming the yearly integrated luminosities of $\mathcal{L}_{pp} = 10$ fb^{-1} and $\mathcal{L}_{p\mathrm{Xe}} = 100$ pb^{-1}.

It is important to note here that the above projections for the constraints on the nuclear gluon were obtained assuming only the modification of nPDFs and absence of other cold nuclear matter effects.[38] One example of an effect that can play a role when gluons are involved, especially in case of AA collisions, is

---

[38]This is a fair assumption for the used heavy quark pseudo-data which are for pA collisions only. Furthemore it was shown [218] that this kind of leading twist factorization approach can be applied with success to a large class of existing data.
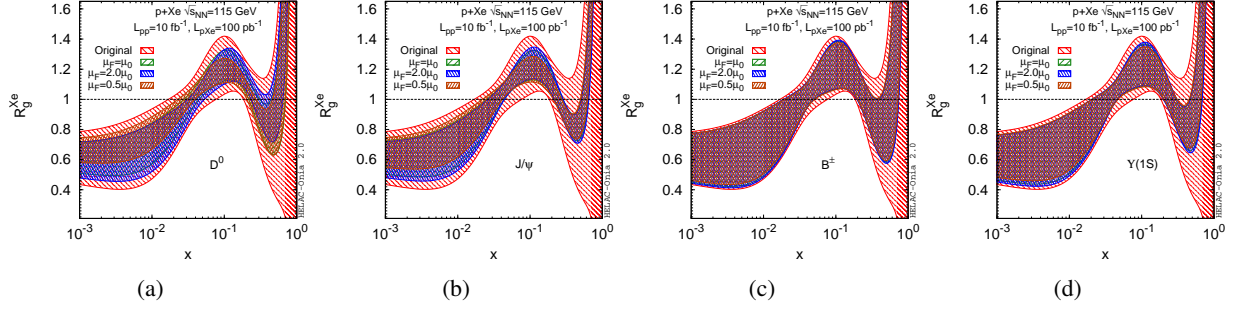
Figure 21: nCTEQ15 nPDFs before and after the reweighting using R_{pXe} pseudo-data shown in Fig. 20 for (a) D^0, (b) J/ψ, (c) B^+, (d) $\Upsilon(1S)$ production at AFTER@LHCb. The plots show ratios R_g^{Xe} of gluon densities encoded in nCTEQ15 over that in CT14 PDFs at scale $Q = 2$ GeV.
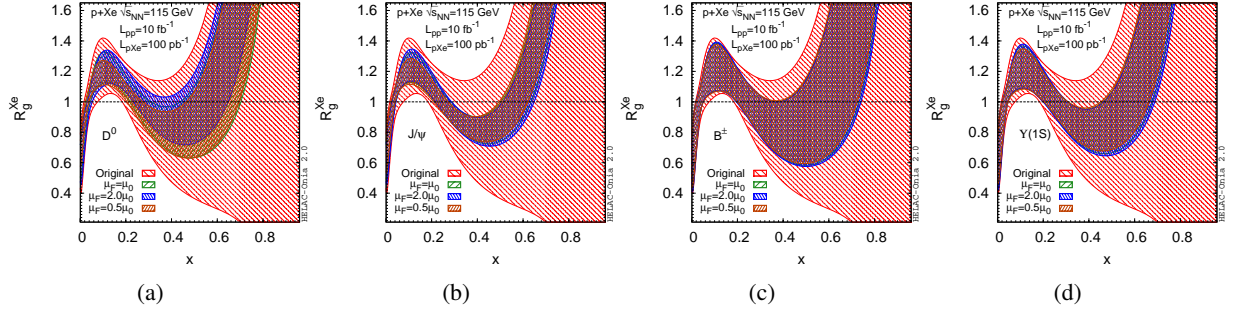
Figure 22: Same as Fig. 21 using a linear x axis in order to highlight the high-x region.

coherent energy loss. It was studied recently in the context of AFTER@LHC [222] and predicts a suppression of pA and AA cross-sections compared to the pp one which is depicted in Fig. 23 for J/ψ and Υ in terms of R_{pA} and R_{AA} factors. AFTER@LHC will allow to further test the applicability of these kind of approaches and maybe even discriminate between them.

5.1.3. Astroparticle physics

Recently, measurements of cosmic rays (CRs) with very high energies, ranging from about tens of MeV up to hundreds of TeV, became possible for many particle species ($e^{\pm}$ [223, 224], γ [225, 226], ν [227, 228], p [229], $\bar{p}$ [230], A [231, 232, 233], $\bar{A}$) and attracted much attention. The mechanism responsible for the generation of such Ultra High-Energy CRs (UHECRs) is still under intense discussion, with two main scenarios: (i) the acceleration of particles due to astrophysical phenomena and (ii) dark matter decay/annihilation. The mechanism generating CRs can only be determined if we can identify characteristic shapes of the spectrum such as sharp cutoffs which will indicate the decay of massive dark matter particles. In this precision test of CRs, the spectrum has to be accurately determined, thus naturally requiring precise investigations of other sources acting as background. Here we present two cases where the AFTER@LHC program can play a critical role.

UHECR neutrinos and the proton charm content. The terrestrial observation of UHE neutrinos lately became possible thanks to IceCube, with the highest energy recorded on the order of PeV [227, 228]. *Atmospheric* neutrinos, generated by the weak decays of final state particles of the collisions between CRs and atmospheric nuclei, are however an important background to these ground observations of cosmic neutrinos.
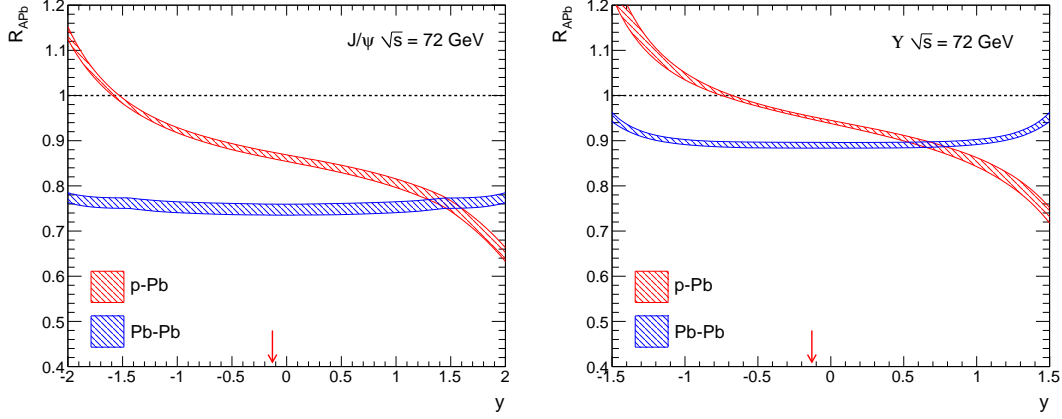
Figure 23: J/ψ (left) and Υ (right) suppression in p–Pb and Pb–Pb collisions at $\sqrt{s}$ = 72 GeV obtained from a coherent energy loss model. Figure taken from [222].

The major source of these atmospheric neutrinos is from the weak decay hadrons. Those originating from the decay of long-lived mesons , like π and K mesons, dominate the energy spectrum below 10^5 GeV. Those with energy above 10^5 GeV are from charm-hadron decays. Indeed charmed hadrons loose significantly less energies in the atmosphere than π and K because they decay almost instantaneously.

The yield of neutrinos from charm naturally follows that of charmed hadrons produced in the collisions of UHECRs and atmospheric nuclei. An accurate evaluation of the charm hadroproduction cross section is therefore crucial to assess their importance. The charm production of pp scattering was first evaluated in perturbative approaches, which considered charm quark-antiquark pairs virtually created by the gluon splitting $g \rightarrow c\bar{c}$. This contribution is mostly relevant at low-x in the target PDF [234, 235] which can also be shadowed.

The relevance of a nonperturbative charm content (or IC) in the projectile proton was also recently considered [236]. Just as most global analyses of PDFs rely on the assumption that the charm and bottom PDFs are generated perturbatively by gluon splitting, $g \rightarrow Q\bar{Q}$, most of the studies of neutrino fluxes were based on the same assumption. The intrinsic charm however has a harder distribution [172, 173] (for a recent review, see [174]) and tends to predict charmed hadrons at higher energies, which would result into higher energy neutrinos.

As we discussed in section 5.1.1, the AFTER@LHC program offers an unprecedented playground to study the excess of charm at high-x. Not only a detector such as that of LHCb used in the fixed target mode can access the high negative x_F, it also have a wide coverage close to 40% [237] of the weighted charm cross section, $x_F^2 d\sigma/dx_F$ which is quasi proportional to the neutrino flux. As a comparison, in the collider mode, it covers less than 10 % of the same weighted cross section [238]. In other words, charmed hadron measurement at AFTER@LHC can provide the most decisive constrain on the non-pertubative charm content in the proton in the region relevant to understand the neutrino-from-charm flux. Fig. 24 shows the uncertainties on the neutrino flux due to that on the IC in the projectile proton [239] (see also [236]).

Antiproton cross section and UHECR Monte-Carlo tuning. Among the cosmic rays, the antiprotons ($\bar{p}$) are the object of a specific attention. In the current understanding, $\bar{p}$ are almost of secondary origin, *i.e.* created through the high energy scattering between the interstellar matter and primary cosmic rays, which were mainly generated by acceleration in supernova remnants [240, 241, 242]. The cosmic antiprotons
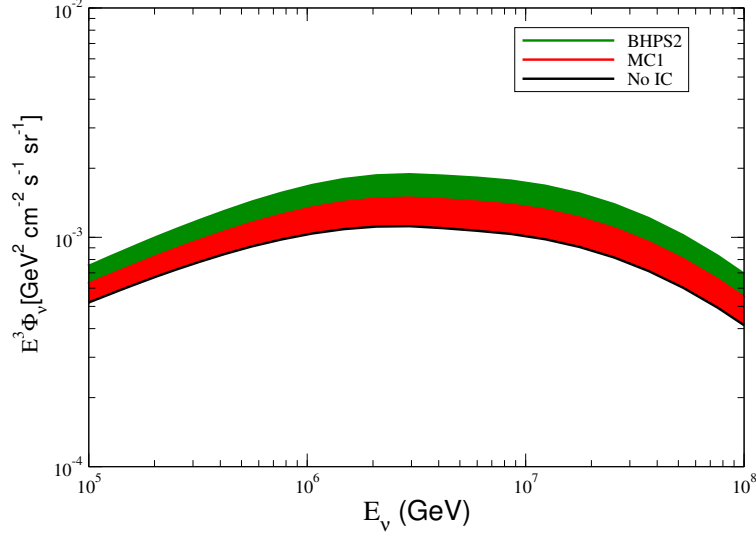
Figure 24: Impact of the uncertainties on the charm content of the proton on the neutrino flux [Courtesy of V. Gonçalves, based on [239]]. The color code and the uncertainty on the D yield correspond to Fig. 17.

were measured by the AMS-02 experiment in the range of 1 GeV to 400 GeV with a typical accuracy of 5% [230]. On the theory side, the spectrum of secondary $\bar{p}$ can be predicted using diffusion equation with the $\bar{p}$ production cross section as input [243, 244, 245]. The determination of the discrepancy between the above two can open a new window on the indirect detection of dark matter or unknown astrophysical mechanisms of CR acceleration.

The accurate evaluation of the cosmic $\bar{p}$ spectrum requires a precise knowledge of their production cross section for several nuclear channels. The nuclear primary CRs are composed of p, ^{4}He, ^{12}C, ^{14}N, ^{16}O. Other nuclei need not to be considered due to their small contribution to $\bar{p}$ production. On the other hand, the interstellar matter, which acts as a fixed target in the cosmic $\bar{p}$ production, is composed of protons and ^{4}He. Other nuclei acting as targets are negligible. The estimation of the contribution of $\bar{p}$ production cross sections for each nuclear channel to the $\bar{p}$ spectrum is roughly 50% for $p + p \rightarrow \bar{p} + X$, 30-40% for $p+^4$He$\rightarrow \bar{p} + X$ (p, ^{4}He can be either target or projectile), 5% for ^{4}He $+^4$He$\rightarrow \bar{p} + X$, and 5% for $p + A \rightarrow \bar{p} + X$ with $A = {}^{12}$C, ^{14}N, ^{16}O [246]. The other channels contribute in all less than 5%.

Here we note that, in unveiling new astrophysical phenomena, the most energetic region of the cosmic antiproton spectrum is the most interesting, since the determination of the high energy CR source (whether it is due to dark matter decays/annihilations or astrophysical accelerations) relies on the shape of the CR spectrum in the high energy region. It is thus required to quantify the high energy part of the production cross section of secondary antiprotons. At the partonic level, the generation of highly energetic $\bar{p}$ is dominantly due to the collision of two gluons with highly asymmetric momentum fractions, and the $\bar{p}$ production cross section off two nuclei is sensitive to the behaviour of the nuclear PDF at high momentum fraction. In typical nuclei, the PDF at high x is enhanced by the Fermi motion, so the precise measurement of $\bar{p}$ production off nuclei are important in the quantitative prediction of the cosmic $\bar{p}$ spectrum.

Currently, the production cross sections of $pp \rightarrow \bar{p} + X$ and $p+^4$He$\rightarrow \bar{p} + X$ (^{4}He as target) were measured in the energy range of AMS-02 [247, 248, 249, 99]. In particular, the LHCb experiment measured the production of $\bar{p}$ from the scattering of p beam off ^{4}He target in the range of $\bar{p}$ momentum 12 GeV - 110 GeV [99, 246], and contributed to the improvement of the prediction of the secondary cosmic $\bar{p}$ spectrum. On the other hand, AFTER@ALICE$_{CB}$ (*i.e.* the ALICE Central Barrel (CB) used in the fixed target mode)

can measure very slow antiprotons, with almost zero momentum. The production of such slow $\bar{p}$ (which are apparently outside the range measurable by AMS-02) with the LHC proton beam correspond to the highest possible energies in the inverse kinematics, where the nuclear target (C, N, O, He) travels at TeV energies, hit an interstellar p at rest and produces a $\bar{p}$ in the limit of $x_F \to 1$.

Having this observation in mind and considering any arbitrary stable nucleus as target, let us discuss more precisely the cases which can be studied with AFTER@ALICE$_{CB}$ and AFTER@LHCb assuming the additional possibility of ^{16}O beam. Using a gas target, the $p+^4$He $\to \bar{p} + X$ process (with p as a projectile) with slow emerging $\bar{p}$ falls within the acceptance of ALICE. Fig. 25 shows the $\bar{p}$ kinematical reach for the ALICE CB for pp collisions for which the ALICE CB performances are similar as for pHe collisions. As expected, $\bar{p}$ with momenta as low as a few hundred MeV (which correspond to a rapidity difference between the He target and the $\bar{p}$, $\Delta y_{\text{He}\bar{p}}$, as low as 0.4) can easily be detected. Such $\bar{p}$ with small $\Delta y_{\text{He}\bar{p}}$ for ^{4}He $+p \to \bar{p} + X$ correspond to the high energy tail of the ^{4}He $+p \to \bar{p} + X$ process (^{4}He as projectile), which is one of the leading process in the cosmic $\bar{p}$ spectrum. Similarly, using C, N or O targets, one can study the high-energy $\bar{p}$ tail for (C,N,O)$+p \to \bar{p} + X$. To the best of our knowledge no other experimental set-up can cover this high energy limit.

(a) $y_{\text{Lab.}}$ coverage
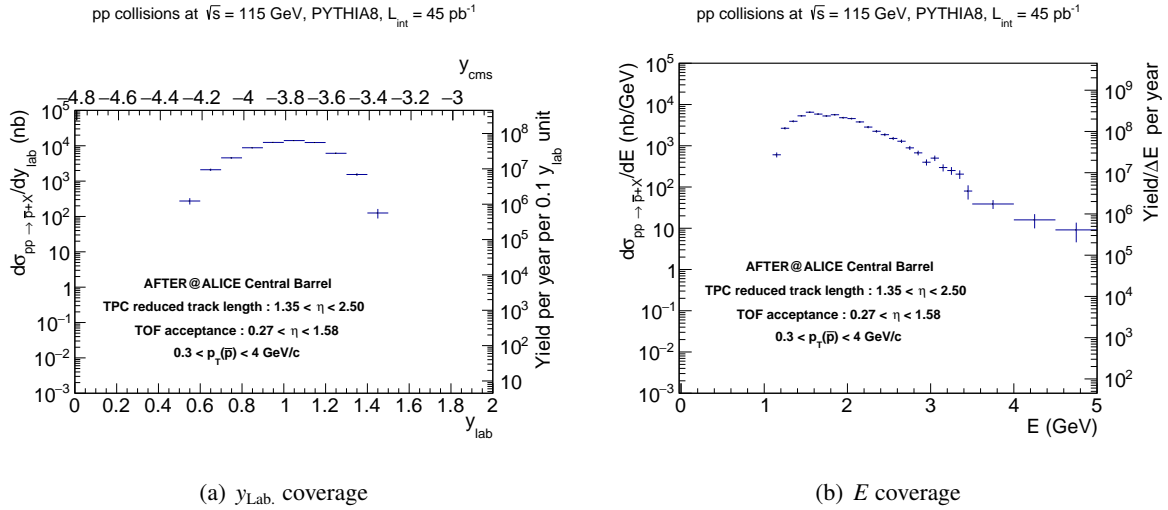
(b) E coverage

Figure 25: The expected kinematical coverage for $\bar{p}$ production for AFTER@ALICE$_{CB}$ with a displaced vertex at $Z = -4700$mm from the original ALICE IP.

With an oxygen beam, the study of the ^{16}O $+p \to \bar{p}+X$ as well as the ^{16}O $+ ^4$He $\to \bar{p}+X$ processes would become possible, in the laboratory frame, which corresponds to the real astrophysical situation. In such a case, the ALICE CB would be able to access the very low energy domain, whereas the LHCb coverage would be similar as for previous He studies, *i.e.* from 10 to 100 GeV. The ^{16}O are the most abundant nuclei in our Universe after the hydrogen and the helium, so such experimental measurements will likely reduce the uncertainty of the cosmic $\bar{p}$ spectrum.

5.2. Spin physics

This section focuses on the case for spin physics at AFTER@LHC, which is simply outstanding in the worldwide context. It can be divided in two parts. The first relies on the use of a polarised target to carry out countless SSA measurements of common probes with a precision unheard of, but also to measure –for

the first time– SSA on rare perturbative probes which would remain unaccessible otherwise [39]. As such, AFTER@LHC opens a completely novel domain of investigation of the Sivers-like effects for a complete decade, in order to eventually access and (indirectly) constrain the OAM of the gluons and the quarks in the proton, but also in the neutron and the deuteron. Such a quest of the parton OAM goes along with a complete tridimensional tomography of the momenta of the partons confined in hadrons.

The second part of the spin physics case bears on the very large luminosities to be accumulated thanks to the fixed-target mode, combined to an acceptance towards low transverse momenta at high x in the target. This allows one to probe in a systematic way a class of azimuthal asymmetries related to the violation of the Lam-Tung relation in Drell-Yan production, and thus to the Boer-Mulders effect [55]. AFTER@LHC also allows to study its counterpart in the gluon sector, with probably the first systematic measurement of the distribution of the linearly-polarised gluons in unpolarised nucleons at large momentum fractions.

SSAs can be described by nonperturbative twist-2 TMD matrix elements and nonperturbative twist-3 collinear matrix elements in different kinematic regions: the TMD picture holds when there are two separate scales (such as the transverse momentum q_T and the invariant mass M of the lepton pair in Drell-Yan production with $\Lambda_{QCD} \leq q_T < M$), whereas the CT3 picture holds when one single hard scale is present (such as the transverse momentum p_T of a pion produced in hadronic collisions with $\Lambda_{QCD} < p_T$). Both nonperturbative descriptions can be related in the the kinematic region of overlap by means of coefficients which are perturbatively calculable. Both twist-2 TMD and twist-3 collinear matrix element contain essential information on the spin structure of the nucleon and their knowledge is intertwined. AFTER@LHC will test with high precision whether these two formalisms offer the right description of SSAs.

We first discuss the (target) STSAs (*i.e.* A_N or A_{UT}), both for quark-induced and gluon-induced processes, which give access to both quark and gluon Sivers functions and several 3-parton correlation functions. Then we present the prospects for the measurement of spin-related azimuthal asymmetries in unpolarised hadron collisions, which also probe either the quark or the gluon content of the nucleon. Besides the discussion of spin and azimuthal asymmetries, we also elaborate on the relation between the TMDs that can be constrained by AFTER@LHC and the OAM. Next we discuss the use of ultraperipheral collisions to access GPDs through exclusive photoproduction processes and quarkonium production. Finally we discuss the possibility to constrain the strange quark helicity distribution at large x through Λ production.

5.2.1. Quark Sivers effect

The STSA A_N is defined as

$$A_N = \frac{1}{\mathcal{P}_{\text{eff}}} \frac{\sigma^\uparrow - \sigma^\downarrow}{\sigma^\uparrow + \sigma^\downarrow}, \tag{13}$$

where $\sigma^{\uparrow(\downarrow)}$ is a differential-production cross section of particles produced with the target spin polarised upwards (downwards), and $\mathcal{P}_{\text{eff}}$ the effective polarisation. The A_N is of particular interest because it was predicted to be small ($A_N \propto m_q/p_T \sim O(10^{-4})$) in the collinear pQCD approach at leading twist, while the measured $A_N \sim 10^{-1}$ at high x_F in polarised collisions over a broad range of energy [250, 251, 52]).

As introduced in section 2, this A_N can be addressed either using the TMD formalism through the Sivers function, or using the CT3 formalism through 3-parton correlation functions. One of the most important predictions, shared by both approaches, is the sign change of this asymmetry between SIDIS and DY processes. We explain below how AFTER@LHC can contribute to precisely measure this sign change.

---

[39]Let us recall that in this c.m.s. energy range RHIC offers significantly lower luminosities with a limited access to the high x in the polarised nucleons.

Moreover, the accurate measurements to be performed by AFTER@LHC will help to constrain the non-perturbative input that enters the TMD evolution kernel [35, 252, 253, 254, 255, 256, 257], which has an important effect on the STSA (see e.g. [258, 259]).

Drell-Yan production. Drell-Yan (DY) lepton-pair production is a unique tool to study the Sivers effect, because it is very well understood theoretically and the Sivers function $f_{1T}^{\perp q}(x, k_T^2)$ for quarks (which represents the number density of unpolarised quarks with transverse momentum k_T and collinear momentum fraction x for a given value of transverse spin of the proton) is predicted to have an opposite sign for DY and semi-inclusive deep inelastic scattering (SIDIS) processes:

$$f_{1T}^{\perp q}(x, k_T^2)_{\text{DY}} = -f_{1T}^{\perp q}(x, k_T^2)_{\text{SIDIS}} . \tag{14}$$

Within the TMD formalism, and up to angular integrations, A_N in $pp^\uparrow$ collisions can be written as

$$A_N \sim \frac{f_1^q(x_1, k_{T1}^2) \otimes f_{1T}^{\perp \bar{q}}(x_2, k_{T2}^2)}{f_1^q(x_1, k_{T1}^2) \otimes f_1^{\bar{q}}(x_2, k_{T2}^2)} , \tag{15}$$

where f_1^q stands for the unpolarised TMDPDF.

The verification of the sign change of the Sivers function is the main physics case of the DY COMPASS run [65], which recently performed the first measurement of the asymmetry in Drell-Yan production [68], and the experiments E1039 [64] and E1027 [260] at Fermilab. The AFTER@LHC programme will allow one to further investigate the quark Sivers effect by measuring DY STSA [261, 262] over a wide range of $x^\uparrow$ ($= x_2$) and masses. With the high precision that AFTER@LHC will be able to achieve, one will accurately measure the Sivers function, if the sign change happens to be already established by the mentioned experiments. In case the asymmetry turns out to be small and these experiments cannot get to a clear answer, then AFTER@LHC will be able to confirm/falsify the sign change. Table 16 shows a compilation of the relevant parameters of future or planned polarised DY experiments. As can be seen, the AFTER@LHC program offer the possibility to measure the Drell-Yan A_N in a broad kinematic range with an exceptional precision.
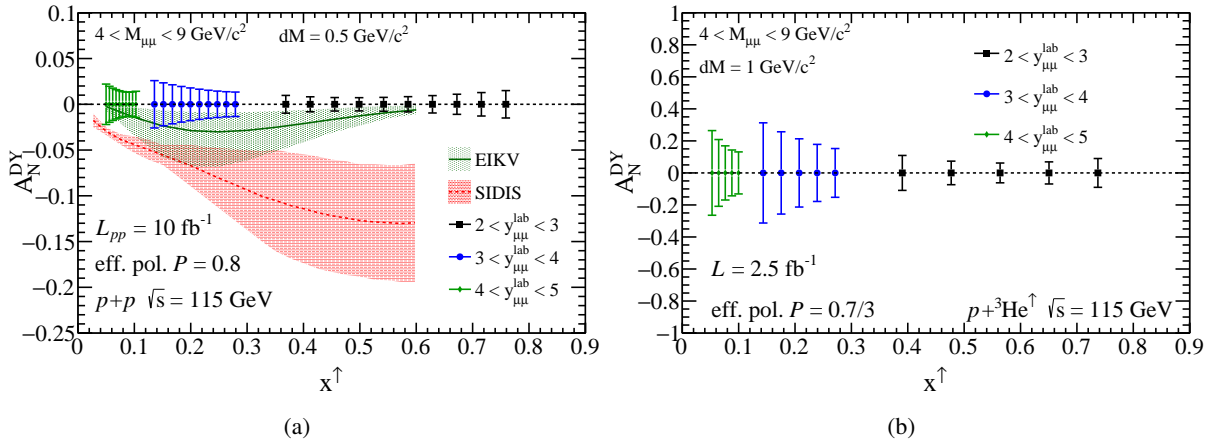
Figure 26: (a) Two predictions (denoted SIDIS [262] and EIKV [258]) of the Drell-Yan A_N as a function of x_F at AFTER@LHC, compared to the projected precision of the measurement [264]. (b) Similar projections for the Drell-Yan A_N as a function of $x^\uparrow$ in $p+^3\text{He}^\uparrow$ collisions at $\sqrt{s} = 115$ GeV [264]. [In both cases, the bars show the statistical uncertainties with the quoted luminosisities accounting for the background subtraction and polarisation-dilution effects].

Experiment	particles	beam energy (GeV)	$\sqrt{s}$ (GeV)	$x^\uparrow$	$\mathcal{L}$ (cm^{-2}s^{-1})	$\mathcal{P}_{\text{eff}}$	$\mathcal{F}$ (cm^{-2}s^{-1})
AFTER@LHCb	$p + p^\uparrow$	7000	115	$0.05 \div 0.95$	$1 \cdot 10^{33}$	80%	$6.4 \cdot 10^{32}$
AFTER@LHCb	$p + {}^3\text{He}^\uparrow$	7000	115	$0.05 \div 0.95$	$2.5 \cdot 10^{32}$	23%	$1.4 \cdot 10^{31}$
AFTER@ALICE$_\mu$	$p + p^\uparrow$	7000	115	$0.1 \div 0.3$	$2.5 \cdot 10^{31}$	80%	$1.6 \cdot 10^{31}$
COMPASS (CERN)	$\pi^- + p^\uparrow$	190	19	$0.05 \div 0.55$	$2 \cdot 10^{33}$	14%	$4.0 \cdot 10^{31}$
PHENIX/STAR (RHIC)	$p^\uparrow + p^\uparrow$	collider	510	$0.05 \div 0.1$	$2 \cdot 10^{32}$	50%	$5.0 \cdot 10^{31}$
E1039 (FNAL)	$p + p^\uparrow$	120	15	$0.1 \div 0.45$	$4 \cdot 10^{35}$	15%	$9.0 \cdot 10^{33}$
E1027 (FNAL)	$p^\uparrow + p$	120	15	$0.35 \div 0.9$	$2 \cdot 10^{35}$	60%	$7.2 \cdot 10^{34}$
NICA (JINR)	$p^\uparrow + p$	collider	26	$0.1 \div 0.8$	$1 \cdot 10^{32}$	70%	$4.9 \cdot 10^{31}$
fsPHENIX (RHIC)	$p^\uparrow + p^\uparrow$	collider	200	$0.1 \div 0.5$	$8 \cdot 10^{31}$	60%	$2.9 \cdot 10^{31}$
fsPHENIX (RHIC)	$p^\uparrow + p^\uparrow$	collider	510	$0.05 \div 0.6$	$6 \cdot 10^{32}$	50%	$1.5 \cdot 10^{32}$
PANDA (GSI)	$\bar{p} + p^\uparrow$	15	5.5	$0.2 \div 0.4$	$2 \cdot 10^{32}$	20%	$8.0 \cdot 10^{30}$

Table 16: Compilation inspired from [1, 19] of the relevant parameters for the future or planned polarised DY experiments. The effective polarisation ($\mathcal{P}_{\text{eff}}$) is a beam polarisation (where relevant) or an average polarisation times a (possible) dilution factor (for a gas target, similar to the one developed for HERMES [87, 263]) or a target polarisation times a dilution factor (for the NH$_3$ target used by COMPASS and E1039). For the AFTER@LHC lines, the numbers correspond to a gas target. $\mathcal{F}$ is the (instantaneous) spin figure of merit of the target defined as $\mathcal{F} = \mathcal{P}_{\text{eff}}^2 \times \mathcal{L}$, with $\mathcal{L}$ being the instantaneous luminosity.

The DY measurement is the key to validate/falsify the Sivers effect for quarks. At AFTER@LHC, the target rapidity range corresponds to a negative x_F ($= x_1 - x_2$) where the A_N asymmetry is predicted to be large (Fig. 26) with large theoretical uncertainties. Fig. 26(a) shows the expected precision for DY A_N measurement at AFTER@LHC for $\mathcal{L} = 10$ fb^{-1} (which corresponds to one year of running) [40], compared to two different theoretical predictions: SIDIS [262] and EIKV [258]. These two works performed fits of A_N in SIDIS data, using two different theoretical setups. The uncertainty band of SIDIS includes the statistical uncertainty of their fitted parameters, while the one of EIKV includes as well an estimate of the theoretical uncertainty arising from neglected higher-order perturbative corrections (by varying the resummation scales by a factor of 2, as it is customary). Thus the DY data at AFTER@LHC will put strict constraints on the Sivers effect for quarks, help to discriminate among different approaches, and accurately test one of the most important predictions of the TMD factorisation formalism, *i.e.* its sign change w.r.t. SIDIS. In addition, given that this effect can be framed as well within the CT3 approach, AFTER@LHC will obtain very useful data to constrain also the 3-parton correlation functions.

AFTER@LHC with a gas target offers also a unique opportunity for studies of STSA in polarised $p + {}^3\text{He}^\uparrow$ collisions. These have been extensively studied at JLab Hall-A by several DIS/SIDIS experiments

---

[40]Statistical uncertainty on A_N is calculated as $\delta_{A_N} = \frac{2}{\mathcal{P}_{\text{eff}}(\sigma^\downarrow + \sigma^\uparrow)^2} \sqrt{(\delta_{\sigma^\uparrow}\sigma^\downarrow)^2 + (\delta_{\sigma^\downarrow}\sigma^\uparrow)^2}$, where $\delta_\sigma = \sqrt{\sigma + 2B}$, σ is a cross section for a given configuration and B is a background in that measurement. The yields are calculated at fixed $y_{\mu\mu}^{\text{lab}} = [2.5, 3.5, 4.5]$, fixed $M_{\mu\mu} = [4.5, 5.5, 6.5, 7.5, 8.5]$ GeV and integrating over the transverse momentum of the lepton pair.

in the last two decades (see e.g. [265, 266]), which the AFTER@LHC program could then complement. Such reactions give access to polarised neutrons and thus to the Sivers functions in a neutron which can shed some light on its isospin dependence. Fig. 26(b) shows the statistical-uncertainty predictions for DY measurements. In the case of ^{3}He$^\uparrow$, a polarisation of P = 70% can be achieved [87]. However, the effective polarisation, $\mathcal{P}_{\text{eff}}$, is diluted by a factor of 3 since only the neutron is polarised in the ^{3}He$^\uparrow$. In addition, the combinatorial background is proportional to the number of binary nucleon-nucleon collisions N_{coll}, thus the background increases by a factor $N_{coll} \approx \sqrt{3}$. An additional isospin factor of 9/6 for DY studies is included. The available integrated luminosity of 2.5 fb^{-1} will allow for an exploratory measurement for DY production and precision study for J/ψ production (see section 5.2.2).

In addition, Drell-Yan lepton-pair production with an unpolarised fixed-target will be extremely valuable to study the simplest TMD function at large x, namely the unpolarised TMD PDF [267, 268, 269, 42, 255, 256]. A good knowledge of unpolarised TMDs is of fundamental importance in order to reliably study azimuthal and spin asymmetries, as they always enter the denominators of these quantities.

Pion and kaon production. Pion and kaon STSAs have been extensively studied in the last three decades at Fermilab, Brookhaven National Laboratory, Jefferson Lab, CERN (COMPASS) and DESY (HERMES) (see e.g. [20, 21, 22, 23, 270, 271, 24, 265]), observing large asymmetries in the valence region at large $x^\uparrow$, which motivated the introduction of the Sivers effect. As for now, similar studies have not been carried out on ^{3}He, thus on a polarised neutron target, which however could give us original insights on the flavour symmetries of the correlation between the partonic transverse momentum and the nucleon spin. Along these lines, the AFTER@LHC programme relying on the LHCb and/or ALICE detectors, can play a crucial role.

Indeed, as shown in Fig. 27, the predicted A_N for pion production with a neutron (a-b) and proton (c-d) targets, based on the generalised parton model (GPM) approach (which is an extension of the parton model to include the transverse-momentum dependence) [41] and the CT3 approach [42], both indicate a "flavour" sign change.

From a pQCD point of view, pion and kaon production at AFTER@LHC can thus improve the current knowledge of the CT3 matrix elements involved in the production and fragmentation mechanisms [273], and help to clarify if the pion and kaon STSAs are really generated mainly by the moment of the Collins function, as recently suggested [34].

$W^\pm$ boson production. So far, only the valence u and d quark Sivers functions have been constrained, while sea quark Sivers functions remain largely unknown [258]. In this sense, STSAs for vector boson production offer a complementary tool to STSAs for Drell-Yan production, giving access to the flavour dependence of the Sivers function. Moreover, they can also serve to test the sign change of the Sivers effect with respect to SIDIS.

As explained in section 5.1.1, roughly 250 W^+ and 60 W^- per year are expected to be collected with a luminosity of 10 fb^{-1}. These yields would allow us to achieve a statistical uncertainty for A_N of roughly $0.1 - 0.2$ [43].

---

[41]Isospin symmetry is used to implement the neutron Sivers functions by using the extracted proton ones in Ref. [262]: $f_{1T}^{\perp u/neutron} = f_{1T}^{\perp d/proton}$ and $f_{1T}^{\perp d/neutron} = f_{1T}^{\perp u/proton}$. This is supported by the STSA on deuteron target measured by COMPASS [24, 272], well compatible with zero. These predictions include both Sivers and Collins contributions, which are added together in the estimates of the central values as well as of the statistical uncertainty bands

[42]Isospin symmetry is used again to implement the neutron twist-3 matrix elements by using the extracted proton ones in Ref. [34]

[43]The uncertainty is calculated in the same way as for Drell-Yan A_N.
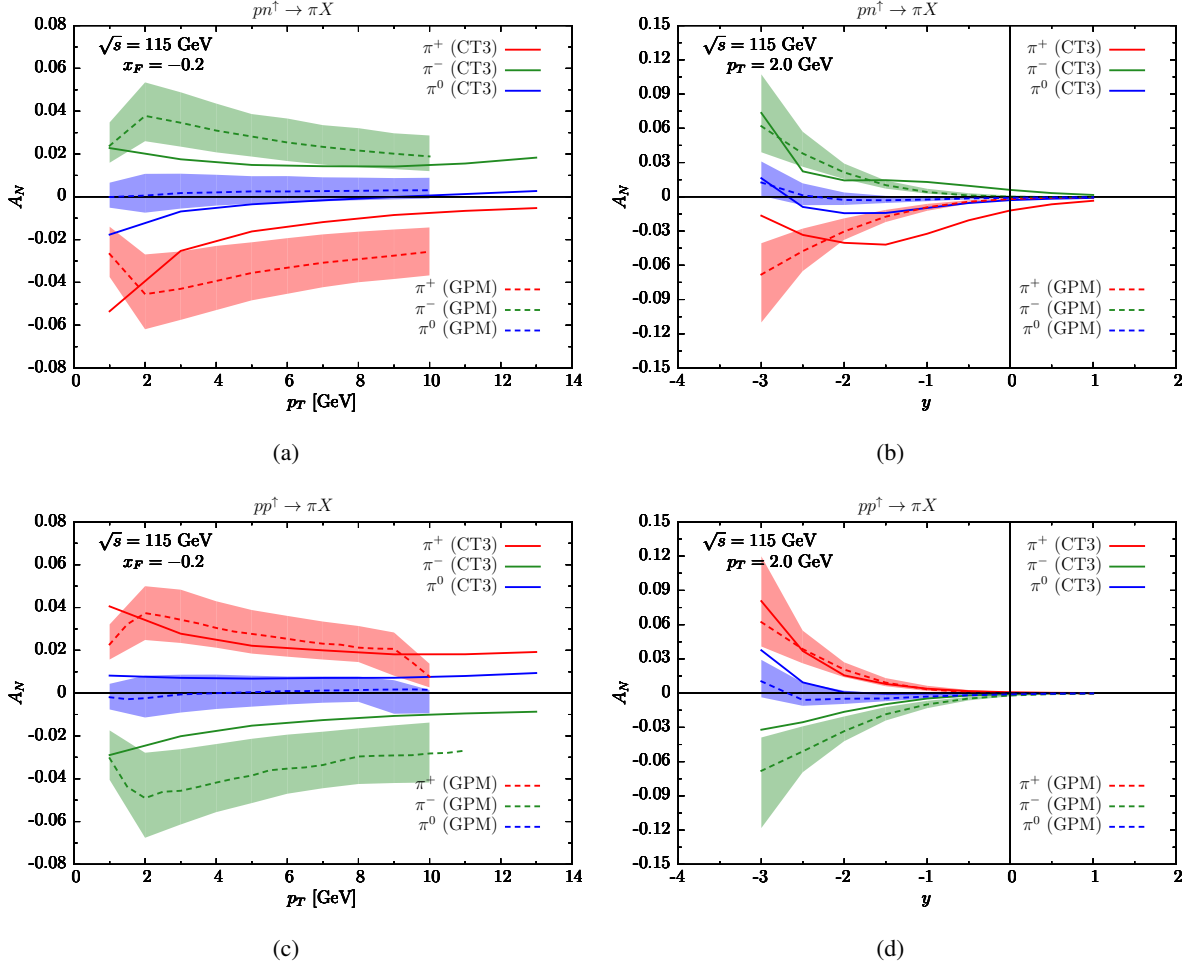
Figure 27: Predicted A_N for pion production as a function of (a) transverse momentum p_T and (b) rapidity y, in the AFTER@LHC kinematics for a neutron target (with ^{3}H$^\uparrow$), based on both GPM and CT3 formalisms. (c-d): same as (a-b) but for a proton target.

We finally comment on the possibility to constrain the sea-quark-helicity distributions at AFTER@LHC by measuring the spin asymmetries for a longitudinally polarised target. At leading order the asymmetries for W^+ and W^- bosons are simply related to the (helicity) PDFs as

$$A_{UL}^{W^+} \propto \frac{g_1^u(x_1)f_1^{\bar{d}}(x_2) - g_1^{\bar{d}}(x_1)f_1^u(x_2)}{f_1^u(x_1)f_1^{\bar{d}}(x_2) + f_1^{\bar{d}}(x_1)f_1^u(x_2)}, \quad A_{UL}^{W^-} \propto \frac{g_1^d(x_1)f_1^{\bar{u}}(x_2) - g_1^{\bar{u}}(x_1)f_1^d(x_2)}{f_1^d(x_1)f_1^{\bar{u}}(x_2) + f_1^{\bar{u}}(x_1)f_1^d(x_2)}, \quad (16)$$

where g_1^q is the helicity PDF of the quark q. Dedicated simulations are however needed to quantify such constraints.

Direct-photon production. The quark Sivers effect can also be studied via direct-photon production STSAs. Fig. 28 shows the expected A_N as a function of the photon p_T for $x_F = -0.2$ (*i.e.* in a range accessible by LHCb) for both aforementioned approaches. Contrary to the DY and π production cases, the predicted signs of A_N differ. This is related to the sign "mismatch" issue (see *e.g.* [274]). Even though the magnitude of A_N is the largest at low p_T (< 1 GeV) where the background is probably very challenging and the application

of pQCD questionable, measurements with a precision on the order of 1% for $x_F = -0.2$ should however be sufficient to discriminante between the predictions of both approaches for p_T above 5 GeV.
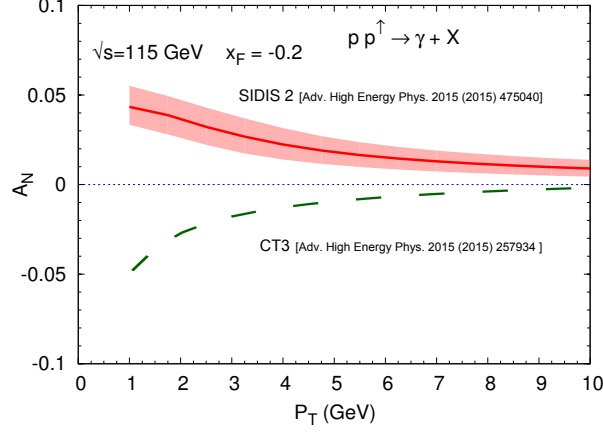
Figure 28: Prediction for the direct-photon A_N as a function of p_T [262, 273] for $x_F = -0.2$. No theoretical uncertainties are shown for the CT3 prediction.

By measuring A_N for quark-induced processes which do not involve fragmentation, in particular prompt photons, compared to charged and neutral pions and kaons, the AFTER@LHC programme will allow one to distinguish the Sivers and Collins mechanisms [19, 275], and in turn constrain the quark contribution to the transverse spin of the proton, along with the constraint from DY production data.

5.2.2. Gluon Sivers effect

Drell-Yan lepton-pair production is the golden process to access the intrinsic transverse motion of quarks in a nucleon. However, there is no analogous process to probe the gluon content, which is both experimentally clean and theoretically well-controlled. For instance, H^0 boson production could be this process, since effectively it is a glue-glue fusion into a colour-singlet, but it is experimentally demanding in terms of luminosity and energy.

In order to do so, then, one of the best tools at our disposal is the production of quarkonium states. In fact, a major strength of AFTER@LHC is the large production rates for open heavy-flavour mesons and quarkonium states, expected for a single year of data taking (roughly 10^6 Υ and 10^9 J/ψ). In addition, these processes are mainly sensitive to the gluon content of the colliding hadrons. They are very useful probes to precisely access and constrain the gluon Sivers effect, which is essentially unknown [276, 51]

Moreover, note that different processes will probe in general different gluon TMD functions, due to their inherent process dependence [277, 62]. In fact, the generalised universality of gluon TMDs is more involved than the one of quark TMDs, due to the richer gauge-link structure in their operator definition. In particular, in the case of the gluon Sivers function, it is believed that all the functions that can be probed in different processes can be reduced to only two independent ones. The AFTER@LHC programme offers a unique possibility to test all these theoretical predictions, either confirming them or quantifying the potential discrepancies, if any.

Open heavy-flavour production. The A_N for open heavy-flavour production gives access to the gluon Sivers effect (see e.g. [278, 279]. It also offers the possibility to study the process dependence of A_N, by measuring charm quarks and anti-quarks separately [280], being a unique probe of the C-parity odd twist-3 tri-gluon correlator [281, 282].

(a)

(b)
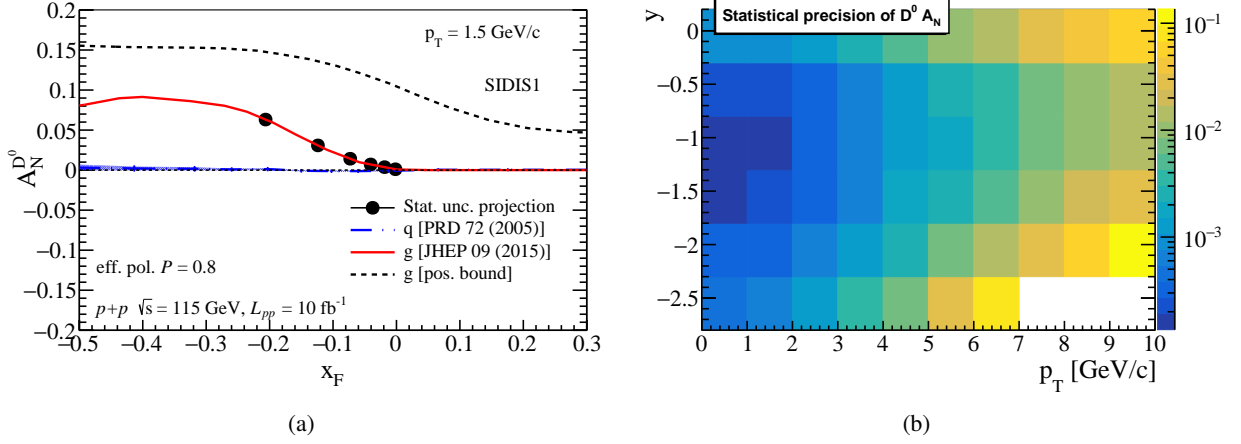
Figure 29: Projections for the statistical precision of open charm A_N as a function of (a) x_F at fixed p_T and of (b) $y_{c.m.s.}$ & p_T, at $\sqrt{s_{NN}}$ = 115 GeV and 10 fb^{-1} of luminosity using an LHCb-like detector. The D-meson yields are taken from FONLL [283, 284] calculation within the LHCb acceptance; the efficiency and the S/B ratio are extrapolated from [100]. The theory curves represent the SIDIS predictions for quarks and gluons, along with the positivity upper bound of the gluon Sivers effect [285, 286].
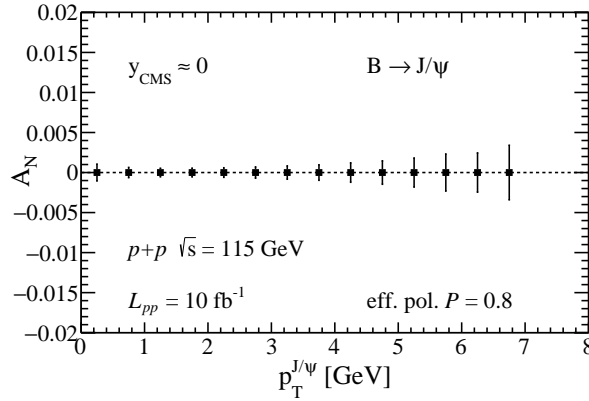
Figure 30: Projections for the statistical precision of open bottom A_N (measured via $B \rightarrow J/\psi$) as a function of p_T at $y_{c.m.s.} \approx 0$ and $\sqrt{s_{NN}}$ = 115 GeV measured with a LHCb-like detector with integrated luminosity of 10 fb^{-1}. The $B \rightarrow J/\psi$ yields are calculated based on the FONLL predictions for the bottom-quark yields, and the $B \rightarrow J/\psi$ fragmentation is calculated using the PYTHIA model. Calculations include the acceptance and reconstruction efficiency of a LHCb-like detector. See [287] for more details.

Fig. 29 shows the estimated statistical precision for charmed-meson A_N at backward and mid-rapidity (in the c.m.s.). As can be seen, even in the case of a moderate target polarisation we would expect a very precise measurement for $p_T \lesssim 5$ GeV/c. Such measurements can only be performed at AFTER@LHC. It can definitely be achieved in the $K\pi$ decay channel, and possibly in the lepton-decay channel, despite of the presence of many more sources for the background (see e.g. [288]).

Fig. 30 shows the estimated statistical precision for open bottom A_N, measured via non-prompt J/ψ, as a function of p_T at mid-rapidity, which is similar to that of the prompt charmonium at the sub-percent level. It is then clear that such measurement would open a new era of precision measurements of STSAs for open heavy-flavour production.

Vector quarkonium production. Fig. 31(a) shows the estimated uncertainties at AFTER@LHC for the Υ A_N as a function of x_F in pp collisions at $\sqrt{s}$ = 115 GeV, while Fig. 31(b) shows the projected uncertainties for J/ψ compared to already existing measurements at $\sqrt{s}$ = 200 GeV [25, 54]. With the expected charmonium yields [289] these results are only limited by the systematic uncertainties, and can thus give a very precise access to the gluon content of the proton over a much wider x range than at RHIC. As for now, the experimental measurements are compatible with zero, which could be due to the following reasons: first, the gluon Sivers function might be zero; second, the effect of the Sivers function might disappear when integrated over p_T, in case it has a node; third, the dominant J/ψ production mechanism is the colour-octet, whose STSA in pp collisions is thought to vanish as compared to the STSA for colour-singlet transition [290]. However, we note that the arguments in support of the latter reason are derived at leading-twist, and thus deviations at the, say, few 10% level of the measured asymmetry should certainly not be excluded. On the other hand, the generation of such STSA through a Collins-like fragmentation mechanism has not been discussed in the literature. In any case, the precise measurements performed within the AFTER@LHC programme can give us a handle to discriminate the discussed scenarios.
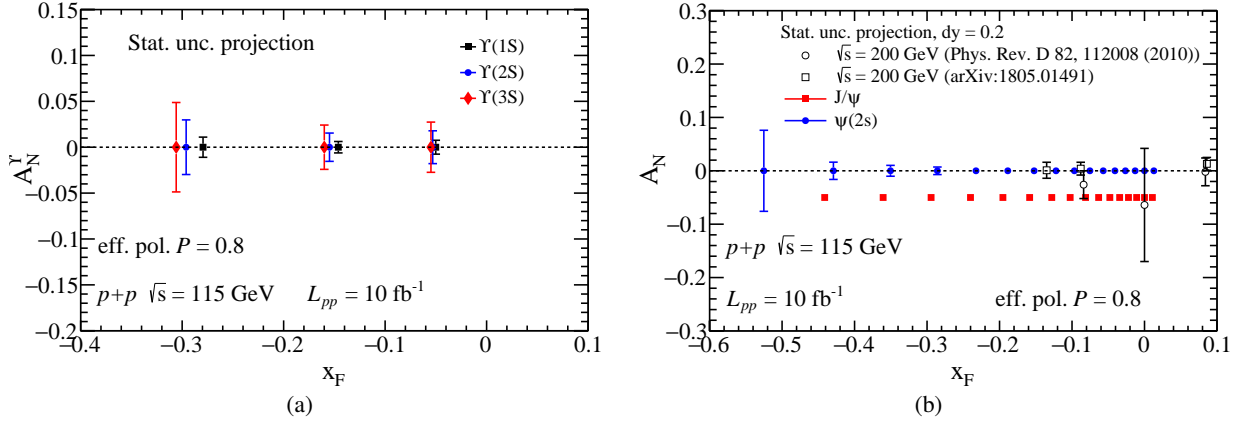
Figure 31: Statistical-precision projections for (a) $\Upsilon(nS)$ and (b) $\psi(nS)$ A_N as a function of x_F compared to the existing measurements [25, 54]. The quarkonium states are assumed to be measured in a di-muon channel with a LHCb-like detector. The signal and the background are calculated in realistic simulations that take into account the performance of the LHCb detector [289, 264].

Fig. 32 shows the expected statistical precision for J/ψ A_N with an ALICE-like detector for $pp^{\uparrow}$ collisions with 45 pb^{-1} of luminosity. The J/ψ and the background yields expected were extrapolated from the J/ψ rapidity spectrum and the signal-to-background ratios of [291] with the procedure described in [264]. The signal-to-background ratio at 115 GeV is 1.2, and an efficiency of 13% was assumed [292]. Even though the luminosity is lower than in the LHCb-like setup, measurements with an ALICE-like detector would provide an independent experimental cross-check for the studies with a LHCb-like detector. This is an indispensable tool for the verification of the experimental observations or discoveries. Such a strategy was, and continues to be, a standard approach in the research programs at, for instance, Tevatron (D0 vs CDF), RHIC (STAR vs. PHENIX) and the LHC (CMS vs ATLAS).

C-even quarkonium production. The production of C-even states can fruitfully be investigated [57, 293, 294, 58]. With an LHCb-like detector[44], STSA for χ_c, χ_b and η_c are possible as demonstrated by studies of

---

[44]*i.e.* with a good momentum and energy resolution for muons, a decent energy resolution for photons, PID for protons and antiprotons and excellent vertexing capabilities.
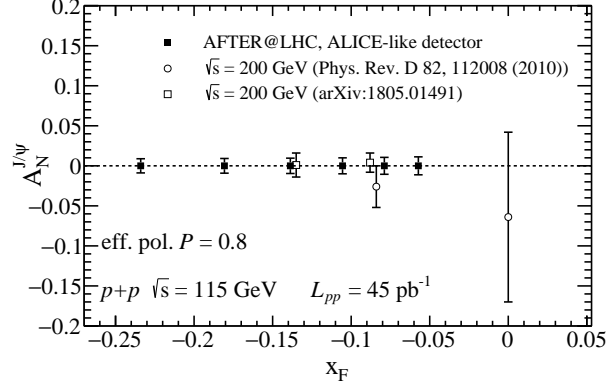
Figure 32: Statistical-precision projections for J/ψ A_N as a function of x_F compared to the existing measurements [25, 54] for AFTER@ALICE$_\mu$. The J/ψ di-muon spectrum is assumed to be measured in the Muon Spectrometer of the ALICE detector. The signal and the background are extrapolated at $\sqrt{s_{NN}} = 115$ GeV from the ALICE measurements in [291].

various χ_c states [295, 296] in the busier collider environment down to a transverse momentum p_T as low as 2 GeV. LHCb allowed for the first study of inclusive η_c production [297] above $p_T = 6$ GeV as well as non-prompt $\eta_c(2S)$ [298]. Prompt studies are definitely within the LHCb reach [299]. At lower energies, the reduced combinatorial background will definitely allow one to access lower p_T with very reasonable statistics. Indeed, the cross section for pseudoscalar-charmonium production should be similar to that of the vector ones. The main differences in the expected yields come from likely smaller branchings (with the notable exception of the $KK\pi$ decay) and detection efficiencies. Measuring the STSA of η_c also gives a clean access to tri-gluon correlation functions [300] but also, if one can measure its p_T dependence, to the transverse momentum dependence of the gluon Sivers function relevant for hadron-induced reactions.
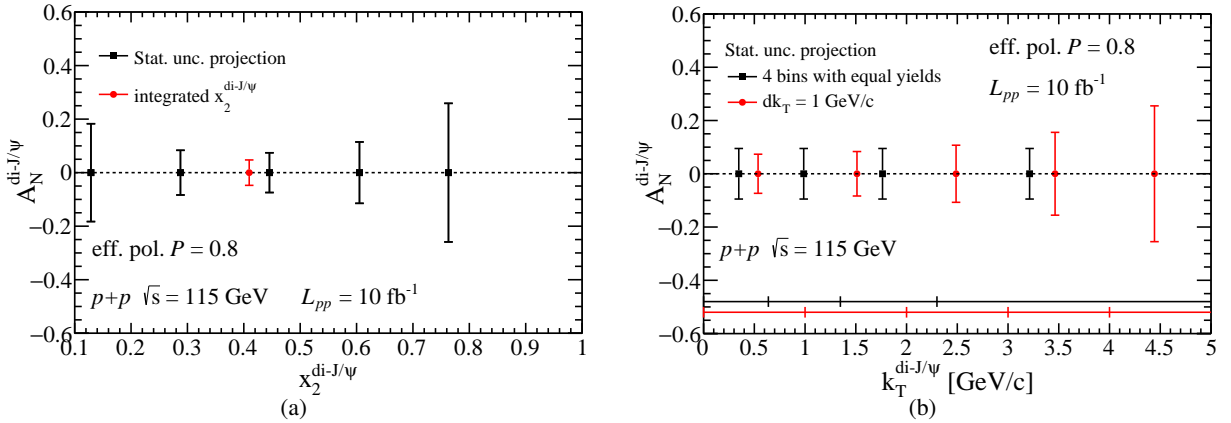
Figure 33: Statistical-precision projections for di-J/ψ A_N as a function of (a) x_F and (b) the pair p_T with a LHCb-like detector. The horizontal lines in (b) denote the width of the p_T bins used for the calculations.

Associated production. Associated-production channels [301, 59, 302, 303, 58, 304, 305] are fundamental tools to access the gluon Sivers effect, and also probe the gluon TMD sector and their evolution [252, 294]. A few different processes are potentially interesting in this context, for instance $J/\psi - J/\psi$, $J/\psi - \gamma, \gamma - \gamma$, $\Upsilon(nS) - \gamma$. The $J/\psi - J/\psi$ production seems to be the most practical one since the yields are not too

small [192] and the measurement is relatively straightforward (compared, for instance, to direct γ studies). Fig. 33 shows the A_N for double J/ψ production as a function of the pair's x_2 and k_T. We consider two scenarios for the analysis of A_N as a function of k_T: bins with a fixed width of 1 GeV/c (dk_T = 1 GeV/c, red points) and bins with equal number of yields. Here, we model the k_T dependence as a Gaussian distribution with the width σ = 2 GeV/c. The x_2-integrated A_N will allow for the determination of the STSA with a few percent precision, and the $A_N(k_T)$ gives access –for the first time– to the k_T dependence of the gluon Sivers TMD up to $k_T \approx 4$ GeV/c.

5.2.3. Quark-induced azimuthal asymmetries

In section 5.2.1 we discussed the extraction of the Sivers asymmetry from the Drell-Yan production cross-section. However this process can also give valuable information on other asymmetries, and thus on other TMDs. In fact, the cross-section for a transversely polarised target (and an unpolarised beam) can be written in terms of the following structure functions [306]:

$$A_{UU}^{cos2\phi} \sim \frac{h_1^{\perp q}(x_1, k_{1T}^2) \otimes h_1^{\perp \bar{q}}(x_2, k_{2T}^2)}{f_1^q(x_1, k_{1T}^2) \otimes f_1^{\bar{q}}(x_2, k_{2T}^2)} \, , \tag{17}$$

$$A_{UT}^{sin\phi_S} \sim \frac{f_1^q(x_1, k_{1T}^2) \otimes f_{1T}^{\perp \bar{q}}(x_2, k_{2T}^2)}{f_1^q(x_1, k_{1T}^2) \otimes f_1^{\bar{q}}(x_2, k_{2T}^2)} \, , \tag{18}$$

$$A_{UT}^{sin(2\phi+\phi_S)} \sim \frac{h_1^{\perp q}(x_1, k_{1T}^2) \otimes h_{1T}^{\perp \bar{q}}(x_2, k_{2T}^2)}{f_1^q(x_1, k_{1T}^2) \otimes f_1^{\bar{q}}(x_2, k_{2T}^2)} \, , \tag{19}$$

$$A_{UT}^{sin(2\phi-\phi_S)} \sim \frac{h_1^{\perp q}(x_1, k_{1T}^2) \otimes h_1^{\bar{q}}(x_2, k_{2T}^2)}{f_1^q(x_1, k_{1T}^2) \otimes f_1^{\bar{q}}(x_2, k_{2T}^2)} \, , \tag{20}$$

where h_1^q is the transversity, $h_1^{\perp q}$ the Boer-Mulders function and $h_{1T}^{\perp q}$ the pretzelosity (f_1^q and $f_{1T}^{\perp q}$ are the already introduced unpolarised TMD PDF and the Sivers function, respectively). The superscript on the A's means that we weight the cross-section with that angular term to single out the corresponding angular modulation.

Let us focus on the Boer-Mulders function $h_1^\perp$, which encodes the correlation between the quark transverse spin and its transverse momentum, namely it represents a spin-orbit effect for the quark inside an unpolarised proton. This function, like the quark Sivers function, is time-reversal odd (T-odd), and thus it changes sign under time-reversal transformations. In particular, a sign change is predicted for $h_1^\perp$ probed in SIDIS and DY production. Moreover, it explains the violation of the Lam-Tung relation in unpolarised DY reaction [56]. Hints about the transverse momentum dependence of the Boer-Mulders function $h_1^\perp$ have been extracted from SIDIS data in [307]. AFTER@LHC will contribute to the study of the Boer-Mulders function in DY production, shedding light on its process dependence and on the TMD formalism in general.

In Fig. 34 we show the expected precision achievable at AFTER@LHC for different angular modulations of the DY production cross-section in different kinematic regions (rapidity, invariant mass, momentum fraction in the (un)polarised target nucleon).

5.2.4. Gluon-induced azimuthal asymmetries

In the quark case, there are two leading-twist TMDs, as we have discussed, the unpolarised $f_1^q(x, k_T^2)$ and the Boer-Mulders $h_1^{\perp q}(x, k_T^2)$ functions. For a gluon in an unpolarised proton, the relevant functions are the unpolarised distribution $f_1^g(x, k_T^2)$ and the distribution of linearly polarised gluons $h_1^{\perp g}(x, k_T^2)$ [40, 41].
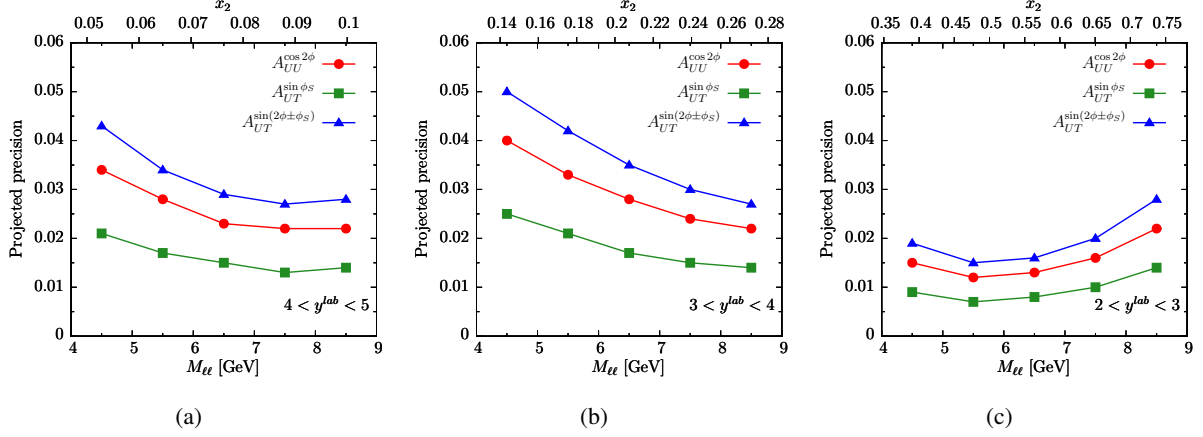
Figure 34: Expected statistical uncertainty on asymmetries in DY production at AFTER@LHCb. Note that the uncertainty of $A_N = A_{UT}$ (see Fig. 26(a)) is $\sqrt{2}$ times smaller than the one of $A_{UT}^{\sin\phi_S}$ (since $A_{UT} = 2A_{UT}^{\sin\phi_S}$). The rapidity has been integrated over the bins specified in the plots, as well as the mass in bins of $dM = 1$ GeV.

The phenomenology of $h_1^{\perp g}$ is potentially easier than that for the Boer-Mulders function in the quark case, because it is T-even and matched onto the twist-2 unpolarised collinear distributions $f_1^{g,q}$, whereas $h_1^{\perp q}$ is matched onto the twist-3 collinear matrix elements, which are so far unknown. However, no experimental extractions of $h_1^{\perp g}$ have been performed yet. Recently, it has been proposed to access both f_1^g and $h_1^{\perp g}$ in di-J/ψ and Υ production in hadronic collisions [308], for which data with sensitivity to transverse momenta have been collected at the LHC. It is expected that $h_1^{\perp g}$ reaches its maximal size in the small-x regime [41, 309, 310, 311]. Its role in different x-regions has yet to be explored. It is also expected to be constrained from azimuthal-asymmetry measurements at the future EIC and the LHeC [312, 277], and also possibly from measurements at RHIC and the LHC [301].

The impact of linearly polarised gluons in H^0 production has been addressed *e.g.* in [313, 314, 315, 294]. Their effect has been predicted for gluon fusion into two photons in [316, 301], for (pseudo)scalar quarkonium production in [57, 58], for vector quarkonium production in [317, 318] and for H^0 plus jet production in [302]. Associated production of quarkonium and Z boson has been investigated in [319]. Associated production of quarkonium plus one photon [59] is also promising, due to the possibility of producing final states with different invariant masses, suited thus to be analysed using TMD factorisation and test TMD evolution. This process, together with $\eta_{c,b}$ production [57, 58] and double J/ψ production [192], can be investigated within the AFTER@LHC programme.

Several processes can be investigated at the proposed AFTER@LHC programme in order to constrain $h_1^{\perp g}$ in yet unexplored kinematic regions. In Table 17 we show the processes in which the effect of the presence of $h_1^{\perp g}$ is the modulation of the transverse-momentum spectrum, while in Table 18 we show the processes for which $h_1^{\perp g}$ creates an azimuthal modulations of the spectrum. We notice that in all the mentioned processes the same $h_1^{\perp g}$ function is probed, since the gauge link structure is the same. As can be seen, overall the AFTER@LHC programme offers a great opportunity to constrain $h_1^{\perp g}$ through all these processes.

Ref. [320] shows that TMD factorisation in gluon-induced quarkonium production in P-wave holds at the one-loop level for $J^{PC} = 0^{++}$ and 2^{++}, whereas it is violated already at that level for 1^{++} states, e.g. $\chi_{c1(1P)}$. The vector nature of these states implies that they are always produced together with a radiated gluon. Thus, at AFTER@LHC it will be possible to study the χ_{c0} (0^{++} state) [57]. Moreover, η_c at low

Process at AFTER@LHC	expected yield	x_2 range	M [GeV]	q_T modulation
η_c	$O(10^6)$	$0.02 \div 0.5$	$O(3)$	$0 \div 80\%$
$\chi_{c0}(1P)$	$O(10^4)$	$0.02 \div 0.5$	$O(3)$	$0 \div 80\%$
$\chi_{c2}(1P)$	$O(10^6)$	$0.02 \div 0.5$	$O(3)$	$< 1\%$
$\chi_{b0}(nP)$	$O(10^2)$	$0.1 \div 1$	$O(10)$	$0 \div 60\%$
$\chi_{b2}(nP)$	$O(10^3)$	$0.1 \div 1$	$O(10)$	$< 1\%$

Table 17: Expected q_T modulations generated by $h_1^{\perp g}$ for a selection of quarkonium-production observables, along with the expected yields and x_2 ranges derived from $x_2 = Me^{Y_{\text{c.m.s.}}}/\sqrt{s}$ for a rapidity coverage $-2.8 < Y_{\text{c.m.s.}} < 0.2$ and $\sqrt{s} = 115$ GeV.

Process at AFTER@LHC	expected yield	x_2 range	M [GeV]	$\langle\cos 2\phi\rangle$	$\langle\cos 4\phi\rangle$
$J/\psi + \gamma$ [59]	$1000 \div 2000$	$0.1 \div 0.6$	$O(10)$	$0 \div 5\%$	$0 \div 2\%$
$J/\psi + J/\psi$ [308]	$300 \div 1500$	$0.1 \div 0.8$	$8 \div 12$	$0 \div 15\%$	$0 \div 20\%$

Table 18: Expected azimuthal asymmetries generated by $h_1^{\perp g}$ for a selection of quarkonium-associated-production observables, along with the expected yields and x_2 ranges derived from $x_2 = Me^{Y_{\text{c.m.s.}}}/\sqrt{s}$ for a rapidity coverage $-2.8 < Y_{\text{c.m.s.}} < 0.2$ and $\sqrt{s} = 115$ GeV.

transverse momentum will be accessed, complementing the high transverse momentum region accessed by LHCb and going beyond RHIC's capabilities.

As already mentioned for the case of quark TMDs, the AFTER@LHC program can be useful also to better constrain the simplest of the gluon TMDs, *i.e.* the unpolarised gluon TMD PDF, which remains so far unconstrained (see however a first attempt in [308]). As its quark counterpart, it enters the denominators of all spin and azimuthal asymmetries, and thus its knowledge is fundamental in order to reliably study any TMD-related asymmetry.

5.2.5. From TMD PDFs to the partonic orbital angular momentum

On top of providing a handle on the intrinsic spin of partons, the TMD formalism intuitively connects with the orbital angular momentum of the quarks, through the correlations proportional to the partonic transverse momenta. In fact, conservation of total angular momentum imposes that off-diagonal TMDs (i.e. those with $\Delta\lambda = (\Lambda' - \Lambda) - (\lambda' - \lambda) \neq 0$, where $\Lambda^{(\prime)}$ and $\lambda^{(\prime)}$ are the initial (final) target and parton light-front helicities) would vanish in absence of orbital angular momentum (OAM). Some of these off-diagonal TMDs appear to be experimentally sizeable [23, 24, 321], confirming henceforth the presence of a significant amount of OAM inside the nucleon. This rises the question as to whether TMDs can be used to quantify more precisely the OAM.

It has been observed within many effective quark models that the expectation value of the *canonical* quark OAM can be expressed in terms of some TMDs [322, 323, 324, 325]

$$
\begin{aligned}
\langle L_{\text{can}}^q \rangle &= \int dx\, d^2k_\perp \left[h_1^q(x, \boldsymbol{k}_\perp^2) - g_{1L}^q(x, \boldsymbol{k}_\perp^2) \right], \\
&= -\int dx\, d^2k_\perp \frac{\boldsymbol{k}_\perp^2}{2M^2} h_{1T}^{\perp q}(x, \boldsymbol{k}_\perp^2).
\end{aligned}
\tag{21}
$$

Unfortunately, it has also been shown that the validity of these relations cannot be extended to QCD [326,

65

327, 328]. Although not exact, they remain phenomenologically interesting as they provide at least some indication about the sign and the magnitude of the canonical quark OAM. Note that the results can be quite different [329, 330] from the *kinetic* quark OAM derived from the Generalised Parton Distributions (GPDs) through the Ji relation [331] which contains also quark-gluon interactions.

Interestingly, Burkardt [332, 333] suggested that the quark Sivers TMD $f_{1T}^{\perp q}(x, k_\perp^2)$ and the quark GPD $E^q(x, \xi, t)$ could be related by a chromodynamic lensing mechanism

$$\int d^2 k_\perp \frac{k_\perp^2}{2M^2} f_{1T}^{\perp q}(x, k_\perp^2) \propto \int d^2 b_\perp \bar{\mathcal{I}}(b_\perp) (S_T \times \partial_{b_\perp})_z \mathcal{E}^q(x, b_\perp^2), \tag{22}$$

where $\bar{\mathcal{I}}(b_\perp)$ is called the lensing function and $\mathcal{E}^q(x, b_\perp^2) = \int \frac{d^2 \Delta_\perp}{(2\pi)^2} e^{-ib_\perp \cdot \Delta_\perp} E^q(x, 0, -\Delta_\perp^2)$. The Sivers function could then be used to constrain the GPD E^q and hence the kinetic OAM via the Ji relation. Despite some support from model calculations [333, 334, 309, 335], such a relation can hardly be put on a firmer theoretical grounds. A variation of it has however been used by Bacchetta and Radici [336] to fit SIDIS data for the Sivers effect with the integral constrained by the anomalous magnetic moments, leading to a new estimate of the total angular momentum $\langle J_{kin}^q \rangle$, in good agreement with most common GPD extractions [337, 338, 339, 340, 341]. A similar relation may a priori hold in the gluon sector, but has never been investigated so far.

In fact, one should not expect any *direct* quantitave relation between TMDs and OAM since the latter requires some information about the correlation between the position and the momentum of the parton, information which is integrated out at the TMD level. However, TMDs provide essential information about several angular-momentum correlations [342] and can be used to constrain, to some extent, the nucleon wave function, providing us *indirectly* with valuable information about its OAM content. Thus the AFTER@LHC programme, with its unique capabilities of measuring quark and gluon TMDs, and in particular Sivers functions, can shed light on the partonic OAM by giving us a handle to indirectly constrain it.

5.2.6. Ultraperipheral collisions

Ultraperipheral collisions (UPCs) provide a unique way to study photoproduction processes in hadron-hadron interactions [343], also in the fixed target experiments [344]. Such processes are conveniently described in the Equivalent Photon Approximation, where the relation between the hadron-hadron cross section, $(d)\sigma^{h_A h_B}$, and the (differential) cross section for a photo-hadron scattering (h_A or h_B), $(d)\sigma^{\gamma h_{A,B}}$, is naturally given by the following convolution with the photon flux

$$d\sigma^{h_A h_B} = \int dk_\gamma \Big(\frac{dn^{h_A}}{dk_\gamma} d\sigma^{\gamma h_B}(s_{\gamma h_B}(k_\gamma)) + \frac{dn^{h_B}}{dk_\gamma} d\sigma^{\gamma h_A}(s_{\gamma h_A}(k_\gamma)) \Big) \quad . \tag{23}$$

Relevant parameters of such photon beams, for various projectiles and targets in AFTER@LHC, can be found in Table 1 of [344].

Exclusive photoproduction processes which can be studied in the UPCs, allow us to describe the internal structure of hadrons in terms of GPDs [345, 346], which through a Ji sum rule are directly related to the total orbital angular momentum carried by quarks and gluons. They also allow us to explore the 3 dimensional "tomography" of hadrons [347].

One of such exclusive processes, that has not yet been measured, is Timelike Compton Scattering [348], contributing to the lepton-pair photoproduction. Although the purely electromagnetic Bethe-Heitler (BH) amplitude gives much larger contribution than the TCS one, it is possible to study the interference term between TCS and BH processes, which may be projected out through the analysis of the angular distribution

	σ_{BH}(pb)	luminosity	events yr $^{-1}$
p on Pb	1940 pb	0.16 fb^{-1}yr^{-1}	3×10^5
p on H	7.1 pb	20 fb^{-1} yr^{-1}	1.4×10^5
Pb on H	5500 pb	11 nb^{-1} yr^{-1}	6×10^3

Table 19: The Bethe-Heitler cross section and number of events predicted for three different modes of operation for AFTER@LHC [344].

of the produced leptons. The ratio of those two contributions for the kinematics relevant to AFTER@LHC was found to be of the order of 10 % [344].

Table 19 gathers the BH cross section, the luminosity and the yearly expected lepton-pair yields in 3 possible operation modes in the kinematic region where the TCS-signal extraction is possible. With a magnitude of 10 % for the interference term, the azimuthal modulation should be observable in the 3 cases.

We also note that the cross sections for η_c production by photon-pair fusion has been derived in [344]. That process, in particular in this energy range, is sensitive on the method used to compute the photon flux in the pp case. We found out that 10^4 η_c can be produced per year in UPCs with AFTER@LHC. The same paper also discussed possible competing hadronic processes via pomeron or odderon exchanges which could interestingly be separated out by a careful analysis of the transverse-momentum dependence of the produced particles. η_c production from $\gamma\gamma$ fusion in UPCs at AFTER@LHC was also discussed in [349].

Exclusive J/ψ production [351] draws a lot of attention due to the fact that at the leading order it is only sensitive to gluon GPDs. It has already been measured in the ultraperipheral collisions at LHCb, ALICE and CMS in the collider mode. However, the AFTER@LHC programme would create a unique possibility to study STSAs in such a process [352], which is sensitive to the yet unknown GPD E_g [353], an important piece of the spin sum rule. This process would also give us access to the gluon Sivers function [354].

In [352] two LHC fixed-target operation modes were studied: proton-hydrogen and lead-hydrogen collisions. The y distribution and p_T distribution for those cases are shown on the Fig. 35. The statistical uncertainties in the bins relevant for the GPD extraction are presented on the Fig. 36, and indicate that AFTER@LHC is able to perform the first determination of E_g. The exclusive vector-meson photoproduction in UPCs at AFTER@LHC was also studied in [355], including that of the light ρ and ω mesons.

5.2.7. Accessing the strange quark helicity densities at high x

The distributions of longitudinally polarised (anti)quarks inside a nucleon are far from well known. For instance, there are still sizable uncertainties in the case of antiquarks (see e.g. [356]). Specifically, understanding of the distribution of polarised strange (s) and antistrange quark distributions (Δs and $\Delta \bar{s}$, respectively), and their possible asymmetry is one of the most intriguing open questions in particle physics. Besides of being a key information on the structure of matter, it is also an essential ingredient of theoretical calculations in astrophysics (Δs enters the hydrodynamical modelling of core-collapse supernova explosions). As of today, the precise value of Δs remains unknown. The region where the quarks carry the majority of the proton momentum (high-x, $x \sim 1$) is of special importance. It is pivotal for revealing the content of nucleons observed in nature: both the quark structure and the total spin of a nucleon are in fact arising from the (valence) quark PDFs at high x. Currently, insufficient data exist in this kinematic range, which leads to unacceptably large uncertainties in the extracted polarised quark PDFs at $x \rightarrow 1$. For example, the d/u quark ratio at high x remains a puzzle. In general, any additional data at high x can reduce the uncertainties in the determination of (un)polarised quark distributions. AFTER@LHC programme provides

(a) *p*H with 7 TeV proton

(b) PbH with 2.76 TeV Pb
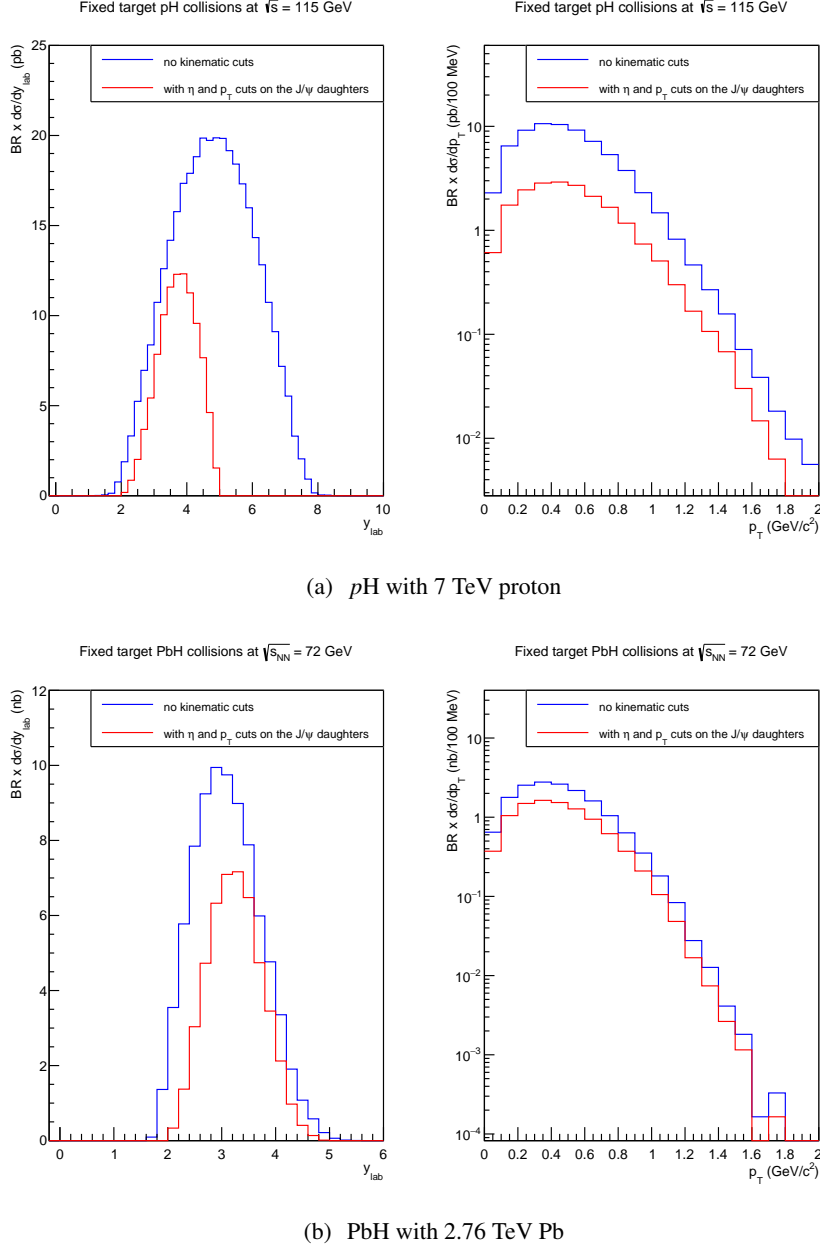
Figure 35: Rapidity-differential (a) and p_T-differential (b) cross sections of the photoproduced J/ψ in the laboratory frame, from the STARLIGHT generator [350]. The blue curves have been produced without applying kinematics cut, while the red curves are produced by applying cuts on the two daughters of the J/ψ ($2 < \eta_{lab}^{\mu^{\pm}} < 5$ and additional p_T cut on each daughter particles ($p_T(e^{\pm}, \mu^{\pm}) > 0.4$ GeV/c) which correspond to a LHCb-like detector.

unmatched opportunities for such studies. The ALICE central detector used in the fixed-target mode covers extremely backward rapidities in the c.m.s., corresponding to $x \to 1$ in the target.

Moreover, ALICE detector excels in particle identification, and it is capable of measuring identified hadrons (for example $\pi^{\pm}$, $K^{\pm}$, K_S^0 mesons and Λ baryons). Therefore, it can provide high-quality data to determine quark and antiquark densities at $x \to 1$. Specifically, it gives access to the strange quark helicity

(a) pH with 7 TeV proton

(b) PbH with 2.76 TeV Pb
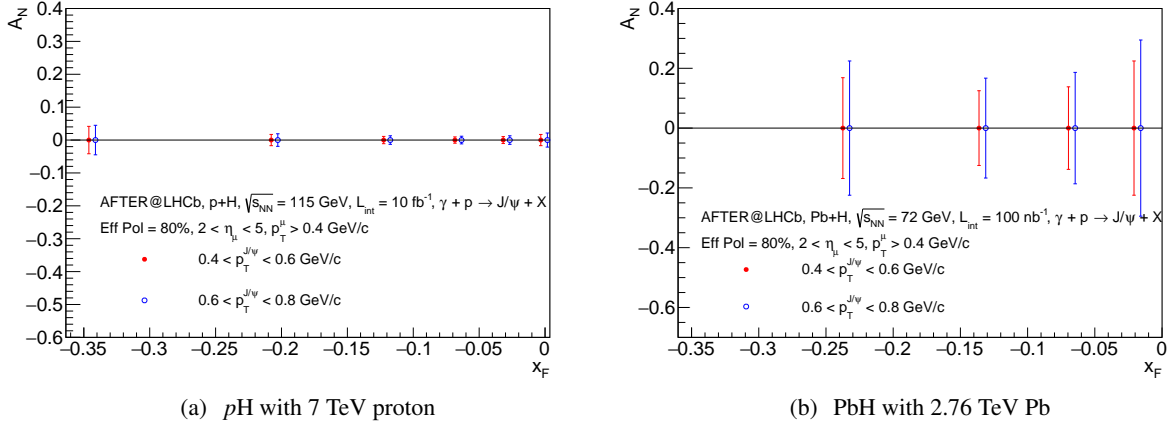
Figure 36: Statistical uncertainty projections for the STSA in exclusive J/ψ photoproduction in UPCs of a proton beam (a) and a lead beam (b) on a hydrogen target.

densities at high x via the measurement of the longitudinal spin transfer D_{LL} from the polarised target to Λ and $\bar{\Lambda}$ hyperons. So far, only limited set of experimental D_{LL} results exist [357, 358], and their precision is far from satisfactory.

The Λ (and $\bar{\Lambda}$) baryons, which contain a strange (anti-strange) quark, are popular tools in studies of spin effects in high-energy collisions because of their self-spin analysing decays in $p\pi^-$ ($\bar{p}\pi^+$). In this decay, a proton is preferably emitted along the spin direction of a parent baryon, which gives easy access to the spin orientation of the latter. We consider the measurement of the longitudinal spin transfer D_{LL} from the polarised target to Λ (and $\bar{\Lambda}$) hyperons, where D_{LL} is defined as is a ratio of the inclusive cross sections with a positive or negative polarisation to the sum of collisions with polarised target:

$$D_{LL} \equiv \frac{\sigma_{pp^+\to\Lambda^+} - \sigma_{pp^+\to\Lambda^-}}{\sigma_{pp^+\to\Lambda^+} + \sigma_{pp^+\to\Lambda^-}}, \tag{24}$$

where + and - signs denote positive or negative polarisation (helicity in this case). Within the perturbative quantum chromodynamics framework, D_{LL} is sensitive to both polarised quark densities and polarised fragmentation functions. However, interpretation of the experimental data depends on the assumed theoretical model. Besides strange quark, the spin transfer from u and d quarks could contribute to measured D_{LL} of Λ; D_{LL} of $\bar{\Lambda}$ provides a cleaner probe of polarised anti-strange quark density.

For the evaluation of the expected statistical precision of D_{LL} measurements, we assumed that one will use a similar technique as in [357]. We estimated the statistical uncertainty on D_{LL} taking $\sigma(D_{LL}) = \frac{1}{\alpha_\Lambda P} \frac{1}{\sqrt{N}}$, where P is an effective target polarisation, $\alpha_\Lambda = 0.642 \pm 0.013$ is the weak decay parameter and N is the overall Λ yield registered in the ALICE detector. The Λ production is simulated with the PYTHIA8 event generator, and our estimation takes into account the geometrical acceptance of ALICE detector for Λ daughters, and the overall Λ reconstruction efficiency [359]. Fig. 37 shows the expected statistical precision of D_{LL} as a function of (a) the transverse momentum and (b) $x^\uparrow$ for the target located in front of the ALICE TPC detector along the beam direction (z_{target} = 4700 cm). The assumed integrated luminosity and target polarisation reflect the expected performance of ALICE TPC detector combined with a polarised hydrogen gas jet target (see section 3.3.2 for details).

With a single year of data taking it will be possible to measure D_{LL} with sub-percent precision for
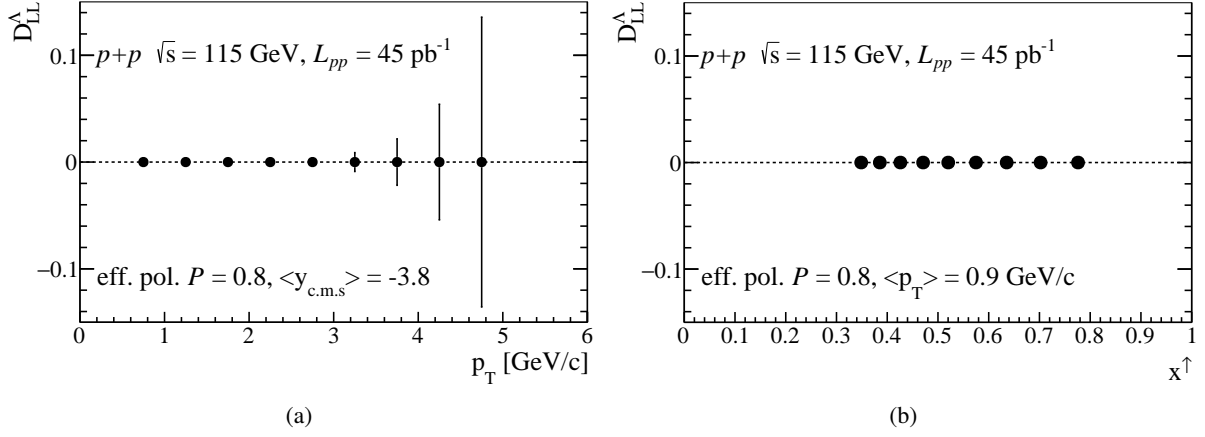
Figure 37: The statistical precision expected for the longitudinal spin transfer D_{LL} to Λ hyperons with the ALICE detector and a target located ahead from the ALICE TPC at z_{target} = 4700 mm. The Λ yields are calculated using the PYTHIA model, taking into account the acceptance of the ALICE TPC detector and a realistic reconstruction efficiency of Λ baryons in the ALICE experiment [359]

$x^\uparrow \to 1$; however, the p_T reach is limited due to fact that the end of the phase space is approached. Therefore, these results could be a challenge for theoretical calculations, given the relevance of perturbative QCD calculations in these predictions. Anyhow, such data give a unique opportunity to study polarised strange and anti-strange quark distributions at $x^\uparrow \to 1$.

As a final remark, we note that similar studies with a LHCb-like detector remain to be explored.

Strange-quark-transversity distribution. The integrated quark transversity, called also as the nucleon tensor charge, is a useful input in the search for new physics beyond the standard model, especially in the context of the electric dipole moment [360, 361] or the neutron beta decay [362]. The quark transversity has recently been extracted through TMD evolution analysis of the Collins azimuthal asymmetries in e^+e^- annihilation and SIDIS processes [363], as well as by a global analysis of *ep* DIS and *pp* collisions [364]. The tensor charges deduced from the above analyses are consistent with each other, but are in conflict with recent lattice QCD results [365, 366, 367, 368]. The extraction of the nucleon tensor charge from experimental data is now under intense debate, and an improvement of the analysis of DIS experimental data considering hadrons in jet final states was recently proposed [369].

Complementary measurements of the transverse spin transfer D_{TT} to hyperons can be carried out at AFTER@LHC programme with a similar precision than that for D_{LL}, discussed above. In such a case, D_{TT} gives access to the transversity distribution of *s* and *s̄* quarks (as well as the transversely-polarised fragmentation functions). These sea-quark distributions will hardly be measurable at any other experimental facility, and thus AFTER@LHC programme will provide a very useful handle to further constrain the nucleon tensor charge.

5.3. Heavy-ion physics

Despite considerable progress achieved in the last three decades at AGS, SPS, RHIC and LHC in understanding the properties of the hadronic matter at extreme conditions [80, 370, 371, 82, 372] produced in high-energy proton-nucleus and nucleus-nucleus collisions, crucial aspects of the resulting system remain obscure. Important open questions regarding the properties of a new phase of matter, assumed to be a Quark Gluon Plasma (QGP), remain to be adressed:

1. the nature of the phase transition between the hadronic matter and the deconfined phase of quark and gluons;

2. the transport properties of this medium, including its specific shear viscosity;

3. the interaction of hard partons with this medium and their energy loss via collisional and radiative processes;

4. the flavour dependence of the energy loss in the hot medium;

5. the thermodynamic properties of this hot medium.

The AFTER@LHC heavy-ion program will take place at the c.m.s. energy of 72 GeV with a 2760 GeV Pb beam. With lighter species the c.m.s. energy is only slightly larger [45]. The Beam Energy Program (BES) at RHIC has shown that in AuAu collisions at $\sqrt{s_{NN}} = 62$ GeV the produced hadrons have a large elliptic flow [373, 374, 375] and jet-quenching effects are observed [376]. These results suggest that quark and gluons are probably deconfined in this energy range, which implies that AFTER@LHC will be capable of studying both the properties of this deconfined medium and the phase transition. The large kinematic coverage of the available detectors together with different colliding systems, and high luminosities, will allow AFTER@LHC to deliver data that can provide definitive answers to aforementioned questions. The purpose of this section is to demonstrate how AFTER@LHC will be able to address them.

5.3.1. *Precise quarkonium studies in a new rapidity and energy domain*

Since more than thirty years, studies of the production of various quarkonium states in heavy-ion collisions have been performed in order to provide insights into the thermodynamic properties of a possible deconfined matter, via the observation of a sequential melting of quarkonia. However, global analyses including SPS, RHIC and LHC data clearly show that such endeavour is much more complex than initially thought [79, 80, 377]. Many facts support this viewpoint: the complexity of both charmonium and bottomonium feed-down combined with the absence of measurements of direct yields; the competition with conventional nuclear effects (see sections 5.1.2 for discussion of one of them, the modification of the PDF in a nucleus), the intrinsic complexity of modelling such a new state of matter and the fate of these bound states when they cross it and finally the smaller cross section of these hard probes compared to light flavoured hadrons.

Indeed, while quarkonium production in *AA* collisions was predicted to be suppressed (relatively to the *pp* case) due to the (Debye-like) screening of the $Q\bar{Q}$ potential in the deconfined medium where the coloured charges are mobile, it is now becoming clear that dynamical effects beyond such a static screening, should be taken into account. These are due to the Landau damping following from the inelastic scatterings of the pair with the constituents of the deconfined medium or to colour rotations of the colour singlet $Q\bar{Q}$ pair leading to its dissociation. Conversely, these colour rotations may also lead to quarkonium regeneration. At high energies, the charmonium production can even be more complex with the possibility of the recombination of uncorrelated charm and anticharm quarks produced in the same collisions.

The bottomonium case seems to provide an easier path to (partially) achieve the goal of using quarkonium sequential suppression as a thermometer. Indeed, the three states are observable[46] in the dimuon channel and $b\bar{b}$ recombination is far less likely. This is even more true in the energy range of AFTER@LHC. This will be the object of the first quarkonium section.

---

[45]For 2890GeV Xe beam, $\sqrt{s_{NN}} = 73.7$ GeV.

[46]Despite the aforementioned caveats related to the oversimplified picture of the thermometer based on the uniqueness of the Debye screening, it is in any case mandatory to measure more than 2 states to calibrate it and then to "measure" a temperature.

In what concerns the charmonium family, in spite of significantly larger cross sections, the situation is much more intricate and unquestionably call for measurements which have never been done. Merely improving the precision of past studies is bound to be insufficient. Indeed, the $\psi(2S)$ state is likely too fragile to fit in any – idealised – thermometer picture. In addition, the access to information about a third state, in this case the χ_c triplet via feed-down, has been shown to be close to impossible since there is no consensus, after 20 years of data, on whether the χ_c suppression is closer to that of the $\psi(2S)$ or of the J/ψ. In this context, AFTER@LHC can play a crucial role by providing completetly novel observations ranging from χ_c suppression measurements to new correlations studies. This will be the object of the second quarkonium section.

Measurements of the 3 $\Upsilon(nS)$ states in pp, pA and AA collisions. In this context, we find useful to start by discussing the unique reach of AFTER@LHC to the $\Upsilon(nS)$ production in *pp*, *pA* and *AA* collisions as a function of the system size (for various colliding systems or vs. collision centrality), p_T and rapidity, in Pb*A* collisions at $\sqrt{s_{NN}}$ = 72 GeV. This lies nearly half way between the SPS and RHIC energy ranges and significantly lower than the only existing studies by CMS at the (collider mode) LHC [378, 379, 380]. Although the relative suppression of the $\Upsilon(nS)$ cannot readily be used as a thermometer it will bring crucial new inputs for our understanding of the nature of the hot medium created in this energy range as opposed to that presently available at the LHC.

(a) (b)

Figure 38: (a) The $\Upsilon(nS)$ signal after the (like-sign) uncorrelated background subtraction with the expected statistical uncertainties in PbXe collisions at $\sqrt{s_{NN}}$ = 72 GeV in $3 < y_{lab} < 5$ for the LHCb-like detector. No nuclear modifications are assumed, $\mathcal{L}_{PbXe}$ = 30 nb^{-1}. (b) statistical uncertainty projections for measurements of the nuclear modification factors R_{PbXe} and $R_{p\mathrm{Xe}}$ [381]. The uncertainties are calculated using yields given in Table 20.

Fig. 38(a) shows the di-muon invariant mass distribution in the $\Upsilon(nS)$ mass range for a single year of data taking with a LHCb-like setup. The expected $\Upsilon(nS)$ yields are clearly large enough with the excellent resolution of LHCb to clearly distinguish each $\Upsilon(nS)$ states in an energy domain where $\Upsilon(nS)$ studies are extremely demanding. The yields together with the signal over background ratios in *pp*, *p*Xe and PbXe collisions are also gathered in Table 20. Projections of the statistical precision of the nuclear modification factors for the $\Upsilon(nS)$ states measured in *p*Xe and PbXe collisions are presented on Fig. 38(b). The statistical uncertainties take into account the background subtraction procedure using the like-sign method. If needed, this can further be improved by using the mixed-event technique. The predictions do not include potential modifications of the $\Upsilon(nS)$ yields due to the nuclear effects.

	(a)			(b)			(c)	
$\Upsilon(1S)$	S	S/B	$\Upsilon(2S)$	S	S/B	$\Upsilon(3S)$	S	S/B
pp	1.33×10^3	29.0	pp	2.92×10^2	8.2	pp	1.37×10^2	10.3
pXe	1.39×10^3	7.8	pXe	3.06×10^2	2.2	pXe	1.44×10^2	2.8
PbXe	4.33×10^3	1.8×10^{-1}	PbXe	9.56×10^2	5.0×10^{-2}	PbXe	4.49×10^2	6.2×10^{-2}

Table 20: $\Upsilon(nS)$ signal yields (S) and signal-over-combinatorial- background ratios (S/B) for pp, pXe and PbXe collisions at $\sqrt{s_{NN}} = 72$ GeV and $3 < y_{Lab.} < 5$ assuming LHCb-like performances [381] with $\int \mathcal{L}_{pp} = 250$ pb^{-1}, $\int \mathcal{L}_{p\text{Xe}} = 2$ pb^{-1} and $\int \mathcal{L}_{\text{PbXe}} = 30$ nb^{-1}.
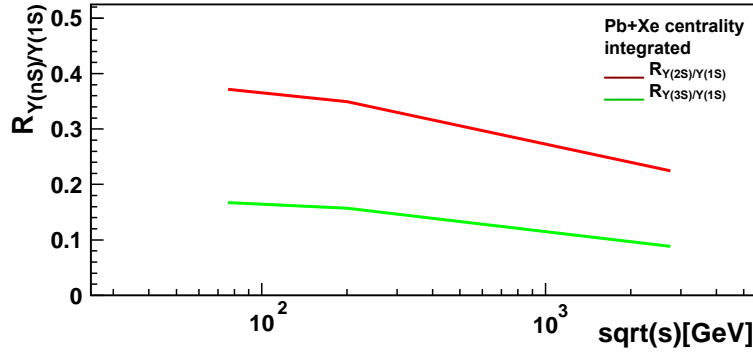
Figure 39: The relative suppression of the excited $\Upsilon(nS)$ states to the $\Upsilon(1S)$ as a function of the energy in iCIM [382].

Fig. 39 shows the expected relative suppression $R_{\Upsilon(nS)/\Upsilon(1S)}$[47] in the improved Comover Interaction Model (iCIM) recently applied to describe the $\Upsilon(nS)$ suppression at the LHC [382]. It can be seen as an effective approach to deal with quarkonium suppression, accounting for the Landau damping – the pair gets broken by a scattering with a gluon – and the colour rotation – a scattering with a gluon turns the pair into a colour-octet state which cannot hadronise any more. Predictions in other approaches are expected to yield similar suppressions. Given the foreseen accuracy of $\Upsilon(nS)$ measurements, the AFTER@LHC program will allow to verify such predictions in a completely new energy domain.

Advanced charmonium studies in heavy-ion collisions. In addition to studies of the $\Upsilon(nS)$ states, the AFTER@LHC program will explore an array of new charmonium observables that are virtually not accessible elsewhere. As compared to the SPS experiments, the higher energies at AFTER@LHC allow for quarkonium-correlation studies. None have been carried so far in pA and AA collisions. The use of a detector like LHCb[48] without absorber enables χ_c studies at backward rapidities where the multiplicities are reduced. As compared to RHIC and LHC experiments, which have to cope with a large combinatorial background, studies of the η_c suppression should be within reach in pA collisions and, possibly, in the most backward part of the acceptance, in semi-central AA collisions. These studies would bear on the natural access toward negative rapidities in the c.m.s. on large luminosities typical of the fixed-target mode and on

---

[47] The relative suppression R is defined as the double ratio of excited Υ states to the $\Upsilon(1S)$ in AA and pp collisions, $R_{\Upsilon(nS)/\Upsilon(1S)} = [\Upsilon(nS)/\Upsilon(1S)]_{AA}/[\Upsilon(nS)/\Upsilon(1S)]_{pp}$ [383, 378].

[48] or maybe the joint usage of the ALICE CB (to detect a photon and a muon) along with the muon arm (to detect the second muon) like in [384].

more modern detectors as compared to those used in the 90's at the SPS and, to a lesser extent, to the ageing RHIC detectors.
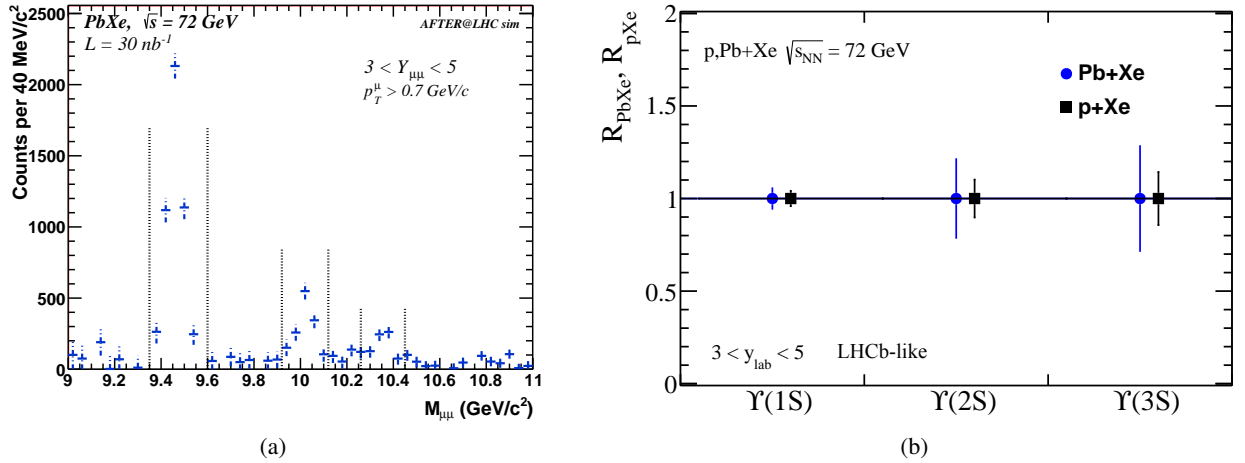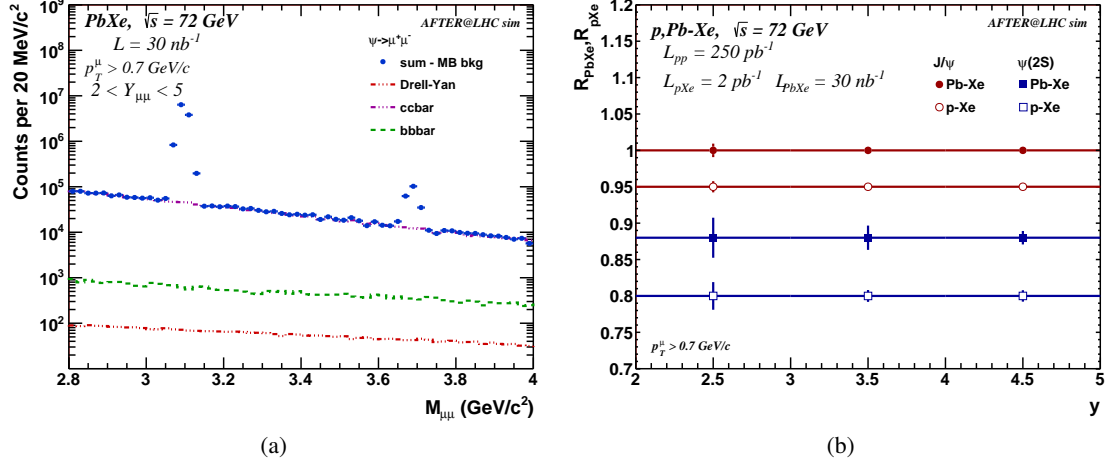

Figure 40: (a) J/ψ and $\psi(2S)$ signal after the (like-sign) uncorrelated-background subtraction with the expected statistical uncertainties for PbXe collisions at $\sqrt{s_{NN}} = 72$ GeV in $2 < y_{c.m.s.} < 5$ for $\int \mathcal{L}_{PbXe} = 30$ nb^{-1}. No nuclear modifications were assumed. (b) Projected statistical precision of the nuclear modification factor as a function of the laboratory rapidity in PbXe (R_{PbXe}) and pXe (R_{pXe}) at $\sqrt{s_{NN}} = 72$ GeV, assuming the uncorrelated background subtraction with the like-sign technique using $\int \mathcal{L}_{pp} = 250$ pb^{-1}, $\int \mathcal{L}_{pXe} = 2$ pb^{-1}, $\int \mathcal{L}_{PbXe} = 30$ nb^{-1} which fits in one month of Pb ion run. Calculations were done for a LHCb-like detector performance. [Figure taken from [381].]

The particularly large pA rates (orders of magnitude larger than those reachable at the collider LHC and RHIC) with a wide rapidity coverage are also crucial to disentangle between the different sources of the charmonium suppression. In that regard, the interpretation of such studies, in an energy range where the charm recombination cannot be relevant [385], will also be much easier. This asset should not be underestimated.

Overall, one expects the measurements of $\psi(2S), \chi_c, J/\psi + J/\psi$ and $J/\psi + D$ productions and correlations to be possible, each of them with enough precision to bring in constraints to the charmonium-suppression puzzle. As an illustration, Fig. 40(a) shows a di-muon invariant mass distribution for PbXe collisions at $\sqrt{s_{NN}} = 72$ GeV in the J/ψ and $\psi(2S)$ mass ranges. It is clear that the background is well under control yielding a very precise determination of the charmonium rates. With such a background for the J/ψ, we find legitimate to highlight the possibility for the aforementioned more demanding studies.

Correspondingly, the statistical projections of the nuclear modification factors in pXe and PbXe collisions as a function of the rapidity presented on Fig. 40(b)[49] allows us to expect a precision at the per cent level for the J/ψ and $\psi(2S)$ cases, depending on the rapidity. Without a doubt, more differential studies as well as elliptic flow v_2 measurements will also be possible. Projections for the other charmonium-like observables remain to be done. However, we anticipate that they should show a precision around the five per cent level, which would be a clear breakthrough in the field since none of them are within the reach of any other experiment at present. Finally, let us stress that the present discussion only bore on a single target, Xe. However, almost independently of the target implementation (see section 3), a few other species could be used – even during a single year. This will allow for systematic studies of the A dependence of the nuclear effects to be complemented with that of the centrality.

---

[49]made with the same assumptions as in the case of $\Upsilon(nS)$ predictions

5.3.2. *Study of the heavy-quark energy-loss mechanism and their interaction with the surrounding nuclear matter*

Heavy quarks (charm and bottom) are unique tools to study and characterise the QGP properties. They are produced in hard-scatterings in the early stage of nuclear collisions and traverse the hot and dense medium loosing their energy. The energy loss and elliptic flow of open heavy flavour hadrons are sensitive to the dynamics of the medium: such measurements could be used to determine the fundamental properties of the QGP, such as the transport coefficients. Precision measurements of elliptic flow of heavy quarks can give insights into degree of thermalisation of the created nuclear matter and can help to discriminate between different models of heavy quark interactions with the QGP [80]. The significant suppression of open heavy flavor production at high p_T and significant elliptic flow of heavy quarks were observed at the top RHIC energy [386, 387, 388, 389]. These experimental data can be described assuming two main effects: medium-induced gluon radiation (radiative energy loss, dE/dx_{rad}) and a collisional energy loss, dE/dx_{coll}, due to binary interactions of partons with other objects in the QGP. A major difficulty in modeling the heavy quark energy loss is that the relative contributions of dE/dx_{coll} and dE/dx_{rad} are still not precisely known [80], and need to be constrained using the experimental data. To better understand the interplay the two processes, precise measurements of suppression of charm and bottom separately are necessary. Figure 41 shows calculations of the nuclear modification factor R_{CP}[50] for D-mesons as a function of p_T in two rapidity ranges for dE/dx_{coll} and dE/dx_{rad}. Since these two mechanisms have a different p_T and rapidity dependence, high quality D^0 data available at AFTER@LHC in PbA collisions at $\sqrt{s_{NN}}$ =72 GeV in different rapidity ranges can help to pin down the dE/dx_{rad} and dE/dx_{coll}.

(a)   (b)
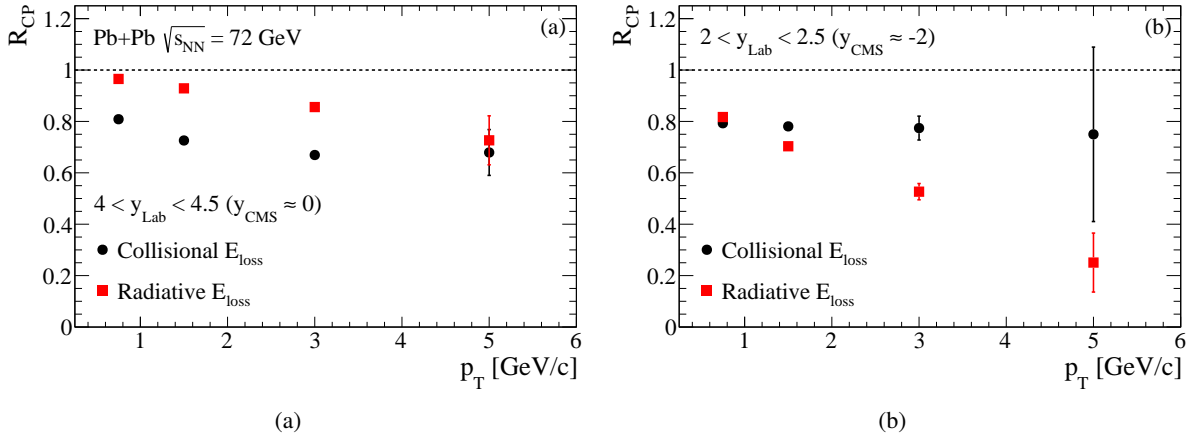
Figure 41: Expected statistical uncertainties of nuclear modification factor R_{CP} for D^0 meson measured by LHCb-like detector in PbPb collisions at $\sqrt{s_{NN}}$ =72 GeV for $\int \mathcal{L}_{\mathrm{PbPb}} = 7$ nb^{-1} [Taken from [287]].

With high statistics data accessible with AFTER@LHC, heavy flavour azimuthal correlations ($D - D$, $J/\psi - D$) and heavy flavour jets can also be studied to further understand the heavy quark in-medium interactions. Simultaneous precise measurements of the D-meson elliptic flow and the nuclear modification factor will allow precise determination of the QGP transport properties, including $\hat{q}$ (which characterises the (squared) momentum transfer per mean free path of the fast parton) and charm quark diffusion coefficients.

---

[50]R_{CP} - central-to-peripheral ratio - ratio of yields in central and peripheral events, normalised by respective numbers of binary collisions.

Moreover, correlation measurements of heavy-flavour pairs provide new means to disentangle collisional from radiative interactions and to test Langevin against Boltzmann transport approaches [390]. In general, the temperature and mass dependence of the transport coefficients can be extracted with precise R_{AA} and v_2 measurements for B and D at various beam energies. AFTER@LHC will extend such a study towards the low energy domain.

Furthermore, the study of D mesons is a natural continuation of the study of J/ψ and $\psi(2S)$ formation and dissociation. Precise measurements of the D meson yields in pA and AA collisions are necessary to constrain the initial-state cold nuclear matter effects, that is the modification of the $c\bar{c}$ production due to shadowing/anti-shadowing. In that sense, D mesons help to established a baseline to understand how the QGP affects the quarkonium production. Finally, nuclear effects on bottom quark production can be also studied via $B \rightarrow J/\psi$ in pA collisions with a good precision [287].

5.3.3. Soft probes at large rapidities – a precise tool to study the bulk properties of the nuclear matter

One of the unique assets of the AFTER@LHC project is a large rapidity coverage. The combined acceptance of the LHCb detector and the central barrel of the ALICE experiment covers the range of $-5.2 \lesssim y^{c.m.s.} \lesssim 0.7$ in the case the 2.76 TeV Pb beam - such a wide kinematic acceptance is not available in the collider experiments. The two detectors offer also excellent particle identification abilities, which altogether provides a large lever arm for studies related to the longitudinal expansion of the nuclear matter in heavy-ion collisions. In contrast, most of the heavy-ion experiments were designed to study the transverse dynamics of such a system at mid-rapidity, thus the longitudinal evolution is hardly accessible there.

The longitudinal dynamics of a system created in nuclear collisions is a topic of intensive experimental [391, 392, 393] and theoretical [394, 395, 396, 397] studies via azimuthal flow, flow correlations and decorrelation measurements. The two- and multi-particle pseudorapidity correlations allow for an examination of the long-range collective phenomena, e.g. the ridge, as well as the initial state fluctuations. The studies of the flow (de)correlation vs. rapidity offer an independent test of theoretical calculations that assume collective dynamics (collective flow). Most of them involve the hydrodynamic phase of the system evolution. Since the flow decorrelation effect increases with the decreasing c.m.s. energy [398], and thanks to its large rapidity coverage, AFTER@LHC will provide an excellent setting for such an analysis. Moreover, a measurement of directed flow v_1 of charmed mesons as a function of rapidity was proposed recently to map out the three-dimensional distribution of the nuclear matter produced in heavy-ion collisions [399]. The large D-meson yields expected in AFTER@LHC will facilitate such a study with an unparalleled precision. In the following paragraphs, we discuss a few examples of other studies involving the "soft" (low p_T) probes that are pivotal for understanding the QGP properties and the QCD phase diagram.

Determination of the temperature dependence of the shear viscosity to entropy density ratio η/s. The shear viscosity η (or a ratio to the viscosity to the entropy s, η/s), is one of the most fundamental properties of the the quark-gluon plasma. Yet our understanding of η/s is far from satisfactory. The η/s cannot be measured directly: it must be derived from a comparison of the experimental data and theoretical calculations (for example hydrodynamic models). After decades of development, these models reached a high predictive power for the QGP macroscopic behaviour at RHIC and LHC energies. Until recently, such calculations focused on the transverse dynamic of the QGP, at the mid-rapidity. Intense efforts have been made to include the medium longitudinal expansion in hydrodynamic models (for example [394]). These calculations indicate that particle yields and the azimuthal anisotropy coefficients v_n measured at large rapidities are powerful tools to study the medium η/s and its temperature dependence (see Fig. 5) [76].

The AFTER@LHC program is well suited for these new frontiers of the QGP hydrodynamic studies, providing a large rapidity coverage to measure several particle azimuthal asymmetries and the possibility to
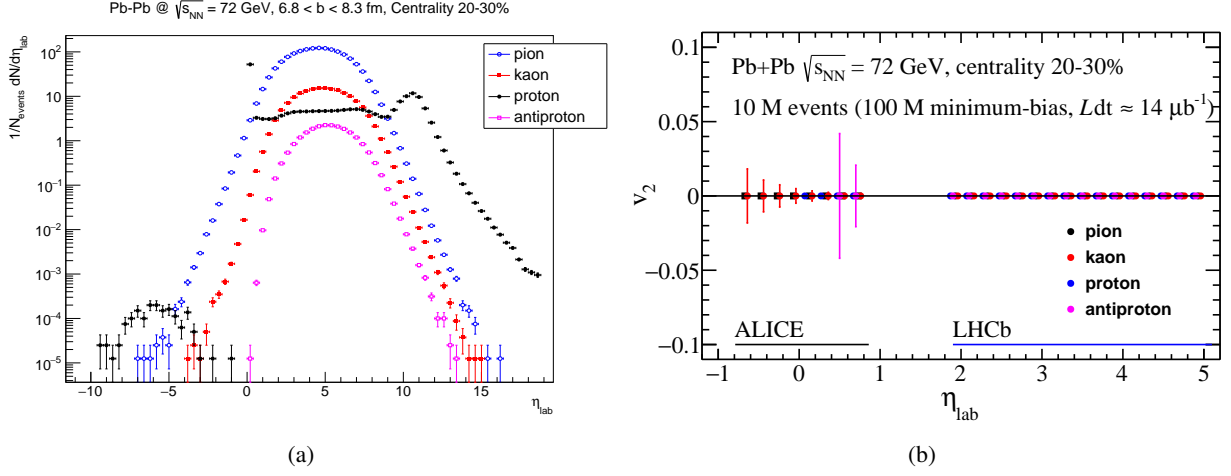
Figure 42: (a) Identified particle yields in mid-central PbPb collisions at $\sqrt{s}$ = 72 GeV and centrality 20-30% from EPOS [97, 132]. (b) Projections for the statistical uncertainty on the measurements of the p_T-integrated (p_T > 0.2 GeV/c for a ALICE-like setup and p_T > 0.5 GeV/c for a LHCb-like detector) elliptic flow of identified hadrons as a function of the pseudorapidity in the laboratory.

obtain large statistics for different targets. Fig. 42(a) shows the particle yields as a function of pseudorapidity (η_{lab}) in mid-central (20-30%) PbPb collisions at $\sqrt{s}$ = 72 GeV obtained using the EPOS model. The expected statistical uncertainties on the elliptic flow (v_2) measurement for identified hadrons with 10 million 20-30% central PbPb events (100 million minimum-bias events) are presented in Fig. 42(b). Even this small data sample, corresponding to an integrated luminosity of 14 μb^{-1}, will allow for a precision study of v_n over a very broad rapidity range. Such high-quality data will facilitate an accurate determination of the temperature dependence of the shear viscosity to entropy ratio, η/s.

We believe that the AFTER@LHC program is essential to acquire full knowledge of the QGP macroscopic properties. This program will complement and continue the existing studies of v_n with high precision thus providing a detailed account of the system evolution (including transverse and longitudinal dynamics) between SPS and the top RHIC energy. Thus, AFTER@LHC will be a perfect place to study collective effects in the system produced in pA to PbA collisions. It will provide high precision studies of the QCD matter, complementary to the ones performed at the RHIC BES program.

The rapidity scan: a new tool to study the QCD phase diagram. Thermal model calculations indicate that the baryonic chemical potential μ_B and the temperature T depend on the rapidity [74]. The recent calculations by the Hadron Resonance Gas (HRG) model [75] and a viscous hydro+cascade model vH-LLE+UrQMD [73] show that in PbPb collisions at AFTER@LHC the μ_B varies strongly with the rapidity: 0 < μ_B < 250 MeV (as vHLLE+UrQMD predicts, see Fig. 4(b)) or even 80 < μ_B < 400 MeV (given by the HRG model, Fig. 43(b)). These μ_B values cover a large fraction of the μ_B range accessible at the RHIC BES program [400, 401], which illustrates Fig. 43(a). The μ_B vs. y dependence suggests that one can perform a "rapidity scan" of the QCD diagram [402, 75], complementary to the BES programs at RHIC and SPS. Measurements of correlations and fluctuations of the conserved quantities (electric charge, baryon and strangeness number etc.) in small rapidity windows could provide a new approach to search for the QCD critical point and possible evidence of the first-order phase transition. However, interpretation of such a data could be a challenge since the origin of the μ_B vs. rapidity dependence is an open question. For example, it might be an effect a superposition of different rapidity spectra of particles produced in a single, homogeneous, fireball; or a product of small subdomains with different μ_B and T values, moving with dif-

ferent longitudinal velocities. The latter would indeed facilitate the phase diagram studies by varying the particle rapidity. Nevertheless, the large rapidity coverage of the AFTER@LHC project, combined with an excellent particle identification capabilities of the ALICE and the LHCb detectors, makes it a perfect place for such a rapidity scan of QCD phase diagram.
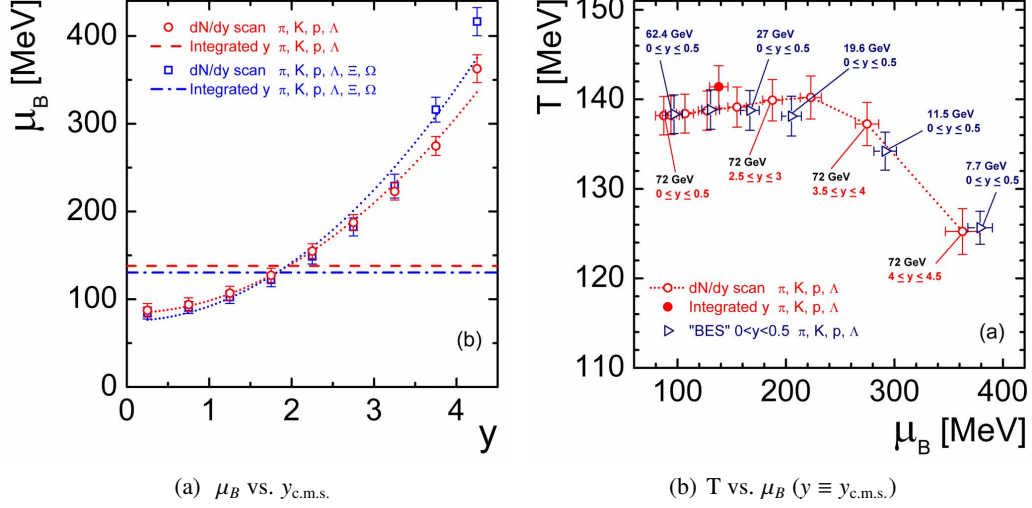
Figure 43: The baryonic chemical potential μ_B (a) and (b) the temperature T in 0-10% most central PbPb collisions at $\sqrt{s_{NN}}$ = 72 GeV from the Hadron Resonance Gas model calculations [75]. The two series of results represent calculations that uses two sets of particle densities as the input (with or without the Ξ and Ω baryons). The uncertainties on the points follows from the assumed relative uncertainties of 10% on the particle yields measured in AFTER@LHC.

5.3.4. *Looking for collectivity in small systems in a new energy domain*

One of the recently most discussed topics in the heavy ion community is the evidence for the collective motion observed in small systems such as *d*Au, *pA* and even in *pp* collisions, and possible formation of Quark-Gluon Plasma droplets in those reactions. Experiments at RHIC and LHC reported collective behaviour of light hadrons in high multiplicity *d*Au [403] and *p*Pb collisions [404]. The v_n are comparable to the ones observed in AuAu and PbPb collisions for the similar multiplicity events. Moreover, recent measurements show that there is a significant positive elliptic flow of heavy-flavour particles and strange baryons in the *pA* at the LHC [405], although its magnitude is lower than the v_2 of light hadrons. There are also hints of non-zero v_2 of heavy quarks in *d*Au collisions at $\sqrt{s_{NN}}$ = 200 GeV at RHIC. These observations are in line with speculations that an enhancement of the heavy-flavour decay electron production in central and minimum bias *d*Au collisions at mid-rapidity at RHIC [406] could indicate a collective phenomenon (radial flow) of heavy quarks [407]. However, the cold nuclear matter effects (in particular the Cronin effect) could be responsible for that enhancement, too.

In addition, other intriguing phenomena were observed in a high-multiplicity *pp* collisions. The production of multi-strange hadrons in such proton-proton collisions is enhanced [408], on the level remarkably similar to the results seen in PbPb collisions. Moreover, heavy flavour particles yields (both the open heavy flavour and charmonium) increase fast with the number of charged particles produced in a *pp* collisions [409, 410, 411]. A few different models are able to qualitatively reproduce such a behaviour, for example the string percolation approach [412], or EPOS [413]. While these calculations significantly differ, they all assume some sort of collective interactions on the parton level.

Currently, two possible origins of the aforementioned phenomena are considered: a QGP formation in small systems, or a common collective motion coming from initial conditions in small and large collision systems. It is an intriguing question which scenario dominates, and AFTER@LHC is in the optimal position to address it. The luminosity available in the AFTER@LHC is orders of magnitude larger than that at RHIC, thus the differential measurement of D-mesons and J/ψ production azimuthal asymmetries v_n will be possible in pp and pA collisions. The precision studies as a function of rapidity, transverse momentum and event multiplicity will shed new light on the problem at hand. As an example, Fig. 44 shows a statistical precision of the measurement of the elliptic flow v_2 of D^0 in pPb collisions in AFTER@LHC in two rapidity ranges. Together with the nuclear modification factor R_{pPb} measurements, these data will provide means to precisely determine a possible collective behaviour of heavy quarks and quantify the cold nuclear matter effects. Moreover, high luminosity data samples available at AFTER@LHC will allow v_n to be measured for identified hadrons with multi-particle correlations methods over a wide rapidity range, which gives an indispensable handle on the collective effects in small systems

While the jury is out on the source of the collective behaviour observed in the small systems (e.g. collective effects on the partonic level, the initial geometry, proton fluctuations), AFTER@LHC offers an unprecedented opportunity to study these effects with multiple probes and over a broad kinematic range.
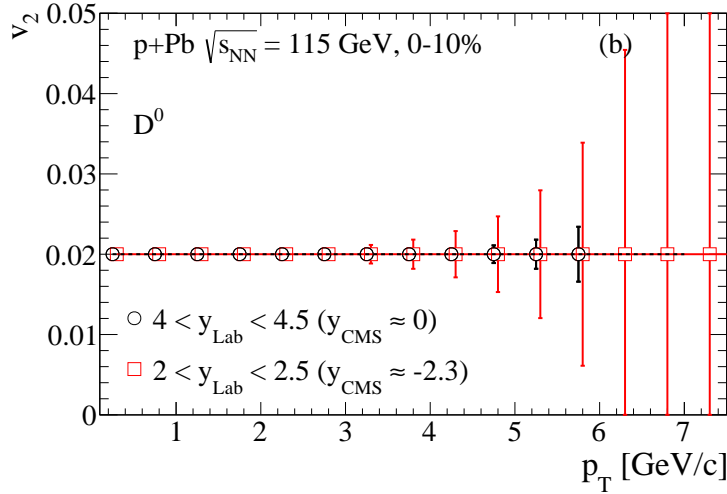
Figure 44: Expected statistical uncertainties of D^0 elliptic flow in pPb collisions at $\sqrt{s_{NN}}$ =115 GeV at mid-rapidity and backward rapidity measured with a LHCb-like detector for $\int \mathcal{L}_{pPb}$ = 160 pb^{-1}. Calculations include the acceptance and reconstruction efficiency of a LHCb-like detector. The results indicate that v_2 will be measured with sub-percent precision over a broad p_T and rapidity range. [Taken from [287]].

5.3.5. *Test of the factorisation of the initial-state effects in AA collisions with Drell-Yan pair production*

Initial state effects observed in pA collisions are currently extrapolated to AA collisions assuming that the effects factorise linearly, that is, that the effects associated to initial state sources are independent in each nucleon-nucleon binary collision. This naïve assumption can be tested using electromagnetic probes: high-p_T isolated photons (inverse Compton process), Drell-Yan, W and Z bosons. These probes are produced from initial state partons and do not interact with the nuclear medium. The nuclear modifications observed for isolated photons, W and Z bosons measured by CMS at mid-rapidity [414, 415, 416] are smaller than ~20% in PbPb collisions. These results rule out a scenario of large production suppression due to initial state effects in heavy ion collisions. However, they cannot test whether processes observed in pA collisions
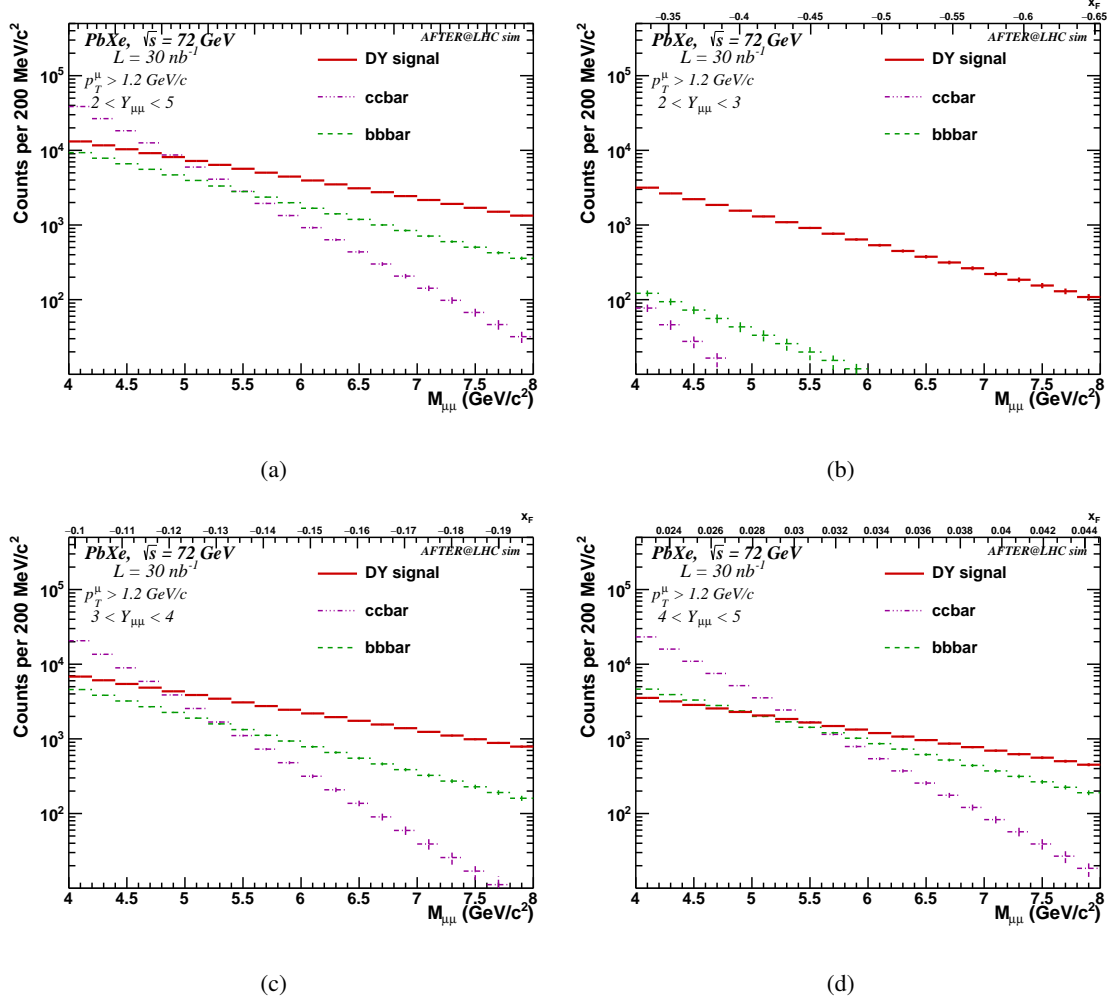
Figure 45: Di-muon invariant-mass distributions ($4 < M_{\mu^+\mu^-} < 8$ GeV/c^2) from Drell-Yan, $c\bar{c}$ and $b\bar{b}$ productions registered with a LHCb-like detector, for PbXe collisions at $\sqrt{s_{NN}} = 72$ GeV with $\int \mathcal{L}_{\text{PbXe}} = 30$ nb^{-1}, assuming $R_{AA} = 1$, in the integrated rapidity range of $2 < y_{\text{lab}} < 5$ (a) and divided into the following ranges: $2 < y_{\text{Lab.}} < 3$ (b), $3 < y_{\text{Lab.}} < 4$ (c) and $4 < y_{\text{Lab.}} < 5$ (d). For (b-d), the upper x-axis represents the corresponding x_F values in a given rapidity range and invariant-mass bin. The combinatorial background is not presented and systematic uncertainties resulting from the background subtraction with with the event-mixing technique are not included.

are magnified in *AA* collisions given the small nuclear modifications observed in *pA* collisions to start with. Theoretical work such as performed in [417] indicates a strong initial state effect boosting in *AA* collisions. A conclusive experimental test on the increase of initial state effects from *pA* to *AA* collisions needs to be performed in a broad Bjorken-x range where significant nuclear modifications are expected in *pA* collisions (See the *pA* physics section, Sec. 5.1.2).

The physics program of AFTER@LHC includes the precise measurements of the Drell-Yan processes which can probe initial state effects on quarks in several *AA* collision species. The greatest challenge in the Drell-Yan measurements in colliders is the large correlated background from $b+\bar{b} \rightarrow B^+ + B^- \rightarrow l^+ l^-$ and $c+\bar{c} \rightarrow D^+ + D^- \rightarrow l^+ l^-$. This background is much smaller at the AFTER@LHC center of mass energy in Pb*A* collisions. Large combinatorial background typically expected in Pb*A* collisions can be precisely
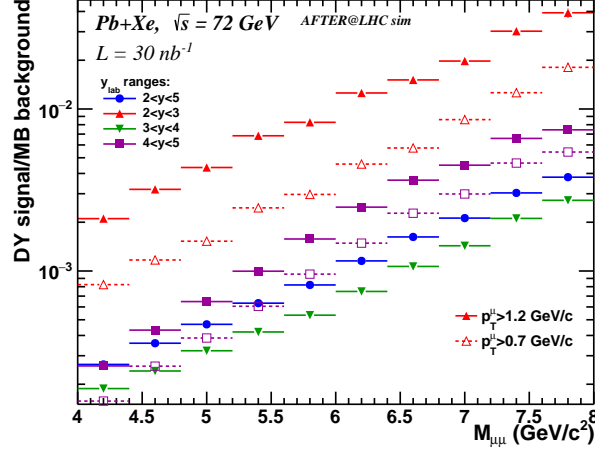
Figure 46: Drell-Yan signal-over-combinatorial-background ratio for a LHCb-like detector as a function of the di-muon invariant mass, for PbXe collisions at $\sqrt{s_{NN}}$ = 72 GeV with $\int \mathcal{L}_{PbXe}$ = 30 nb^{-1} and for $2 < y_{lab} < 5$, $2 < y_{lab} < 3$, $3 < y_{lab} < 4$ and $4 < y_{lab} < 5$. The solid lines represent the S/B with the default Drell-Yan single-muon cut of $p_T^\mu > 1.2$ GeV/c, and dashed lines represent the S/B with $p_T^\mu > 0.7$ GeV/c. No nuclear modifications assumed.

Drell-Yan, Pb-Xe at $\sqrt{s_{NN}}$ = 72 GeV

	M: 4-5 GeV/c^2			M: 5-6 GeV/c^2		
	signal ($\times 10^3$)	bkg. ($\times 10^6$)	S/B ($\times 10^{-3}$)	signal	bkg.	S/B
y_{lab}: 2-3	11.48	4.38	2.6	4.77	0.76	6.3
y_{lab}: 3-4	26.85	121.90	0.2	15.58	36.6	0.4
y_{lab}: 4-5	15.33	45.08	0.3	8.28	8.05	1.0
	M: 6-7 GeV/c^2			M: 7-8 GeV/c^2		
	signal	bkg.	S/B	signal	bkg.	S/B
y_{lab}: 2-3	1.92	0.14	13.9	0.82	0.03	28.1
y_{lab}: 3-4	8.80	9.68	0.9	5.11	2.42	2.1
y_{lab}: 4-5	5.09	1.68	3.0	2.78	0.44	6.3

Table 21: Drell-Yan yields ($\times 10^3$), uncorrelated background yields ($\times 10^6$) and Drell-Yan over the uncorrelated backgroud ratios ($\times 10^{-3}$) for Pb-Xe collisions at $\sqrt{s_{NN}}$ = 72 GeV in 4 di-muon invariant mass ranges between 4 and 8 GeV/c^2 and three rapidity ranges between 2 and 5, with single μ $p_T > 1.2$ GeV/c. Results for LHCb-like performance and $\mathcal{L}_{PbXe}$ = 30 nb^{-1}.

determined with the mixed-event technique and large amount of like-sign di-leptons to reduce uncertainties in the combinatorial background normalisation. Figure 45 shows the invariant mass distributions of the di-muon pairs in different rapidity intervals, and Fig. 46 demonstrates the signal-to-background ratios in PbXe collisions $\sqrt{s_{NN}}$ = 72 GeV. Table 21 shows the Drell-Yan signal and background yields and signal-to-background (S/B) ratios in those reactions. Overall, the background is significant in the low mass range (M: 4-5 GeV/c^2), but it will be suppressed by imposing a stringent cut on the muon transverse momentum. Figure 46 indicates, that the S/B increases significantly when a single muon cut of $p_T^\mu > 1.2$ GeV/c is applied, compared to the $p_T^\mu > 0.7$ GeV/c case. Nonetheless, while the measurement could be challenging in some kinematic ranges, the expected yields will allow for a definitive test of factorisation of initial state

effects from *pA* to *AA* collisions.

6. Conclusions

Unlike the Fermilab-Tevatron and DESY-HERA colliders (with proton beams in the TeV range), no fixed-target program was planned for the LHC. In this review, we have put forward a strong physics case for such a program both for the multi-TeV proton and ion LHC beams. Such a physics case relies on extensive theory work and projection studies which have been performed with LHCb and ALICE-like detectors which allow for unprecedented precision studies in the backward hemisphere of *pp*, *pA* and *AA* collisions.

These projections cover the 3 main research axes of the physics case, namely that of the nucleon and nucleus structure at high momentum fractions, that of the nucleon-spin decomposition in terms of the partonic degrees of freedom and that of the properties of the nuclear matter at extreme conditions such as those resulting from ultra-relativistic heavy-ion collisions.

They are relevant for different possible implementations which we have reviewed including the state-of-the-art solutions provided by modern polarised gas targets or the beam splitting with a bent crystal. For each of the possible implementations, we have also detailed the expected luminosities compatible with the LHCb and ALICE detector capabilities. For a number of studies where such projections are not yet available, we have collected the existing theory predictions for *e.g.* cross sections, spin and azimuthal asymmetries or nuclear modification factors.

Overall, we believe that the present review constitutes a very solid basis for the elaboration of a rich and fruitful LHC fixed-target program starting as early as 2020.

7. Appendices

7.1. Schematic view of the H-jet system used at the BNL-RHIC collider
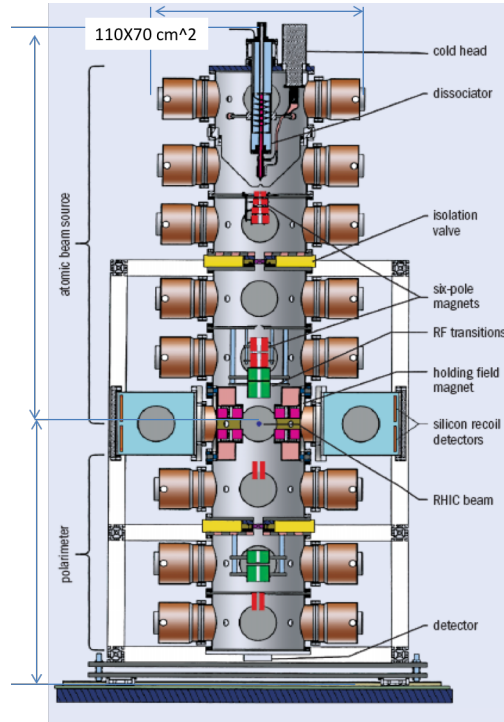
Figure 47: Schematic view of the H-jet system used at BNL-RHIC collider.

7.2. Possible setup of the beam-splitted option upstream of LHCb
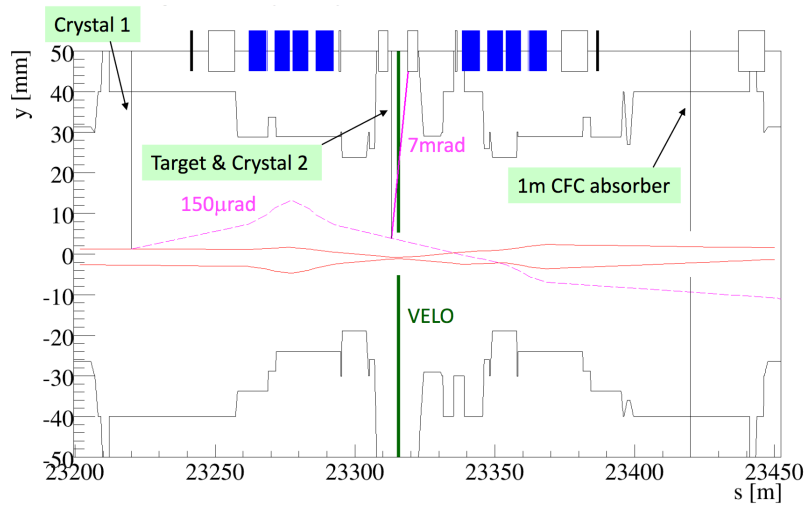
Figure 48: Possible setup of the beam-splitted option upstream of LHC [From [418]]

84

7.3. Schematic view of the E1039 target
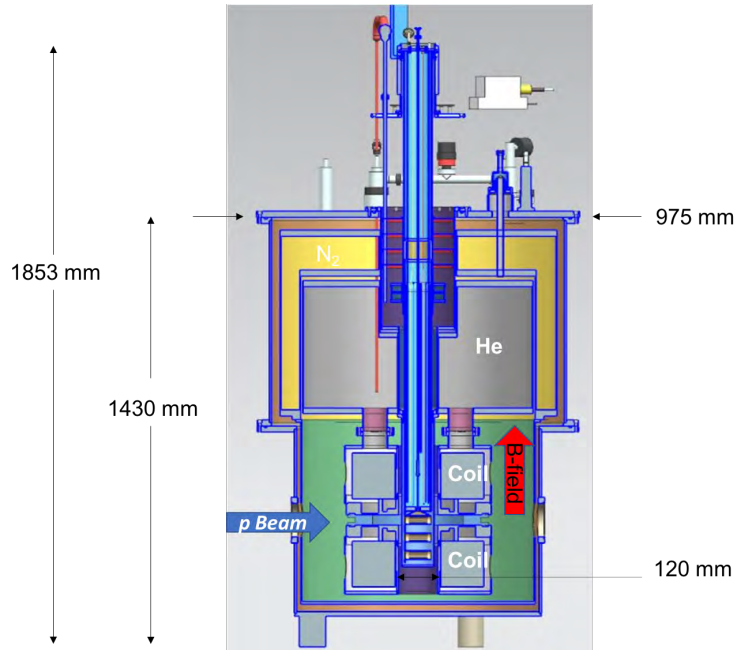
Figure 49: Schematic view of the E1039 target.

7.4. Schematic view of the COMPASS target
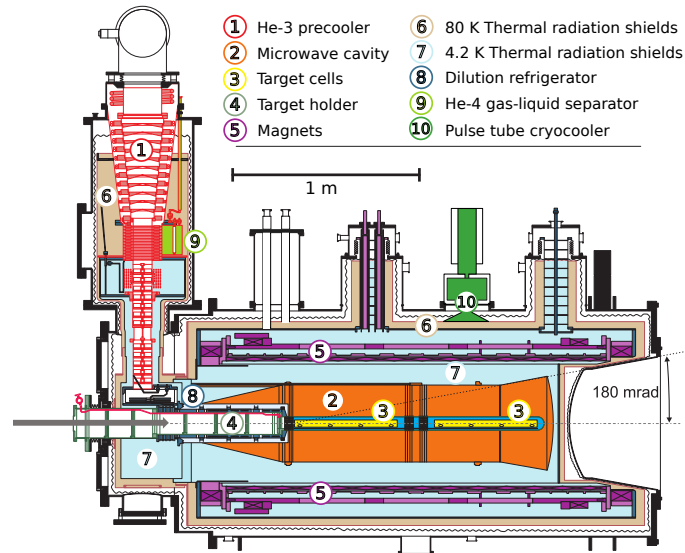
Figure 50: Schematic side view of the COMPASS target. We would like to highlight the two sets of 55 cm long target cells (denoted (3)) and the 2.5T solenoid and 0.6T dipole magnets (denoted (5)). The direction of the beam is represented by the grey arrow.

7.5. Schematic view of the ALICE detector
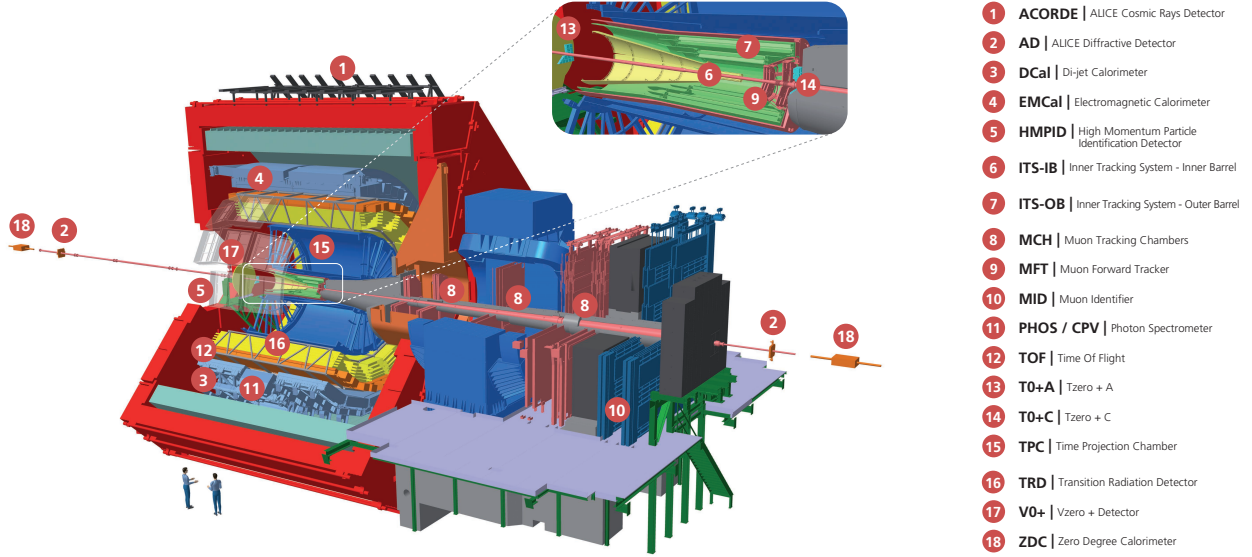
Figure 51: Schematic view of the ALICE detectors for the LHC Run 3, after the upgrades. Figure courtesy of CERN.

7.6. Schematic view of the LHCb detector
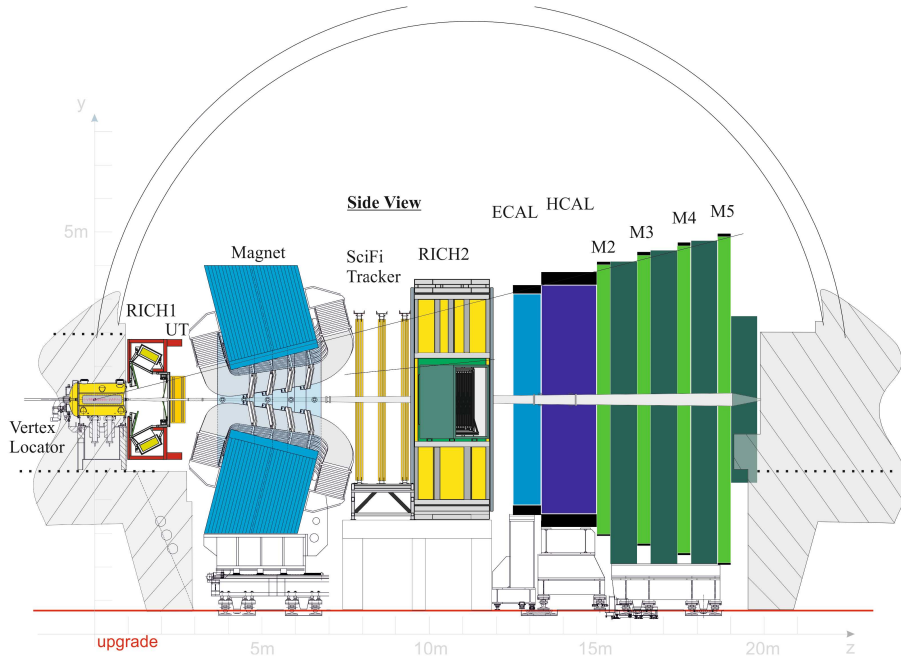
Figure 52: Schematic view of the LHCb detectors for the LHC Run3. The main subsystems include the Vertex Locator, the Silicon Micro-strip Upstream Tracker (UT), the Scintillating Fiber (SciFi) Tracker, the Muon Chambers (M2 - M5), the Hadron Calorimeter (HCAL), the Electromagnetic Calorimeter (ECAL) and the RICH detectors. Figure courtesy of CERN.

References

[1] S. J. Brodsky, F. Fleuret, C. Hadjidakis, and J. P. Lansberg, "Physics Opportunities of a Fixed-Target Experiment using the LHC Beams," *Phys. Rept.* **522** (2013) 239–255, `arXiv:1202.6585 [hep-ph]`.

[2] **European Muon** Collaboration, J. J. Aubert *et al.*, "The ratio of the nucleon structure functions F_2^N for iron and deuterium," *Phys. Lett.* **B123** (1983) 275–278.

[3] V. Bertone, S. Carrazza, and J. Rojo, "APFEL: A PDF Evolution Library with QED corrections," *Comput. Phys. Commun.* **185** (2014) 1647–1668, `arXiv:1310.1394 [hep-ph]`.

[4] K. J. Eskola, P. Paakkinen, H. Paukkunen, and C. A. Salgado, "EPPS16: Nuclear parton distributions with LHC data," *Eur. Phys. J.* **C77** no. 3, (2017) 163, `arXiv:1612.05741 [hep-ph]`.

[5] K. Kovarik *et al.*, "nCTEQ15 - Global analysis of nuclear parton distributions with uncertainties in the CTEQ framework," *Phys. Rev.* **D93** no. 8, (2016) 085037, `arXiv:1509.00792 [hep-ph]`.

[6] D. de Florian, R. Sassot, P. Zurita, and M. Stratmann, "Global Analysis of Nuclear Parton Distributions," *Phys. Rev.* **D85** (2012) 074028, `arXiv:1112.6324 [hep-ph]`.

[7] M. Hirai, S. Kumano, and T. H. Nagai, "Determination of nuclear parton distribution functions and their uncertainties in next-to-leading order," *Phys. Rev.* **C76** (2007) 065207, `arXiv:0709.3038 [hep-ph]`.

[8] L. B. Weinstein, E. Piasetzky, D. W. Higinbotham, J. Gomez, O. Hen, and R. Shneor, "Short Range Correlations and the EMC Effect," *Phys. Rev. Lett.* **106** (2011) 052301, `arXiv:1009.5666 [hep-ph]`.

[9] S. J. Brodsky, K. Y.-J. Chiu, J.-P. Lansberg, and N. Yamanaka, "The gluon and charm content of the deuteron," `arXiv:1805.03173 [hep-ph]`.

[10] E. Leader and C. Lorce, "The angular momentum controversy: What's it all about and does it matter?," *Phys. Rept.* **541** (2014) 163–248, `arXiv:1309.4235 [hep-ph]`.

[11] M. Wakamatsu, "Is gauge-invariant complete decomposition of the nucleon spin possible?," *Int. J. Mod. Phys.* **A29** (2014) 1430012, `arXiv:1402.4193 [hep-ph]`.

[12] M. Wakamatsu, "Unravelling the physical meaning of the Jaffe-Manohar decomposition of the nucleon spin," `arXiv:1607.04018 [hep-ph]`.

[13] M. Burkardt, C. A. Miller, and W. D. Nowak, "Spin-polarized high-energy scattering of charged leptons on nucleons," *Rept. Prog. Phys.* **73** (2010) 016201, `arXiv:0812.2208 [hep-ph]`.

[14] **European Muon** Collaboration, J. Ashman *et al.*, "A Measurement of the Spin Asymmetry and Determination of the Structure Function g(1) in Deep Inelastic Muon-Proton Scattering," *Phys. Lett.* **B206** (1988) 364.

[15] D. de Florian, R. Sassot, M. Stratmann, and W. Vogelsang, "Global Analysis of Helicity Parton Densities and Their Uncertainties," *Phys. Rev. Lett.* **101** (2008) 072001, `arXiv:0804.0422 [hep-ph]`.

[16] **STAR** Collaboration, L. Adamczyk *et al.*, "Precision Measurement of the Longitudinal Double-spin Asymmetry for Inclusive Jet Production in Polarized Proton Collisions at $\sqrt{s} = 200$ GeV," *Phys. Rev. Lett.* **115** no. 9, (2015) 092002, `arXiv:1405.5134 [hep-ex]`.

[17] D. de Florian, R. Sassot, M. Stratmann, and W. Vogelsang, "Evidence for polarization of gluons in the proton," *Phys. Rev. Lett.* **113** no. 1, (2014) 012001, `arXiv:1404.4293 [hep-ph]`.

[18] U. D'Alesio and F. Murgia, "Azimuthal and Single Spin Asymmetries in Hard Scattering Processes," *Prog. Part. Nucl. Phys.* **61** (2008) 394–454, `arXiv:0712.4328 [hep-ph]`.

[19] V. Barone, F. Bradamante, and A. Martin, "Transverse-spin and transverse-momentum effects in high-energy processes," *Prog. Part. Nucl. Phys.* **65** (2010) 267–333, `arXiv:1011.0909 [hep-ph]`.

[20] **FNAL-E704** Collaboration, D. L. Adams *et al.*, "Analyzing power in inclusive π^+ and π^- production at high x_F with a 200-GeV polarized proton beam," *Phys. Lett.* **B264** (1991) 462–466.

[21] **BRAHMS** Collaboration, I. Arsene *et al.*, "Single Transverse Spin Asymmetries of Identified Charged Hadrons in Polarized p+p Collisions at $\sqrt{s} = 62.4$ GeV," *Phys. Rev. Lett.* **101** (2008) 042001, `arXiv:0801.1078 [nucl-ex]`.

[22] **STAR** Collaboration, B. I. Abelev *et al.*, "Forward Neutral Pion Transverse Single Spin Asymmetries in p+p Collisions at $\sqrt{s} = 200$ GeV," *Phys. Rev. Lett.* **101** (2008) 222001, `arXiv:0801.2990 [hep-ex]`.

[23] **HERMES** Collaboration, A. Airapetian *et al.*, "Single-spin asymmetries in semi-inclusive deep-inelastic scattering on a transversely polarized hydrogen target," *Phys. Rev. Lett.* **94** (2005) 012002, `arXiv:hep-ex/0408013 [hep-ex]`.

[24] **COMPASS** Collaboration, V. Yu. Alexakhin *et al.*, "First measurement of the transverse spin asymmetries of the deuteron in semi-inclusive deep inelastic scattering," *Phys. Rev. Lett.* **94** (2005) 202002, `arXiv:hep-ex/0503002 [hep-ex]`.

[25] **PHENIX** Collaboration, A. Adare *et al.*, "Measurement of Transverse Single-Spin Asymmetries for J/ψ Production in Polarized $p + p$ Collisions at $\sqrt{s} = 200$ GeV," *Phys. Rev.* **D82** (2010) 112008, `arXiv:1009.4864 [hep-ex]`. [Erratum: Phys. Rev.D86,099904(2012)].

[26] S. J. Brodsky, D. S. Hwang, and I. Schmidt, "Initial state interactions and single spin asymmetries in Drell-Yan processes," *Nucl. Phys.* **B642** (2002) 344–356, `arXiv:hep-ph/0206259 [hep-ph]`.

[27] J. C. Collins, "Leading twist single transverse-spin asymmetries: Drell-Yan and deep inelastic scattering," *Phys. Lett.* **B536** (2002) 43–48, `arXiv:hep-ph/0204004 [hep-ph]`.

[28] S. J. Brodsky, D. S. Hwang, and I. Schmidt, "Final state interactions and single spin asymmetries in semiinclusive deep inelastic scattering," *Phys. Lett.* **B530** (2002) 99–107, `arXiv:hep-ph/0201296 [hep-ph]`.

[29] Y. Koike, W. Vogelsang, and F. Yuan, "On the Relation Between Mechanisms for Single-Transverse-Spin Asymmetries," *Phys. Lett.* **B659** (2008) 878–884, `arXiv:0711.0636 [hep-ph]`.

[30] A. V. Efremov and O. V. Teryaev, "On Spin Effects in Quantum Chromodynamics," *Sov. J. Nucl. Phys.* **36** (1982) 140. [Yad. Fiz.36,242(1982)].

[31] A. V. Efremov and O. V. Teryaev, "QCD Asymmetry and Polarized Hadron Structure Functions," *Phys. Lett.* **B150** (1985) 383.

[32] J.-w. Qiu and G. F. Sterman, "Single transverse spin asymmetries," *Phys. Rev. Lett.* **67** (1991) 2264–2267.

[33] K. Kanazawa, Y. Koike, A. Metz, and D. Pitonyak, "Towards an explanation of transverse single-spin asymmetries in proton-proton collisions: the role of fragmentation in collinear factorization," *Phys. Rev.* **D89** no. 11, (2014) 111501, `arXiv:1404.1033 [hep-ph]`.

[34] L. Gamberg, Z.-B. Kang, D. Pitonyak, and A. Prokudin, "Phenomenological constraints on A_N in $p^\uparrow p \to \pi X$ from Lorentz invariance relations," *Phys. Lett.* **B770** (2017) 242–251, `arXiv:1701.09170 [hep-ph]`.

[35] J. Collins, *Foundations of perturbative QCD*. Cambridge University Press, 2013. `http://www.cambridge.org/de/knowledge/isbn/item5756723`.

[36] M. G. Echevarria, A. Idilbi, and I. Scimemi, "Factorization Theorem For Drell-Yan At Low q_T And Transverse Momentum Distributions On-The-Light-Cone," *JHEP* **07** (2012) 002, `arXiv:1111.4996 [hep-ph]`.

[37] M. G. Echevarria, A. Idilbi, and I. Scimemi, "Soft and Collinear Factorization and Transverse Momentum Dependent Parton Distribution Functions," *Phys. Lett.* **B726** (2013) 795–801, `arXiv:1211.1947 [hep-ph]`.

[38] M. G. Echevarria, A. Idilbi, and I. Scimemi, "Unified treatment of the QCD evolution of all (un-)polarized transverse momentum dependent functions: Collins function as a study case," *Phys. Rev.* **D90** no. 1, (2014) 014003, `arXiv:1402.0869 [hep-ph]`.

[39] A. Bacchetta and P. J. Mulders, "Deep inelastic leptoproduction of spin-one hadrons," *Phys. Rev.* **D62** (2000) 114004, `arXiv:hep-ph/0007120 [hep-ph]`.

[40] P. J. Mulders and J. Rodrigues, "Transverse momentum dependence in gluon distribution and fragmentation functions," *Phys. Rev.* **D63** (2001) 094021, `arXiv:hep-ph/0009343 [hep-ph]`.

[41] D. Boer, S. Cotogno, T. van Daal, P. J. Mulders, A. Signori, and Y.-J. Zhou, "Gluon and Wilson loop TMDs for hadrons of spin ≤ 1," `arXiv:1607.01654 [hep-ph]`.

[42] R. Angeles-Martinez *et al.*, "Transverse Momentum Dependent (TMD) parton distribution functions: status and prospects," *Acta Phys. Polon.* **B46** no. 12, (2015) 2501–2534, `arXiv:1507.05267 [hep-ph]`.

[43] F. Hautmann, H. Jung, M. Kramer, P. J. Mulders, E. R. Nocera, T. C. Rogers, and A. Signori, "TMDlib and TMDplotter: library and plotting tools for transverse-momentum-dependent parton distributions," *Eur. Phys. J.* **C74** (2014) 3220, `arXiv:1408.3015 [hep-ph]`.

[44] D. W. Sivers, "Single Spin Production Asymmetries from the Hard Scattering of Point-Like Constituents," *Phys. Rev.* **D41** (1990) 83.

[45] D. W. Sivers, "Hard scattering scaling laws for single spin production asymmetries," *Phys. Rev.* **D43** (1991) 261–263.

[46] J.-w. Qiu and G. F. Sterman, "Single transverse spin asymmetries in hadronic pion production," *Phys. Rev.* **D59** (1999) 014004, `arXiv:hep-ph/9806356 [hep-ph]`.

[47] N. Hammon, O. Teryaev, and A. Schafer, "Single spin asymmetry for the Drell-Yan process," *Phys. Lett.* **B390** (1997) 409–412, `arXiv:hep-ph/9611359 [hep-ph]`.

[48] D. Boer, P. J. Mulders, and O. V. Teryaev, "Single spin asymmetries from a gluonic background in the Drell-Yan process," *Phys. Rev.* **D57** (1998) 3057–3064, `arXiv:hep-ph/9710223 [hep-ph]`.

[49] D. Boer and P. J. Mulders, "Color gauge invariance in the Drell-Yan process," *Nucl. Phys.* **B569** (2000) 505–526, `arXiv:hep-ph/9906223 [hep-ph]`.

[50] J.-w. Qiu and G. F. Sterman, "Single transverse spin asymmetries in direct photon production," *Nucl. Phys.* **B378** (1992) 52–78.

[51] D. Boer, C. Lorce, C. Pisano, and J. Zhou, "The gluon Sivers distribution: status and future prospects," *Adv. High Energy Phys.* **2015** (2015) 371396, `arXiv:1504.04332 [hep-ph]`.

[52] **PHENIX** Collaboration, A. Adare *et al.*, "Measurement of transverse-single-spin asymmetries for midrapidity and forward-rapidity production of hadrons in polarized p+p collisions at $\sqrt{s}$ =200 and 62.4 GeV," *Phys. Rev.* **D90** no. 1, (2014) 012006, `arXiv:1312.1995 [hep-ex]`.

[53] **COMPASS** Collaboration, C. Adolph *et al.*, "First measurement of the Sivers asymmetry for gluons using SIDIS data," *Phys. Lett.* **B772** (2017) 854–864, `arXiv:1701.02453 [hep-ex]`.

[54] **PHENIX** Collaboration, C. Aidala *et al.*, "Single-spin asymmetry of *J/ψ* production in *p*+*p*, *p*+Al, and *p*+Au collisions with transversely polarized proton beams at $\sqrt{s_{NN}}$ = 200 GeV," `arXiv:1805.01491 [hep-ex]`.

[55] D. Boer and P. J. Mulders, "Time reversal odd distribution functions in leptoproduction," *Phys. Rev.* **D57** (1998) 5780–5786, `arXiv:hep-ph/9711485 [hep-ph]`.

[56] C. S. Lam and W.-K. Tung, "A Parton Model Relation Sans QCD Modifications in Lepton Pair Productions," *Phys. Rev.* **D21** (1980) 2712.

[57] D. Boer and C. Pisano, "Polarized gluon studies with charmonium and bottomonium at LHCb and AFTER," *Phys. Rev.* **D86** (2012) 094007, `arXiv:1208.3642 [hep-ph]`.

[58] A. Signori, "Gluon TMDs in quarkonium production," *Few Body Syst.* **57** no. 8, (2016) 651–655, `arXiv:1602.03405 [hep-ph]`.

[59] W. J. den Dunnen, J. P. Lansberg, C. Pisano, and M. Schlegel, "Accessing the Transverse Dynamics and Polarization of Gluons inside the Proton at the LHC," *Phys. Rev. Lett.* **112** (2014) 212001, `arXiv:1401.7611 [hep-ph]`.

[60] J. P. Lansberg *et al.*, "Spin physics and TMD studies at A Fixed-Target ExpeRiment at the LHC (AFTER@LHC)," *EPJ Web Conf.* **85** (2015) 02038, `arXiv:1410.1962 [hep-ex]`.

[61] M. G. A. Buffing, A. Mukherjee, and P. J. Mulders, "Generalized Universality of Higher Transverse Moments of Quark TMD Correlators," *Phys. Rev.* **D86** (2012) 074030, `arXiv:1207.3221 [hep-ph]`.

[62] M. G. A. Buffing, A. Mukherjee, and P. J. Mulders, "Generalized Universality of Definite Rank Gluon Transverse Momentum Dependent Correlators," *Phys. Rev.* **D88** (2013) 054027, `arXiv:1306.5897 [hep-ph]`.

[63] M. G. A. Buffing, *Color and TMD Universality in Hadronic Interactions*. PhD thesis, NIKHEF, Amsterdam, 2015-09-02. `http://www.nikhef.nl/pub/services/biblio/theses_pdf/thesis_M_Buffing.pdf`.

[64] A. Klein *et al.*, "Letter of Intent for a Drell-Yan experiment with a polarized proton target.,".

[65] **COMPASS** Collaboration, C. Quintans, "Future Drell-Yan measurements in COMPASS," *J. Phys. Conf. Ser.* **295** (2011) 012163.

[66] **STAR** Collaboration, L. Adamczyk *et al.*, "Measurement of the transverse single-spin asymmetry in $p^{\uparrow} + p \rightarrow W^{\pm}/Z^0$ at RHIC," *Phys. Rev. Lett.* **116** no. 13, (2016) 132301, `arXiv:1511.06003 [nucl-ex]`.

[67] E.-C. Aschenauer *et al.*, "The RHIC Cold QCD Plan for 2017 to 2023: A Portal to the EIC," `arXiv:1602.03922 [nucl-ex]`.

[68] **COMPASS** Collaboration, M. Aghasyan *et al.*, "First measurement of transverse-spin-dependent azimuthal asymmetries in the Drell-Yan process," *Phys. Rev. Lett.* **119** no. 11, (2017) 112002, `arXiv:1704.00488 [hep-ex]`.

[69] D. Boer, P. J. Mulders, and F. Pijlman, "Universality of T odd effects in single spin and azimuthal asymmetries," *Nucl. Phys.* **B667** (2003) 201–241, `arXiv:hep-ph/0303034 [hep-ph]`.

[70] X. Ji, J.-W. Qiu, W. Vogelsang, and F. Yuan, "A Unified picture for single transverse-spin asymmetries in hard processes," *Phys. Rev. Lett.* **97** (2006) 082002, `arXiv:hep-ph/0602239 [hep-ph]`.

[71] X. Ji, J.-w. Qiu, W. Vogelsang, and F. Yuan, "Single Transverse-Spin Asymmetry in Drell-Yan Production at Large and Moderate Transverse Momentum," *Phys. Rev.* **D73** (2006) 094017, `arXiv:hep-ph/0604023 [hep-ph]`.

[72] X. Ji, J.-W. Qiu, W. Vogelsang, and F. Yuan, "Single-transverse spin asymmetry in semi-inclusive deep inelastic scattering," *Phys. Lett.* **B638** (2006) 178–186, `arXiv:hep-ph/0604128 [hep-ph]`.

[73] I. Karpenko, "Rapidity scan in heavy ion collisions at $\sqrt{s_{NN}}$ = 72 GeV using a viscous hydro + cascade model," `arXiv:1805.11998 [nucl-th]`.

[74] F. Becattini and J. Cleymans, "Chemical Equilibrium in Heavy Ion Collisions: Rapidity Dependence," *J. Phys.* **G34** (2007) S959–964, `arXiv:hep-ph/0701029 [hep-ph]`.

[75] V. Begun, D. Kikola, V. Vovchenko, and D. Wielanek, "Estimation of the freeze-out parameters reachable in the AFTER@LHC project," `arXiv:1806.01303 [nucl-th]`.

[76] G. Denicol, A. Monnai, and B. Schenke, "Moving forward to constrain the shear viscosity of QCD matter," *Phys. Rev. Lett.* **116** no. 21, (2016) 212301, `arXiv:1512.01538 [nucl-th]`.

[77] B. Schenke, "Bulk evolution of heavy ion collisions in the beam energy scan: New developments and first results." Quark Matter 2015, 27 September - 3 October, 2015, Kobe, Japan.

[78] C. Lourenco and H. K. Wohri, "Heavy flavour hadro-production from fixed-target to collider energies," *Phys. Rept.* **433** (2006) 127–180, `arXiv:hep-ph/0609101 [hep-ph]`.

[79] R. Rapp, D. Blaschke, and P. Crochet, "Charmonium and bottomonium production in heavy-ion collisions," *Prog. Part. Nucl. Phys.* **65** (2010) 209–266, `arXiv:0807.2470 [hep-ph]`.

[80] A. Andronic *et al.*, "Heavy-flavour and quarkonium production in the LHC era: from protonproton to heavy-ion collisions," *Eur. Phys. J.* **C76** no. 3, (2016) 107, `arXiv:1506.03981 [nucl-ex]`.

[81] L. Kluberg, "20 years of J/psi suppression at the CERN SPS: Results from experiments NA38, NA51 and NA50," *Eur. Phys. J.* **C43** (2005) 145–156.

[82] **PHENIX** Collaboration, K. Adcox *et al.*, "Formation of dense partonic matter in relativistic nucleus-nucleus collisions at

RHIC: Experimental evaluation by the PHENIX collaboration," *Nucl. Phys.* **A757** (2005) 184–283, arXiv:nucl-ex/0410003 [nucl-ex].

[83] T. Matsui and H. Satz, "*J/ψ* Suppression by Quark-Gluon Plasma Formation," *Phys. Lett.* **B178** (1986) 416–422.

[84] M. Ferro-Luzzi, "Proposal for an absolute luminosity determination in colliding beam experiments using vertex detection of beam-gas interactions," *Nucl. Instrum. Meth.* **A553** (2005) 388–399.

[85] R. Aaij *et al.*, "Performance of the LHCb Vertex Locator," *JINST* **9** (2014) P09007, arXiv:1405.7808 [physics.ins-det].

[86] **LHCb** Collaboration, E. Maurice, "Fixed-target physics at LHCb," in *5th Large Hadron Collider Physics Conference (LHCP 2017) Shanghai, China, May 15-20, 2017.* 2017. arXiv:1708.05184 [hep-ex]. http://inspirehep.net/record/1616496/files/arXiv:1708.05184.pdf.

[87] E. Steffens and W. Haeberli, "Polarized gas targets," *Reports on Progress in Physics* **66** no. 11, (2003) 1887. http://stacks.iop.org/0034-4885/66/i=11/a=R02.

[88] A. Zelenski *et al.*, "Absolute polarized H-jet polarimeter development, for RHIC," *Nucl. Instrum. Meth.* **A536** (2005) 248–254.

[89] W. Scandale *et al.*, "Observation of channeling for 6500 GeV/ c protons in the crystal assisted collimation setup for LHC," *Phys. Lett.* **B758** (2016) 129–133.

[90] A. B. Kurepin, N. S. Topilskaya, and M. B. Golubeva, "Charmonium production in fixed-target experiments with SPS and LHC beams at CERN," *Phys. Atom. Nucl.* **74** (2011) 446–452. [Yad. Fiz.74,467(2011)].

[91] K. Ehret, "Commissioning of the HERA-B internal target: Using the HERA proton ring as a B factory," *Nucl. Instrum. Meth.* **A446** (2000) 190–198.

[92] **STAR** Collaboration, K. C. Meehan, "Fixed Target Collisions at STAR," *Nucl. Phys.* **A956** (2016) 878–881.

[93] O. S. Bruning, P. Collier, P. Lebrun, S. Myers, R. Ostojic, J. Poole, and P. Proudlock, "LHC Design Report Vol.1: The LHC Main Ring,".

[94] M. Benedikt, P. Collier, V. Mertens, J. Poole, and K. Schindl, "LHC Design Report. 3. The LHC injector chain,".

[95] C. Barschel, *Precision luminosity measurement at LHCb with beam-gas imaging.* PhD thesis, RWTH Aachen U., 2014. http://inspirehep.net/record/1339684/files/CERN-THESIS-2013-301.pdf.

[96] **LHCb** Collaboration, R. Aaij *et al.*, "Precision luminosity measurements at LHCb," *JINST* **9** no. 12, (2014) P12005, arXiv:1410.0149 [hep-ex].

[97] T. Pierog, I. Karpenko, J. M. Katzy, E. Yatsenko, and K. Werner, "EPOS LHC: Test of collective hadronization with data measured at the CERN Large Hadron Collider," *Phys. Rev.* **C92** no. 3, (2015) 034906, arXiv:1306.0121 [hep-ph].

[98] A. Ferrari, P. R. Sala, A. Fasso, and J. Ranft, "FLUKA: A multi-particle transport code (Program version 2005),".

[99] **LHCb** Collaboration, T. L. Collaboration, "Measurement of antiproton production in *p*He collisions at $\sqrt{s_{NN}}$ = 110 GeV,".

[100] **LHCb** Collaboration, T. L. Collaboration, "Measurement of *J/ψ* and *D*^{0} production in *p*Ar collisions at $\sqrt{s_{NN}}$ = 110 GeV,".

[101] H. Okada *et al.*, "Measurement of the analyzing power in pp elastic scattering in the peak CNI region at RHIC," *Phys. Lett.* **B638** (2006) 450–454, arXiv:nucl-ex/0502022 [nucl-ex].

[102] A. Poblaguev *et al.*, "The HJET polarimeter in RHIC Run 2017 ," *PoS* **PSTP2017** (2017) 022.

[103] C. Barschel, P. Lenisa, A. Nass, and E. Steffens, "A Gas Target Internal to the LHC for the Study of pp Single-Spin Asymmetries and Heavy Ion Collisions," *Adv. High Energy Phys.* **2015** (2015) 463141.

[104] M. Mikirtychyants *et al.*, "The Polarized H and D Atomic Beam Source for ANKE at COSY-Julich," *Nucl. Instrum. Meth.* **A721** (2013) 83–98, arXiv:1212.1840 [physics.ins-det].

[105] K. Grigoryev *et al.*, "Machine studies for the development of storage cells at the ANKE facility of COSY," *Nucl. Instrum. Meth.* **A599** (2009) 130–139.

[106] G. Ciullo, M. Statera, P. Lenisa, A. Nass, and G. Tagliente, "The H and D Polarized Target for Spin-Filtering Measurements at COSY," *Int. J. Mod. Phys. Conf. Ser.* **40** (2016) 1660149.

[107] W. A. Dezarn *et al.*, "Polarized internal gas target for hydrogen and deuterium at the IUCF Cooler Ring," *Nucl. Instrum. Meth.* **A362** (1995) 36–40.

[108] **HERMES** Collaboration, A. Airapetian *et al.*, "The HERMES polarized hydrogen and deuterium gas target in the HERA electron storage ring," *Nucl. Instrum. Meth.* **A540** (2005) 68–101, arXiv:physics/0408137 [physics].

[109] P. Di Nezza, "Polarized fixed target at LHC." Physics Beyond Collider, Annual Workshop, November 21-22, 2017.

[110] J. Jowett, H. Braun, M. Gresham, E. Mahner, A. Nicholson, and E. Shaposhnikova, "Limits to the performance of the LHC with ion beams," **EPAC2004** (2004) .

[111] J. Jowett. Personal communication.

[112] G. Arduini, K. Elsener, G. Fidecaro, M. Gyr, W. Herr, J. Klem, U. I. Uggerhoj, and E. Weisse, "On the energy dependence of proton beam extraction with a bent crystal," *Phys. Lett.* **B422** (1998) 325–333.

[113] A. Asseev *et al.*, "First observation of luminosity driven extraction using channeling with a bent crystal," *Phys. Rev. ST*

Accel. Beams **1** (1998) 022801.

[114] A. G. Afonin *et al.*, "Observation and comparative analysis of proton beam extraction or collimation by different planar channels of a bent crystal," *Phys. Rev. ST Accel. Beams* **15** (2012) 081001.

[115] W. Scandale *et al.*, "Comparative results on collimation of the SPS beam of protons and Pb ions with bent crystals," *Phys. Lett.* **B703** (2011) 547–551.

[116] W. Scandale *et al.*, "First results on the SPS beam collimation with bent crystals," *Phys. Lett.* **B692** (2010) 78–82.

[117] W. Scandale *et al.*, "Strong reduction of the off-momentum halo in crystal assisted collimation of the SPS beam," *Phys. Lett.* **B714** (2012) 231–236.

[118] V. M. Biryukov, Yu. A. Chesnokov, V. I. Kotov, V. Guidi, C. Malagu, G. Martinelli, M. Stefancich, D. Vincenzi, and W. Scandale, "Crystal deflector for highly efficient channeling extraction of a proton beam from accelerators," *Rev. Sci. Instrum.* **73** (2002) 3170–3173.

[119] A. Baurichter *et al.*, "Channeling of high-energy particles in bent crystals: Experiments at the CERN SPS," *Nucl. Instrum. Meth.* **B164-165** (2000) 27–43.

[120] W. Scandale, "Experimental insertions for the LHC," in *ECFA Large Hadron Collider (LHC) Workshop: Physics and Instrumentation Aachen, Germany, October 4-9, 1990*, pp. 760–764. 1990.

[121] E. Uggerhoj and U. I. Uggerhj, "Strong crystalline fields: A possibility for extraction from the LHC," *Nucl. Instrum. Meth.* **B234** (2005) 31–39.

[122] http://crysbeam.roma1.infn.it/index.html.

[123] A. S. Fomin *et al.*, "Feasibility of measuring the magnetic dipole moments of the charm baryons at the LHC using bent crystals," *JHEP* **08** (2017) 120, arXiv:1705.03382 [hep-ph].

[124] E. Bagli *et al.*, "Electromagnetic dipole moments of charged baryons with bent crystals at the LHC," *Eur. Phys. J.* **C77** no. 12, (2017) 828, arXiv:1708.08483 [hep-ex].

[125] F. J. Botella, L. M. Garcia Martin, D. Marangotto, F. M. Vidal, A. Merli, N. Neri, A. Oyanguren, and J. R. Vidal, "On the search for the electric dipole moment of strange and charm baryons at LHC," *Eur. Phys. J.* **C77** no. 3, (2017) 181, arXiv:1612.06769 [hep-ex].

[126] S. Montesano *et al.*, "Testing the Double-Crystal setup for Physics Beyond Collider experiments in the UA9-SPS Experiment," **IPAC2018** (2018) TUPAF043.

[127] **COMPASS** Collaboration, M. Pesek and J. Matousek, "COMPASS polarized target for Drell-Yan," *PoS* **PSTP2013** (2013) 009.

[128] N. Doshita *et al.*, "Performance of the COMPASS polarized target dilution refrigerator," *Nucl. Instrum. Meth.* **A526** (2004) 138–143.

[129] J. Ball *et al.*, "First results of the large COMPASS 6LiD polarized target," *Nucl. Instrum. Meth.* **A498** (2003) 101–111.

[130] S. Goertz, W. Meyer, and G. Reicherz, "Polarized H, D and He-3 targets for particle physics experiments," *Prog. Part. Nucl. Phys.* **49** (2002) 403–489. [Erratum: Prog. Part. Nucl. Phys.51,309(2003)].

[131] K. Kondo *et al.*, "Polarization measurement in the COMPASS polarized target," *Nucl. Instrum. Meth.* **A526** (2004) 70–75.

[132] K. Werner, F.-M. Liu, and T. Pierog, "Parton ladder splitting and the rapidity dependence of transverse momentum spectra in deuteron-gold collisions at RHIC," *Phys. Rev.* **C74** (2006) 044902, arXiv:hep-ph/0506232 [hep-ph].

[133] **ALICE** Collaboration, K. Aamodt *et al.*, "The ALICE experiment at the CERN LHC," *JINST* **3** (2008) S08002.

[134] **ALICE** Collaboration, B. B. Abelev *et al.*, "Performance of the ALICE Experiment at the CERN LHC," *Int. J. Mod. Phys.* **A29** (2014) 1430044, arXiv:1402.4476 [nucl-ex].

[135] C. Hadjidakis, "Physics opportunities and feasibility studies with ALICE in a fixed-target mode." Physics Beyond Collider, General Meeting, June 14, 2018.

[136] **LHCb** Collaboration, A. A. Alves, Jr. *et al.*, "The LHCb Detector at the LHC," *JINST* **3** (2008) S08005.

[137] **LHCb** Collaboration, R. Aaij *et al.*, "LHCb Detector Performance," *Int. J. Mod. Phys.* **A30** no. 07, (2015) 1530022, arXiv:1412.6352 [hep-ex].

[138] **LHCb** Collaboration, "LHCb VELO Upgrade Technical Design Report," Tech. Rep. CERN-LHCC-2013-021. LHCB-TDR-013, Nov, 2013. http://cds.cern.ch/record/1624070.

[139] **LHCb** Collaboration, "LHCb Tracker Upgrade Technical Design Report," Tech. Rep. CERN-LHCC-2014-001. LHCB-TDR-015, Feb, 2014. http://cds.cern.ch/record/1647400.

[140] **LHCb** Collaboration, R. Aaij *et al.*, "Expression of Interest for a Phase-II LHCb Upgrade: Opportunities in flavour physics, and beyond, in the HL-LHC era," Tech. Rep. CERN-LHCC-2017-003, CERN, Geneva, Feb, 2017. https://cds.cern.ch/record/2244311.

[141] K. C. Akiba *et al.*, "The HeRSCheL detector: high-rapidity shower counters for LHCb," *JINST* **13** no. 04, (2018) P04017, arXiv:1801.04281 [physics.ins-det].

[142] M. Ferro-Luzzi, S. Redaelli, and C. Hadjidakis, "Studies for future fixed-target experiments at the LHC in the framework of the CERN Physics Beyond Colliders study," **IPAC2018** (2018) TUPAF045.

[143] G. Graziani, "LHCb as a fixed target experiment." Physics Beyond Collider, General Meeting, June 14, 2018.

[144] J. Gao, M. Guzzi, J. Huston, H.-L. Lai, Z. Li, P. Nadolsky, J. Pumplin, D. Stump, and C. P. Yuan, "CT10 next-to-next-to-leading order global analysis of QCD," *Phys. Rev.* **D89** no. 3, (2014) 033009, `arXiv:1302.6246 [hep-ph]`.

[145] **NNPDF** Collaboration, R. D. Ball *et al.*, "Parton distributions for the LHC Run II," *JHEP* **04** (2015) 040, `arXiv:1410.8849 [hep-ph]`.

[146] L. A. Harland-Lang, A. D. Martin, P. Motylinski, and R. S. Thorne, "Parton distributions in the LHC era: MMHT 2014 PDFs," *Eur. Phys. J.* **C75** no. 5, (2015) 204, `arXiv:1412.3989 [hep-ph]`.

[147] S. Alekhin, J. Blumlein, and S. Moch, "The ABM parton distributions tuned to LHC data," *Phys. Rev.* **D89** no. 5, (2014) 054028, `arXiv:1310.3059 [hep-ph]`.

[148] J. F. Owens, A. Accardi, and W. Melnitchouk, "Global parton distributions with nuclear and finite-Q^2 corrections," *Phys. Rev.* **D87** no. 9, (2013) 094012, `arXiv:1212.1702 [hep-ph]`.

[149] P. Jimenez-Delgado and E. Reya, "Delineating parton distributions and the strong coupling," *Phys. Rev.* **D89** no. 7, (2014) 074049, `arXiv:1403.1852 [hep-ph]`.

[150] G. Moreno *et al.*, "Dimuon production in proton - copper collisions at $\sqrt{s}$ = 38.8 GeV," *Phys. Rev.* **D43** (1991) 2815–2836.

[151] **NuSea** Collaboration, J. C. Webb *et al.*, "Absolute Drell-Yan dimuon cross-sections in 800 GeV / c pp and pd collisions," `arXiv:hep-ex/0302019 [hep-ex]`.

[152] J. C. Webb, *Measurement of continuum dimuon production in 800-GeV/C proton nucleon collisions.* PhD thesis, New Mexico State U., 2003. `arXiv:hep-ex/0301031 [hep-ex]`. `http://lss.fnal.gov/cgi-bin/find_paper.pl?thesis-2002-56`.

[153] **NuSea** Collaboration, R. S. Towell *et al.*, "Improved measurement of the anti-d / anti-u asymmetry in the nucleon sea," *Phys. Rev.* **D64** (2001) 052002, `arXiv:hep-ex/0103030 [hep-ex]`.

[154] O. Nachtmann, "Inequalities for structure functions of deep inelastic lepton-nucleon scattering giving tests of basic algebraic structures," *Nucl. Phys.* **B38** (1972) 397–417.

[155] S. J. Brodsky and G. R. Farrar, "Scaling Laws at Large Transverse Momentum," *Phys. Rev. Lett.* **31** (1973) 1153–1156.

[156] R. D. Ball, E. R. Nocera, and J. Rojo, "The asymptotic behaviour of parton distributions at small and large x," *Eur. Phys. J.* **C76** no. 7, (2016) 383, `arXiv:1604.00024 [hep-ph]`.

[157] A. Accardi, L. T. Brady, W. Melnitchouk, J. F. Owens, and N. Sato, "Constraints on large-x parton distributions from new weak boson production and deep-inelastic scattering data," *Phys. Rev.* **D93** no. 11, (2016) 114017, `arXiv:1602.03154 [hep-ph]`.

[158] F. E. Close, "Nu w(2) at small omega' and resonance form-factors in a quark model with broken su(6)," *Phys. Lett.* **43B** (1973) 422–426.

[159] G. R. Farrar and D. R. Jackson, "Pion and Nucleon Structure Functions Near x=1," *Phys. Rev. Lett.* **35** (1975) 1416.

[160] W. Melnitchouk and A. W. Thomas, "Neutron / proton structure function ratio at large x," *Phys. Lett.* **B377** (1996) 11–17, `arXiv:nucl-th/9602038 [nucl-th]`.

[161] F. E. Close and W. Melnitchouk, "Symmetry breaking and quark-hadron duality in structure functions," *Phys. Rev.* **C68** (2003) 035210, `arXiv:hep-ph/0302013 [hep-ph]`.

[162] R. J. Holt and C. D. Roberts, "Distribution Functions of the Nucleon and Pion in the Valence Region," *Rev. Mod. Phys.* **82** (2010) 2991–3044, `arXiv:1002.4666 [nucl-th]`.

[163] C. D. Roberts, R. J. Holt, and S. M. Schmidt, "Nucleon spin structure at very high-x," *Phys. Lett.* **B727** (2013) 249–254, `arXiv:1308.1236 [nucl-th]`.

[164] H. Paukkunen and P. Zurita, "PDF reweighting in the Hessian matrix approach," *JHEP* **12** (2014) 100, `arXiv:1402.6623 [hep-ph]`.

[165] S. Alekhin *et al.*, "HERAFitter," *Eur. Phys. J.* **C75** no. 7, (2015) 304, `arXiv:1410.4412 [hep-ph]`.

[166] R. Boughezal, J. M. Campbell, R. K. Ellis, C. Focke, W. Giele, X. Liu, F. Petriello, and C. Williams, "Color singlet production at NNLO in MCFM," *Eur. Phys. J.* **C77** no. 1, (2017) 7, `arXiv:1605.08011 [hep-ph]`.

[167] S. Dulat, T.-J. Hou, J. Gao, M. Guzzi, J. Huston, P. Nadolsky, J. Pumplin, C. Schmidt, D. Stump, and C. P. Yuan, "New parton distribution functions from a global analysis of quantum chromodynamics," *Phys. Rev.* **D93** no. 3, (2016) 033006, `arXiv:1506.07443 [hep-ph]`.

[168] R. Gavin, Y. Li, F. Petriello, and S. Quackenbush, "W Physics at the LHC with FEWZ 2.1," *Comput. Phys. Commun.* **184** (2013) 208–214, `arXiv:1201.5896 [hep-ph]`.

[169] T. Jezo, M. Klasen, D. R. Lamprea, F. Lyonnet, and I. Schienbein, "NLO+NLL limits on W' and Z' gauge boson masses in general extensions of the Standard Model," *JHEP* **12** (2014) 092, `arXiv:1410.4692 [hep-ph]`.

[170] R. Bonciani, T. Jezo, M. Klasen, F. Lyonnet, and I. Schienbein, "Electroweak top-quark pair production at the LHC with Z' bosons to NLO QCD in POWHEG," *JHEP* **02** (2016) 141, `arXiv:1511.08185 [hep-ph]`.

[171] F. Lyonnet, A. Kusina, T. Jezo, K. Kovark, F. Olness, I. Schienbein, and J.-Y. Yu, "On the intrinsic bottom content of the

nucleon and its impact on heavy new physics at the LHC," *JHEP* **07** (2015) 141, arXiv:1504.05156 [hep-ph].

[172] S. J. Brodsky, J. C. Collins, S. D. Ellis, J. F. Gunion, and A. H. Mueller, "Intrinsic Chevrolets at the SSC," in *Electroweak Symmetry Breaking. Proceedings, Workshop, Berkeley, USA, June 3-22, 1984*. 1984. http://www-public.slac.stanford.edu/sciDoc/docMeta.aspx?slacPubNumber=SLAC-PUB-15471.

[173] S. J. Brodsky, P. Hoyer, C. Peterson, and N. Sakai, "The Intrinsic Charm of the Proton," *Phys. Lett.* **B93** (1980) 451–455.

[174] S. J. Brodsky, A. Kusina, F. Lyonnet, I. Schienbein, H. Spiesberger, and R. Vogt, "A review of the intrinsic heavy quark content of the nucleon," *Adv. High Energy Phys.* **2015** (2015) 231547, arXiv:1504.06287 [hep-ph].

[175] **European Muon** Collaboration, J. J. Aubert *et al.*, "Production of charmed particles in 250 GeV μ^+ - iron interactions," *Nucl. Phys.* **B213** (1983) 31–64.

[176] B. W. Harris, J. Smith, and R. Vogt, "Reanalysis of the EMC charm production data with extrinsic and intrinsic charm at NLO," *Nucl. Phys.* **B461** (1996) 181–196, arXiv:hep-ph/9508403 [hep-ph].

[177] **NNPDF** Collaboration, R. D. Ball, V. Bertone, M. Bonvini, S. Carrazza, S. Forte, A. Guffanti, N. P. Hartland, J. Rojo, and L. Rottoli, "A Determination of the Charm Content of the Proton," arXiv:1605.06515 [hep-ph].

[178] **R608** Collaboration, P. Chauvat *et al.*, "Production of $\Lambda(c)$ With Large X(f) at the ISR," *Phys. Lett.* **B199** (1987) 304.

[179] **SELEX** Collaboration, F. G. Garcia *et al.*, "Hadronic production of Lambda(c) from 600-GeV/c pi-, Sigma- and p beams," *Phys. Lett.* **B528** (2002) 49–57, arXiv:hep-ex/0109017 [hep-ex].

[180] S. Groote and S. Koshkarev, "Production of doubly charmed baryons nearly at rest," *Eur. Phys. J.* **C77** no. 8, (2017) 509, arXiv:1704.02850 [hep-ph].

[181] S. Koshkarev and S. Groote, "Double quarkonium production at high Feynman-x," *Nucl. Phys.* **B915** (2017) 384–391, arXiv:1611.08149 [hep-ph].

[182] S. Koshkarev, "Production of the Doubly Heavy Baryons, B_c Meson and the All-charm Tetraquark at AFTER@LHC with Double Intrinsic Heavy Mechanism," arXiv:1610.06125 [hep-ph]. [Acta Phys. Polon.B48,163(2017)].

[183] G. Chen, X.-G. Wu, J.-W. Zhang, H.-Y. Han, and H.-B. Fu, "Hadronic production of Ξ_{cc} at a fixed-target experiment at the LHC," *Phys. Rev.* **D89** no. 7, (2014) 074020, arXiv:1401.6269 [hep-ph].

[184] M. Siddikov. Personal communication.

[185] I. Schmidt and M. Siddikov, "Production of pentaquarks in pA-collisions," *Phys. Rev.* **D93** no. 9, (2016) 094005, arXiv:1601.05621 [hep-ph].

[186] B. A. Kniehl, G. Kramer, I. Schienbein, and H. Spiesberger, "Open charm hadroproduction and the charm content of the proton," *Phys. Rev.* **D79** (2009) 094009, arXiv:0901.4130 [hep-ph].

[187] B. A. Kniehl, G. Kramer, I. Schienbein, and H. Spiesberger, "Inclusive Charmed-Meson Production at the CERN LHC," *Eur. Phys. J.* **C72** (2012) 2082, arXiv:1202.0439 [hep-ph].

[188] V. A. Bednyakov, M. A. Demichev, G. I. Lykasov, T. Stavreva, and M. Stockton, "Searching for intrinsic charm in the proton at the LHC," *Phys. Lett.* **B728** (2014) 602–606, arXiv:1305.3548 [hep-ph].

[189] M. Czakon, N. P. Hartland, A. Mitov, E. R. Nocera, and J. Rojo, "Pinning down the large-x gluon with NNLO top-quark pair differential distributions," *JHEP* **04** (2017) 044, arXiv:1611.08609 [hep-ph].

[190] **PROSA** Collaboration, O. Zenaiev *et al.*, "Impact of heavy-flavour production cross sections measured by the LHCb experiment on parton distribution functions at low x," *Eur. Phys. J.* **C75** no. 8, (2015) 396, arXiv:1503.04581 [hep-ph].

[191] R. Gauld and J. Rojo, "Precision determination of the small-x gluon from charm production at LHCb," *Phys. Rev. Lett.* **118** no. 7, (2017) 072001, arXiv:1610.09373 [hep-ph].

[192] J.-P. Lansberg and H.-S. Shao, "Double-quarkonium production at a fixed-target experiment at the LHC (AFTER@LHC)," *Nucl. Phys.* **B900** (2015) 273–294, arXiv:1504.06531 [hep-ph].

[193] J.-P. Lansberg and H.-S. Shao, "Production of $J/\psi + \eta_c$ versus $J/\psi + J/\psi$ at the LHC: Importance of Real α_s^5 Corrections," *Phys. Rev. Lett.* **111** (2013) 122001, arXiv:1308.0474 [hep-ph].

[194] J.-P. Lansberg and H.-S. Shao, "J/ψ -pair production at large momenta: Indications for double parton scatterings and large α_s^5 contributions," *Phys. Lett.* **B751** (2015) 479–486, arXiv:1410.8822 [hep-ph].

[195] D. d'Enterria and J. Rojo, "Quantitative constraints on the gluon distribution function in the proton from collider isolated-photon data," *Nucl. Phys.* **B860** (2012) 311–338, arXiv:1202.1762 [hep-ph].

[196] **FERMILAB-E706** Collaboration, G. Alverson *et al.*, "Production of direct photons and neutral mesons at large transverse momenta by π^- and p beams at 500-GeV/c," *Phys. Rev.* **D48** (1993) 5–28.

[197] **Fermilab E706** Collaboration, L. Apanasevich *et al.*, "Evidence for parton k_T effects in high p_T particle production," *Phys. Rev. Lett.* **81** (1998) 2642–2645, arXiv:hep-ex/9711017 [hep-ex].

[198] **Fermilab E706** Collaboration, L. Apanasevich *et al.*, "Measurement of direct photon production at Tevatron fixed target energies," *Phys. Rev.* **D70** (2004) 092009, arXiv:hep-ex/0407011 [hep-ex].

[199] H. Baer, J. Ohnemus, and J. F. Owens, "A Next-to-leading Logarithm Calculation of Direct Photon Production," *Phys. Rev.* **D42** (1990) 61–71.

[200] P. Aurenche, P. Chiappetta, M. Fontannaz, J. P. Guillet, and E. Pilon, "Next-to-leading order bremsstrahlung contribution to prompt photon production," *Nucl. Phys.* **B399** (1993) 34–62.

[201] L. E. Gordon and W. Vogelsang, "Polarized and unpolarized isolated prompt photon production beyond the leading order," *Phys. Rev.* **D50** (1994) 1901–1916.

[202] E. Laenen, G. Oderda, and G. F. Sterman, "Resummation of threshold corrections for single particle inclusive cross-sections," *Phys. Lett.* **B438** (1998) 173–183, `arXiv:hep-ph/9806467 [hep-ph]`.

[203] S. Catani, M. L. Mangano, and P. Nason, "Sudakov resummation for prompt photon production in hadron collisions," *JHEP* **07** (1998) 024, `arXiv:hep-ph/9806484 [hep-ph]`.

[204] N. Kidonakis and J. F. Owens, "Effects of higher order threshold corrections in high E(T) jet production," *Phys. Rev.* **D63** (2001) 054019, `arXiv:hep-ph/0007268 [hep-ph]`.

[205] N. Kidonakis and J. F. Owens, "Next-to-next-to-leading order soft gluon corrections in direct photon production," *Int. J. Mod. Phys.* **A19** (2004) 149–158, `arXiv:hep-ph/0307352 [hep-ph]`.

[206] D. de Florian and W. Vogelsang, "Threshold resummation for the prompt-photon cross section revisited," *Phys. Rev.* **D72** (2005) 014014, `arXiv:hep-ph/0506150 [hep-ph]`.

[207] D. Higinbotham, G. A. Miller, O. Hen, and K. Rith, "The EMC effect still puzzles after 30 years," *CERN Cour.* **53N4** (2013) 24, `arXiv:1305.7143 [hep-ph]`.

[208] S. Malace, D. Gaskell, D. W. Higinbotham, and I. Cloet, "The Challenge of the EMC Effect: existing data and future directions," *Int. J. Mod. Phys.* **E23** no. 08, (2014) 1430013, `arXiv:1405.1270 [nucl-ex]`.

[209] K. J. Eskola, H. Paukkunen, and C. A. Salgado, "EPS09: A New Generation of NLO and LO Nuclear Parton Distribution Functions," *JHEP* **04** (2009) 065, `arXiv:0902.4154 [hep-ph]`.

[210] I. Schienbein, J. Y. Yu, K. Kovarik, C. Keppel, J. G. Morfin, F. Olness, and J. F. Owens, "PDF Nuclear Corrections for Charged and Neutral Current Processes," *Phys. Rev.* **D80** (2009) 094004, `arXiv:0907.2357 [hep-ph]`.

[211] D. M. Alde *et al.*, "Nuclear dependence of dimuon production at 800 GeV. FNAL-772 experiment," *Phys. Rev. Lett.* **64** (1990) 2479–2482.

[212] **NuSea** Collaboration, M. A. Vasilev *et al.*, "Parton energy loss limits and shadowing in Drell-Yan dimuon production," *Phys. Rev. Lett.* **83** (1999) 2304–2307, `arXiv:hep-ex/9906010 [hep-ex]`.

[213] W. T. Giele and S. Keller, "Implications of hadron collider observables on parton distribution function uncertainties," *Phys. Rev.* **D58** (1998) 094023, `arXiv:hep-ph/9803393 [hep-ph]`.

[214] N. Sato, J. F. Owens, and H. Prosper, "Bayesian Reweighting for Global Fits," *Phys. Rev.* **D89** no. 11, (2014) 114020, `arXiv:1310.1089 [hep-ph]`.

[215] **NNPDF** Collaboration, R. D. Ball, V. Bertone, F. Cerutti, L. Del Debbio, S. Forte, A. Guffanti, J. I. Latorre, J. Rojo, and M. Ubiali, "Reweighting NNPDFs: the W lepton asymmetry," *Nucl. Phys.* **B849** (2011) 112–143, `arXiv:1012.0836 [hep-ph]`. [Erratum: Nucl. Phys.B855,927(2012)].

[216] A. Kusina, F. Lyonnet, D. B. Clark, E. Godat, T. Jezo, K. Kovarik, F. I. Olness, I. Schienbein, and J. Y. Yu, "Vector boson production in proton-lead and lead-lead collisions at the LHC and its impact on nCTEQ15 PDFs," `arXiv:1610.02925 [nucl-th]`.

[217] R. Vogt, "Gluon Shadowing Effects on J/ψ and Υ Production in p + Pb Collisions at $\sqrt{s_{NN}}$ = 115 GeV and p + Pb Collisions at $\sqrt{s_{NN}}$ = 72 GeV at AFTER@LHC," *Adv. High Energy Phys.* **2015** (2015) 492302, `arXiv:1510.03976 [hep-ph]`.

[218] A. Kusina, J.-P. Lansberg, I. Schienbein, and H.-S. Shao, "Gluon shadowing and antishadowing in heavy-flavor production at the LHC," `arXiv:1712.07024 [hep-ph]`.

[219] J.-P. Lansberg and H.-S. Shao, "Towards an automated tool to evaluate the impact of the nuclear modification of the gluon density on quarkonium, D and B meson production in proton-nucleus collisions," *Eur. Phys. J.* **C77** no. 1, (2017) 1, `arXiv:1610.05382 [hep-ph]`.

[220] H.-S. Shao, "HELAC-Onia: An automatic matrix element generator for heavy quarkonium physics," *Comput. Phys. Commun.* **184** (2013) 2562–2570, `arXiv:1212.5293 [hep-ph]`.

[221] H.-S. Shao, "HELAC-Onia 2.0: an upgraded matrix-element and event generator for heavy quarkonium physics," *Comput. Phys. Commun.* **198** (2016) 238–259, `arXiv:1507.03435 [hep-ph]`.

[222] F. Arleo and S. Peigne, "Quarkonium suppression from coherent energy loss in fixed-target experiments using LHC beams," *Adv. High Energy Phys.* **2015** (2015) 961951, `arXiv:1504.07428 [hep-ph]`.

[223] **AMS** Collaboration, M. Aguilar *et al.*, "Precision Measurement of the $(e^+ + e^-)$ Flux in Primary Cosmic Rays from 0.5 GeV to 1 TeV with the Alpha Magnetic Spectrometer on the International Space Station," *Phys. Rev. Lett.* **113** (2014) 221102.

[224] **DAMPE** Collaboration, G. Ambrosi *et al.*, "Direct detection of a break in the teraelectronvolt cosmic-ray spectrum of electrons and positrons," *Nature* **552** (2017) 63–66, `arXiv:1711.10981 [astro-ph.HE]`.

[225] **Fermi-LAT** Collaboration, W. B. Atwood *et al.*, "The Large Area Telescope on the Fermi Gamma-ray Space Telescope Mission," *Astrophys. J.* **697** (2009) 1071–1102, `arXiv:0902.1089 [astro-ph.IM]`.

[226] **Fermi-LAT** Collaboration, M. Ajello *et al.*, "Fermi-LAT Observations of High-Energy γ-Ray Emission Toward the Galactic Center," *Astrophys. J.* **819** no. 1, (2016) 44, `arXiv:1511.02938 [astro-ph.HE]`.

[227] **IceCube** Collaboration, M. G. Aartsen *et al.*, "Constraints on Ultrahigh-Energy Cosmic-Ray Sources from a Search for Neutrinos above 10 PeV with IceCube," *Phys. Rev. Lett.* **117** no. 24, (2016) 241101, `arXiv:1607.05886 [astro-ph.HE]`. [Erratum: Phys. Rev. Lett.119,no.25,259902(2017)].

[228] **IceCube** Collaboration, M. G. Aartsen *et al.*, "Measurement of the ν_μ energy spectrum with IceCube-79," *Eur. Phys. J.* **C77** no. 10, (2017) 692, `arXiv:1705.07780 [astro-ph.HE]`.

[229] **AMS** Collaboration, M. Aguilar *et al.*, "Precision Measurement of the Proton Flux in Primary Cosmic Rays from Rigidity 1 GV to 1.8 TV with the Alpha Magnetic Spectrometer on the International Space Station," *Phys. Rev. Lett.* **114** (2015) 171103.

[230] **AMS** Collaboration, M. Aguilar *et al.*, "Antiproton Flux, Antiproton-to-Proton Flux Ratio, and Properties of Elementary Particle Fluxes in Primary Cosmic Rays Measured with the Alpha Magnetic Spectrometer on the International Space Station," *Phys. Rev. Lett.* **117** no. 9, (2016) 091103.

[231] **AMS** Collaboration, M. Aguilar *et al.*, "Precision Measurement of the Helium Flux in Primary Cosmic Rays of Rigidities 1.9 GV to 3 TV with the Alpha Magnetic Spectrometer on the International Space Station," *Phys. Rev. Lett.* **115** no. 21, (2015) 211101.

[232] **AMS** Collaboration, M. Aguilar *et al.*, "Observation of the Identical Rigidity Dependence of He, C, and O Cosmic Rays at High Rigidities by the Alpha Magnetic Spectrometer on the International Space Station," *Phys. Rev. Lett.* **119** no. 25, (2017) 251101.

[233] **AMS** Collaboration, M. Aguilar *et al.*, "Observation of New Properties of Secondary Cosmic Rays Lithium, Beryllium, and Boron by the Alpha Magnetic Spectrometer on the International Space Station," *Phys. Rev. Lett.* **120** no. 2, (2018) 021101.

[234] R. Enberg, M. H. Reno, and I. Sarcevic, "Prompt neutrino fluxes from atmospheric charm," *Phys. Rev.* **D78** (2008) 043005, `arXiv:0806.0418 [hep-ph]`.

[235] A. Bhattacharya, R. Enberg, M. H. Reno, I. Sarcevic, and A. Stasto, "Perturbative charm production and the prompt atmospheric neutrino flux in light of RHIC and LHC," *JHEP* **06** (2015) 110, `arXiv:1502.01076 [hep-ph]`.

[236] R. Laha and S. J. Brodsky, "IC at IC: IceCube can constrain the intrinsic charm of the proton," `arXiv:1607.08240 [hep-ph]`.

[237] F. Riehn. Personal communication.

[238] R. M. Ulrich, C. Baus, R. Engel, A. Fedynitch, U. Kraemer, T. Pierog, and F. Riehn, "The impact of a fixed-target experiment with LHC beam for astroparticle physics," *PoS* **ICRC2015** (2016) 407.

[239] A. V. Giannini, V. P. Goncalves, and F. S. Navarra, "On the intrinsic charm contribution to the prompt atmospheric neutrino flux," `arXiv:1803.01728 [hep-ph]`.

[240] I. A. Grenier, J. H. Black, and A. W. Strong, "The Nine Lives of Cosmic Rays in Galaxies," *Ann. Rev. Astron. Astrophys.* **53** (2015) 199–246.

[241] P. Blasi, "The Origin of Galactic Cosmic Rays," *Astron. Astrophys. Rev.* **21** (2013) 70, `arXiv:1311.7346 [astro-ph.HE]`.

[242] A. W. Strong, I. V. Moskalenko, and V. S. Ptuskin, "Cosmic-ray propagation and interactions in the Galaxy," *Ann. Rev. Nucl. Part. Sci.* **57** (2007) 285–327, `arXiv:astro-ph/0701517 [astro-ph]`.

[243] I. V. Moskalenko and A. W. Strong, "Production and propagation of cosmic ray positrons and electrons," *Astrophys. J.* **493** (1998) 694–707, `arXiv:astro-ph/9710124 [astro-ph]`.

[244] A. E. Vladimirov, S. W. Digel, G. Johannesson, P. F. Michelson, I. V. Moskalenko, P. L. Nolan, E. Orlando, T. A. Porter, and A. W. Strong, "GALPROP WebRun: an internet-based service for calculating galactic cosmic ray propagation and associated photon emissions," *Comput. Phys. Commun.* **182** (2011) 1156–1161, `arXiv:1008.3642 [astro-ph.HE]`.

[245] E. Orlando, G. Johannesson, I. V. Moskalenko, T. A. Porter, and A. Strong, "GALPROP cosmic-ray propagation code: recent results and updates," 2017. `arXiv:1712.09755 [astro-ph.HE]`. `http://inspirehep.net/record/1645188/files/arXiv:1712.09755.pdf`.

[246] M. Korsmeier, F. Donato, and M. Di Mauro, "Production cross sections of cosmic antiprotons in the light of new data from NA61 and LHCb experiments," *Phys. Rev.* **D97** (2018) 103019, `arXiv:1802.03030 [astro-ph.HE]`.

[247] M. di Mauro, F. Donato, A. Goudelis, and P. D. Serpico, "New evaluation of the antiproton production cross section for cosmic ray studies," *Phys. Rev.* **D90** no. 8, (2014) 085017, `arXiv:1408.0288 [hep-ph]`.

[248] R. Kappl and M. W. Winkler, "The Cosmic Ray Antiproton Background for AMS-02," *JCAP* **1409** (2014) 051, `arXiv:1408.0299 [hep-ph]`.

[249] F. Donato, D. Maurin, P. Salati, A. Barrau, G. Boudoul, and R. Taillet, "Anti-protons from spallations of cosmic rays on interstellar matter," *Astrophys. J.* **563** (2001) 172–184, `arXiv:astro-ph/0103150 [astro-ph]`.

[250] B. E. Bonner *et al.*, "Analyzing Power Measurement in Inclusive pi0 Production at High x(f)," *Phys. Rev. Lett.* **61** (1988) 1918.

[251] **E704, E581** Collaboration, D. L. Adams *et al.*, "Comparison of spin asymmetries and cross-sections in π^0 production by 200 GeV polarized anti-protons and protons," *Phys. Lett.* **B261** (1991) 201–206.

[252] M. G. Echevarria, A. Idilbi, A. Schafer, and I. Scimemi, "Model-Independent Evolution of Transverse Momentum Dependent Distribution Functions (TMDs) at NNLL," *Eur. Phys. J.* **C73** no. 12, (2013) 2636, `arXiv:1208.1281 [hep-ph]`.

[253] T. C. Rogers, "An overview of transverse-momentumdependent factorization and evolution," *Eur. Phys. J.* **A52** no. 6, (2016) 153, `arXiv:1509.04766 [hep-ph]`.

[254] J. Collins and T. C. Rogers, "Connecting Different TMD Factorization Formalisms in QCD," *Phys. Rev.* **D96** no. 5, (2017) 054011, `arXiv:1705.07167 [hep-ph]`.

[255] A. Bacchetta, F. Delcarro, C. Pisano, M. Radici, and A. Signori, "Extraction of partonic transverse momentum distributions from semi-inclusive deep-inelastic scattering, Drell-Yan and Z-boson production," *JHEP* **06** (2017) 081, `arXiv:1703.10157 [hep-ph]`.

[256] I. Scimemi and A. Vladimirov, "Analysis of vector boson production within TMD factorization," *Eur. Phys. J.* **C78** no. 2, (2018) 89, `arXiv:1706.01473 [hep-ph]`.

[257] I. Scimemi and A. Vladimirov, "Systematic analysis of double-scale evolution," `arXiv:1803.11089 [hep-ph]`.

[258] M. G. Echevarria, A. Idilbi, Z.-B. Kang, and I. Vitev, "QCD Evolution of the Sivers Asymmetry," *Phys. Rev.* **D89** (2014) 074013, `arXiv:1401.5078 [hep-ph]`.

[259] P. Sun and F. Yuan, "Energy Evolution for the Sivers Asymmetries in Hard Processes," *Phys. Rev.* **D88** (2013) 034016, `arXiv:1304.5037 [hep-ph]`.

[260] L. D. Isenhower *et al.*, "Polarized Drell-Yan measurements with the Fermilab Main Injector,".

[261] T. Liu and B.-Q. Ma, "Azimuthal asymmetries in lepton-pair production at a fixed-target experiment using the LHC beams (AFTER)," *Eur. Phys. J.* **C72** (2012) 2037, `arXiv:1203.5579 [hep-ph]`.

[262] M. Anselmino, U. D'Alesio, and S. Melis, "Transverse single-spin asymmetries in proton-proton collisions at the AFTER@LHC experiment in a TMD factorisation scheme," *Adv. High Energy Phys.* **2015** (2015) 475040, `arXiv:1504.03791 [hep-ph]`.

[263] E. Steffens, "Estimation of the performance of a HERMES-type gas target internal to the LHC," *PoS* **PSTP2015** (2015) 019.

[264] D. Kikola, M. G. Echevarria, C. Hadjidakis, J.-P. Lansberg, C. Lorce, L. Massacrier, C. M. Quintans, A. Signori, and B. Trzeciak, "Feasibility Studies for Single Transverse-Spin Asymmetry Measurements at a Fixed-Target Experiment Using the LHC Proton and Lead Beams (AFTER@LHC)," *Few Body Syst.* **58** no. 4, (2017) 139, `arXiv:1702.01546 [hep-ex]`.

[265] **Jefferson Lab Hall A** Collaboration, X. Qian *et al.*, "Single Spin Asymmetries in Charged Pion Production from Semi-Inclusive Deep Inelastic Scattering on a Transversely Polarized ^{3}He Target," *Phys. Rev. Lett.* **107** (2011) 072003, `arXiv:1106.0363 [nucl-ex]`.

[266] **Jefferson Lab Hall A** Collaboration, J. Huang *et al.*, "Beam-Target Double Spin Asymmetry A_{LT} in Charged Pion Production from Deep Inelastic Scattering on a Transversely Polarized He-3 Target at $1.4 < Q^2 < 2.7$ GeV^2," *Phys. Rev. Lett.* **108** (2012) 052001, `arXiv:1108.0489 [nucl-ex]`.

[267] A. Signori, A. Bacchetta, M. Radici, and G. Schnell, "Investigations into the flavor dependence of partonic transverse momentum," *JHEP* **11** (2013) 194, `arXiv:1309.3507 [hep-ph]`.

[268] M. Anselmino, M. Boglione, J. O. Gonzalez Hernandez, S. Melis, and A. Prokudin, "Unpolarised Transverse Momentum Dependent Distribution and Fragmentation Functions from SIDIS Multiplicities," *JHEP* **04** (2014) 005, `arXiv:1312.6261 [hep-ph]`.

[269] U. D'Alesio, M. G. Echevarria, S. Melis, and I. Scimemi, "Non-perturbative QCD effects in q_T spectra of Drell-Yan and Z-boson production," *JHEP* **11** (2014) 098, `arXiv:1407.3311 [hep-ph]`.

[270] **HERMES** Collaboration, A. Airapetian *et al.*, "Transverse target single-spin asymmetry in inclusive electroproduction of charged pions and kaons," *Phys. Lett.* **B728** (2014) 183–190, `arXiv:1310.5070 [hep-ex]`.

[271] **COMPASS** Collaboration, C. Adolph *et al.*, "II - Experimental investigation of transverse spin asymmetries in $\mu - p$ SIDIS processes: Sivers asymmetries," *Phys. Lett.* **B717** (2012) 383–389, `arXiv:1205.5122 [hep-ex]`.

[272] **COMPASS** Collaboration, E. S. Ageev *et al.*, "A New measurement of the Collins and Sivers asymmetries on a transversely polarised deuteron target," *Nucl. Phys.* **B765** (2007) 31–70, `arXiv:hep-ex/0610068 [hep-ex]`.

[273] K. Kanazawa, Y. Koike, A. Metz, and D. Pitonyak, "Transverse single-spin asymmetries in proton-proton collisions at the AFTER@LHC experiment," *Adv. High Energy Phys.* **2015** (2015) 257934, `arXiv:1502.04021 [hep-ph]`.

[274] L. Gamberg and Z.-B. Kang, "Single transverse spin asymmetry of prompt photon production," *Phys. Lett.* **B718** (2012) 181–188, `arXiv:1208.1962 [hep-ph]`.

REFERENCES

[275] U. D'Alesio and F. Murgia, "Azimuthal and Single Spin Asymmetries in Hard Scattering Processes," *Prog. Part. Nucl. Phys.* **61** (2008) 394–454, `arXiv:0712.4328 [hep-ph]`.

[276] **COMPASS** Collaboration, K. Kurek and A. Szabelski, "The Gluon Contribution to the Sivers Effect COMPASS results," *J. Phys. Conf. Ser.* **678** no. 1, (2016) 012055.

[277] C. Pisano, D. Boer, S. J. Brodsky, M. G. A. Buffing, and P. J. Mulders, "Linear polarization of gluons and photons in unpolarized collider experiments," *JHEP* **10** (2013) 024, `arXiv:1307.3417 [hep-ph]`.

[278] R. M. Godbole, A. Kaushik, and A. Misra, "Transverse Single Spin Asymmetry in $p + p^\uparrow \to D + X$," `arXiv:1606.01818 [hep-ph]`.

[279] U. D'Alesio, F. Murgia, C. Pisano, and P. Taels, "Probing the gluon Sivers function in $p^\uparrow p \to J/\psi X$ and $p^\uparrow p \to D X$," *Phys. Rev.* **D96** no. 3, (2017) 036011, `arXiv:1705.04169 [hep-ph]`.

[280] Z.-B. Kang, J.-W. Qiu, W. Vogelsang, and F. Yuan, "Accessing tri-gluon correlations in the nucleon via the single spin asymmetry in open charm production," *Phys. Rev.* **D78** (2008) 114013, `arXiv:0810.3333 [hep-ph]`.

[281] X.-D. Ji, "Gluon correlations in the transversely polarized nucleon," *Phys. Lett.* **B289** (1992) 137–142.

[282] H. Beppu, Y. Koike, K. Tanaka, and S. Yoshida, "Contribution of Twist-3 Multi-Gluon Correlation Functions to Single Spin Asymmetry in Semi-Inclusive Deep Inelastic Scattering," *Phys. Rev.* **D82** (2010) 054005, `arXiv:1007.2034 [hep-ph]`.

[283] M. Cacciari, M. Greco, and P. Nason, "The P(T) spectrum in heavy flavor hadroproduction," *JHEP* **05** (1998) 007, `arXiv:hep-ph/9803400 [hep-ph]`.

[284] M. Cacciari, S. Frixione, and P. Nason, "The p(T) spectrum in heavy flavor photoproduction," *JHEP* **03** (2001) 006, `arXiv:hep-ph/0102134 [hep-ph]`.

[285] M. Anselmino, M. Boglione, U. D'Alesio, E. Leader, and F. Murgia, "Accessing Sivers gluon distribution via transverse single spin asymmetries in $p^\uparrow p \to DX$ processes at RHIC," *Phys. Rev.* **D70** (2004) 074025, `arXiv:hep-ph/0407100 [hep-ph]`.

[286] U. D'Alesio, F. Murgia, and C. Pisano, "Towards a first estimate of the gluon Sivers function from A_N data in pp collisions at RHIC," *JHEP* **09** (2015) 119, `arXiv:1506.03078 [hep-ph]`.

[287] D. Kikola, "Prospects for Open Heavy Flavor Measurements in Heavy Ion and p + A Collisions in a Fixed-Target Experiment at the LHC," *Adv. High Energy Phys.* **2015** (2015) 783134.

[288] **PHENIX** Collaboration, C. Aidala *et al.*, "Cross section and transverse single-spin asymmetry of muons from open heavy-flavor decays in polarized $p+p$ collisions at $\sqrt{s}$ = 200 GeV," *Phys. Rev.* **D95** no. 11, (2017) 112001, `arXiv:1703.09333 [hep-ex]`.

[289] L. Massacrier, B. Trzeciak, F. Fleuret, C. Hadjidakis, D. Kikola, J. P. Lansberg, and H. S. Shao, "Feasibility studies for quarkonium production at a fixed-target experiment using the LHC proton and lead beams (AFTER@LHC)," *Adv. High Energy Phys.* **2015** (2015) 986348, `arXiv:1504.05145 [hep-ex]`.

[290] F. Yuan, "Heavy Quarkonium Production in Single Transverse Polarized High Energy Scattering," *Phys. Rev.* **D78** (2008) 014024, `arXiv:0801.4357 [hep-ph]`.

[291] **ALICE** Collaboration, J. Adam *et al.*, "Inclusive quarkonium production at forward rapidity in pp collisions at $\sqrt{s}$ = 8 TeV," *Eur. Phys. J.* **C76** no. 4, (2016) 184, `arXiv:1509.08258 [hep-ex]`.

[292] **ALICE** Collaboration, B. B. Abelev *et al.*, "Measurement of quarkonium production at forward rapidity in pp collisions at $\sqrt{s}$ = 7 TeV," *Eur. Phys. J.* **C74** no. 8, (2014) 2974, `arXiv:1403.3648 [nucl-ex]`.

[293] D. Boer and W. J. den Dunnen, "TMD evolution and the Higgs transverse momentum distribution," *Nucl. Phys.* **B886** (2014) 421–435, `arXiv:1404.6753 [hep-ph]`.

[294] M. G. Echevarria, T. Kasemets, P. J. Mulders, and C. Pisano, "QCD evolution of (un)polarized gluon TMDPDFs and the Higgs q_T-distribution," *JHEP* **07** (2015) 158, `arXiv:1502.05354 [hep-ph]`.

[295] **LHCb** Collaboration, R. Aaij *et al.*, "Measurement of the ratio of prompt χ_c to J/ψ production in pp collisions at $\sqrt{s}$ = 7 TeV," *Phys. Lett.* **B718** (2012) 431–440, `arXiv:1204.1462 [hep-ex]`.

[296] **LHCb** Collaboration, R. Aaij *et al.*, "Measurement of the cross-section ratio $\sigma(\chi_{c2})/\sigma(\chi_{c1})$ for prompt χ_c production at $\sqrt{s}$ = 7 TeV," *Phys. Lett.* **B714** (2012) 215–223, `arXiv:1202.1080 [hep-ex]`.

[297] **LHCb** Collaboration, R. Aaij *et al.*, "Measurement of the $\eta_c(1S)$ production cross-section in proton-proton collisions via the decay $\eta_c(1S) \to p\bar{p}$," *Eur. Phys. J.* **C75** no. 7, (2015) 311, `arXiv:1409.3612 [hep-ex]`.

[298] **LHCb** Collaboration, R. Aaij *et al.*, "Observation of $\eta_c(2S) \to p\bar{p}$ and search for $X(3872) \to p\bar{p}$ decays," *Phys. Lett.* **B769** (2017) 305–313, `arXiv:1607.06446 [hep-ex]`.

[299] J.-P. Lansberg, H.-S. Shao, and H.-F. Zhang, "η_c' Hadroproduction at Next-to-Leading Order and its Relevance to ψ' Production," `arXiv:1711.00265 [hep-ph]`.

[300] A. Schafer and J. Zhou, "Transverse single spin asymmetry in hadronic c,b production," *Phys. Rev.* **D88** no. 1, (2013) 014008, `arXiv:1302.4600 [hep-ph]`.

[301] J.-W. Qiu, M. Schlegel, and W. Vogelsang, "Probing Gluonic Spin-Orbit Correlations in Photon Pair Production," *Phys.*

Rev. Lett. **107** (2011) 062001, `arXiv:1103.3861 [hep-ph]`.

[302] D. Boer and C. Pisano, "Impact of gluon polarization on Higgs boson plus jet production at the LHC," *Phys. Rev.* **D91** no. 7, (2015) 074024, `arXiv:1412.5556 [hep-ph]`.

[303] J. P. Lansberg, "Back-to-back isolated photon-quarkonium production at the LHC and the transverse-momentum-dependent distributions of the gluons in the proton," *Int. J. Mod. Phys. Conf. Ser.* **40** (2016) 1660015, `arXiv:1502.02263 [hep-ph]`.

[304] A. Signori, *Flavor and Evolution Effects in TMD Phenomenology.* PhD thesis, Vrije U., Amsterdam, 2016. `https://userweb.jlab.org/~asignori/research/PhD_thesis_Andrea.pdf`.

[305] D. Boer, "Gluon TMDs in quarkonium production," *Few Body Syst.* **58** no. 2, (2017) 32, `arXiv:1611.06089 [hep-ph]`.

[306] S. Arnold, A. Metz, and M. Schlegel, "Dilepton production from polarized hadron hadron collisions," *Phys. Rev.* **D79** (2009) 034005, `arXiv:0809.2262 [hep-ph]`.

[307] V. Barone, S. Melis, and A. Prokudin, "The Boer-Mulders effect in unpolarized SIDIS: An Analysis of the COMPASS and HERMES data on the $\cos 2\phi$ asymmetry," *Phys. Rev.* **D81** (2010) 114026, `arXiv:0912.5194 [hep-ph]`.

[308] J.-P. Lansberg, C. Pisano, F. Scarpa, and M. Schlegel, "Pinning down the linearly-polarized gluons inside unpolarized protons using quarkonium-pair production at the LHC," `arXiv:1710.01684 [hep-ph]`.

[309] S. Meissner, A. Metz, and K. Goeke, "Relations between generalized and transverse momentum dependent parton distributions," *Phys. Rev.* **D76** (2007) 034002, `arXiv:hep-ph/0703176 [HEP-PH]`.

[310] A. Metz and J. Zhou, "Distribution of linearly polarized gluons inside a large nucleus," *Phys. Rev.* **D84** (2011) 051503, `arXiv:1105.1991 [hep-ph]`.

[311] F. Dominguez, J.-W. Qiu, B.-W. Xiao, and F. Yuan, "On the linearly polarized gluon distributions in the color dipole model," *Phys. Rev.* **D85** (2012) 045003, `arXiv:1109.6293 [hep-ph]`.

[312] D. Boer, S. J. Brodsky, P. J. Mulders, and C. Pisano, "Direct Probes of Linearly Polarized Gluons inside Unpolarized Hadrons," *Phys. Rev. Lett.* **106** (2011) 132001, `arXiv:1011.4225 [hep-ph]`.

[313] S. Catani and M. Grazzini, "QCD transverse-momentum resummation in gluon fusion processes," *Nucl. Phys.* **B845** (2011) 297–323, `arXiv:1011.3918 [hep-ph]`.

[314] D. Boer, W. J. den Dunnen, C. Pisano, M. Schlegel, and W. Vogelsang, "Linearly Polarized Gluons and the Higgs Transverse Momentum Distribution," *Phys. Rev. Lett.* **108** (2012) 032002, `arXiv:1109.1444 [hep-ph]`.

[315] D. Boer, W. J. den Dunnen, C. Pisano, and M. Schlegel, "Determining the Higgs spin and parity in the diphoton decay channel," *Phys. Rev. Lett.* **111** no. 3, (2013) 032002, `arXiv:1304.2654 [hep-ph]`.

[316] P. M. Nadolsky, C. Balazs, E. L. Berger, and C. P. Yuan, "Gluon-gluon contributions to the production of continuum diphoton pairs at hadron colliders," *Phys. Rev.* **D76** (2007) 013008, `arXiv:hep-ph/0702003 [HEP-PH]`.

[317] A. Mukherjee and S. Rajesh, "Probing Transverse Momentum Dependent Parton Distributions in Charmonium and Bottomonium Production," *Phys. Rev.* **D93** no. 5, (2016) 054018, `arXiv:1511.04319 [hep-ph]`.

[318] A. Mukherjee and S. Rajesh, "Linearly polarized gluons in charmonium and bottomonium production in color octet model," *Phys. Rev.* **D95** no. 3, (2017) 034039, `arXiv:1611.05974 [hep-ph]`.

[319] B. Gong, J.-P. Lansberg, C. Lorce, and J. Wang, "Next-to-leading-order QCD corrections to the yields and polarisations of J/Psi and Upsilon directly produced in association with a Z boson at the LHC," *JHEP* **03** (2013) 115, `arXiv:1210.2430 [hep-ph]`.

[320] J. P. Ma, J. X. Wang, and S. Zhao, "Breakdown of QCD Factorization for P-Wave Quarkonium Production at Low Transverse Momentum," *Phys. Lett.* **B737** (2014) 103–108, `arXiv:1405.3373 [hep-ph]`.

[321] M. Boglione and A. Prokudin, "Phenomenology of transverse spin: past, present and future," *Eur. Phys. J.* **A52** no. 6, (2016) 154, `arXiv:1511.06924 [hep-ph]`.

[322] B.-Q. Ma and I. Schmidt, "The Quark orbital angular momentum in a light cone representation," *Phys. Rev.* **D58** (1998) 096008, `arXiv:hep-ph/9808202 [hep-ph]`.

[323] J. She, J. Zhu, and B.-Q. Ma, "Pretzelosity $h_{1T}^{\perp}$ and quark orbital angular momentum," *Phys. Rev.* **D79** (2009) 054008, `arXiv:0902.3718 [hep-ph]`.

[324] H. Avakian, A. V. Efremov, P. Schweitzer, and F. Yuan, "The transverse momentum dependent distribution functions in the bag model," *Phys. Rev.* **D81** (2010) 074035, `arXiv:1001.5467 [hep-ph]`.

[325] A. V. Efremov, P. Schweitzer, O. V. Teryaev, and P. Zavada, "Images of Quark Intrinsic Motion in Covariant Parton Model," *PoS* **DIS2010** (2010) 253, `arXiv:1008.3827 [hep-ph]`.

[326] C. Lorce, B. Pasquini, and M. Vanderhaeghen, "Unified framework for generalized and transverse-momentum dependent parton distributions within a 3Q light-cone picture of the nucleon," *JHEP* **05** (2011) 041, `arXiv:1102.4704 [hep-ph]`.

[327] C. Lorce and B. Pasquini, "Pretzelosity TMD and Quark Orbital Angular Momentum," *Phys. Lett.* **B710** (2012) 486–488, `arXiv:1111.6069 [hep-ph]`.

[328] C. Lorce and B. Pasquini, "On the Origin of Model Relations among Transverse-Momentum Dependent Parton Distributions," *Phys. Rev.* **D84** (2011) 034039, `arXiv:1104.5651 [hep-ph]`.

[329] M. Burkardt and H. BC, "Angular Momentum Decomposition for an Electron," *Phys. Rev.* **D79** (2009) 071501, `arXiv:0812.1605 [hep-ph]`.

[330] C. Lorce and B. Pasquini, "Quark Wigner Distributions and Orbital Angular Momentum," *Phys. Rev.* **D84** (2011) 014015, `arXiv:1106.0139 [hep-ph]`.

[331] X.-D. Ji, "Gauge-Invariant Decomposition of Nucleon Spin," *Phys. Rev. Lett.* **78** (1997) 610–613, `arXiv:hep-ph/9603249 [hep-ph]`.

[332] M. Burkardt, "Impact parameter dependent parton distributions and transverse single spin asymmetries," *Phys. Rev.* **D66** (2002) 114005, `arXiv:hep-ph/0209179 [hep-ph]`.

[333] M. Burkardt, "Chromodynamic lensing and transverse single spin asymmetries," *Nucl. Phys.* **A735** (2004) 185–199, `arXiv:hep-ph/0302144 [hep-ph]`.

[334] M. Burkardt and D. S. Hwang, "Sivers asymmetry and generalized parton distributions in impact parameter space," *Phys. Rev.* **D69** (2004) 074032, `arXiv:hep-ph/0309072 [hep-ph]`.

[335] L. Gamberg and M. Schlegel, "Final state interactions and the transverse structure of the pion using non-perturbative eikonal methods," *Phys. Lett.* **B685** (2010) 95–103, `arXiv:0911.1964 [hep-ph]`.

[336] A. Bacchetta and M. Radici, "Constraining quark angular momentum through semi-inclusive measurements," *Phys. Rev. Lett.* **107** (2011) 212001, `arXiv:1107.5755 [hep-ph]`.

[337] M. Guidal, M. V. Polyakov, A. V. Radyushkin, and M. Vanderhaeghen, "Nucleon form-factors from generalized parton distributions," *Phys. Rev.* **D72** (2005) 054013, `arXiv:hep-ph/0410251 [hep-ph]`.

[338] M. Diehl, T. Feldmann, R. Jakob, and P. Kroll, "Generalized parton distributions from nucleon form-factor data," *Eur. Phys. J.* **C39** (2005) 1–39, `arXiv:hep-ph/0408173 [hep-ph]`.

[339] S. Ahmad, H. Honkanen, S. Liuti, and S. K. Taneja, "Generalized Parton Distributions from Hadronic Observables: Zero Skewness," *Phys. Rev.* **D75** (2007) 094003, `arXiv:hep-ph/0611046 [hep-ph]`.

[340] S. V. Goloskokov and P. Kroll, "The Target asymmetry in hard vector-meson electroproduction and parton angular momenta," *Eur. Phys. J.* **C59** (2009) 809–819, `arXiv:0809.4126 [hep-ph]`.

[341] M. Diehl and P. Kroll, "Nucleon form factors, generalized parton distributions and quark angular momentum," *Eur. Phys. J.* **C73** no. 4, (2013) 2397, `arXiv:1302.4604 [hep-ph]`.

[342] C. Lorce and B. Pasquini, "Multipole decomposition of the nucleon transverse phase space," *Phys. Rev.* **D93** no. 3, (2016) 034040, `arXiv:1512.06744 [hep-ph]`.

[343] A. J. Baltz, "The Physics of Ultraperipheral Collisions at the LHC," *Phys. Rept.* **458** (2008) 1–171, `arXiv:0706.3356 [nucl-ex]`.

[344] J. P. Lansberg, L. Szymanowski, and J. Wagner, "Lepton-pair production in ultraperipheral collisions at AFTER@LHC," *JHEP* **09** (2015) 087, `arXiv:1504.02733 [hep-ph]`.

[345] M. Diehl, "Generalized parton distributions," *Phys. Rept.* **388** (2003) 41–277, `arXiv:hep-ph/0307382 [hep-ph]`.

[346] A. V. Belitsky and A. V. Radyushkin, "Unraveling hadron structure with generalized parton distributions," *Phys. Rept.* **418** (2005) 1–387, `arXiv:hep-ph/0504030 [hep-ph]`.

[347] M. Burkardt, "Impact parameter dependent parton distributions and off forward parton distributions for $\zeta \to 0$," *Phys. Rev.* **D62** (2000) 071503, `arXiv:hep-ph/0005108 [hep-ph]`. [Erratum: Phys. Rev.D66,119903(2002)].

[348] E. R. Berger, M. Diehl, and B. Pire, "Time - like Compton scattering: Exclusive photoproduction of lepton pairs," *Eur. Phys. J.* **C23** (2002) 675–689, `arXiv:hep-ph/0110062 [hep-ph]`.

[349] V. P. Goncalves and W. K. Sauter, "η_c production in photon-induced interactions at a fixed target experiment at LHC as a probe of the odderon," *Phys. Rev.* **D91** no. 9, (2015) 094014, `arXiv:1503.05112 [hep-ph]`.

[350] S. R. Klein, J. Nystrand, J. Seger, Y. Gorbunov, and J. Butterworth, "STARlight: A Monte Carlo simulation program for ultra-peripheral collisions of relativistic ions," *Comput. Phys. Commun.* **212** (2017) 258–268, `arXiv:1607.03838 [hep-ph]`.

[351] D. Yu. Ivanov, A. Schafer, L. Szymanowski, and G. Krasnikov, "Exclusive photoproduction of a heavy vector meson in QCD," *Eur. Phys. J.* **C34** no. 3, (2004) 297–316, `arXiv:hep-ph/0401131 [hep-ph]`. [Erratum: Eur. Phys. J.C75,no.2,75(2015)].

[352] L. Massacrier, J. P. Lansberg, L. Szymanowski, and J. Wagner, "Quarkonium-photoproduction prospects at a fixed-target experiment at the LHC (AFTER@LHC)," in *Photon 2017: International Conference on the Structure and the Interactions of the Photon and 22th International Workshop on Photon-Photon Collisions and the International Workshop on High Energy Photon Colliders CERN, Geneva, Switzerland, May 22-26, 2017*. 2017. `arXiv:1709.09044 [nucl-ex]`. `http://inspirehep.net/record/1625748/files/arXiv:1709.09044.pdf`.

[353] J. Koempel, P. Kroll, A. Metz, and J. Zhou, "Exclusive production of quarkonia as a probe of the GPD E for gluons," *Phys. Rev.* **D85** (2012) 051502, `arXiv:1112.1334 [hep-ph]`.

[354] V. P. Goncalves, "Investigating the transverse single spin asymmetry in the inelastic J/Ψ photoproduction in $p^\uparrow p$ and $p^\uparrow A$ collisions," *Phys. Rev.* **D97** no. 1, (2018) 014001, arXiv:1710.01674 [hep-ph].

[355] V. P. Goncalves and M. M. Jaime, "Exclusive vector meson photoproduction in fixed - target collisions at the LHC," arXiv:1802.04713 [hep-ph].

[356] **NNPDF** Collaboration, E. R. Nocera, R. D. Ball, S. Forte, G. Ridolfi, and J. Rojo, "A first unbiased global determination of polarized PDFs and their uncertainties," *Nucl. Phys.* **B887** (2014) 276–308, arXiv:1406.5539 [hep-ph].

[357] **STAR** Collaboration, B. I. Abelev *et al.*, "Longitudinal Spin Transfer to Lambda and anti-Lambda Hyperons in Polarized Proton-Proton Collisions at $\sqrt{s}$ = 200 GeV," *Phys. Rev.* **D80** (2009) 111102, arXiv:0910.1428 [hep-ex].

[358] **COMPASS** Collaboration, M. Alekseev *et al.*, "Measurement of the Longitudinal Spin Transfer to Lambda and Anti-Lambda Hyperons in Polarised Muon DIS," *Eur. Phys. J.* **C64** (2009) 171–179, arXiv:0907.0388 [hep-ex].

[359] **ALICE** Collaboration, K. Aamodt *et al.*, "Strange particle production in proton-proton collisions at sqrt(s) = 0.9 TeV with ALICE at the LHC," *Eur. Phys. J.* **C71** (2011) 1594, arXiv:1012.3257 [hep-ex].

[360] J. Engel, M. J. Ramsey-Musolf, and U. van Kolck, "Electric Dipole Moments of Nucleons, Nuclei, and Atoms: The Standard Model and Beyond," *Prog. Part. Nucl. Phys.* **71** (2013) 21–74, arXiv:1303.2371 [nucl-th].

[361] N. Yamanaka, B. K. Sahoo, N. Yoshinaga, T. Sato, K. Asahi, and B. P. Das, "Probing exotic phenomena at the interface of nuclear and particle physics with the electric dipole moments of diamagnetic atoms: A unique window to hadronic and semi-leptonic CP violation," *Eur. Phys. J.* **A53** no. 3, (2017) 54, arXiv:1703.01570 [hep-ph].

[362] M. Gonzlez-Alonso, O. Naviliat-Cuncic, and N. Severijns, "New physics searches in nuclear and neutron β decay," arXiv:1803.08732 [hep-ph].

[363] Z.-B. Kang, A. Prokudin, P. Sun, and F. Yuan, "Extraction of Quark Transversity Distribution and Collins Fragmentation Functions with QCD Evolution," *Phys. Rev.* **D93** no. 1, (2016) 014009, arXiv:1505.05589 [hep-ph].

[364] M. Radici and A. Bacchetta, "First Extraction of Transversity from a Global Analysis of Electron-Proton and Proton-Proton Data," *Phys. Rev. Lett.* **120** no. 19, (2018) 192001, arXiv:1802.05212 [hep-ph].

[365] G. S. Bali, S. Collins, B. Glssle, M. Gockeler, J. Najjar, R. H. Rodl, A. Schafer, R. W. Schiel, W. Sldner, and A. Sternbeck, "Nucleon isovector couplings from N_f = 2 lattice QCD," *Phys. Rev.* **D91** no. 5, (2015) 054501, arXiv:1412.7336 [hep-lat].

[366] T. Bhattacharya, V. Cirigliano, R. Gupta, H.-W. Lin, and B. Yoon, "Neutron Electric Dipole Moment and Tensor Charges from Lattice QCD," *Phys. Rev. Lett.* **115** no. 21, (2015) 212002, arXiv:1506.04196 [hep-lat].

[367] C. Alexandrou *et al.*, "Nucleon scalar and tensor charges using lattice QCD simulations at the physical value of the pion mass," *Phys. Rev.* **D95** no. 11, (2017) 114514, arXiv:1703.08788 [hep-lat]. [Erratum: Phys. Rev.D96,no.9,099906(2017)].

[368] **JLQCD** Collaboration, N. Yamanaka, S. Hashimoto, T. Kaneko, and H. Ohki, "Nucleon charges with dynamical overlap fermions," arXiv:1805.10507 [hep-lat].

[369] A. Accardi and A. Bacchetta, "Accessing the nucleon transverse structure in inclusive deep inelastic scattering," *Phys. Lett.* **B773** (2017) 632–638, arXiv:1706.02000 [hep-ph].

[370] N. Brambilla *et al.*, "QCD and Strongly Coupled Gauge Theories: Challenges and Perspectives," *Eur. Phys. J.* **C74** no. 10, (2014) 2981, arXiv:1404.3723 [hep-ph].

[371] **STAR** Collaboration, J. Adams *et al.*, "Experimental and theoretical challenges in the search for the quark gluon plasma: The STAR Collaboration's critical assessment of the evidence from RHIC collisions," *Nucl. Phys.* **A757** (2005) 102–183, arXiv:nucl-ex/0501009 [nucl-ex].

[372] **BRAHMS** Collaboration, I. Arsene *et al.*, "Quark gluon plasma and color glass condensate at RHIC? The Perspective from the BRAHMS experiment," *Nucl. Phys.* **A757** (2005) 1–27, arXiv:nucl-ex/0410020 [nucl-ex].

[373] **STAR** Collaboration, L. Adamczyk *et al.*, "Centrality dependence of identified particle elliptic flow in relativistic heavy ion collisions at $\sqrt{s_{NN}}$=7.7-62.4 GeV," *Phys. Rev.* **C93** no. 1, (2016) 014907, arXiv:1509.08397 [nucl-ex].

[374] **STAR** Collaboration, L. Adamczyk *et al.*, "Elliptic flow of identified hadrons in Au+Au collisions at $\sqrt{s_{NN}}$ = 7.7-62.4 GeV," *Phys. Rev.* **C88** (2013) 014902, arXiv:1301.2348 [nucl-ex].

[375] **STAR** Collaboration, L. Adamczyk *et al.*, "Inclusive charged hadron elliptic flow in Au + Au collisions at $\sqrt{s_{NN}}$ = 7.7 - 39 GeV," *Phys. Rev.* **C86** (2012) 054908, arXiv:1206.5528 [nucl-ex].

[376] **STAR** Collaboration, L. Adamczyk *et al.*, "Beam Energy Dependence of Jet-Quenching Effects in Au+Au Collisions at $\sqrt{s_{NN}}$ = 7.7, 11.5, 14.5, 19.6, 27, 39, and 62.4 GeV," arXiv:1707.01988 [nucl-ex].

[377] N. Brambilla *et al.*, "Heavy quarkonium: progress, puzzles, and opportunities," *Eur. Phys. J.* **C71** (2011) 1534, arXiv:1010.5827 [hep-ph].

[378] **CMS** Collaboration, A. M. Sirunyan *et al.*, "Suppression of Excited Υ States Relative to the Ground State in Pb-Pb Collisions at $\sqrt{s_{NN}}$=5.02TeV," *Phys. Rev. Lett.* **120** no. 14, (2018) 142301, arXiv:1706.05984 [hep-ex].

[379] **CMS** Collaboration, V. Khachatryan *et al.*, "Suppression of $\Upsilon(1S)$, $\Upsilon(2S)$ and $\Upsilon(3S)$ production in PbPb collisions at $\sqrt{s_{NN}}$ = 2.76 TeV," *Phys. Lett.* **B770** (2017) 357–379, arXiv:1611.01510 [nucl-ex].

REFERENCES

[380] **CMS** Collaboration, S. Chatrchyan *et al.*, "Observation of sequential Upsilon suppression in PbPb collisions," *Phys. Rev. Lett.* **109** (2012) 222301, `arXiv:1208.2826 [nucl-ex]`. [Erratum: Phys. Rev. Lett.120,no.19,199903(2018)].

[381] B. Trzeciak, C. Da Silva, E. G. Ferreiro, C. Hadjidakis, D. Kikola, J. P. Lansberg, L. Massacrier, J. Seixas, A. Uras, and Z. Yang, "Heavy-ion Physics at a Fixed-Target Experiment Using the LHC Proton and Lead Beams (AFTER@LHC): Feasibility Studies for Quarkonium and Drell-Yan Production," *Few Body Syst.* **58** no. 5, (2017) 148, `arXiv:1703.03726 [nucl-ex]`.

[382] E. G. Ferreiro and J.-P. Lansberg, "Is bottomonium suppression in proton-nucleus and nucleus-nucleus collisions at LHC energies due to the same effects?," `arXiv:1804.04474 [hep-ph]`.

[383] **CMS** Collaboration, S. Chatrchyan *et al.*, "Indications of suppression of excited Υ states in PbPb collisions at $\sqrt{s_{NN}}$ = 2.76 TeV," *Phys. Rev. Lett.* **107** (2011) 052302, `arXiv:1105.4894 [nucl-ex]`.

[384] C. Mayer, "Charmonium photoproduction in ultra-peripheral and peripheral Pb-Pb and p-Pb collisions with ALICE at the LHC." Quark Matter, May 14, 2018.

[385] **STAR** Collaboration, L. Adamczyk *et al.*, "Energy dependence of J/ψ production in Au+Au collisions at $\sqrt{s_{NN}}$ = 39, 62.4 and 200 GeV," *Phys. Lett.* **B771** (2017) 13–20, `arXiv:1607.07517 [hep-ex]`.

[386] **STAR** Collaboration, L. Adamczyk *et al.*, "Measurement of D^0 Azimuthal Anisotropy at Midrapidity in Au+Au Collisions at $\sqrt{s_{NN}}$=200GeV," *Phys. Rev. Lett.* **118** no. 21, (2017) 212301, `arXiv:1701.06060 [nucl-ex]`.

[387] **STAR** Collaboration, L. Adamczyk *et al.*, "Observation of D^0 Meson Nuclear Modifications in Au+Au Collisions at $\sqrt{s_{NN}}$ = 200GeV," *Phys. Rev. Lett.* **113** no. 14, (2014) 142301, `arXiv:1404.6185 [nucl-ex]`.

[388] **STAR** Collaboration, L. Adamczyk *et al.*, "Elliptic flow of electrons from heavy-flavor hadron decays in Au + Au collisions at $\sqrt{s_{NN}}$ = 200, 62.4, and 39 GeV," *Phys. Rev.* **C95** no. 3, (2017) 034907, `arXiv:1405.6348 [hep-ex]`.

[389] **PHENIX** Collaboration, A. Adare *et al.*, "Heavy Quark Production in $p + p$ and Energy Loss and Flow of Heavy Quarks in Au+Au Collisions at $\sqrt{s_{NN}}$ = 200 GeV," *Phys. Rev.* **C84** (2011) 044905, `arXiv:1005.1627 [nucl-ex]`.

[390] A. Beraudo *et al.*, "Extraction of Heavy-Flavor Transport Coefficients in QCD Matter," `arXiv:1803.03824 [nucl-th]`.

[391] **ATLAS** Collaboration, G. Aad *et al.*, "Measurement of event-plane correlations in $\sqrt{s_{NN}}$ = 2.76 TeV lead-lead collisions with the ATLAS detector," *Phys. Rev.* **C90** no. 2, (2014) 024905, `arXiv:1403.0489 [hep-ex]`.

[392] **ATLAS** Collaboration, T. A. collaboration, "Correlated long-range mixed-harmonic fluctuations in pp, p+Pb and low-multiplicity Pb+Pb collisions with the ATLAS detector," CERN. CERN, Geneva, 2018.

[393] **ATLAS** Collaboration, M. Aaboud *et al.*, "Measurement of longitudinal flow decorrelations in Pb+Pb collisions at $\sqrt{s_{NN}}$ = 2.76 and 5.02 TeV with the ATLAS detector," *Eur. Phys. J.* **C78** no. 2, (2018) 142, `arXiv:1709.02301 [nucl-ex]`.

[394] B. Schenke, S. Jeon, and C. Gale, "Elliptic and triangular flow in event-by-event (3+1)D viscous hydrodynamics," *Phys. Rev. Lett.* **106** (2011) 042301, `arXiv:1009.3244 [hep-ph]`.

[395] P. Bozek, W. Broniowski, and J. Moreira, "Torqued fireballs in relativistic heavy-ion collisions," *Phys. Rev.* **C83** (2011) 034911, `arXiv:1011.3354 [nucl-th]`.

[396] J. Jia and P. Huo, "Forward-backward eccentricity and participant-plane angle fluctuations and their influences on longitudinal dynamics of collective flow," *Phys. Rev.* **C90** no. 3, (2014) 034915, `arXiv:1403.6077 [nucl-th]`.

[397] K. Xiao, F. Liu, and F. Wang, "Event-plane decorrelation over pseudorapidity and its effect on azimuthal anisotropy measurements in relativistic heavy-ion collisions," *Phys. Rev.* **C87** no. 1, (2013) 011901, `arXiv:1208.1195 [nucl-th]`.

[398] X.-Y. Wu, L.-G. Pang, G.-Y. Qin, and X.-N. Wang, "Longitudinal fluctuations and decorrelations of anisotropic flows at the LHC and RHIC energies," `arXiv:1805.03762 [nucl-th]`.

[399] S. Chatterjee and P. Bozek, "Large directed flow of open charm mesons probes the three dimensional distribution of matter in heavy ion collisions," *Phys. Rev. Lett.* **120** no. 19, (2018) 192301, `arXiv:1712.01189 [nucl-th]`.

[400] D. Keane, "The Beam Energy Scan at the Relativistic Heavy Ion Collider," *J. Phys. Conf. Ser.* **878** no. 1, (2017) 012015.

[401] **STAR** Collaboration, L. Adamczyk *et al.*, "Bulk Properties of the Medium Produced in Relativistic Heavy-Ion Collisions from the Beam Energy Scan Program," *Phys. Rev.* **C96** no. 4, (2017) 044904, `arXiv:1701.07065 [nucl-ex]`.

[402] J. Brewer, S. Mukherjee, K. Rajagopal, and Y. Yin, "Searching for the QCD critical point via the rapidity dependence of cumulants," `arXiv:1804.10215 [hep-ph]`.

[403] **PHENIX** Collaboration, A. Adare *et al.*, "Quadrupole Anisotropy in Dihadron Azimuthal Correlations in Central d+Au Collisions at $\sqrt{s_{NN}}$=200 GeV," *Phys. Rev. Lett.* **111** no. 21, (2013) 212301, `arXiv:1303.1794 [nucl-ex]`.

[404] **CMS** Collaboration, S. Chatrchyan *et al.*, "Multiplicity and transverse momentum dependence of two- and four-particle correlations in pPb and PbPb collisions," *Phys. Lett.* **B724** (2013) 213–240, `arXiv:1305.0609 [nucl-ex]`.

[405] **CMS** Collaboration, C. Collaboration, "Observation of prompt J/ψ meson elliptic flow in high-multiplicity pPb collisions at $\sqrt{s_{NN}}$ = 8.16 TeV,".

[406] **PHENIX** Collaboration, A. Adare *et al.*, "Cold-nuclear-matter effects on heavy-quark production in d+Au collisions at

$\sqrt{s_{NN}}$ = 200 GeV," *Phys. Rev. Lett.* **109** no. 24, (2012) 242301, `arXiv:1208.1293 [nucl-ex]`.

[407] A. M. Sickles, "Possible Evidence for Radial Flow of Heavy Mesons in d+Au Collisions," *Phys. Lett.* **B731** (2014) 51–56, `arXiv:1309.6924 [nucl-th]`.

[408] **ALICE** Collaboration, J. Adam *et al.*, "Enhanced production of multi-strange hadrons in high-multiplicity proton-proton collisions," *Nature Phys.* **13** (2017) 535–539, `arXiv:1606.07424 [nucl-ex]`.

[409] **STAR** Collaboration, J. Adam *et al.*, "J/ψ production cross section and its dependence on charged-particle multiplicity in $p + p$ collisions at $\sqrt{s}$ = 200 GeV," `arXiv:1805.03745 [hep-ex]`.

[410] **ALICE** Collaboration, B. Abelev *et al.*, "J/ψ Production as a Function of Charged Particle Multiplicity in pp Collisions at $\sqrt{s}$ = 7 TeV," *Phys. Lett.* **B712** (2012) 165–175, `arXiv:1202.2816 [hep-ex]`.

[411] **ALICE** Collaboration, J. Adam *et al.*, "Measurement of charm and beauty production at central rapidity versus charged-particle multiplicity in proton-proton collisions at $\sqrt{s}$ = 7 TeV," *JHEP* **09** (2015) 148, `arXiv:1505.00664 [nucl-ex]`.

[412] E. G. Ferreiro and C. Pajares, "High multiplicity pp events and J/ψ production at LHC," *Phys. Rev.* **C86** (2012) 034903, `arXiv:1203.5936 [hep-ph]`.

[413] K. Werner, B. Guiot, I. Karpenko, and T. Pierog, "Analysing radial flow features in p-Pb and p-p collisions at several TeV by studying identified particle production in EPOS3," *Phys. Rev.* **C89** no. 6, (2014) 064903, `arXiv:1312.1233 [nucl-th]`.

[414] **CMS** Collaboration, S. Chatrchyan *et al.*, "Measurement of isolated photon production in pp and PbPb collisions at $\sqrt{s_{NN}}$ = 2.76 TeV," *Phys. Lett.* **B710** (2012) 256–277, `arXiv:1201.3093 [nucl-ex]`.

[415] **CMS** Collaboration, S. Chatrchyan *et al.*, "Study of W boson production in PbPb and pp collisions at $\sqrt{s_{NN}}$ = 2.76 TeV," *Phys. Lett.* **B715** (2012) 66–87, `arXiv:1205.6334 [nucl-ex]`.

[416] **CMS** Collaboration, S. Chatrchyan *et al.*, "Study of Z production in PbPb and pp collisions at $\sqrt{s_{NN}}$ = 2.76 TeV in the dimuon and dielectron decay channels," *JHEP* **03** (2015) 022, `arXiv:1410.4825 [nucl-ex]`.

[417] B. Z. Kopeliovich, H. J. Pirner, I. K. Potashnikova, and I. Schmidt, "Mutual boosting of the saturation scales in colliding nuclei," *Phys. Lett.* **B697** (2011) 333–338, `arXiv:1007.1913 [hep-ph]`.

[418] W. Scandale, "Optical layout for the measurement of Short Living Baryon Magnetic Moment using Bended Crystals at LHC." Physics Beyond Collider, Kickoff Workshop, September 6-7, 2016.